Application and Control of Series Active Conditioners in Electrical Distribution Systems

by
Javier Roldán Pérez

supervised by
Prof. Dr. Aurelio García Cerrada
Prof. Dr. Juan Luis Zamora Macho

a dissertation submitted to ICAI School of Engineering
in partial fulfilment of the requirements for the
degree of doctor of philosophy

ICAI School of Engineering
Universidad Pontificia Comillas

Madrid, January 2015

To Amaia, with love.

Karl: "I don't want to eat you. I don't want to eat anybody. It's just I get so hungry. I'm just too big."
Young Ed Bloom: "Did you ever think maybe you're not too big—but, maybe this town's just too small?"

Big Fish (2003), by Tim Burton

Acknowledgements

First of all, I would like to thank Prof. Dr. Aurelio García Cerrada, who has supervised this work. Without his guidance, persistent help, and patience this thesis would not have been possible. He has given me insightful comments and suggestions, and he has spent a lot of time improving the quality of this work. I also would like to thank Prof. Dr. Juan Luis Zamora Macho, who has co-supervised this work. He has given me constructive comments and warm encouragement, and he has made enormous contributions to this thesis. I also appreciate the feedback offered by Pablo García Ganzález, Luis Rouco Rodríguez, and Luis Pagola y de las Heras during the initial steps of this thesis. Special thanks go to Pedro Roncero, Enrique Acha, Emilio Bueno, and Ana Rodríguez for their collaboration in this work.

I would particularly like to thank Miguel Ochoa, who helped me during the most difficult times; he has made enormous contributions to this thesis and he has helped me every time I needed it. Discussions with Aurelio, Juan Luis, and Miguel have been illuminating the most difficult parts of this work. I really appreciate the friendship and help offered by Luis Díez and Javier Renedo during the long working hours in the R+D laboratory. My intellectual debt is to Alberto Rodríguez Cabero, who helped me developing the design of the proportional-resonant controllers.

I would like to show my greatest appreciation to Josep María Guerrero, who hold me in the Microgrid Team at Aalborg University. I really appreciate his comments, support, and friendship. Special thanks also go to Juan Carlos Vasquez, Tomislav Dragricevich, and the rest of the Microgrid Team for their warm support. It has been a privilege to be part of such an exceptional group.

I would like to express my gratitude to INDRA S.A. for their financial support. Without their support the paper included in Appendix D would have never been possible. I also would like to express my gratitude to the Spanish Government, which has partially financed this thesis with the projects ENE2006-13705 and ENE2011-28527-C04-01. Thanks are also due to Ingeteam, RTR S.A., EDIBON S.A., and the Spanish Government's project REDES 2025, which have partially financed different research projects I have been involved within IIT. REDES 2025 was a FEDER (European Regional Development Funds) supported project.

I thank Universidad Pontificia Comillas for the permission to use the laboratory facilities and for the opportunity to teach in the university. Special thanks go to Jose María and Antonio for their help developing the hardware of the prototype. I also want to express my gratitude to the members of the Electronics, Control, and Communications Department, and to the members of the IIT for their support and friendship during these years.

Last but not the least, I would like to thank my wife, Amaia, for her understanding and endless love along these years; she has been there every time I need it. I also want to thank my parents and my family for their encouragement and love during this years.

Abstract

In recent years, the size of electric power systems has greatly increased and the requirements to ensure their proper operation have become highly demanding. Traditionally, the concept of voltage quality (or power quality, loosely speaking) is referred to the average voltage level at the point of common coupling. In most cases, an irregular voltage value is caused by contingencies in the electrical system such as short-circuit faults, which lead to over-currents in distribution feeders that result in a sudden reduction of the voltage level (commonly known as “voltage sags”). End users connected to the grid may be affected by voltage sags, which can eventually lead to production downtime and, in some cases, equipment terminal damage. A more recent concept of voltage quality is not only tied to the average voltage level but also to the voltage waveform. In this sense, voltage harmonics are the major cause of voltage quality deterioration and they are essentially generated by non-linear equipment such as diode or thyristor rectifiers acting on the system impedances. Harmonics may produce pulsation torques in large electric motors, extra iron losses in electric rotating machines, and extra copper losses in the whole system.

A Dynamic Voltage Restorer (DVR) is a power electronics device conceived to protect sensitive loads against voltage sags and swells. A DVR is connected in series with an electrical distribution line and, typically, it consists of a voltage-source converter (VSC), a DC capacitor, a coupling transformer, batteries, and an AC filter. When a voltage sag takes place, the DVR injects the required voltage in series with the feeding line and the load voltage remains unchanged. This will protect sensitive loads and would also improve the low-voltage ride-through capability of distributed generators connected downstream the DVR. The main advantage of DVRs is that only a portion of the power consumed by the load is supplied from the batteries. This means that batteries can be made much smaller than in a typical UPS and cost can be reduced. These reductions in the battery size and cost make DVRs very attractive for high-power applications where a UPS may be infeasible.

A Series Active Power Filter (SeAPF) is another power electronics device aimed at eliminating voltage or current harmonic distortion and it shares the same basic topology with a DVR. For example, if the grid voltage is polluted with harmonics or

is unbalanced, a SeAPF can inject a series-compensating voltage and the load would see an ideal voltage. A SeAPF can be used to improve the load-voltage quality using an appropriate controller and this filtering capability can be added seamlessly to a DVR. A DVR able to compensate voltage harmonics is commonly known as a Series Active Conditioner (SAC), although it is sometimes called versatile DVR or static series compensator (SSC).

This thesis deals with the application and control of a SAC in an electrical distribution system. This device is devoted to protect a sensitive load against a wide variety of voltage disturbances such as voltage sags, swells, and imbalances, as well as voltage harmonics. A state of the art is presented and several control alternatives are studied in detail, with emphasis on harmonic-control algorithms. Power-flow limits and the DC-link voltage control of the VSC are also studied in detail. All the proposals in this thesis were implemented and tested on a prototype. Finally, conclusions and guidelines for further research are presented.

Contents

List of Figures xiv

List of Tables xxii

List of Symbols xxiv

List of Acronyms xxxv

1 Introduction 1
1.1 Background and Overview . . . 1
1.1.1 Voltage Sags: Consequences and Solutions . . . 2
1.1.2 Harmonics and Power Quality . . . 3
1.1.3 Series-Active Compensation . . . 3
1.1.4 SAC Control Techniques . . . 4
1.1.5 Series-Compensation Strategies . . . 5
1.2 Contributions and Scope of this Thesis . . . 5
1.3 Thesis Outline . . . 6

2 Series Active Compensation: State of the Art 9
2.1 Voltage Disturbances . . . 9
2.1.1 Voltage Sags and Swells . . . 9
2.1.2 Voltage Flicker . . . 11
2.1.3 Voltage Harmonics . . . 11
2.2 Series-Connected Devices and Their Alternatives . . . 12
2.2.1 Dynamic Voltage Restorer (DVR) . . . 12
2.2.2 Series Active Power Filter (SeAPF) . . . 12
2.2.3 Alternatives to a Series Active Conditioner . . . 13
2.3 Topologies and Components of an SAC . . . 15
2.3.1 Power Converter . . . 15
2.3.2 Coupling Transformer . . . 16
2.3.3 AC-filter Design . . . 17

2.3.4 Energy-Storage System 18
2.4 Series Compensation Strategies 19
2.4.1 Methods to Compensate Voltage Sags 19
2.4.2 Unbalance Compensation 20
2.4.3 Swell Compensation 21
2.4.4 Active- and Reactive-Power Flow 21
2.4.5 Short-Circuit Current Limitation 22
2.5 Control Structure 22
2.5.1 Open- vs Closed-Loop Control Techniques 22
2.5.2 A Versatile Control 23
2.6 Main Controller 24
2.6.1 Single-Loop Control Strategies 24
2.6.2 Multi-Loop Control Strategies 24
2.7 Harmonic Controller 25
2.7.1 Repetitive Controller (RC) 25
2.7.2 Proportional-Resonant Controllers (PRCs) 27
2.7.3 DFT-Based Controllers 28
2.7.4 Other Harmonic-Control Algorithms 28
2.8 Chapter Summary 29

3 Modelling and Control of an SAC 31
3.1 Overview of a Series Active Conditioner 31
3.2 Model of a Series Active Conditioner 33
3.2.1 Per-Unit Model 33
3.2.2 Continuous-Time Modelling 34
3.2.3 Discrete-Time Model 35
3.2.4 Plant Model with Delays 36
3.3 State-Feedback Controller 37
3.3.1 Design of the Controller 37
3.3.2 Incremental Controller 38
3.4 State-Feedback Controller Application 39
3.4.1 Main Controller Design and Analysis 39
3.4.2 Performance of the State-Feedback Controller 42
3.4.3 Influence of the Load 50
3.5 Alternatives for the Main Controller 51
3.5.1 PID Controller 52
3.5.2 Cascade Controller 52
3.6 Main Controller Trade-offs 54
3.7 Model of the Coupling Transformer 56
3.7.1 Single- and Three-Phase Magnetic Circuit Modelling 56

3.7.2 Limitation and Control of the Magnetic Flux 58
3.8 Chapter Summary 59

4 Troubleshooting a Digital RC 61
4.1 Repetitive Controller Overview 61
4.1.1 Discrete-Time Formulation 61
4.2 Stability Analysis 62
4.3 Steady-State Performance Analysis 64
4.3.1 RC Sensitivity Function 64
4.3.2 Frequency Deviation 65
4.4 Design Criteria 66
4.4.1 $Q(z)$ Filter Design 66
4.4.2 K_x Design 66
4.5 Troubleshooting RCs Implementation 69
4.5.1 Frequency Deviation 69
4.5.2 Providing Internal Stability 73
4.5.3 RC Implementation 75
4.6 Application of a RC to an SAC 76
4.7 Repetitive Controller Alternatives 84
4.7.1 Odd-Harmonic Repetitive Controller 85
4.7.2 Reducing the Buffer Size 86
4.7.3 $nk \pm m$ Repetitive Controller 86
4.7.4 Other Repetitive Controller Alternatives 88
4.8 High-Order Repetitive Controller 88
4.8.1 Constrains of the Weighting Coefficients 89
4.8.2 Selection of the Weighting Coefficients 90
4.8.3 Comparison of HORCs 91
4.9 Applying RC Alternatives 92
4.10 Chapter Summary 96

5 Revisiting Proportional-Resonant Controllers 97
5.1 Proportional-Resonant Controllers Overview 97
5.1.1 Stability Assessment with PRCs 98
5.2 A New Proposal to Design Discrete-Time PRCs 100
5.2.1 Overview of the Design Method 100
5.2.2 Core Normalisation 100
5.2.3 Parametrization and Design Conditions 102
5.2.4 Designing the Compensator Parameters 102
5.2.5 Singular Values of the Compensator Parameters 103
5.3 Grid-Frequency Changes 103

5.3.1 Steady-State Error when the Grid-Frequency Changes 103
5.3.2 Using Taylor Polynomials to Adapt the Controller 104
5.3.3 Application of Chebishov Polynomials 104
5.3.4 Nesting Property of Chebyshov Polynomials 105
5.4 Application of PRCs to an SAC 106
5.5 Performance with Large Frequency Variations 111
5.6 From Repetitive to Resonant Controllers 113
5.7 Chapter Summary 114

6 Steady-State SVB Harmonic Controller 117
6.1 Overview of the Proposed Controller 117
6.1.1 Adaptive Version of the SVB Controller 119
6.2 Steady-State Modelling and Decoupling 119
6.2.1 Steady-State Modelling Equations 119
6.2.2 Plant Modelling Using a Slow Sampling Period 120
6.2.3 Steady-State Decoupling Equations 120
6.3 Steady-State Controller Design 121
6.4 Stability Analysis 121
6.5 Adaptive SVB Controller 123
6.5.1 Plant Model Identification 123
6.5.2 Remarks on Plant Identification 123
6.6 Application of the Steady-State SVB Controller 124
6.6.1 Controller Implementation 124
6.6.2 Series Active Conditioner (SAC) 126
6.6.3 Current SeAPF (CSeAPF) 129
6.7 Chapter Summary 133

7 Power Flow Analysis and Control 135
7.1 Power-Flow Controller Overview 135
7.2 Synchronisation with the Load Current 136
7.3 Application of the Load-Voltage Constraints 138
7.4 Consequences of Load-Voltage Constraints 138
7.5 Power-Flow Controller With Voltage Constraints 140
7.5.1 Reference Voltage Calculation 140
7.5.2 Implementation of the Load-Voltage Constraints 140
7.5.3 Minimum Power Compensation of Voltage Sags 142
7.5.4 Load Impedance Identification 143
7.5.5 Tips for the Controller Implementation 143
7.6 Application of the Power Controller 144
7.6.1 Experimental Results 144

7.7 Chapter Summary 148

8 Conclusions and Further Research 149
8.1 Summary and Conclusions 149
8.2 Suggestions for Further Research 152

Bibliography 155

A Prototype Description 177
A.1 Hardware Description 177
A.2 Data Acquisition and Control System 179
A.2.1 Measurement Chains 179
A.2.2 Controller Implementation and Data Logging 179
A.2.3 Pulse-Width Modulation 179
A.3 Execution Time Measurement 180

B Sag Detection Algorithm 181
B.1 Sag Detection Techniques Overview 181
B.2 Algorithm Description 181
B.2.1 A First Approach to Voltage Sag Detection 181
B.2.2 Improving the Quadrature Signal Estimation 182
B.2.3 Parameter Design 183
B.3 Experimental Results 184

C Repetitive Controller Proofs 185
C.1 High-Order Repetitive Controllers 185
C.1.1 Stability-Based Constraints for HORCs 185
C.1.2 Period-Robust RC Coefficients Derivation 186

D Helping PV Inverters Ride Through Sags 187
D.1 Introduction 188
D.2 Proposed Solution 189
D.2.1 Device Topology and Principles 189
D.2.2 Grid-Connected Controller 190
D.2.3 Grid-Isolated Controller 190
D.3 Controller Elements 191
D.3.1 Synchronous Reference Frame 191
D.3.2 State-Variable Modelling 192
D.3.3 Decoupling Equations 192
D.3.4 Incremental Controller 193
D.4 CCM Modelling and Control 193
D.5 VCM Modelling and Control 195

D.6 DC-Voltage Modelling and Control 196
D.6.1 DC-Voltage Controller in CCM 196
D.6.2 DC-Voltage Controller in VCM 196
D.7 Synchronous Reference Frame Generation 196
D.8 Prototype Description 198
D.9 Results 198
D.10 Conclusion 201

List of Figures

2.1 Types of sags according to the *abc* classification. 10
2.2 (a) Voltage-sourced load and (b) current-sourced load. 11
2.3 (a) Dynamic voltage restorer (DVR) and (b) current SeAPF. 12
2.4 (a) SeAPF placed in the DC-side of a non-linear load and (b) hybrid SeAPF. 13
2.5 (a) Uninterruptible power supply (UPS), (b) static synchronous compensator (STATCOM), (c) shunt active power filter (ShAPF), and (d) Unified power quality conditioner (UPQC). 14
2.6 (a) Multi-pulse converter and (b) modular converter based on two H-bridges. 15
2.7 Positioning the AC filter at (a) the grid-side of the transformer, (b) the converter-side of the transformer, and (c) the load-side of the SAC. . . 17
2.8 SAC topologies using an additional rectifier. The rectifier can be connected to (a) the load-side or (b) the grid-side of the SAC. 18
2.9 Voltage sag compensation strategies. (a) In-phase, (b) pre-sag, (c) phase-advance, and (d) minimum-power compensation method. 19
2.10 Swell compensation using (a) in-phase and (b) phase-advance compensation. Reactive power compensation with (c) constant and (d) flexible load voltage limits. 21
2.11 The most relevant SAC control strategies: (a) open-loop control, (b) single-loop control, (c) multi-loop control, and (d) single-loop control with current feed-forward. 22
2.12 (a) Plug-in and (b) cascade versions of the versatile control structure. 24
2.13 (a) High-order RC (HORC) and (b) multi-rate RC. 26
2.14 Block diagram of a DFT-based controller. 28

3.1 Single-phase schematics of the proposed set-up and the controller of an SAC. 32
3.2 Overview of the control strategy for an SAC. Two independent controllers are used: one for the d-axis and another one for the q-axis. 32

3.3 (a) Direct load-voltage controller and (b) split-reference controller. . . . 33

3.4 Single-phase electrical model for the SAC. 35

3.5 Application of a SF controller to an SAC. Two independent controllers are used, one for each axis (the state-variable predictions are not shown for simplicity). 38

3.6 Incremental implementation of a SF controller. $\Delta(\cdot)$ stands for the incremental operator and $\Sigma(\cdot)$ stands for the accumulation operator (the state-variable predictions are not shown for simplicity). 39

3.7 (left) Pole-zero diagram of (grey) the uncompensated plant in (3.13) ($w''_d[k]$ is the input and $u_{c-d}[k]$ is the output) and (black) the compensated plant, $F_p^d(z)$. (right) Bode diagram of (grey) the uncompensated plant and (black) the compensated plant. 40

3.8 Bode plot of $F_p^d(z)$, $F_p^q(z)$, $F_p^{dq}(z)$, and $F_p^{qd}(z)$, (black) with predictions and (grey) without predictions. 41

3.9 Step response of (left) $F_p^d(z)$ and (right) $F_p^{dq}(z)$ (solid) using predictions and (dashed) without predictions. 41

3.10 Mitigation of a sag (60 % retained voltage) with the SF controller. . . . 42

3.11 Mitigation of a 60 % retained-voltage sag with a SF controller using in-phase compensation (signals referred to a SRF). 43

3.12 FFT modulus of the series-injected voltage: (a) phase-a and (b) d-axis. 44

3.13 Voltage sag compensation (35 % retained voltage) with the SF controller. 44

3.14 Mitigation of a sag type D_a (50 % retained voltage) with the SF controller. 45

3.15 Voltage sag compensation (60 % retained) with harmonics in the grid voltage. 46

3.16 FFT magnitudes of (a) the grid and (b) the load voltage when the SAC is in normal operation and the grid is polluted with harmonics. 47

3.17 Mitigation of a 60 % retained voltage sag when the load is a diode bridge with (a to e) a C-filter and (f to j) an L-filter. 48

3.18 (left) Space-vector diagram and (right) active and reactive power required to restore the load voltage (60 % retained voltage and $\phi = 30$ deg). 49

3.19 Mitigation of a 60 % retained voltage sag using minimum-power compensation. (e and f) Power delivered by the SAC and (g and h) power delivered by the grid. The DC link is maintained constant with the additional rectifier (see Appendix A.) 49

3.20 Voltage sag compensation (65 % retained voltage) when the speed of the phase rotation is limited using (3.24). 51

3.21 Frequency response of the plant when using a parallel RL load, for different values of ϕ (ϕ is the angle of the load impedance). In all cases (except in the one called "no load") the load consumes the nominal current at the rated voltage. 52
3.22 Simplified block diagram of an SAC with a cascade controller. 53
3.23 Root locus of (a) $F_i'(s)$ and (b) $F_i(z)$, shifting the value of K_{p-i}. The arrows indicate the zero-pole movement when K_{p-i} increases. 54
3.24 (left) Open-loop Nichols chart and (right) closed-loop Bode diagram for (solid) the SF, (dotted) the PID, and (dashed) the cascade controllers. 54
3.25 d-axis component of the series-injected voltage for the PID, the cascade, and the SF controllers (left) with the load and (right) without the load. 55
3.26 dq-axis components of the series-injected voltage for the PID, the cascade, and the SF controllers when the load is connected. 55
3.27 Detailed single-phase model of the coupling transformer and the SAC. . 56
3.28 (left) DC component of λ_m for different values of $|u_{cf}|$ and (right) transient response of λ_m for (a) $\alpha_i = \pi/2$ and (b) $\alpha_i = 0$. 57
3.29 Compensation of a 35 % retained voltage sag (a to d) without using any inrush mitigation method and (e to h) using the proposed method. . . 59

4.1 Repetitive controller applied in a plug-in structure. 62
4.2 (left) $|\hat{S}(e^{j\theta_s/N})|$ versus $|H(e^{j\theta_s/N})|$ for $\theta_s = \pm 30°, \pm 60°, \pm 90°, \pm 120°, \pm 150°$, and $\pm 180°$, where "°" means deg. (right) $|\hat{S}(e^{j\theta_s/N})|$ versus θ_s, with $\left|H(e^{j\theta_s/N})\right| = 1$. 64
4.3 RC steady-state performance when the grid frequency deviates. Recall that, ideally, $|\hat{S}(e^{jh\omega_g t_s})| = 0$ for each harmonic h. 65
4.4 (left) Stability regions and (right) particular cases for K_x =0.5, 0.8, 1.2, and 1.5. The region under the surface is stable while that above the surface is unstable. 67
4.5 $|S(e^{j\theta_s/N})|$ versus θ_s for $K_x = 0.5$, 0.8, 1.2, and 1.5. 68
4.6 (left) Modulus (ω) of the smallest pole (continuous-time domain), varying K_x, and (right) transient response of $S(z)$ for different values of K_x. . . 69
4.7 $\hat{S}(z)$ updating N to the nearest integer value with (left) $t_s = 1/5000$ s ($N = 100$ for $\omega_g = 2\pi 50$ rad/s) and (right) $t_s = 1/10000$ s ($N = 200$). . 70
4.8 Fractional delay approximation using (a) a Padé filter and (b) a Thiran filter when $l_e = 0.7$ (the base frequency is the sampling frequency). . . 72
4.9 $\hat{S}(z)$ for the RC updating N and l_e in $L(z)$ (first order Padé) (left) with $t_s = 1/5000$ s ($N = 100$) and (right) with $t_s = 1/10000$ s ($N = 200$) . . 72
4.10 $\hat{S}(z)$ with $L(z)$ using (a) a first-order Padé filter, (b) a first-, (c) a second-, and (d) a third-order Thiran filter. 74
4.11 Application of a RC in a stationary RF. 75

4.12 Implementation of a frequency-adaptive RC for one axis. 76
4.13 Control scheme of an SAC showing the main and the harmonic controller. 77
4.14 Frequency response of $F_e(z)$. The bandwidth of $Q(z)$ is 1350 Hz. 78
4.15 (left) $|\hat{S}(e^{j\theta_s/N})|$ for $K_x = 0.5$ and (right) RC stability regions. 78
4.16 Error and transformer current when an unstable RC is applied to the SAC. 79
4.17 (a) Grid voltage and load voltage (b) without and (c) with the Padé filter. 80
4.18 FFT results at key frequencies of (a) the grid voltage and the load voltage (b) without and (c) with the Padé filter. 80
4.19 Transient of the load voltage when the RC is turned on. 81
4.20 SAC performance when the grid frequency suddenly changes. (a) (grey) Estimated frequency and (black) filtered frequency, (b) value of N, (c) value of l_e, and (d) THD of the load voltage. 81
4.21 Compensation of a three-phase sag with harmonics using a RC+$L(z)$. . 82
4.22 Compensation of an unbalanced voltage sag. (a and e) Grid voltage, (b and f) series-injected voltage, (c and g) load voltage, and (d and h) load current. 83
4.23 Nonlinear load: (a) Grid voltage, (b) series-injected voltage, (c) load voltage, (d) load current, (e) voltage harmonics, and (f) current harmonics (left) with and (right) without a RC. 84
4.24 Steady-state performance of a ODD-RC when the grid frequency deviates (only odd harmonics). 85
4.25 Bode diagram of the $nk \pm m$-RC for (left) $n = 6$ and $m = 1$ and (right) for (solid) $m = 1$, (dotted) $m = 0.5$, and (dashed) $m = 0$. 87
4.26 Schematics of an $nk \pm m$ repetitive controller. 88
4.27 Block diagram of a high-order repetitive controller (HORC). 89
4.28 (left) $|\hat{S}(e^{j\theta_s/N})|$ for a second- and a third-order PR-RC and (right) for a second- and a third- order NR-RC. 93
4.29 $|\hat{S}(e^{j\theta_s/N})|$ for (a) a second-order NR-RC, (b) a third-order NR-RC, (c) a second-order PR-RC, and (d) a third-order PR-RC. Notice that the vertical scales are different. PR means PR-RC and NR means NR-RC. 93
4.30 Harmonic magnitudes for the RC alternatives. (black) Grid voltage, (grey) load voltage without $L(z)$ and (white) load voltage with $L(z)$. $\delta\omega_g = 0.5$ %. 94
4.31 d-axis load voltage when RCa are turned on using an ODD-RC, an EVEN-RC, a $6k$-RC, a $6k \pm 1$-RC, a PR_2-RC, and a NR_2-RC. 95

5.1 (a) Implementation of PRCs as a plug-in and (b) equivalent system to study closed-loop stability. 98
5.2 Nyquist diagram of a PRC (a) with $h = 1$, $N_1'(s) = s\omega_g$, and $F_p'(s) = 1$, and (b) with $F_p'(s) = e^{j\phi_h^p}$ (constant delay). 99

5.3 Bode diagram of the open-loop transfer function of a system with PRCs. The phase margins are ϕ_m^{h+} and ϕ_m^{h-}, while the gain margins are A_m^h in dB. 99
5.4 Frequency response of (5.6) for $\omega_g = 2\pi 50$ rad/s, $t_s = 1/5400$ s and $h = 10$, 20, and 30 ($a = 1$). 101
5.5 PRC implementation: (a) resonator and (b) frequency-adaptive mechanism. 106
5.6 Frequency response of $G(z)$ with alternative β_h^1 and $K_h = K \; \forall \; h$. . . . 107
5.7 Frequency response of $G(z)$ with alternative β_h^2 and $K_h = K \; \forall \; h$. . . . 107
5.8 Frequency response of $G(z)$ when $K_{20} = K$, $K_{20} = 2K$, and $K_{20} = 3K$ (20th harmonic corresponds to 1000 Hz). 108
5.9 d-axis error when PRCs are turned on using (a) β_h^1 and (b) β_h^2. 109
5.10 Sag and harmonic mitigation using PRCs (auxiliary) and a SF (main) controller. 109
5.11 FFT of (black) the grid voltage and the load voltage using (grey) β_h^1 and (white) β_h^2. (left) No frequency deviation and (right) $\delta\omega_g = 0.5$ %. . . . 110
5.12 $|S(e^{j\omega_g(1+\delta\omega_g)ht_s})|$ with (a) β_h^1 and (b) β_h^2. 110
5.13 (a) (grey) PLL frequency and (black) filtered version of the PLL frequency, (b) d-axis error, and (c) load voltage THD for a step change in the grid frequency. 111
5.14 Load voltage FFT depicted at key frequencies for different frequency-adaptive methods (β_h^1). (black) Grid voltage and (white) load voltage. . 112
5.15 Bode diagram of the plant with the PRCs when there is a frequency deviation of $\delta\omega_g = 10$ % and the resonant poles are updated in the controllers. 113
5.16 Abrupt change in the grid frequency from $\delta\omega_g = 8$ % to $\delta\omega_g = 12$ %. . . 113

6.1 SVB controller overview. The controller is implemented using a slow sampling period, called t_s^∇. The plant model can be estimated each sampling period (t_s^∇) and updated in $\mathbf{X}_{(h)}^\nabla$ 118
6.2 System model using the slow sampling period. 120
6.3 Control system diagram adding the uncertainty model ($\mathbf{\Delta}_{(h)}^\nabla$). 122
6.4 Control schemes to be tested. (a) Voltage-harmonic filter (SAC) and (b) current-harmonic filter (CSeAPF). 125
6.5 Practical implementation of the steady-state SVB controller. (a) Harmonic identification, (b) command reconstruction, and (c) slow sampling period controller. 125
6.6 SAC transient performance using the SVB controller when the load is linear. (a) Grid voltage, (b) series-injected voltage, (c) load voltage, and (d) load current. 126

6.7 Voltage sag compensation when applying the SVB controller to an SAC. (a) Grid voltage, (b) series-injected voltage, (c) load voltage, and (d) load current. 127

6.8 (a) Frequency estimated by the PLL, (b) d-axis error, and (c) load voltage THD when the grid frequency suddenly changes from 50 Hz to 50.25 Hz. 128

6.9 Real and imaginary part of the error for the 13th harmonic using $\alpha_d = 0.2$ when (a) $\hat{\mathbf{P}}_{(13)} \approx \mathbf{P}_{(13)}$ and (b) $\hat{\mathbf{P}}_{(13)} \not\approx \mathbf{P}_{(13)}$ (90 degrees mismatch). . . 128

6.10 First attempt to eliminate current harmonics with PRCs in a CSeAPF. (a) dq-axis components of the load voltage and (b) dq-axis components of the load current. 129

6.11 CSeAPF transient response. (a) Grid voltage, (b) series-injected voltage, (c) load voltage, (d) filter inductor current, and (e) load current. 130

6.12 Steady-state performance of the CSeAPF using the steady-state SVB controller. (a) Grid voltage, (b) series-injected voltage, (c) load current, and (d) harmonic components (black) before and (white) after the application of the controller. 131

6.13 Compensation of a three-phase voltage sag (75 % retained voltage) when the CSeAPF is protecting a voltage-sourced non-linear load. (a) Grid voltage, (b) series-injected voltage, (c) load voltage, (d) filter inductor current, and (e) load current. 132

6.14 Compensation of a three-phase voltage sag (75 % retained voltage) when the CSeAPF is protecting a voltage-sourced non-linear load. (a) Grid voltage, (b) series-injected voltage, (c) load voltage, (d) filter inductor current, and (e) load current. 133

7.1 SAC setup with the proposed decoupled power controller. 136

7.2 (a) Space-vector diagram of the VSRF (dq) and the CSRF ($d'q'$) and (b) equivalent circuit to study the power flow thought an SAC. 137

7.3 (left) Active- and (right) reactive-power injection capability of the SAC when (solid) $|\vec{u}_g| = 1$ and (dashed) $|\vec{u}_g| = 0.8$. 139

7.4 Load voltage constraint implementation. Active power is modified with u'_{c-d}, while u'_{c-q} modifies reactive power. Load-voltage constraints imposes limits on both u'_{c-d} and u'_{c-q}. Active power is taken care of first and the remaining voltage-injection capability may be used for reactive-power compensation. 141

7.5 Possible solutions for $\vec{u}_c$ with $|\vec{u}_l| = u_l^- = u_l^+$ when the load is inductive. 142

7.6 Power-flow controller implementation. 142

7.7 (a) DC-link voltage, (b) power controller angles, (c) active power exchange, (d) reactive power exchange, (e) grid voltage module, (f) load voltage module, (g) d'-axis series-injected voltage, and (h) q'-axis series-injected voltage for a step in u_{dc}^*. 145
7.8 (a) DC-link voltage, (b) power controller angles, (c) active power exchange, (d) reactive power exchange, (e) grid voltage module, (f) load voltage module, (g) d'-axis series-injected voltage, and (h) q'-axis series-injected voltage for a step in q^*. 146
7.9 (a) DC-link voltage, (b) power-controller angles, (c) active-power exchange, (d) reactive-power exchange, (e) grid-voltage module, (f) load-voltage module, (g) d'-axis series-injected voltage, and (h) q'-axis series-injected voltage for a voltage sag. 147
7.10 (a) Grid voltage, (b) series-injected voltage, (c) load voltage, (d) harmonics magnitude before the voltage sag, (e) DC-link voltage, (f) SAC power flow, (g) power consumed by the load, and (h) power delivered by the grid when the grid voltage is polluted with harmonics and a voltage sag takes place. 148

A.1 Schematics of the prototype. The power can be taken from (a) an auxiliary electrical network, (b) the grid-side of the SAC, or (c) the load-side of the SAC. 178
A.2 Total execution time in the dSpace platform when a subsystem is enabled. 180

B.1 Bode diagram of $U'(z)/U(z)$ for different values of N_r. 183
B.2 Performance of the sag detection algorithm for a three-phase voltage sag (60% retained voltage), (a to d) without and (e to h) with harmonics, (solid) phase-a, (dashed) phase-b, and (dotted) phase-c. 184

D.1 (a) Reactive current in the new Spanish grid code and (b) sag duration in the new Spanish grid code. 188
D.2 Schematics of the proposed solution. 190
D.3 Block diagram when the proposed device is connected to the grid. . . . 191
D.4 Block diagram when the proposed device is isolated from the grid. . . . 191
D.5 Schematics for the proposed device in CCM (INT closed) and VCM (INT open). 193
D.6 Block diagram of the reference-frame generation to control the proposed device. 197
D.7 (a) Difference between θ_{pll} and θ during an unbalanced voltage sag and (b) grid voltage d-axis (black) and q-axis (grey). 198
D.8 Three-phase voltage sag: (a) grid voltage and (b) PV inverter voltage. . 199

D.9 Three-phase voltage sag: (a) grid current, (b) PV-inverter current, and (c) DC voltage. 199
D.10 Reconnection: (a) PV-inverter voltage, (b) grid current, (c) PV current, and (d) angle difference between the grid and the PV inverters. 200
D.11 Three-phase voltage sag. (a) (black) d-axis and (grey) q-axis of the grid voltage, (b) PV-inverter voltage, (c) proposed device current, and (d) angle difference between the grid and the PV inverters. 201
D.12 Unbalanced voltage sag beginning and end: (a) d-axis (black) and q-axis (grey) of the grid voltage, (b) PV-inverter voltage, (c) PV-inverter current, and (d) phase difference between the grid and PV inverters. . . 202

List of Tables

3.1 Base values to be used in this thesis. 34

4.1 Coefficients for an nth order Thiran filter. 76
4.2 Parameters to carry out the RC tests (see Appendix A for more delails). 77
4.3 Load voltage THD using a first-, a second-, and a third-order Thiran filter. 80
4.4 Weighting coefficients for a second-, a third-, and a fourth-order PR-RC and for a second-, a third-, and a fourth-order NR-RC. The sub-index means “order”. 91
4.5 Range of K_x for different weighting-coefficient configurations. 92

5.1 Computational burden and THD using different RC adaptive mechanisms, for $\delta\omega_g = 0$, 0.5, 1, and 3 %. “-” means “unstable”. 112

List of Symbols

Greek Symbols

α_d	Gain of the SVB controller, see (6.11)
α_h	Parameter of a PRC compensator, see (5.7)
α_i	Initial angle of the series-injected voltage, see (3.33)
β	Advance angle, see Fig. 3.18
β_h	Parameter of a PRC compensator, see (5.7)
β_h^1, β_h^2	Alternatives to calculate the value of β_h, see (5.19)
$\mathbf{\Delta}_{(h)}^{\triangledown}$	Model of the uncertainty, in matrix form. See (6.14)
$\mathbf{\Gamma}$	Discrete-time input matrix of a system, see (3.4)
$\mathbf{\Gamma}_u$, $\mathbf{\Gamma}_i$	Discrete-time input matrix related to u_i and i_l, respectively. See (3.5)
$\mathbf{\Gamma}_w$	Matrix related to the virtual commands ($\vec{w}$), see (3.8)
$\mathbf{\Gamma}_d$, $\mathbf{\Gamma}_q$, $\mathbf{\Gamma}_{dq}$	d-axis, q-axis, and coupling terms of the discrete-time input matrix, see (3.5)
$\mathbf{\Phi}$	Discrete-time state matrix of a system, see (3.4)
$\mathbf{\Phi}_x$	Matrix related to the decoupling equations, see (3.9)
$\mathbf{\Phi}_d$, $\mathbf{\Phi}_q$, $\mathbf{\Phi}_{dq}$	d-axis, q-axis, and coupling terms of the discrete-time state matrix, see (3.5)
$\delta\omega_g$	Frequency deviation in percentage, see (4.14)
δe	Command signal generated by the harmonic controller, see Fig. 3.1

$\delta_{(h)}$	Magnitude modelling error for the harmonic (h), see (6.14)
ϵ	A small value, see page 103
η_h	Normalisation factor of a PRC, see page 100
$\gamma_{11}^i, \ldots, \gamma_{42}^i$	Terms of the matrix $\mathbf{\Gamma}_i$, see (3.7)
$\gamma_{11}^u, \ldots, \gamma_{42}^u$	Terms of the matrix $\mathbf{\Gamma}_u$, see (3.7)
$\hat{\omega}_g$	Estimation of the grid frequency, in rad/s. See page 70
$\hat{\omega}_g^f$	Filtered estimation of the grid frequency, in rad/s. See page 70
$\lambda_m^{dc},\ \lambda_m^{ac}$	DC- and AC-component of the magnetising flux, see (3.34)
λ_r	Design parameter of the filter $Q_{hp}(z)$, see (4.38)
λ_x	Auxiliary variable used to compute the limits of K_x, see (4.20)
$\lambda_{t-c},\ \lambda_{t-l},\ \lambda_m$	Flux-linkages of the primary and secondary windings of the coupling transformer, and magnetising flux. See (3.30)
ω	Frequency in rad/s
ω_b	Base frequency, see Table 3.1
ω_c	Repetitive controller bandwidth, see page 64
ω_g	Grid frequency in rad/s, see page 35
ω_n	Nominal frequency, see Table 3.1
ϕ	Angle of the impedance, see Fig. 3.18
$\phi_h^g,\ \phi_h^c,\ \phi_h^r,\ \phi_h^p$	Open-loop, compensator, core, and plant phase at the resonant frequency of a PRC. See (5.14)
$\phi_m^+,\ \phi_m^-$	Positive and negative phase margins of a system with PRCs, see (5.4)
$\phi_{(h)}$	Phase modelling error for the harmonic (h), see (6.14)
$\phi_{11}, \ldots, \phi_{44}$	Terms of the matrix $\mathbf{\Phi}$, see (3.6)
$\theta_e(\omega)$	Angle of the modelling errors, see page 66
θ_g	Angle estimated by the PLL, see Fig. 4.11

θ_s	Period of one harmonic, in rad/s. See page 64
θ_t	Phase rotation of the coupling transformer, see Table 3.1
ε	Fractional part of the sampling period not included in N, see (4.26)
φ	Current synchronisation angle, see Fig. 3.18
ζ	Integral term of the SF controller, see (3.16)

Uppercase Latin Symbols

$\mathbf{0}$	Matrix full of zeros of the appropriate size
$\boldsymbol{A}$	State matrix of a continuous-time state-variable representation, see (3.1)
$\boldsymbol{B}$	Input matrix of a continuous-time state-variable representation, see (3.1)
$\boldsymbol{K}_d$, $\boldsymbol{K}_q$	d- and q-axis gain vectors of the SF controller, see page 38
$\boldsymbol{R}(\varphi)$	Rotation matrix, see (7.5)
$\hat{F}_p(z)$	Model of $F_p(z)$, see (4.8)
$\hat{S}(z)$	Simplified sensitivity function, see (4.12)
$\mathbf{C}^{\triangledown}_{(h)}(z^{\triangledown})$	Controller matrix of the SVB controller, see page 117
$\mathbf{E}^{\triangledown}_{(h)}$	Steady-state d- and q-axis components of the error and the coupled error signals, respectively, in matrix form. See (6.7)
$\mathbf{F}^{\triangledown}_{(h)}(z^{\triangledown})$	Closed-loop transfer function of the plant with the SVB controller, see (6.12)
$\mathbf{I}$	Identity matrix of the appropriate size
$\mathbf{P}_{(h)}$, $\hat{\mathbf{P}}_{(h)}$	Frequency response of $\vec{P}(z)$, in matrix form, and model of $\mathbf{P}_{(h)}$. See page 119
$\mathbf{U}^{\triangledown}_{(h)}$	Steady-state d- and q-axis components of the command signal, in matrix form. See (6.7)
$\mathbf{X}^{\triangledown}_{(h)}$	Decoupling matrix of the SVB controller, see page 117
$\mathbf{Z}^{\triangledown}(z^{\triangledown})$	Transfer function of a delay, in matrix form. See (6.8)

$\vec{D}(z)$	z-domain space vector of the disturbance signal, see page 119
$\vec{E}(z)$	z-domain space vector of the error signal, see page 119
$\vec{P}(z)$	z-domain space-vector-based transfer function of the plant, see page 119
$\vec{U}(z)$	z-domain space vector of the plant output signal, see page 119
$\vec{Y}(z)$	z-domain space vector of the plant input signal, see page 119
$A_h^g,\ A_h^c,\ A_h^r,\ A_h^p$	Open-loop, compensator, core, and plant gain at the resonance frequency of a PRC. See (5.13)
A_m	Gain margin of a system, see page 99
$A_x(z)$	Denominator of $\hat{F}_p(z)$, see (4.9)
$B_x^-(z),\ B_x^+(z)$	Numerator of $\hat{F}_p(z)$ with and without NMP zeros, respectively. See (4.9)
C_f	Filter capacitor, see Fig. 3.4
C_h	Coefficients of a Taylor polynomial, see (5.22)
C_{dc}	DC-link capacitor, see Fig. 3.1
D	Total delay approximated by a Thiran filter, see page 73
$E(z)$	Error of a control system in the z-domain, see Fig. 4.1
$F_p^d(z),\ F_p^q(z)$	d- and q-axis closed-loop transfer functions, see (3.21)
$F_p^{dq}(z),\ F_p^{qd}(z)$	Closed-loop transfer functions of the coupling terms, see (3.21)
$F_{(h)}$	Auxiliary variable used to compute $\mathbf{F}^{\triangledown}_{(h)}(z)$, see (6.17)
$F_e(z)$	Discrete-time transfer function of $E(z)/R(z)$, see (4.7) and (5.21)
$G'(s),\ G(z)$	s- and z-domain open-loop transfer function of a system, see (5.4)
$G_e(\omega)$	Modulus of the modelling errors, see page 66
$G_h(z)$	Open-loop transfer function of a system with one PRC, see (5.5)
$G_x(z)$	Discrete-time transfer function of the RC compensator, see (4.7)
$H(z)$	Transfer function of $W(z)Q(z)$, see (4.12)

I_b	Base current, see Table 3.1
I_n	Nominal current, see Table 3.1
$K_h,\ K$	Gain of a PRC and gain of all the PRCs, respectively. See (5.1) and page 103
K_p	Proportional gain of a PID, see (3.27)
K_s	Gain of the RC core, see (4.39)
K_x	Gain of a repetitive controller, see Fig. 4.1
L	Integer part of total delay approximated by a Thiran filter, see page 73
$L(z)$	Frequency-adaptive filter of a RC, see (4.3)
L_g	Inductive part of the grid impedance, see page 35
L_l	Inductive part of the load impedance, see (3.25)
L_t	Leakage inductance of the coupling transformer, see Fig. 3.4
L_f	Filter inductance, see Fig. 3.4
L_{t-c}, L_{t-l}, L_m	Inductances of the coupling transformer model, see (3.31)
M	Size of the filter $Q(z)$, see (4.16)
N	Number of samples within one period of the grid voltage, see (4.2) and (6.5)
$N'_h(s),\ N_h(z)$	s- and z-domain compensator of a proportional-resonant controller, respectively. See page 97
N_d	Filter of a PID, see (3.27)
NC	Number of calculations, see (5.27) and (5.30)
P_l	Active power consumed by the load, see pages 77 and 178
$PR'(s),\ PR(z)$	s- and z-domain transfer function of all the PRCs in parallel. See (5.2) and (5.3)
$PR'_h(s),\ PR_h(z)$	s- and z-domain core of a proportional-resonant controller, respectively. See (5.1)

$PR_h^c(z)$, $PR_h^r(z)$	Transfer function of the compensator and the core of a PRC, respectively. See (5.7)
$Q(z)$	Filter that limits the RC bandwidth, see page 62
Q_l	Reactive power consumed by the load, see pages 77 and 178
$Q_{hp}(z)$, $Q_{lp}(z)$	High- and low-pass filter of $Q(z)$, see page 74
$R(z)$	Reference of a control system in the z-domain, see Fig. 4.1
R_g	Resistive part of the grid impedance, see page 35
R_l	Resistive part of the load impedance, see (3.25)
R_t	Resistive part of the leakage inductance, see Fig. 3.4
R_{t-c}, R_{t-l}	Resistive part of the primary and secondary windings of the coupling transformer, see (3.30)
$RC(z)$	Discrete-time transfer function of a RC, see Fig. 4.1
$RC_o(s)$	Core of a repetitive controller, see (4.1)
$S(z)$	RC sensitivity function, see (4.7) and (5.21)
S_b	Base power (VA), see Table 3.1
SR_β	Slew-rate limit of phase-angle rotation, see (3.24)
T_d	Differential time constant of a PID, see (3.27)
T_i	Integral time constant of a PID, see (3.27)
U_b	Base voltage, see Table 3.1
$U_c(z)$	z-transform of $u_c(t)$ (both d- and q-axis), see (3.21)
U_n	Nominal voltage, see Table 3.1
$W(z)$	Transfer-function related to the RC core, see (4.3)
$Y(z)$	Output of a control system in the z-domain, see Fig. 4.1
Z_b	Base impedance, see Table 3.1
Z_g	Impedance of the grid, see Fig. 3.4
Z_l	Impedance of the load, see Fig. 3.4

Functions and Operators

$+$	Pseudo-inverse matrix, see (3.10)
$\Delta(\cdot)$	Incremental operator, see page 39
$\Sigma(\cdot)$	Accumulation operator, see page 39
t	Transposed matrix, see (3.10)
$T_h(\cdot)$	hth-order Taylor polynomial, see (5.24)

Lowercase Latin Symbols

$\boldsymbol{u}$	Input vector of a state-variable representation, see (3.1)
$\boldsymbol{x}$	State vector of a state-variable representation, see (3.1)
$\boldsymbol{x}_d$, $\boldsymbol{x}_q$	d- and q-axis components of the state vector $\boldsymbol{x}$, see (3.5)
$\hat{\boldsymbol{x}}$	Predicted value of the state-variable vector $\boldsymbol{x}$, see (3.15)
a	Damping factor of a PRC core, see (5.8)
a_i	Coefficients of a discrete-time filter, see (4.16)
a_t	Conversion ratio of the coupling transformer, see Table 3.1
e	Error of the control system, see Fig. 3.1
$e^{\bigtriangledown}_{(h)-d}$, $e^{\bigtriangledown}_{(h)-q}$	Real- and imaginary-part of the decoupled error signal for the harmonic (h), see page 117
$e^{c\bigtriangledown}_{(h)-d}$, $e^{c\bigtriangledown}_{(h)-q}$	Real- and imaginary-part of the coupled error signal for the harmonic (h), see page 117
h	Harmonic index
i	Generic index
i_c	Current through the filter capacitor, see Fig. 3.4
i_f	Current through L_f, see Fig. 3.4
i_g	Current through the grid, see Fig. 3.4
i_l	Current consumed by the load, see Fig. 3.4

i_r	Rest-of-the-load current, see Fig. 3.4
i'_{l-d}, i'_{l-q}	d- and q-axis components of $\vec{\imath}_l$ in the CSRF, see (7.5)
i_{t-c}, i_{t-l}	Current through the primary and secondary windings of the coupling transformer, see (3.31)
j	Imaginary unit
k	Between square brackets or as a subscript of square brackets means discrete-time sample, see page 35
l_e	Fractional part of a delay, see (4.27)
m	Maximum value of an index
n	Maximum value of an index
p	Active power injected by the SAC, see (7.3)
p^+, p^-	Maximum and minimum limit of active-power injection, see page 140
p_g	Active power delivered by the grid, see page 136
p_l	Active power consumed by the load, see page 136
q	Reactive power injected by the SAC, see (7.3)
q^+, q^-	Maximum and minimum limit of reactive-power injection. See page 140
q_g	Reactive power delivered by the grid, see page 136
q_l	Reactive power consumed by the load, see page 136
s	Laplace variable
t	Time variable
t_c	Equivalent delay introduced by the main controller, see page 58
t_p	Period of the disturbance, see page 61
t_s	Sampling period of the control system, see page 35
$t_s^{\triangledown}$	Slow sampling-period of a control system, see page 117
t_{sw}	Switching period, see pages 77 and 178

u_i''	Converter output voltage computed two steps before being applied, see (3.14)
$u^{\triangledown}_{(h)-d}$, $u^{\triangledown}_{(h)-q}$	Real- and imaginary-part of the command signal for the harmonic (h), see page 117
u_c	Series-injected voltage, see Fig. 3.4
u_e	Command generated by the harmonic controller plus the error $(e + \delta e)$, see Fig. 3.1
u_g	Grid voltage, see Fig. 3.4
u_i	Voltage generated by the voltage source converter, see Fig. 3.4
u_l	Voltage across the load, see Fig. 3.4
u_l^+, u_l^-	Maximum and minimum limit of the load voltage, see page 138
u'_{c-d}, u'_{c-q}	d- and q-axis components of $\vec{u}_c$ in the CSRF, see Section 7.2
u'^+_{c-d}, u'^-_{c-d}	Maximum and minimum limit of u'_{c-d}, see (7.20)
u'^+_{c-q}, u'^-_{c-q}	Maximum and minimum limit of u'_{c-q}, see (7.22)
u_{cf}	Voltage across the filter capacitor, see Fig. 3.4
u_{dc}	Voltage of the DC-link, see Fig. 3.1
u'_{g-d}, u'_{g-q}	d- and q-axis components of $\vec{u}_g$ in the CSRF, see Section 7.2
u'_{l-d}, u'_{l-q}	d- and q-axis components of $\vec{u}_l$ in the CSRF, see Section 7.2
w	Virtual command signal, see Fig. 3.2
w'	Virtual command signal delayed one sample, see (3.11)
w''	Controller output signal, see (3.12)
$z^{\triangledown}$	z-variable using the slow sampling period $(t_s^{\triangledown})$, see page 117

Subscripts and Superscripts

(h)	For an specific harmonic, see page 119
$*$	Set-point value, see page 32
α	α-axis component, see page 58

β	β-axis component, see page 58
$\vec{}$	Space vector or vector-based transfer function, see page 31
d	d-axis component, see page 31
q	q-axis component, see page 31

List of Acronyms

$6k$-RC	$6k$-harmonic repetitive controller
$n \pm m$-RC	$n \pm m$-harmonic repetitive controller
AC	Alternating current
APF	Active power filter
CR	Command reconstruction
CSeAPF	Current series active power filter
CSRF	Current synchronized reference frame
DC	Direct current
DFT	Discrete Fourier transform
DSP	Digital signal processor
EVEN-RC	Even-harmonic repetitive controller
FFT	Fast Fourier transform
FIR	Finite impulse response
HE	Harmonic estimation
HORC	High-order repetitive controller
HP	High pass
IGBT	Insulated gate bipolar transistor
NMP	Non-minimum phase
NR-RC	Noise-robust repetitive controller
MRF	Multiple-reference frame
LPF	Low-pass filter
ODD-RC	Odd-harmonic repetitive controller

PCC	Point of common coupling
PE	Power electronics
PFC	Power factor corrector
PI	Proportional-integral
PID	Proportional-integral-differential
PLL	Phase-locked loop
PRC	Proportional-resonant controller
PR-RC	Period-robust repetitive controller
PWM	Pulse-width modulation
RC	Repetitive controller
RF	Reference frame
SAC	Series active conditioner
SeAPF	Series active power filter
ShAPF	Shunt active power filter
SF	State feedback
SRF	Synchronous reference frame
SSR	Solid state relay
STATCOM	Static compensator
SVB	Space-vector based
THD	Total harmonic distortion
UPQC	Unified power quality conditioner
UPS	Uninterruptible power supply
VSC	Voltage-sourced converter
VSeAPF	Voltage series active power filter
VSRF	Voltage synchronized reference frame

Chapter 1

Introduction

This thesis deals with the application and control of a series active conditioner in an electrical distribution system. This device (based on a voltage source converter VSC) is devoted to protect a sensitive load against a wide variety of voltage disturbances such as voltage sags, swells, and imbalances, as well as voltage harmonics. A state of the art is presented and several control alternatives are studied in detail, with emphasis on harmonic-control algorithms. Power-flow limits and the DC-link voltage control of the VSC are also studied in detail. All the proposals in this thesis were implemented and tested on a prototype. Finally, conclusions and guidelines for further research are presented.

1.1 Background and Overview

Electric power has become a commodity not only in industry but also in domestic applications. In consequence, the size of electric power systems has greatly increased and the requirements to ensure their proper operation have become highly demanding. According to Fuchs and Masoum [1]:

> The term "power quality" is used synonymously with "supply reliability", "service quality", "voltage quality", "quality of supply" and "quality of consumption". It is generally meant to express the quality of voltage and/or the quality of current and can be defined as: the measure, analysis and improvement of the bus voltage to maintain a sinusoidal waveform at rated voltage and frequency.

This definition includes momentary and steady-state phenomena. Very similarly, "power quality" is defined in by Dugan et al. [2] as:

> Any power problem manifested in voltage, current or frequency deviations that results in failure or malfunction of customer equipment.

Although "power quality" is a convenient term for power, voltage, and current, the solutions investigated in this thesis are actually more related to the quality of voltage rather than power or current.

Initially, the concept of voltage quality (or power quality, loosely speaking) was referred to the average voltage level at the point of common coupling (PCC). In most cases, an improper value is caused by contingencies in the electrical system such as short-circuit faults, which lead to over-currents in distribution feeders that result in a sudden reduction of the voltage level (commonly known as "voltage sags") [1]. End users connected to the grid may be affected by voltage sags, which can eventually lead to production downtime and, in some cases, equipment terminal damage. A more recent concept of voltage quality is not only tied to the average voltage level but also to the voltage waveform [2]. Voltage harmonics are the major cause of voltage quality deterioration and they are essentially generated by non-linear equipment such as diode or thyristor rectifiers acting on the system impedances. However, saturation of distribution transformers can generate voltage harmonics as well [3]. Harmonics may produce pulsation torques in large electric motors, extra iron losses in electric rotating machines, and extra copper losses in the whole system [4, 5].

For a long time already, power electronics (PE) solutions have been applied to improve the overall electrical system performance and breakthroughs in switching technologies have facilitated a widespread use of voltage-source converters (VSCs)[1] for this purpose. Nowadays, VSCs have become the benchmark technology and they are widely used for grid-connected applications. Among them, power quality solutions based on VSCs have become very popular since they provide great versatility using a rather common technology.

1.1.1 Voltage Sags: Consequences and Solutions

Most downtimes in industry are related to voltage sags [7]. Unfortunately, it is difficult to immunize equipment against voltage sags. In fact, if a sag lasts for a long time, equipment shut down is inevitable.

Uninterruptible power supplies (UPSs) are a common solution for protecting sensitive loads against voltage sags [8]. UPSs are widely applied to protect low-power loads such as computers or small electronic loads. These devices replace the grid when a voltage sag takes place and, when the voltage level recovers, loads are gently reconnected to the grid. However, a UPS has to deliver all the power consumed by the loads during the sag. This means that a UPS requires large batteries to protect loads against long-duration voltage sags and, consequently, its application is greatly restricted by the size and cost of the batteries.

[1]Yazdani and Iravani [6], who are reputed authors in this fied, use the term "voltage-sourced converters". However, the one used here seems to be more widely spread.

1.1.2 Harmonics and Power Quality

A great deal of modern electrical equipment is DC fed, so an AC-DC converter is required at the front end. AC-DC converters are commonly built with switching devices that, in many cases, lead to a non-sinusoidal current consumption. All but the fundamental component of these currents are commonly known as "harmonic currents" and they cause harmonic voltage drop in power transformers and electrical distribution lines. Electrical standards are intended to ensure proper operation and compatibility of all electrical equipment and they impose limits on the amount of both current harmonics injected to the grid and voltage harmonics at the PCC [9]. Current-harmonic consumption is reduced if converters are designed using VSC-based technologies. In this case, it is easier to comply with regulations, although cost increases. Power factor correctors (PFCs) can be applied to limit the current-harmonic consumption as well, but each load must have its own PFC [10].

Shunt passive filters are a classic solution to filter out current harmonics. These filters are cheap and can be applied to installations already working, so full upgrade of each individual load is not required [11]. However, shunt passive filters can lead to unwanted resonances and their filter capability is strongly related to the grid and the load conditions since they provide no flexibility. In most cases, a shunt active power filter (ShAPF) could replace a passive filter. ShAPFs can provide a large current-harmonic attenuation and their performance do not depend on the grid conditions. The cost of this device is still high, but it may be cost effective if it is applied to a group of non-linear loads.

1.1.3 Series-Active Compensation

A Dynamic Voltage Restorer (DVR) is a PE device conceived to protect sensitive loads against voltage sags and swells. A DVR is connected in series with an electrical distribution line and, typically, it consists of a VSC, a DC capacitor, a coupling transformer, batteries, and an AC filter. When a voltage sag takes place, a DVR injects the required voltage in series with the feeding line and the load voltage remains unchanged [12]. This will protect sensitive loads and would also improve the low-voltage ride-through capability of distributed generators connected downstream the DVR. The main advantage of DVRs is that only a portion of the power consumed by the load is supplied from the batteries. This means that batteries can be made much smaller than in a typical UPS and cost can be reduced. These reductions in the battery size and cost make DVRs very attractive for high-power applications where a UPS may be infeasible.

When non-linear loads are of the so-called voltage-sourced type, a ShAPF leads to poor results. In this case, Green and Marks [13] suggest replacing the ShAPF with a Series Active Power Filter (SeAPF), which has the same basic topology of a DVR, although the batteries can be removed because no active-power injection is required.

The performance of a SeAPF can be improved adding a shunt passive filter close to the load, and this alternative is commonly known as a hybrid SeAPF [14]. In some cases, a hybrid SeAPF is cheaper than a SeAPF because, although a hybrid SeAPF is made of more components, their ratings can be reduced [13].

A SeAPF can be used to improve the load-voltage quality using an appropriate controller and this filtering capability can be added seamlessly to a DVR [15]. A DVR able to compensate voltage harmonics is commonly known as a Series Active Conditioner (SAC), although is sometimes called versatile DVR [15] or static series compensator (SSC) [16, 17]. However, the name SAC will be used from now on because it is clearer according to the author's opinion.

1.1.4 SAC Control Techniques

The control system is of paramount importance in an SAC because the way in which it is undertaken has a major impact on the device performance. First of all, the transient response of the output voltage needs to be fast enough to ensure that the load remains unaware when a voltage sag takes place. However, this requirement is difficult to accomplish because the AC filter leads to a lightly-damped resonance that makes the controller design rather delicate. This resonance needs to be passively or actively damped to avoid large voltage excursions when the SAC is switched on and to improve controlabillity. Passive damping reduces the efficiency, so active damping is the most attractive solution to explore [18]: state-feedback [19], cascade [20], and Posicast [21] controllers are alternatives that have been studied for this purpose because of their potential advantages.

Voltage harmonics may appear as a result of non-linear loads connected far away. In addition, if the sensitive load to be protected is non-linear, its harmonic currents would produce harmonic voltage drops in the coupling transformer and the AC filter of the SAC. In any of these cases, a harmonic-control algorithm is required to provide a clean load voltage [22].

Proportional-resonant controllers (PRCs) are widely used to deal with harmonics in power systems [23] and their digital implementation has drawn much attention because, if they are not carefully implemented, their performance deteriorate and stability might be threatened [24]. Another alternative to compensate harmonics are repetitive controllers (RCs), which are quite popular in the PE field [25]. RCs are easy to design and their computational burden does not depend on the number of harmonics to be compensated. Therefore, a RC is an excellent solution to deal with a large (or undetermined) number of harmonics. However, some implementation aspects need to be carefully studied and, in particular, the poor performance when the frequency deviates has recently drawn much of the researchers' attention [26, 27].

In general, a harmonic controller (PRC or RC) requires an accurate knowledge of the plant in which harmonics are to be eliminated and researchers are actively seeking for robust performance without a detailed knowledge of the plant.

1.1.5 Series-Compensation Strategies

The way in which an SAC compensates the load voltage when a voltage sag takes place determines the power-flow through it [28]. Hence, active-power flow in series-connected devices has been thoroughly studied in the literature trying to minimise energy-storage requirements [29, 30]. The energy requirements during a voltage sag is reduced rotating the phase of the load voltage, although sensitive loads may not tolerate this phase rotation [31].

While active-power flow received much attention in the literature, reactive-power compensation with SACs has been seldom studied and certainly requires further attention [32, 33].

1.2 Contributions and Scope of this Thesis

The main objective of this thesis has been to investigate and improve the control aspects of an SAC. The major contributions along these lines can be spelt out as follows:

1. Three different control techniques have been investigated and implemented in an SAC to provide a fast and damped transient response. Furthermore, the saturation of the coupling transformer during transients has been modelled and studied in detail.

2. The implementation of a RC to provide a high-quality voltage waveform to a sensitive load has been fully analysed. RCs have been widely applied in PE applications, but they had never been implemented before in an SAC prototype. The poor performance when the grid frequency varies has been greatly improved in this thesis. Moreover, many alternatives to improve the RC performance are described and were tested in the prototype.

3. An easy method to design high-performance PRCs has been proposed. Furthermore, the performance when the grid frequency varies is addressed in this thesis using a novel approach that provides excellent results with a very low computational burden.

4. A steady-state-based control algorithm has been proposed to reject voltage harmonics when the plant dynamics are unknown. The tests carried out have shown excellent performance.

5. This thesis also provides a comprehensive study of the power flow through an SAC. The insight provided helped to develop a control method where active and reactive

power can be controlled independently while taking the load-voltage constraints into account.

6. An SAC prototype has been built and all the proposals of this thesis have been validated experimentally.

Some of the results presented in Chapters 3 and 4 were compiled and published [34]:

- J. Roldán-Pérez, A. García-Cerrada, J. L. Zamora-Macho, P. Roncero-Sánchez, and E. Acha, "Troubleshooting a Digital Repetitive Controller for a Versatile Dynamic Voltage Restorer" *International Journal of Electrical Power & Energy Systems*, vol. 57, pp. 105−115

In addition, several parts of Chapter 3 and the experimental platform were used in another application that produced the following paper (included in Appendix D). This application emphasizes that the control systems developed in this thesis can be applied in a wide variety of circumstances:

- J. Roldán-Pérez, A. García-Cerrada, J. L. Zamora-Macho, and M. Ochoa-Giménez, "Helping All Generations of Photovoltaic Inverters Ride-Through Voltage Sags" *IET Power Electronics*, Accepted for publication, available on-line on June 2014, doi:10.1049/iet-pel.2013.0552

In addition, the author of this thesis collaborated actively in:

- M. Ochoa-Giménez, J. Roldán-Pérez, A. García-Cerrada, and J. L. Zamora-Macho, "Space-Vector-based Controller for Current-Harmonic Suppression with a Shunt Active Power Filter". *European Power Electronics and Drives Journal (EPE Journal)*, vol. 24, no. 2, 2014

1.3 Thesis Outline

This thesis is divided into 8 chapters and 4 appendices: chapters describe the essential work of this thesis, while appendices include important information that could be omitted in a first reading, but should be useful for a more detailed analysis.

Chapter 1 provides a brief introduction to SACs, summarizes the contributions of this work, and gives an outline for this dissertation.

Chapter 2 presents the background material and the state of the art in series-active compensation for electrical systems. First of all, the types of voltage disturbances are described. Thereafter, the SAC topology is analysed in detail and the fundamentals of series active compensation are described. Finally, control systems (including harmonic-control algorithms) in use are outlined and their main advantages and disadvantages are underlined to stablish the niche that has motivated this thesis.

Chapter 3 explains the fundamentals of the so-called "main controller" proposed for an SAC. The control system is presented with three alternatives: a state-feedback, a PID, and a cascade controller. The dynamics of the coupling transformer are discussed and all the proposals are tested on the SAC prototype.

Chapter 4 deals with the application of a RC to an SAC. First of all, RC basics are explained and two problems related to its application to an SAC are identified: internal instability when using a coupling transformer and poor performance when the grid frequency varies. Solutions for both problems are given in this Chapter. In addition, several alternatives to the classical RC are analysed.

Chapter 5 provides a novel formulation to simplify the design of discrete-time PRCs. In addition, it describes a method to adapt PRCs when the frequency varies that has a low computational burden.

Chapter 6 proposes a steady-state-based control algorithm that makes it possible to compensate harmonics without prior knowledge of the plant. Theoretical and experimental results confirm the validity of this approach.

Chapter 7 proposes a novel technique to control the power flow in a series-connected device. This approach greatly simplifies the power-flow calculations so that power-flow limits can be better understood. The ideas are tested on the prototype.

Chapter 8 highlights the conclusions and gives guidelines for further research.

This thesis ends with the appendices. Appendix A describes the prototype in detail. Appendix B contains a sag detection algorithm developed for this thesis. Appendix C contains mathematical proofs used in Chapter 4 and, finally, Appendix D contains the additional paper mentioned before.

Chapter 2

Series Active Compensation: State of the Art

This chapter presents the state of the art in series active compensation for electrical distributions systems and highlights the problems that are to be studied in the rest of the thesis. Section 2.1 describes the most relevant voltage disturbances, with special emphasis on voltage sags and voltage harmonics. Section 2.2 introduces the dynamic voltage restorer (DVR), the series active power filter (SeAPF), and the series active conditioner (SAC). This section also explores alternatives to series-connected devices. Section 2.3 analyses the SAC topology and Section 2.4 describes the series compensation methods, paying special attention to sag-compensation strategies. Section 2.5 briefly explains the proposed control structure, which consists of a main and a harmonic controller. The alternatives for the main controller are described in Section 2.6, while the alternatives for the harmonic controller are described in Section 2.7. Finally, the main unsolved issues to be addressed in this thesis are underlined in Section 2.8.

2.1 Voltage Disturbances

This section explains voltage sags, swells, imbalances, harmonics, and flicker. The non-linear loads that are likely to generate harmonics are also explained.

2.1.1 Voltage Sags and Swells

A voltage sag is a sudden reduction in the average value of the grid voltage with a duration between one cycle and a few seconds [35]. Voltage sags are generally caused by short-circuit faults in the power network [36] or by the starting of large-rating electric motors [37, 38]. They cause the disconnection of sensitive equipment, distributed generators, and industrial processes with significant economical losses. Moreover, faults in the power system can lead to a phase-angle variation in the grid voltage, which is commonly known as a "phase jump" [35]. This phenomenon may cause important damages to equipment that works synchronously with the grid voltage such as controlled rectifiers [7].

When a voltage sag takes place both the voltage magnitude and the phase-angle of each phase may change. The phasor configuration during the sag depends primarily on the type of fault that originated the sag, the connection of the transformers involved, the loads (if any), and the way in which the voltages are being measured (line-to-line or line-to-ground) [39]. In general, line-to-ground measurements are preferred to prevent the loss of the homopolar voltage information. There exist many approaches to classify voltage sags, but the most popular and simplest one, which is called *abc*, classifies the sags according to their phasor configuration [40]. Another method is based on the so-called symmetrical-component decomposition, which is less intuitive, but provides the theoretical basis for the *abc* method [41]. Space vectors can be used to characterise voltage sags as well [42], although these are less popular.

Fig. 2.1 depicts the phasor diagrams for the sags defined in the *abc* classification. Types B and E are the only ones that contain a homopolar voltage component [35]. Sags type B are due to line-to-ground (LG) faults and sags type E are due to line-to-line-to-ground (LLG) faults. Sags type A are due to three-phase faults (LLLG) or due to the starting of large-rating electric motors [38]. Sags type C appear due to line-to-line (LL) faults or when another type of sag is propagated through the windings of distribution transformers (transformer propagation). The rest of sag types (D, F, and G) only appear when another type of sag is propagated [39, 43]. In this thesis, sags

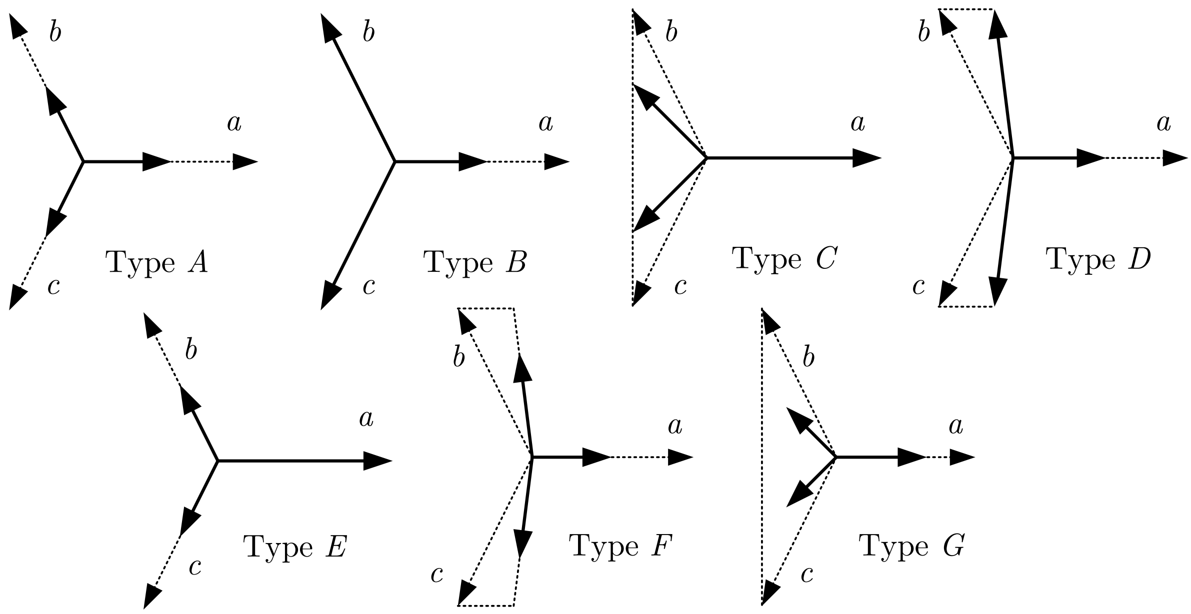

Figure 2.1: Types of sags according to the *abc* classification.

are named with the letter of their class and a subscript with their characteristic phase, which is the phase that is different. For instance, a sag type B like the one in Fig 2.1 is named B_a, whereas a sag type C like the one in Fig. 2.1 is named C_a.

A voltage swell is a sudden increase of the average value of the grid voltage and it can take place in multi-ground [44] or ungrounded electrical systems [42]. In addition, some types of sags that were previously explained can lead to swells in the line-to-line voltages (e.g. u_{bc} in the type D in Fig. 2.1). Ignatova et al. [42] add two swell types to the abc classification (H and I). These swell types appear when a LG or a LLG fault takes place in an ungrounded system.

2.1.2 Voltage Flicker

The voltage flicker is a fluctuation of the voltage magnitude with a frequency between 0.01 Hz and 30 Hz. This fluctuation generates oscillations in the light emanated from lamps that are annoying for the human sight [45, 46]. Consequently, there are many case studies and standards regarding voltage flicker [47, 48]. Flicker is produced by, for example, AC electric arc furnaces [49], rolling mills, welders, and wind-energy conversion systems [50].

2.1.3 Voltage Harmonics

There are, basically, two types of non-linear loads and their mechanisms to generate current and voltage harmonics are different. The first type has a capacitance-dominated DC-side (see Fig. 2.2 (a)), while the other one has an inductance-dominated DC-side [13, 51] (see Fig. 2.2 (b)). In the inductance-dominated type the DC voltage (u_{dc}) is imposed by the grid voltage (u_l) and the DC-side current (i_{dc}) defines the grid current (i_l) (assuming L_{dc} is large enough). Therefore, this type of load behaves similarly to a current source (current-source load [13]). In the capacitance-dominated type, the AC load voltage (u_l) is imposed by the capacitor voltage (u_{dc}) when a pair of diodes are biased (assuming C_{dc} has a large value). Therefore, this type of load behaves similarly to a voltage source (voltage-source load [13]).

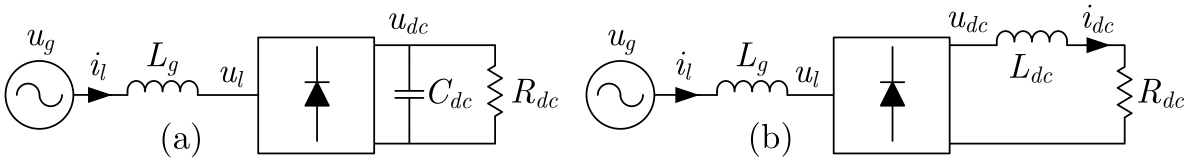

Figure 2.2: (a) Voltage-sourced load and (b) current-sourced load.

2.2 Series-Connected Devices and Their Alternatives

2.2.1 Dynamic Voltage Restorer (DVR)

Fig. 2.3 (a) shows the electrical layout of a DVR. A DVR is connected between the PCC and the sensitive load to be protected and its primary function is to supply constant voltage ($u_l(t)$) to the sensitive load in spite of the voltage sags at the PCC. This protects sensitive loads and should improve the fault ride-through capability of distributed generators such as wind [52] or solar plants [53]. A DVR controls the load voltage $u_l(t)$. Therefore, the load voltage is measured and compared with an ideal voltage set-point, called $u_l^*(t)$, which is calculated depending on the voltage-compensation method to be used [29]. The compensating device is based on a PWM VSC with a DC capacitor (C_{dc}), a coupling transformer, and an auxiliary power supply that provides the required power when a voltage sag takes place [54].

2.2.2 Series Active Power Filter (SeAPF)

A SeAPF is depicted in Fig. 2.3 (b) and it looks very much like a DVR. It can be used for several purposes:

1. *Voltage filtering*: If the grid voltage is polluted with harmonics or is unbalanced a SeAPF can inject a series-compensating voltage and the load would see an ideal voltage [14]. In the rest of the thesis this device will be called voltage SeAPF (VSeAPF).

2. *Current filtering*: If a load is non-linear and it consumes current harmonics with a sinusoidal load voltage, cleaning the load voltage would bring a current-distortion problem to the grid. In this situation, one may have to purposely distort the load voltage to obtain a sinusoidal current (see Fig. 2.3 (b)) [55, 56]. Several references report that this is the case with diode bridges with a large smoothing DC capacitor [51, 55, 56]. If the load is non-linear, it might not be affected by

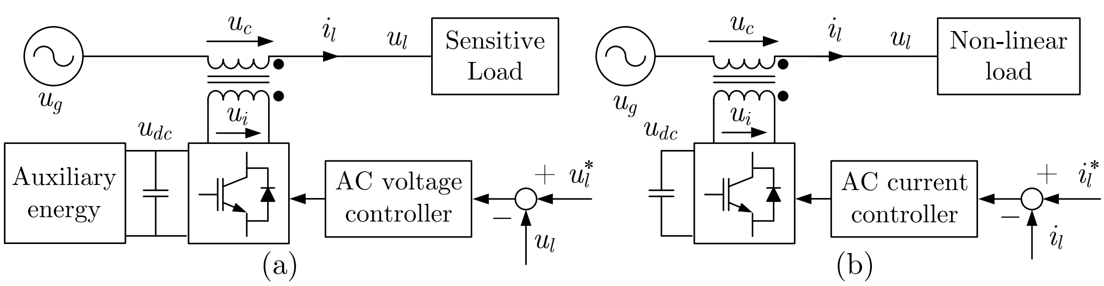

Figure 2.3: (a) Dynamic voltage restorer (DVR) and (b) current SeAPF.

voltage distortion and, if the load is linear, both filtering strategies (voltage and current) lead to similar results because a sinusoidal voltage leads to a sinusoidal current in steady state. In this thesis the SeAPF will be called current SeAPF (CSeAPF) if it is used to prevent current harmonics.

3. *Mixed objectives*: A SeAPF can compensate, for example, unbalance components of the grid voltage and current harmonics generated by the load [57] and, in some cases, reactive power [33].

A CSeAPF can also be applied to the DC-side of a non-linear load to compensate current harmonics [58, 59], as shown in Fig. 2.4 (a), but this alternative is less versatile because the CSeAPF only compensates the harmonics of the load in which it has been installed.

A shunt-passive filter can be added to the series-compensating device to improve its performance [60, 61, 62, 63]. An example of this topology is depicted in Fig. 2.4 (b), where the passive filter consists of two resonant brunches, tuned at the 5th and 7th harmonic, and a high-pass (HP) filter. The passive filter can also be designed to improve the load power factor, if necessary [64]. This passive filter provides good results with low losses [11]. However, a passive filter can lead to undesired resonances in the power system [65], but more important, the harmonic attenuation strongly depends on the load and the grid impedances [11]. Therefore, the series converter is intended to ensure a large harmonic attenuation in spite of the grid and load conditions [66].

2.2.3 Alternatives to a Series Active Conditioner

Uninterruptible power supplies (UPSs) are the most common solution to protect sensitive loads against voltage sags [8]. An off-line UPS is depicted in Fig. 2.5 (a) and it consists of a shunt-connected VSC, a DC capacitor, an auxiliary energy supply, an AC filter, and a transfer switch. When the sag is detected the transfer switch replaces the grid voltage with the voltage generated by the VSC. During the sag, the VSC generates a constant voltage and all the power consumed by the load is taken from the energy-storage element: this means that the batteries need to be larger than those of an SAC because an SAC delivers only a fraction of the total amount of the active power

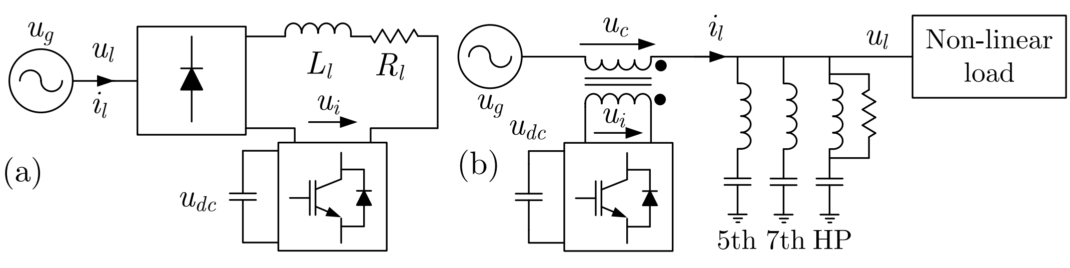

Figure 2.4: (a) SeAPF placed in the DC-side of a non-linear load and (b) hybrid SeAPF.

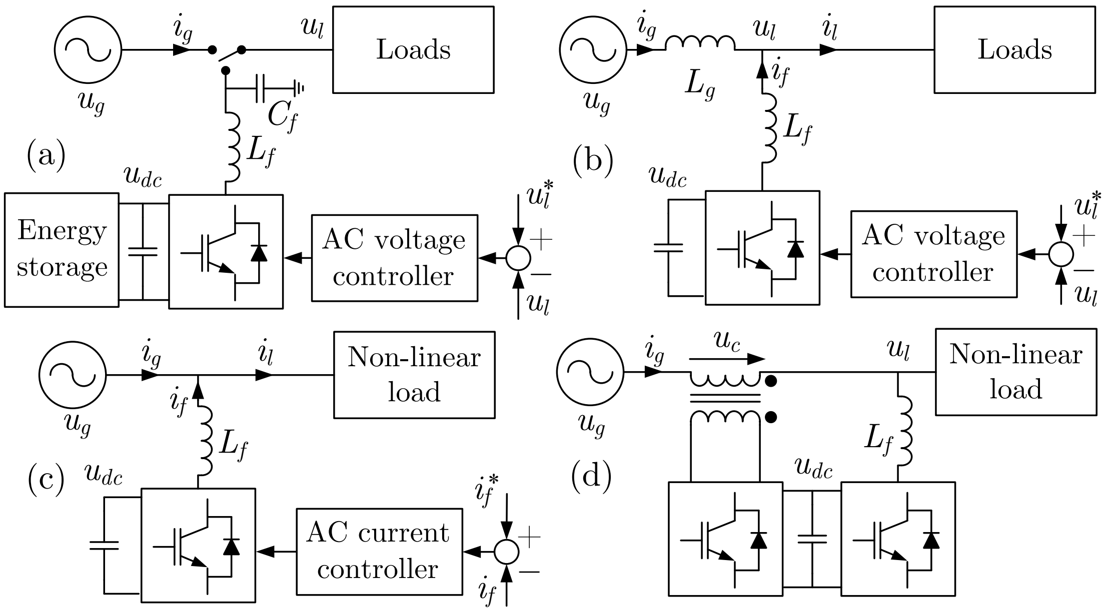

Figure 2.5: (a) Uninterruptible power supply (UPS), (b) static synchronous compensator (STATCOM), (c) shunt active power filter (ShAPF), and (d) Unified power quality conditioner (UPQC).

(this difference is more important for shallow voltage sags). When the sag ends, the transfer switch reconnects the load to the grid, orderly. A UPS was first proposed in 1969 to protect computers against voltage sags [67]. However, UPSs are expensive when considering large industrial loads because of the large-size batteries [8].

A STATCOM is a PE device conceived to inject (absorb) reactive power into (from) the grid. A STATCOM is based on a VSC with a DC capacitor and an AC filter, as shown in Fig. 2.5 (b). If the grid inductance is large, the reactive power injected modifies the load voltage, so it can be controlled [68, 69, 70, 71]. However, this device suffers from many drawbacks when it is used as a voltage-sag compensator. For instance, it can not compensate deep voltage sags because this would require a large grid current [72, 68, 73]. In addition, its voltage-restoration capability depends to a great extent on the grid impedance, making it almost impossible to compensate voltage sags when the short-circuit impedance at the PCC is small. STATCOMs, however, are a very popular alternative to help maintaining the voltage profile in power systems because of their flexible reactive-power control [70].

A shunt APF (ShAPF) consists of a VSC, a DC capacitor, and an AC filter, and it is depicted in Fig 2.5 (c). A ShAPF compensates the harmonic currents generated by the load (i_l) controlling the injected current (i_f) and it is the most common solution to ameliorate the power (current) quality [26, 74]. This device is also adequate to compensate reactive power [26] (compare Fig. 2.5 (b) and (c)), although in this case the efficiency decreases because of the conduction losses. In general, a ShAPF is replaced by a SeAPF only if the load behaves like a voltage source [51].

Finally, a UPQC is depicted in Fig 2.5 (d) and it consists of two VSCs. The first VSC is connected in series with the line using a coupling transformer and the second VSC is connected in parallel to the load-side of the transformer using an AC filter [75]. The series converter compensates voltage harmonics and voltage sags, while the shunt converter compensates current harmonics and reactive power. This device may look like the ultimate solution for power quality problems but, unfortunately, its price is excessive because of the large number of components and its potential still needs more research [76].

2.3 Topologies and Components of an SAC

2.3.1 Power Converter

The three-legged three-wire converter is the most common topology used in power systems for DC to AC conversion and it is also very popular for SACs [77, 78, 79, 80, 81]. If the coupling transformer provides a neutral point, the SAC can be used together with a four-wire converter to inject homopolar-voltage components [31, 82, 83]. However, three independent H-bridges with common [84, 85, 86, 87, 88] or isolated [89, 90] DC-links are also popular because each H-bridge can be used together with a single-phase transformer and each phase can be controlled independently [15]. DC capacitors can be avoided for an SAC using direct (matrix) converters [91, 92, 93, 94, 95], but in this case the number of switches increases and the control system becomes more complex.

Multilevel converters are becoming popular for SACs [70]. For instance, Loh et al. [96] present an SAC based on a multi-pulse converter consisting of several independent voltage-sourced H-bridges, as shown in Fig. 2.6 (a), where the DC capacitors

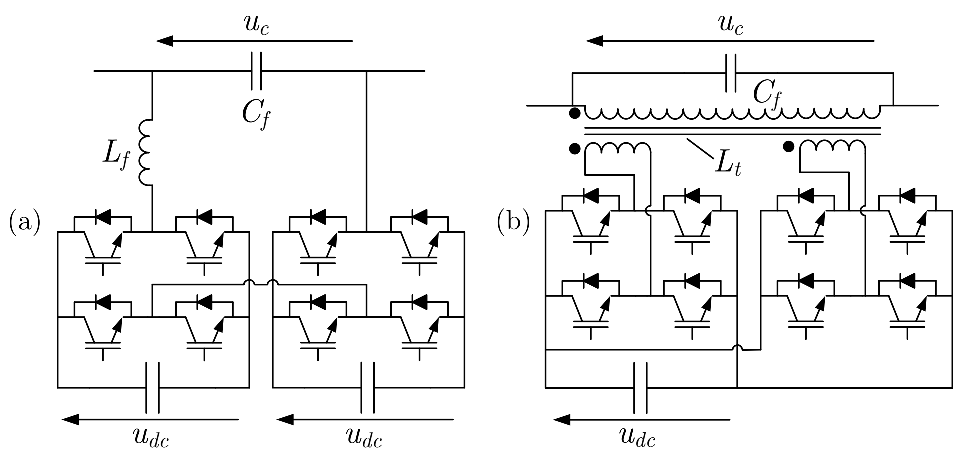

Figure 2.6: (a) Multi-pulse converter and (b) modular converter based on two H-bridges.

must be isolated and the H-bridges are connected in series. The output voltage can have a low ripple if a large number of levels are used, suggesting that the filter capacitor can be suppressed [96, 97]. Another alternative proposed by Wang et al. [98] uses a modular converter based on H-bridges that share the same DC link. This time, the H-bridges are connected in series using a phase-shifting transformer with multiple windings. This topology is depicted in Fig. 2.6 (b). A compact (non-modular) multilevel topology (diode-clamped) is used by Barros and Silva [99] and, finally, the flying capacitor topology is used by Roncero-Sánchez et al. [37] in a simulation study.

2.3.2 Coupling Transformer

The coupling transformer typically consists of three independent single-phase transformers [86, 87, 88, 93, 99, 100]. The grid side of the transformer is always connected in series, while the converter side can be wye connected [80, 101], delta connected [102], or independently connected [87, 88]. The last alternative can only be used with three independent single-phase converters. Nevertheless, three-phase transformers with a single core can also be applied [79]. The coupling transformer is a heavy and expensive component, so it should be designed carefully, taking into account the steady-state voltage-drop across the transformer, the transformation ratio, and the saturation of the core [31].

The coupling transformer is subject to an abrupt change in the input voltage when the converter starts working. Assuming zero remanent flux:

$$u(t) = |u|\sin(\omega_g t + \alpha_i), \text{ so } \lambda(t) = \int_0^t u(t)dt = \underbrace{\frac{|u|}{\omega_g}\cos(\alpha_i)}_{\text{DC component}} - \underbrace{\frac{|u|}{\omega_g}\cos(\omega_g t + \alpha_i)}_{\text{AC component}}, \quad (2.1)$$

where $u(t)$ is the input voltage, α_i is the initial angle of $u(t)$, ω_g is the grid frequency, and $\lambda(t)$ is the transformer flux linkage [103]. It can be seen that the voltage variation generates a DC-flux component that can saturate the coupling transformer. To overcome this problem the transformer can be designed to withstand twice the nominal flux, but this increases the transformer size [104]. Alternatively, some authors have developed active methods to reduce (even eliminate) this DC component [31, 104, 105, 106]. In fact, it can be shown that the DC flux is eliminated if the compensation starts with $\alpha_i = \pm\pi/2$ (assuming zero remanent flux) in each phase [104]. Another simple solution is presented by Nielsen [31] and consists in setting the VSC voltage to zero when the transformer current reaches a pre-established value. This is probably the easiest solution to implement, but it can lead to unexpected results. Fitzer et al. [106] developed a more complex method that consists in modifying the output voltage using an adaptive form factor tailored to minimise the DC-component of the flux. This technique provides an excellent performance since the load is hardly disturbed, but it is more difficult to apply than those techniques presented above. In any case, DC-flux reduction techniques slow down the compensation of voltage sags [104].

SACs can be connected without a transformer when using three H-bridges with isolated DC-links. This topology was first proposed by Li et al. [90] and it has been referred many times in the literature mainly because of the potential price savings [29, 89, 107, 108]. Multilevel converters based on series-connected H-bridges suit transformer-less applications very well [107]. However, each DC capacitor requires an isolated DC charger, so the price rises. Jimichi et al. [109] proposes a transformer-less SAC in which the DC chargers are based on high-frequency DC-DC converters with great potential price saving.

2.3.3 AC-filter Design

An SAC requires an AC filter to suppress the high-frequency harmonics generated by the PWM process. In the literature, there are two basic approaches for this filter:

1. *High-voltage AC filter*: The filter capacitor is placed at the grid side of the coupling transformer, as shown in Fig. 2.7 (a). The transformer leakage inductance (L_t) and the filter capacitor (C_f) give the required effect [37, 80, 110]. This approach requires less passive elements than others, but the capacitor voltage rating has to be equal to or higher than the grid nominal voltage [111]. Furthermore, the design is not very flexible since the transformer leakage inductance is more difficult to design (and change) than, for example, an additional inductor.
2. *Low-voltage AC filter*: The LC filter is placed at the converter-side of the transformer (see Fig. 2.7 (b)) and it consist of the filter inductor (L_f) and the filter capacitor (C_f) [112]. The coupling transformer is connected in series with load and, therefore, it has a low impact on the filter performance. Using this filter configuration the voltage rating of the capacitor is smaller and this is preferred in high- and medium-voltage applications [87, 113]. In addition, this topology is more flexible than the previous one since L_f and C_f can be selected freely [113].

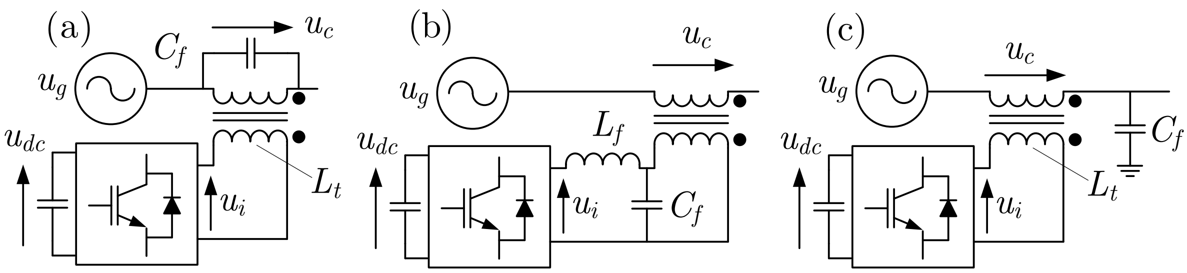

Figure 2.7: Positioning the AC filter at (a) the grid-side of the transformer, (b) the converter-side of the transformer, and (c) the load-side of the SAC.

However, the additional inductor might generate an excessive voltage drop if it is not carefully designed [80].

Other authors place the filter capacitor at the load side [99] (see Fig. 2.7 (c)), or both at the grid and the load side [80]. However, these topologies have one considerable drawback: when the SAC is bypassed (this is often the case in DVR applications) the capacitor remains connected to the grid.

In any case, the resonance frequency of the *LC* filter should be low enough to filter out the switching harmonics, but not too low because this would slow down the transient response. In fact, the *LC* filter resonance can deteriorate the SAC performance, especially when the loads are non-linear [31]. The simplest countermeasure is to add a resistor close to the filter capacitor but, unfortunately, this produces additional losses, questioning the viability of the SAC. Another solution is to actively damp the *LC* filter resonance with the controller [18, 19].

2.3.4 Energy-Storage System

The energy-storage system can be, for example, lead-acid batteries [114], supercacitors [115], a flyweel [78, 91], or a superconducting magnetic energy storage [77, 81]. In some cases, the energy stored in the DC capacitors might be enough to compensate a sag with a limited depth and duration. However, this could lead to a large and costly capacitor bank [54]. Another approach involves using an auxiliary rectifier that provides the power during the sag and, as shown in Fig. 2.8, the rectifier (diode bridge in this case) can be connected to the:

1. *Load side of the SAC:* The additional power is taken from the load-side of the transformer, as shown in Fig. 2.8 (a). Therefore, the DC-link voltage remains constant whatever the depth of the sag is, suggesting that the SAC can compensate deep voltage sags. However, the SAC have to withstand the load current plus the rectifier current because all the power is taken from the grid. Therefore, the transformer and the VSC need to be oversized, as shown by Nielsen et al. [54]

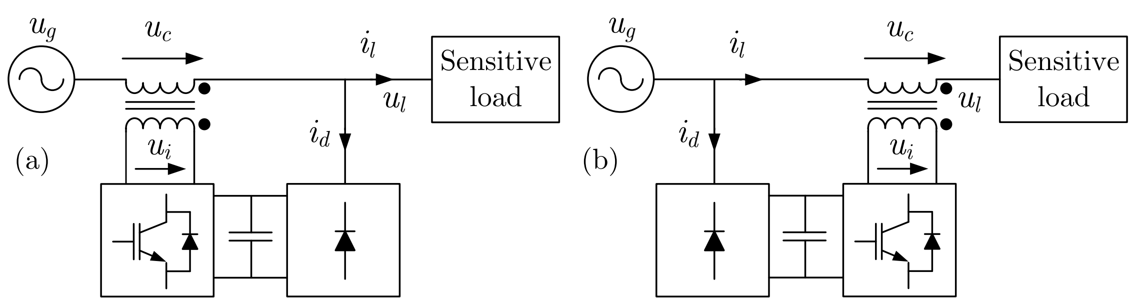

Figure 2.8: SAC topologies using an additional rectifier. The rectifier can be connected to (a) the load-side or (b) the grid-side of the SAC.

and Jimichi et al. [85]. In addition, the current harmonics of the rectifier generate voltage harmonics across the transformer and the AC filter, thus deteriorating the load voltage quality.

2. *Grid side of the SAC:* When a sag takes place the additional power (and current) is directly taken from the grid (Fig. 2.8 (b)), so there is no need to modify the SAC ratings. However, the DC-link voltage decreases according to the sag depth. Therefore, this topology is adequate to restore shallow voltage sags [85]. In addition, the diode bridge pours harmonic currents into the grid, leading to voltage harmonics at the PCC [31].

In both cases the distribution feeder is overloaded during a voltage sag because the power delivered to the load must be taken from the grid, eventually. Therefore, if the grid voltage decreases, the grid current has to increase and this might be unacceptable with the current trend on grid codes, like in the Spanish case [116].

2.4 Series Compensation Strategies

2.4.1 Methods to Compensate Voltage Sags

The methods to compensate voltage sags have been widely studied in the literature because they have a big impact on the SAC performance [31, 117, 118]. Fig. 2.9 shows the space-vector diagrams of the most important compensation methods, where $\vec{u}_p$ is the load voltage prior to the voltage sag, $\vec{u}_g$ is the grid voltage during the sag, $\vec{u}_c$ is the compensating voltage, $\vec{u}_l$ is the load voltage during the sag, ϕ is the angle of the load impedance, and $|\vec{u}_g + \vec{u}_c| = |\vec{u}_l| = 1$ pu. The compensation methods are:

1. *In-phase compensation*: The compensating voltage is injected in phase with the grid voltage, as shown in Fig. 2.9 (a). This method is also called minimum-voltage compensation because the modulus of the series-injected voltage is minimised.
2. *Pre-sag compensation*: The magnitude and phase of the load voltage are similar to those existing prior to the voltage sag. This compensation strategy is depicted

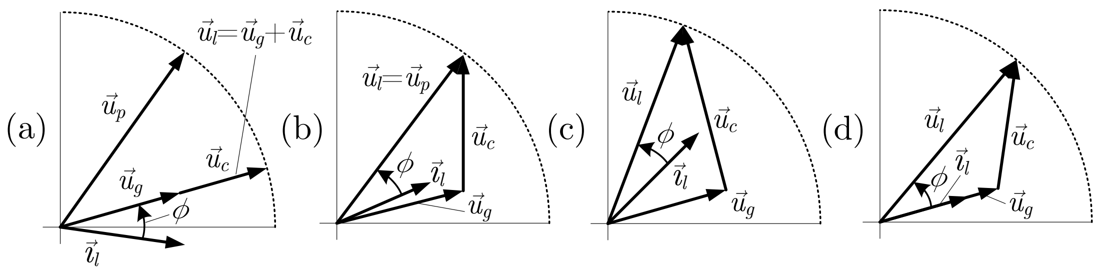

Figure 2.9: Voltage sag compensation strategies. (a) In-phase, (b) pre-sag, (c) phase-advance, and (d) minimum-power compensation method.

in Fig. 2.9 (b). In this case, the power flow through the SAC is unpredictable and it is strongly related to the phase jump [31].

3. *Phase-advance compensation*: The sag is compensated rotating the load voltage with respect to the grid voltage (Fig. 2.9 (c)). This modifies the active and reactive power required to compensate the sag. This compensation method is mandatory if a grid code establishes the active- and reactive-power injection during voltage sags [32]. However, sensitive loads may be disturbed by the phase rotation [119].

4. *Minimum-power compensation*: This method is a special case of the phase-advance method in which the phase-angle rotation is selected to minimise the power required to restore the load voltage [117]. This phase-angle rotation is the one that forces $\vec{u}_g$ to be in phase with $\vec{\imath}_l$, as shown in Fig. 2.9 (d). However, some other considerations should be taken into account if there are restrictions on the series-injected voltage [118].

In any case, the compensation method must be carefully selected depending on the application. For example, if the load is a controlled rectifier, in-phase compensation is more adequate to avoid disturbing the control circuits [119]. Phase-advance and minimum-power compensation are more suitable to be applied with highly inductive loads, otherwise the energy saving is negligible. Al-Hadidi et al. [107] propose a novel method to reduce the power requirements: an inductor is connected in parallel with the original load, leading to higher energy savings when applying minimum-power compensation. Unfortunately, the DVR has to withstand the load current plus the additional-inductor current, thus increasing its rating.

2.4.2 Unbalance Compensation

Line-to-ground (LG) and line-to-line (LL) faults are the most common types of faults in electrical distribution systems and both lead to unbalanced voltage sags [120]. Furthermore, the grid voltage can be balanced but, if there are unbalanced loads, the load voltage can be unbalanced too. This effect is more severe in microgrids or isolated systems.

In some electrical networks the distribution transformers do not block homopolar voltages coming from the high-voltage side [82]. Therefore, any LG fault generates an unbalanced voltage sag with a homopolar component. Homopolar components may also appear in four-wire systems when single-phase loads are connected between one phase and the neutral wire. Sags with homopolar components should be compensated using a three-legged VSC with the middle point of the DC capacitors connected to the neutral point of the coupling transformer [82] or, alternatively, a four-legged VSC [83].

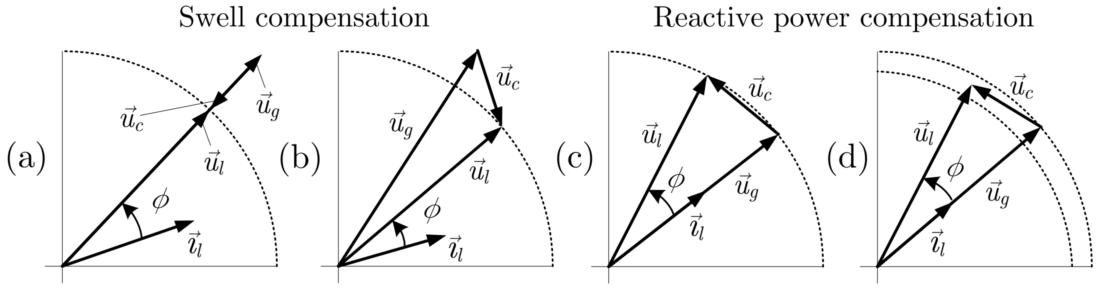

Figure 2.10: Swell compensation using (a) in-phase and (b) phase-advance compensation. Reactive power compensation with (c) constant and (d) flexible load voltage limits.

2.4.3 Swell Compensation

The SAC may absorb active power if it compensates voltage swells using in-phase compensation. The space-vector diagram that describes this situation is depicted in Fig. 2.10 (a). In this case, the DC capacitor voltage would increase indefinitely or, at least, until a protection element switches the device off. This problem can be solved rotating the angle between $\vec{u}_g$ and $\vec{u}_l$ because this modifies the active power injection, as shown in Fig. 2.10 (b) [108].

2.4.4 Active- and Reactive-Power Flow

Active-power injection can be modified rotating the angle of the load voltage, as previously explained in Section 2.4.1. Furthermore, reactive-power flow can be modified in the same way [121, 122]. However, reactive-power compensation with SACs has been rarely studied because, if the load-voltage magnitude has to be 1 pu, there is only one degree of freedom and it is commonly used to manage the active-power flow (see Fig. 2.10 (c)) [33, 122, 123]. This prevents reactive-power compensation in most cases.

When the grid voltage is close to its nominal value the DC-link voltage can be controlled in closed loop modifying the series-injected voltage [28, 89, 124]. Even so, the active-power flow is difficult to control because its dynamics depends on the load [89], which may be unknown or may change during operation. For instance, Sgn et al. [89] control an SAC in closed loop that is forced to absorb active power to charge the batteries. The charging process is thoroughly analysed, revealing that its dynamics are significantly affected by the load.

The load voltage limits must be flexible to control the active- and the reactive-power flow at the same time (Fig. 2.10 (d)) [28]. Active- and reactive-power using non-flexible constraints has been widely studied by Chung et al. [28] and by Choi et al. [118]. However, the effects of flexible load-voltage limits have been seldom studied [28].

2.4.5 Short-Circuit Current Limitation

A short circuit fault at the load side can easily damage the SAC, permanently [31]. Babaei and Kangarlu [125] and Badrkhani et al. [126] show that an SAC can be protected switching on the bypass or, alternatively, injecting the voltage required to limit the current. Obviously, when limiting the current through by injecting voltage the load voltage can not be maintained at its rated value. Even more, the load voltage would become almost zero to avoid the over-current, as shown by Mahdianpoor et al. [112]. This is only possible if the SAC is able to inject the grid nominal voltage leading, probably, to an expensive device [127].

2.5 Control Structure

2.5.1 Open- vs Closed-Loop Control Techniques

SACs are sometimes controlled using open-loop techniques, as shown in Fig. 2.11 (a), where u_l is the load voltage, u_c is the series-injected voltage, u_i is the converter output voltage, and "$*$" stands for "reference". Using these control techniques stability is always ensured if the plant is stable. However, performance deteriorates when there are disturbances. Open-loop control has clear drawbacks, among them:

- Accurate set-point tracking is only possible if the plant model is known, exactly [31].
- Disturbances can not be rejected.
- It is almost impossible to track voltage harmonics [88].

Open-loop control techniques have been applied by Jimichi et al. [104] to an SAC, obtaining a fast transient, but the performance is poor if the AC filter includes a capacitor because of the LC filter resonance [111, 113, 128].

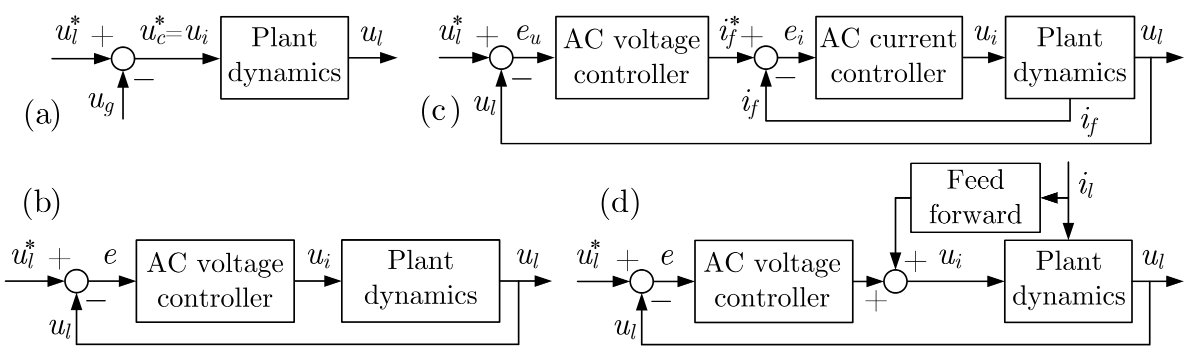

Figure 2.11: The most relevant SAC control strategies: (a) open-loop control, (b) single-loop control, (c) multi-loop control, and (d) single-loop control with current feedforward.

In most cases, SACs are controlled using a feedback control scheme like the one depicted in Fig. 2.11 (b) [37, 129, 130], where e is the control system error ($e = u_l^* - u_l$). As shown in Fig. 2.11 (d), the current consumed by the sensitive load can be added as a feed-forward signal [37]. Using feedback control the output voltage can be accurately controlled if the closed-loop system is stable. However, feedback control is not easy in this case because (a) the load modifies the plant dynamics and (b) the LC filter resonance is difficult to damp using a controller based on a single loop [18].

The easiest solution to damp the resonance is to add a resistor close to the AC capacitor, but this increases the losses. A multi-loop control scheme, like the one depicted in Fig. 2.11 (c), is a classic solution to deal with the resonance: first, the current through the filter inductor (i_l) is controlled by the inner AC-current controller and, secondly, the load voltage (u_l) is controlled by the AC-voltage controller. With this control scheme the resonance can be actively damped and no extra passive elements are required [18]. Nevertheless, the control system requires extra measurements.

The SAC control system can be implemented using a synchronous reference frame (SRF) [86], an static RF [131], or in natural magnitudes (abc) [128]. If the controller is applied using natural magnitudes or in a stationary RF ($\alpha\beta$), decoupling equations are not required. However, a resonant controller is needed to achieve zero steady-state error for the fundamental component [131]. By far, the most common alternative is to use a SRF because the fundamental components of all magnitudes are constant values in steady state [6]. Therefore, a PI controller is enough to track balanced voltage sags, although the dq-axis dynamics are coupled. In addition, a phase-locked loop (PLL) is needed to synchronize the SRF with the grid voltage [6].

An alternative controller is presented by Badrkhani Ajaei et al. [110]. This alternative is implemented using time-varying phasors that do not require a PLL and makes it possible to control each phase, independently. However, the transient response is slower when compared to other control algorithms because the phasors have to be estimated.

2.5.2 A Versatile Control

A control structure for a SAC is presented by Roncero-Sánchez et al. [37] with, basically, the plug-in structure in Fig. 2.12 (a). The main controller is in charge of tracking the fundamental component of the error, while the harmonic (auxiliary) controller eliminates the harmonic components. Therefore, the device is not only used to restore the nominal voltage level when a sag takes place but also to provide a clean load voltage in steady state. The harmonic controller can use several alternatives, like repetitive [22, 26], resonant [132], or DFT-based controllers [133]. Roncero-Sánchez et al. [15] present this versatile control using a repetitive controller in series with the so-called main controller, as shown in (Fig. 2.12 (b)). The idea is, nevertheless, equivalent to the plug-in structure presented by García-Cerrada et al. [26].

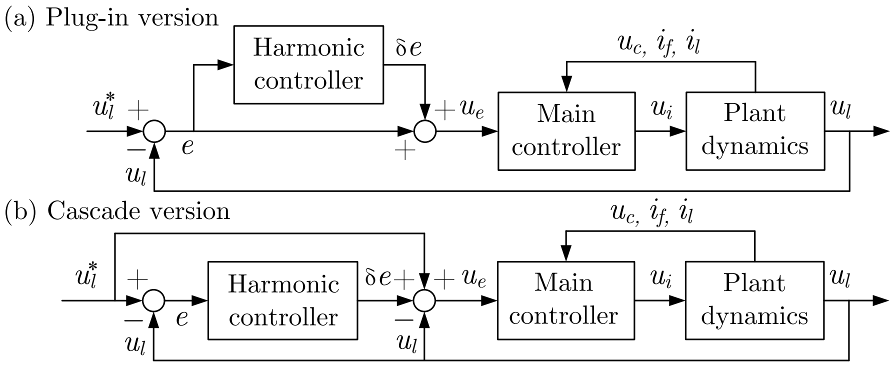

Figure 2.12: (a) Plug-in and (b) cascade versions of the versatile control structure.

2.6 Main Controller

2.6.1 Single-Loop Control Strategies

The SAC can be controlled using a single control loop for the main controller mentioned before. For instance, Goharrizi et al. [128] control a DVR with an *LC* filter using a PID controller, which gives a fast transient response with a reduced overshoot. However, the load voltage quality deteriorates when the loads are non-linear. Alternatively, Roncero-Sánchez et al. [134] damp the *LC* filter resonance using a PI controller plus a notch filter tuned at the resonant frequency: the notch filter eases the PI controller design, but the result does not seem to be very robust.

A Posicast controller is an interesting alternative to damp resonant systems using a single loop, as shown by Hung [21]. This kind of controller is very easy to design and to implement and it has been applied to control an SAC by Mahdianpoor et al. [112]. However, a Posicast controller leads to poor results when the system dynamics are not accurately known. Alternatively, the output voltage can be controlled with a hysteresis controller [135, 136], but this technique could be difficult to apply to resonant plants [135]. Artificial-intelligent techniques have also been applied to an SAC to compensate voltage sags: fuzzy logic is applied by Teke et al. [137], while neural networks are applied by Jurado [138] and by Elnady and Salama [139]. However, these alternatives are not very popular because their design is not straightforward and their performance is difficult to predict.

2.6.2 Multi-Loop Control Strategies

The so-called "virtual resistor" control technique can be used to actively damp the *LC* filter resonance trying to emulate the dynamic behaviour of a resistance with an inner current loop [18]. However, the control system delays may reduce the validity of this approach. Loh et al. [20] and Blasko and Kaura [140] study several multi-loop control strategies to damp the LC filter resonance, concluding that an SAC is less sensitive to current harmonics if the capacitor current is used as the inner control variable.

The resonance can be damped as well using a state-feedback controller and placing the closed-loop poles in appropriate locations, as shown by Cheng et al. [19]. This kind of controller is very straightforward to design, but it is sometimes difficult to figure out which one is the close-loop pole position that leads to acceptable stability margins. Alternatively, Hasanzadeh et al. [141] select the controller gains using a linear-quadratic (LQ) regulator, trying to optimize the transient response. Addressing the problem in this way the closed-loop poles position is no longer a problem but, however, the value of the weighting gains for the LQ problem may be difficult to find. Finally, Saleh et al. [142] apply wavelets to control an SAC using a multi-loop control strategy, obtaining accurate results.

2.7 Harmonic Controller

2.7.1 Repetitive Controller (RC)

RCs have become very popular (including PEs applications) because the computational burden required to suppress a good number of harmonics of a signal is moderate and their design is quite straightforward [143, 26]. The most popular RC applications in PEs are UPSs to protect non-linear loads [144, 145], APFs [26, 146, 147], and PFCs [148, 149]. The core of a RC takes the form of

$$RC\,(s) = \frac{e^{-t_p s}}{1 - e^{-t_p s}}, \text{ with poles in } s = \pm jh2\pi/t_p \text{ and } h = 0, 1, 2, \ldots, \tag{2.2}$$

where t_p is the period of the error. Ideally, the sampling period (t_s) is selected to satisfy $N = t_p/t_s \in \mathbb{N}$, so (2.2) is discretised replacing $e^{-t_p s}$ with z^{-N} [26].

A RC has never been implemented in an SAC before the work done for this thesis. Authors such as Roncero-Sánchez et al. [15, 37] only show simulation results. In fact, a few problems summarised below and to be discussed later in this thesis needed further attention before a practical implementation could be carried out (see Chapter 4).

Frequency Deviation in Repetitive Controllers

If the grid frequency deviates, t_p/t_s is bound not to be an integer number and the RC performance deteriorates [27]. This means that harmonics of the fundamental frequency can not be eliminated from the load voltage. A solution proposed to tackle this problem is the so-called high-order RC (HORC) described by Steinbuch et al. [27], which is depicted in Fig. 2.13 (a). The weighting coefficients (W_i) can be selected to improve the RC robustness against frequency variations. The HORC is robust against small frequency deviations but, unfortunately, it requires more storage space than a RC and its stability margins are smaller than those of the RC. A multi-rate alternative for a RC is presented by Cao and Ledwich [150] to solve the frequency deviation problem (Fig. 2.13 (b)). In this case the whole controller (except the RC) is implemented using a constant sampling period (t_s), while the RC is implemented using a variable sampling period (t_r) which ensures that $N = t_p/t_r$ always leads to an integer number. The samples required for the RC are obtained re-sampling the error signal and the same procedure is used to compute the output of the RC. The multi-rate RC provides good results, but (a) it is difficult to implement and (b) there is no easy way to study closed-loop stability. Novel solutions to tackle this problem have drawn a good deal of the attention in this thesis and they will be presented in Chapter 4.

Internal Stability and the Transformer Magnetising Inductance

The coupling transformer of an SAC would block any DC voltage produced by the VSC and this fact can be modelled using a zero ($s = 0$ using the Laplace variable) in the plant. This zero is cancelled by an unstable pole in the RC, leading to a closed-loop system that is internally unstable (this is demonstrated in Chapter 4). This means that, even if the closed-loop transfer function from the reference voltage to the output voltage is stable, there might be at least one input-to-internal-variable closed-loop transfer function in the system that is unstable [151, 152, 153]. This problem was not detected by Roncero-Sánchez et al. [15, 37] because ideal measuring devices were used for the simulation. In practice, any offset in the measurements would cause the VSC controller to inject a DC voltage trying to cancel the offset. However, the DC voltage would never pass to the secondary of the transformer and the VSC would keep trying to increase its DC output voltage to eliminate the error. Although the control system should not be required to amend the offset problem, it should always produce a bounded output when the inputs are bounded. In other words, internal stability should be guaranteed.

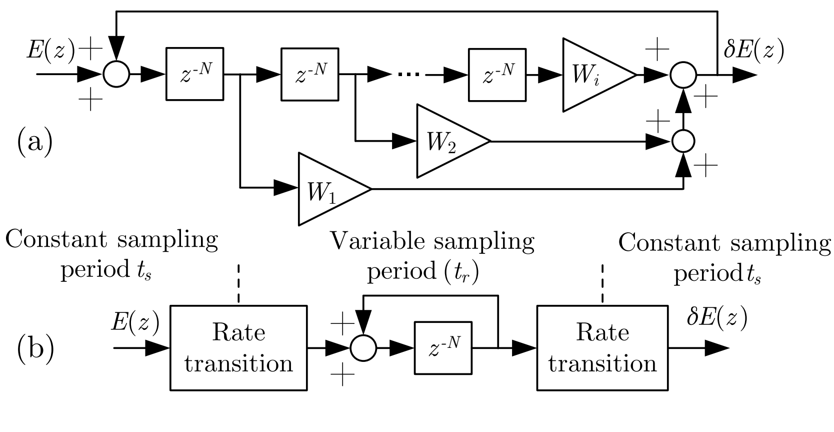

Figure 2.13: (a) High-order RC (HORC) and (b) multi-rate RC.

Alternatives to Improve the Performance of Repetitive Controllers

A popular alternative is the odd-harmonic RC proposed by Costa-Castelló et al. [154], which has been referred many times in the literature [146, 155]. This RC only compensates odd harmonics in the error signal and it requires one half of the memory storage when compared to a classical RC. Moreover, the transient response is twice as fast as that of the RC [155]. Another alternative presented by Lu et al. [156] and Chen et al. [157] only compensates $6k \pm 1$ harmonics. This RC is very interesting for power system applications because harmonics in power systems are typically of these frequencies [103]. Chen et al. [158] plug multiple RCs in parallel with different periods so that the controller can eliminate harmonics of multiple periods. Accordingly, the gain of each RC can be tuned, separately, to improve the transient response. Given the importance role played by RCs in this thesis, the alternatives mentioned above will be discussed further in Chapter 4.

2.7.2 Proportional-Resonant Controllers (PRCs)

PRCs are commonly used to compensate harmonics in power systems since they represent a simple and reliable solution [23, 159]. When applying PRCs, the harmonics to be compensated can be set freely, being a suitable solution not only for the typical harmonics but also for sub- and inter-harmonics, if they are known. There exist simple approaches to design PRCs [160], most of them based on the well-known Nyquist stability criterion [132] or sensitivity functions [161]. PRCs stability has been studied in detail by García-Cerrada [132] for continuous-time applications, revealing that it is necessary to include some phase lead in the controller to compensate the phase delay of the plant.

The most common expression of PRCs for continuous-time applications is studied by Yepes et al. [160] and it is parametrized as follows:

$$PR_h(s) = K_h \frac{s\cos(\phi_h^p) - \omega_g h \sin(\phi_h^p)}{s^2 + (w_g h)^2}, \tag{2.3}$$

where ω_g is the fundamental frequency, h is the harmonic number, ϕ_h^p is the plant phase-delay at $\omega_g h$, and K_h is a gain. Each harmonic (h) to be tackled requires its own PRC. The controller in (2.3) compensates the phase contribution of the plant, providing a phase lead of $-\phi_h^p$ at $\omega_g h$. García-Cerrada et al. [132] propose another parametrization:

$$PR_h(s) = K_h \frac{\dfrac{\alpha_h}{\omega_g h} s + 1}{f_h \dfrac{\alpha_h}{\omega_g h} s + 1} \frac{\omega_g h s}{s^2 + (\omega_g h)^2}. \tag{2.4}$$

For each harmonic, α_h and f_h are designed to achieve the required phase lead. In addition, the interaction between PRCs is low because of the derivative term. However, a systematic design of the compensator parameters is complicated.

PRCs implementation has drawn researchers' attention because, if the controllers are designed in continuous time and then discretized, performance deteriorates if the process is not done carefully and stability problems can arise [162]. Yepes et al. [24] implement PRCs using several discretization methods, concluding that the most appropriate way to discretize PRCs is the impulse-invariant method.

Yepes et al. [24] and Pinzón-Ardila [163] show that the performance of PRCs deteriorates with small frequency variations, even within the narrow limits allowed in electric power systems [164]. Discrete-time PRCs can be adapted to amend frequency variations, but this would require the computation of several trigonometric functions. This difficulty motivated the work developed by Yepes et al. [24], where good results are obtained using low-order Taylor approximations for the trigonometric functions. Both, design and discretisation of PRCs have also been given a second thought in this thesis and some interesting contributions are explained in Chapter 5.

2.7.3 DFT-Based Controllers

The discrete Fourier transform (DFT) is a very selective filter that has already been proposed as the core of power electronics controllers to suppress harmonics [133]. Fig. 2.14 shows the schematics of the DFT-based controller proposed by Le Roux [133]. The DFT is applied to the error signal ($e(t)$) to obtain the DFT coefficients of each harmonic ($e_{(h)}(t)$) and a PI controller can be applied because harmonics have been transformed into constant values. Finally, the command signal produced by each controller is transformed back to the time domain using the inverse DFT. This controller provides accurate results, but the computational burden is high when considering a long list of harmonics. Contributions of this thesis to algorithms closely related to the DFT-based controllers are covered in Chapter 6.

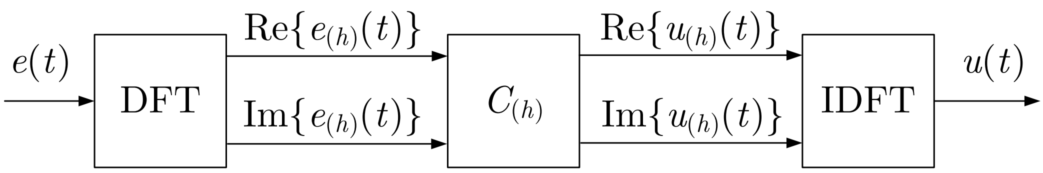

Figure 2.14: Block diagram of a DFT-based controller.

2.7.4 Other Harmonic-Control Algorithms

Algorithms based on least-mean squares [165, 166], iterative learning controllers [167, 168], or multiple-reference frame (MRF) controllers [169, 170] have also been used to deal with harmonics in PE applications. Between them, MRF controllers are the most popular. MRF controllers refer each harmonic to a RF that rotates synchronously with the harmonic to be tackled. Therefore, each three-phase harmonic is transformed into a complex signal with constant real and imaginary components and an integral controller can be applied. The output of each integral controller is rotated again and the result is added to the command of the main controller. Unfortunately, all these rotations lead to a very heavy computational burden. Matavelli [169] demonstrated that a MRF controller can be transformed into an equivalent PRC and, therefore, PRCs are always preferred for the implementation. Very recently, however, Ochoa-Giménez et al. [171] demonstrated that a MRF controller can be implemented much more efficiently than previously recognised, leaving the door opened for further research beyond the scope of this thesis.

2.8 Chapter Summary

This chapter has shown the state of the art in series active compensation and it has revealed technical problems that need further research. Summarising:

- The control of the output voltage of the AC filter in an SAC is not straightforward and it is studied in Chapter 3. The transformer saturation is also studied in this chapter.
- RCs have two relevant problems when they are applied to SACs: internal instability caused by the coupling transformer and the performance deterioration when the frequency varies. Both problems are addressed in Chapter 4.
- The discrete-time design of PRCs and their performance when the frequency deviates from its design value is studied in Chapter 5.
- DFT-based controllers have not been studied in detail in the literature, and there is still much room for improvement. These controllers are studied in Chapter 6.
- Power flow using flexible load voltage limits has seldom been investigated in the literature, and it seems to be an interesting aspect because it gives some freedom to control active and reactive power at the same tine. This topic is studied in Chapter 7.

Chapter 3

First Steps Towards the Control a Series Active Conditioner

This chapter describes the first steps towards the control of an SAC. Section 3.1 presents an overview of the hardware and the control system of an SAC and Section 3.2 describes its dynamic model. Section 3.3 describes the application of a state-feedback (SF) controller and in Section 3.4 this controller is tested in the SAC prototype. Section 3.5 presents two alternatives to the SF controller: a PID and a "cascade" controller. All the alternatives are compared in Section 3.6. Section 3.7 presents a detailed model of the coupling transformer to provide some insight into the transformer saturation problem. Finally, the conclusions of this chapter are summarised in Section 3.8.

3.1 Overview of a Series Active Conditioner

An SAC is depicted in Fig. 3.1. The VSC is connected in series with the PCC using an LC filter (L_f and C_f) and a coupling transformer (the leakage inductance is called L_t and the copper losses are modelled with R_t). The DC-link capacitor is called C_{dc}.

Fig. 3.2 portrays the overall structure of the control system proposed for an SAC. The electrical system dynamics are represented by the the block called "plant dynamics". Space vectors will be marked with a right arrow over the variable name (e.g. $\vec{u}_l(t) = u_{l-d}(t) + ju_{l-q}(t)$) and, to simplify Fig. 3.2 and others, the time dependence of signals will be purposely omitted in most of them. Subscripts d and q stand for direct axis and quadrature axis, respectively. Park's transformation will be used to model the electrical system based on a reference frame that rotates synchronously with the d-axis component of the grid voltage space vector ($\vec{u}_g$). This reference frame will be called "synchronous reference frame" (SRF) and it is chosen to force $u_{g-q} = 0$, so $|\vec{u}_g| = u_{g-d}$. Therefore, the d- and q-axis dynamics will be coupled and a set of decoupling equations is required to design independent controllers for each axis [103].

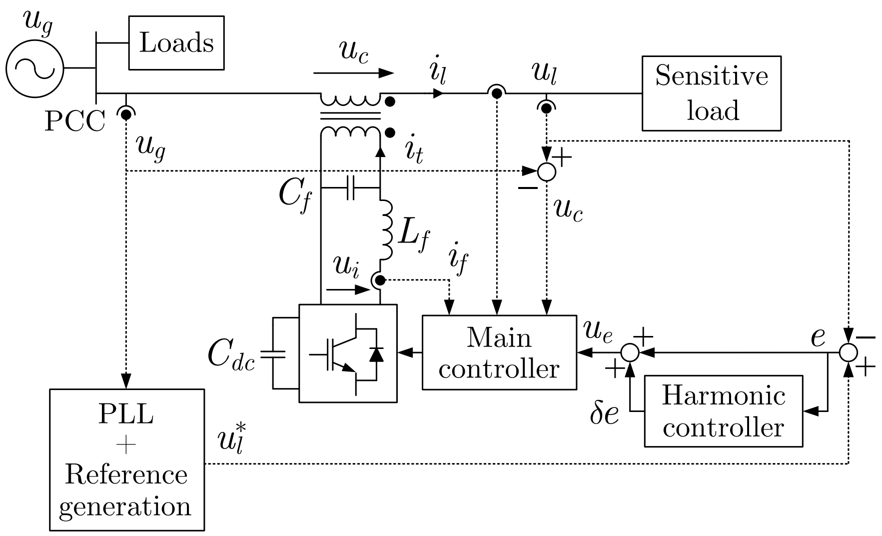

Figure 3.1: Single-phase schematics of the proposed set-up and the controller of an SAC.

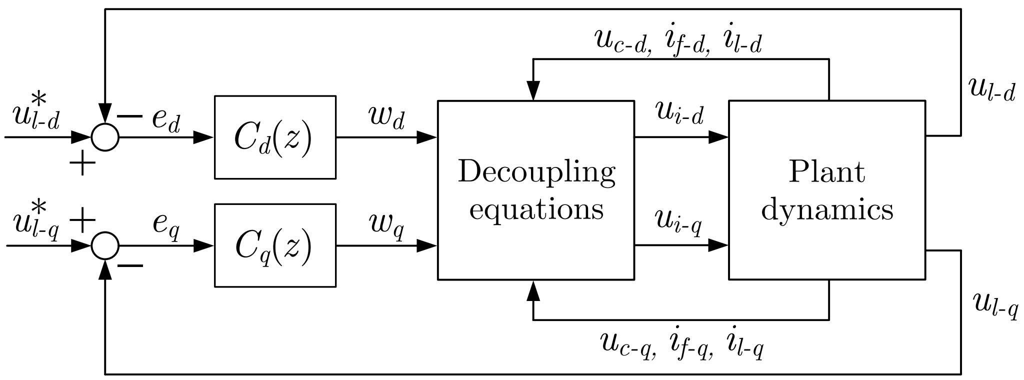

Figure 3.2: Overview of the control strategy for an SAC. Two independent controllers are used: one for the d-axis and another one for the q-axis.

Fig. 3.3 shows two alternatives to implement the SAC controller (only the d-axis is shown). In both cases, the controller is divided into two parts: a main controller and an auxiliary one. The former is designed to control the positive sequence of the load-voltage. The latter compensates the load voltage harmonics (harmonic controller). The load voltage $u_{l-d}(t)$ is controlled manipulating the converter output voltage, $u_{i-d}(t)$. The harmonic controller has been configured as a plug-in and this configuration makes it possible to design the main and the harmonic controllers independently [22]. First of all, the closed-loop system with only the main controller in place has to be made as fast as possible, but well damped in spite of the lightly-damped filter consisting of L_f and C_f [87]. A well-designed main controller will ease the design of the harmonic one in a second stage. The harmonic controller should maintain closed-loop stability while addressing voltage harmonics accurately.

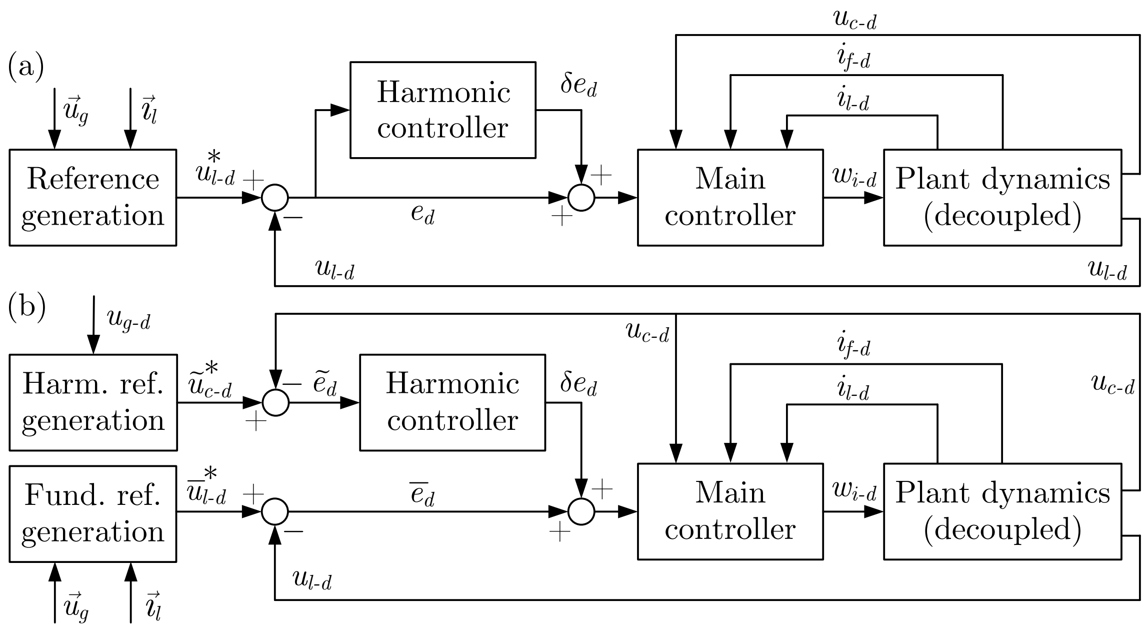

Figure 3.3: (a) Direct load-voltage controller and (b) split-reference controller.

In Fig. 3.3 (a) the control system is set to follow, directly, the load-voltage set-point and, therefore, this approach will be called here "direct load-voltage controller". The reference signal ($u^*_{l-d}(t)$) is generated taking into account the grid voltage value ($\vec{u}_g(t)$) and, if required, the load current ($\vec{\imath}_l(t)$). The reference signal only contains the fundamental component (a DC signal using a SRF) and the harmonic controller is used to reject the voltage harmonics in the supply so that they do not reach the load. Fig. 3.3 (b) shows a more sophisticated control structure for the SAC that will be called "split-reference controller". In this case the set-point signal is split into two, namely, the one called $\overline{u}^*_{l-d}(t)$, which contains the set-point signal for the fundamental component of the load voltage and another one, called $\tilde{u}^*_{c-d}(t)$, which contains the harmonic components to be rejected. With the control structure in Fig. 3.3 (b) the harmonics to be compensated can be selected freely. Moreover, as shown in Chapter 6, this approach makes it possible to use the SAC as a CSeAPF (current filter). Notice that closed-loop stability can be assessed regardless of the control structure to be used because the main difference between them lies only in the place where set-point values and disturbances enter the control system.

3.2 Model of a Series Active Conditioner

3.2.1 Per-Unit Model

Per-unit (pu) models ease the interpretation of the results and the implementation of control algorithms in DSPs. There exist many approaches to select the base values depending on the application [163], but in this thesis the base values for the three-phase voltages and currents have been chosen so that rated voltages and currents of the device produce unit-magnitude vectors when referred to a SRF. These base values are summarized in Table 3.1, where θ_t is the phase-voltage rotation between the primary side (VSC) and the secondary side (grid) of the coupling transformer, and a_t is the conversion ratio ($1 : a_t e^{j\theta_t}$). All the base values are referred to the grid side of the coupling transformer [6]. Subscript b stands for base and subscript n stands for nominal.

Variable name	Base name	VSC side	Grid side
Apparent power (VA)	S_b	$\sqrt{3}U_n I_n$	$\sqrt{3}U_n I_n$
Phase voltage (V)	U_b	$U_n/(a_t e^{j\theta_t})$	U_n
Current (A)	I_b	$\sqrt{3}I_n(a_t e^{-j\theta_t})$	$\sqrt{3}I_n$
Impedance (Ω)	Z_b	$U_n/(\sqrt{3}I_n a_t^2)$	U_n/I_n
Frequency (rad/s)	ω_b	ω_n	ω_n

Table 3.1: Base values to be used in this thesis.

Some important remarks regarding the information displayed in Table 3.1 are:

1. The modulus of rated voltages and currents referred to a SRF (dq-axis) equal 1 pu if (a) the base values in Table 3.1 are used and (b) a power-invariant Park's transformation is applied [172]. If these conditions are met, rated instantaneous active and reactive powers equal 1 pu as well.
2. Rated three-phase signals are transformed into three-phase signals with a peak value of $\sqrt{2/3}$ after dividing them by their base value. Therefore, three-phase waveforms will be portrayed multiplied by $\sqrt{3/2}$ so that the rated peak value equals 1 pu.

However, when designing and implementing controllers no base frequency will be used ($\omega_b = 1$) because it is easier to interpret the designs using natural dimensions (hertz or seconds) rather than per-units. In the rest of the thesis results will be shown using per-unit values unless otherwise stated.

3.2.2 Continuous-Time Modelling

A single-phase equivalent circuit for an SAC is depicted in Fig. 3.4, where Z_g models the line impedance and $i_g(t)$ is the supply current, which consists of the sensitive-load current ($i_l(t)$) and the rest-of-the-load current ($i_r(t)$). The current through L_f is $i_f(t)$ and $i_c(t)$ is the current through C_f. R_f models the copper losses of the filter inductor (assuming they are frequency independent), L_t is the transformer leakage inductance, and R_t models the transformer copper losses. Since all variables are in pu, there is no need to include the transformer conversion ratio. Finally, assuming that L_t is negligible when compared with the load impedance and $u_c(t) \approx u_{cf}(t)$, the state-variable model for the SAC referred to a SRF is:

$$\frac{d\boldsymbol{x}(t)}{dt} = \boldsymbol{A}\boldsymbol{x}(t) + \boldsymbol{B}\boldsymbol{u}(t), \tag{3.1}$$

with

$$\boldsymbol{A} = \begin{bmatrix} -\frac{R_f}{L_f} & -\frac{1}{L_f} & \omega_g & 0 \\ \frac{1}{C_f} & 0 & 0 & \omega_g \\ -\omega_g & 0 & -\frac{R_f}{L_f} & -\frac{1}{L_f} \\ 0 & -\omega_g & \frac{1}{C_f} & 0 \end{bmatrix}, \ \boldsymbol{x}(t) = \begin{bmatrix} i_{f-d} \\ u_{c-d} \\ i_{f-q} \\ u_{c-q} \end{bmatrix}_t, \tag{3.2}$$

$$\boldsymbol{B} = \begin{bmatrix} \frac{1}{L_f} & 0 & 0 & 0 \\ 0 & -\frac{1}{C_f} & 0 & 0 \\ 0 & 0 & \frac{1}{L_f} & 0 \\ 0 & 0 & 0 & -\frac{1}{C_f} \end{bmatrix}, \qquad \boldsymbol{u}(t) = \begin{bmatrix} u_{i-d} \\ i_{l-d} \\ u_{i-q} \\ i_{l-q} \end{bmatrix}_t, \tag{3.3}$$

where all the electrical variables are represented by space vectors of dq components in per-unit values after applying Park's transformation [103]. The command signal is $\vec{u}_i(t)$, $\vec{\imath}_l(t)$ is a disturbance, and ω_g is the synchronous frequency. Subscript t in $\boldsymbol{x}$ and $\boldsymbol{u}$ highlights the time dependence of signals.

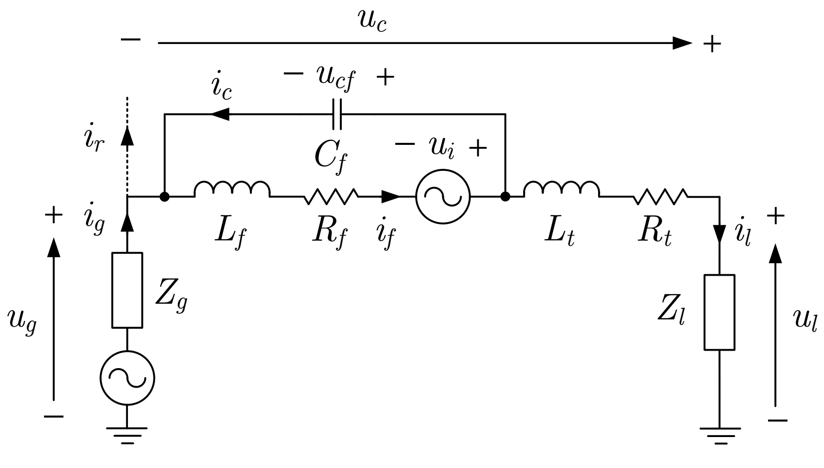

Figure 3.4: Single-phase electrical model for the SAC.

3.2.3 Discrete-Time Model

A discrete-time model can be calculated using a zero-order hold (ZOH) in (3.1) [173]:

$$\boldsymbol{x}[k+1] = \boldsymbol{\Phi}\boldsymbol{x}[k] + \boldsymbol{\Gamma}\boldsymbol{u}[k], \tag{3.4}$$

where $\boldsymbol{\Phi} = e^{\boldsymbol{A}t_s}$, $\boldsymbol{\Gamma} = \left(\int_0^{t_s} e^{\boldsymbol{A}t} dt\right) \boldsymbol{B}$, and t_s is the sampling period. Using a SRF and separating inputs and disturbances (3.4) can be written as

$$\begin{bmatrix} \boldsymbol{x}_d \\ \boldsymbol{x}_q \end{bmatrix}_{k+1} = \underbrace{\begin{bmatrix} \boldsymbol{\Phi}_d & \boldsymbol{\Phi}_{dq} \\ -\boldsymbol{\Phi}_{dq} & \boldsymbol{\Phi}_q \end{bmatrix}}_{\boldsymbol{\Phi}} \begin{bmatrix} \boldsymbol{x}_d \\ \boldsymbol{x}_q \end{bmatrix}_k + \underbrace{\begin{bmatrix} \boldsymbol{\Gamma}_d & \boldsymbol{\Gamma}_{dq} \\ -\boldsymbol{\Gamma}_{dq} & \boldsymbol{\Gamma}_q \end{bmatrix}}_{\boldsymbol{\Gamma}_u} \begin{bmatrix} u_{i-d} \\ u_{i-q} \end{bmatrix}_k + \boldsymbol{\Gamma}_i \begin{bmatrix} i_{l-d} \\ i_{l-q} \end{bmatrix}_k \tag{3.5}$$

where

$$\boldsymbol{\Phi}_d = \begin{bmatrix} \phi_{11} & \phi_{12} \\ \phi_{21} & \phi_{22} \end{bmatrix}, \ \boldsymbol{\Phi}_{dq} = \begin{bmatrix} \phi_{13} & \phi_{14} \\ \phi_{23} & \phi_{24} \end{bmatrix}, \ \boldsymbol{\Phi}_q = \begin{bmatrix} \phi_{33} & \phi_{34} \\ \phi_{43} & \phi_{44} \end{bmatrix}, \tag{3.6}$$

$$\boldsymbol{\Gamma}_d = \begin{bmatrix} \gamma_{11}^u \\ \gamma_{21}^u \end{bmatrix}, \ \boldsymbol{\Gamma}_{dq} = \begin{bmatrix} \gamma_{12}^u \\ \gamma_{22}^u \end{bmatrix}, \ \boldsymbol{\Gamma}_q = \begin{bmatrix} \gamma_{32}^u \\ \gamma_{42}^u \end{bmatrix}, \ \boldsymbol{\Gamma}_i = \begin{bmatrix} \gamma_{11}^i & \gamma_{12}^i \\ \gamma_{21}^i & \gamma_{22}^i \\ \gamma_{31}^i & \gamma_{32}^i \\ \gamma_{41}^i & \gamma_{42}^i \end{bmatrix}. \tag{3.7}$$

The subscript k indicates the discrete-time sample of a continuous-time signal. If disturbances and the system state variables in (3.5) can all be measured, (3.5) can be rewritten as:

$$\begin{bmatrix} \boldsymbol{x}_d \\ \boldsymbol{x}_q \end{bmatrix}_{k+1} = \begin{bmatrix} \boldsymbol{\Phi}_d & \mathbf{0} \\ \mathbf{0} & \boldsymbol{\Phi}_q \end{bmatrix} \begin{bmatrix} \boldsymbol{x}_d \\ \boldsymbol{x}_q \end{bmatrix}_k + \underbrace{\begin{bmatrix} \boldsymbol{\Gamma}_d & \mathbf{0} \\ \mathbf{0} & \boldsymbol{\Gamma}_q \end{bmatrix}}_{\boldsymbol{\Gamma}_w} \begin{bmatrix} w_d \\ w_q \end{bmatrix}_k, \tag{3.8}$$

where $w_d[k]$ and $w_q[k]$ are two virtual inputs and $\mathbf{0}$ is a matrix full of zeros of the appropriate size. The actual converter output voltage can be calculated using

$$\begin{bmatrix} u_{i-d} \\ u_{i-q} \end{bmatrix}_k = \boldsymbol{\Gamma}_u^+ \boldsymbol{\Gamma}_w \begin{bmatrix} w_d \\ w_q \end{bmatrix}_k - \boldsymbol{\Gamma}_u^+ \boldsymbol{\Gamma}_i \begin{bmatrix} i_{l-d} \\ i_{l-q} \end{bmatrix}_k - \boldsymbol{\Gamma}_u^+ \underbrace{\begin{bmatrix} \mathbf{0} & \boldsymbol{\Phi}_{dq} \\ -\boldsymbol{\Phi}_{dq} & \mathbf{0} \end{bmatrix}}_{\boldsymbol{\Phi}_x} \begin{bmatrix} \boldsymbol{x}_d \\ \boldsymbol{x}_q \end{bmatrix}_k, \tag{3.9}$$

where $\boldsymbol{\Gamma}_u^+$ is the left pseudo-inverse matrix of $\boldsymbol{\Gamma}_u$:

$$\boldsymbol{\Gamma}_u^+ = \left(\boldsymbol{\Gamma}_u^t \boldsymbol{\Gamma}_u\right)^{-1} \boldsymbol{\Gamma}_u^t, \tag{3.10}$$

and t means "transposed". The solution presented in (3.9) minimizes the coupling terms because it is obtained using the pseudo-inverse matrix.

3.2.4 Plant Model with Delays

For control purposes, the accuracy of plant model improves if the calculus delay and the delay caused by the anti-aliasing filters are included in the discrete-time model [26]. The former is naturally modelled by a one-sample delay in the command signal. The latter can also be modelled by a one-sample delay in the command signal if the appropriate

Bessel filters are used for all the measurements [163]. The output calculated by the controller is $\vec{w}''[k]$ and the new state-variables that model the delays are[1]:

$$\begin{aligned} \vec{w}'[k+1] &= \vec{w}''[k], && (3.11) \\ \vec{w}[k+1] &= \vec{w}'[k], && (3.12) \end{aligned}$$

and the discrete-time model of the plant in (3.8) can be written as (only the d-axis shown):

$$\begin{bmatrix} \boldsymbol{x}_d \\ w_d \\ w'_d \end{bmatrix}_{k+1} = \begin{bmatrix} \boldsymbol{\Phi}_d & \boldsymbol{\Gamma_d} & \mathbf{0} \\ \mathbf{0} & 0 & 1 \\ \mathbf{0} & 0 & 0 \end{bmatrix} \begin{bmatrix} \boldsymbol{x}_d \\ w_d \\ w'_d \end{bmatrix}_{k} + \begin{bmatrix} \mathbf{0} \\ 0 \\ 1 \end{bmatrix} w''_d[k]. \tag{3.13}$$

Therefore, the controller will calculate $\vec{w}''[k]$, which is the input of the plant model (3.13) in k. Calling $\vec{u}''_i[k] = \vec{u}_i[k+2]$ the actual VSC voltage to be applied in $k+2$, one can use the decoupling equation (3.9) as:

$$\begin{bmatrix} u''_{i-d} \\ u''_{i-q} \end{bmatrix}_k = \boldsymbol{\Gamma}_u^+ \boldsymbol{\Gamma}_w \begin{bmatrix} w''_d \\ w''_q \end{bmatrix}_k - \boldsymbol{\Gamma}_u^+ \boldsymbol{\Gamma}_i \begin{bmatrix} i_{l-d} \\ i_{l-q} \end{bmatrix}_{k+2} - \boldsymbol{\Gamma}_u^+ \boldsymbol{\Phi}_x \boldsymbol{x}[k+2]. \tag{3.14}$$

Clearly, the values of $\vec{u}''_i[k]$ (to be applied in $k+2$) in (3.14) depend on the state variables and the load current at instant $k+2$, which are not available at k. However, the value of $\boldsymbol{x}[k+2]$ can be predicted two steps ahead and replaced in (3.14) using the approach presented by García-Cerrada et al. [26, 174], yielding

$$\hat{\boldsymbol{x}}[k+2/k] = \begin{bmatrix} \boldsymbol{\Phi}_d & \mathbf{0} \\ \mathbf{0} & \boldsymbol{\Phi}_q \end{bmatrix}^2 \boldsymbol{x}[k] + \begin{bmatrix} \boldsymbol{\Phi}_d & \mathbf{0} \\ \mathbf{0} & \boldsymbol{\Phi}_q \end{bmatrix} \begin{bmatrix} w''_d \\ w''_q \end{bmatrix}_{k-1} + \begin{bmatrix} \boldsymbol{\Gamma}_d & \mathbf{0} \\ \mathbf{0} & \boldsymbol{\Gamma}_q \end{bmatrix} \begin{bmatrix} w''_d \\ w''_q \end{bmatrix}_k. \tag{3.15}$$

In addition, assuming that the load current varies slowly, $\vec{\imath}_l[k+2] \approx \vec{\imath}_l[k]$, so the decoupling equations in (3.14) can be applied seamlessly.

3.3 State-Feedback Controller

3.3.1 Design of the Controller

Integrals for the errors of the output variables ($\vec{e} = \vec{u}_l^* - \vec{u}_l = \vec{u}_c^* - \vec{u}_c$) can be added easily using extra state variables in the model [22, 26]:

$$\vec{\zeta}\,[k+1] = \vec{\zeta}\,[k] + t_s\left(\vec{u}_c^*\,[k] - \vec{u}_c\,[k]\right). \tag{3.16}$$

[1]The delays have been modelled directly in the SRF, although they are produced in *abc* and they generate a coupling effect when they are referred to a SRF. However, these coupling effects can be easily compensated when conditioning the converter output voltage [172].

The open-loop equations for the d-axis are (similar for the q-axis):

$$\begin{bmatrix} i_{f-d} \\ u_{c-d} \\ w_d \\ w'_d \\ \zeta_d \end{bmatrix}_{k+1} = \begin{bmatrix} \phi_{11} & \phi_{12} & \gamma^u_{11} & 0 & 0 \\ \phi_{21} & \phi_{22} & \gamma^u_{21} & 0 & 0 \\ 0 & 0 & 0 & 1 & 0 \\ 0 & 0 & 0 & 0 & 0 \\ 0 & -t_s & 0 & 0 & 1 \end{bmatrix} \begin{bmatrix} i_{f-d} \\ u_{c-d} \\ w_d \\ w'_d \\ \zeta_d \end{bmatrix}_k + \begin{bmatrix} 0 & 0 \\ 0 & 0 \\ 0 & 0 \\ 1 & 0 \\ 0 & t_s \end{bmatrix} \begin{bmatrix} w''_d \\ u^*_{c-d} \end{bmatrix}_k , \tag{3.17}$$

and the controller will calculate:

$$w''_d[k] = \boldsymbol{K}_d \begin{bmatrix} \boldsymbol{x}_d \\ w_d \\ w'_d \\ \zeta_d \end{bmatrix}_k , \tag{3.18}$$

while the actual values of the command are computed with (3.14). The main controller can be designed as a proportional SF controller and it is depicted in Fig 3.5. In that figure, $\boldsymbol{K}_d$ and $\boldsymbol{K}_q$ are row vectors that contain the gain values for the d- and q-axis controllers, respectively. The controller gains can be designed using any pole-placement algorithm [22, 26].

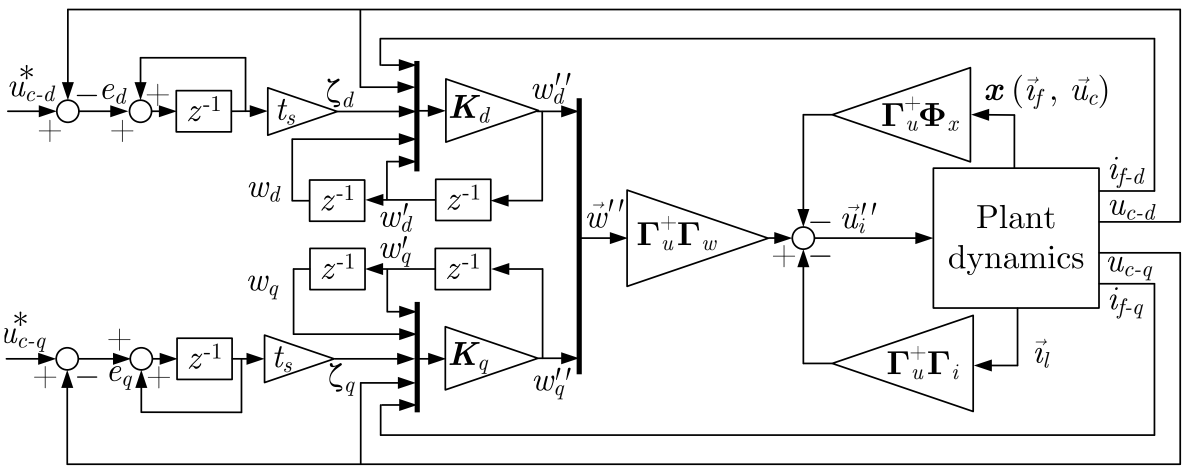

Figure 3.5: Application of a SF controller to an SAC. Two independent controllers are used, one for each axis (the state-variable predictions are not shown for simplicity).

3.3.2 Incremental Controller

The initial connection to the grid might cause large variations in the command signals and oscillations in the controlled variables. This can be avoided using incremental controllers [175]. For this purpose, the control system output can be rewritten as follows:

$$\begin{bmatrix} u''_{i-d} \\ u''_{i-q} \end{bmatrix}_k = \begin{bmatrix} u''_{i-d} \\ u''_{i-q} \end{bmatrix}_{k-1} + \begin{bmatrix} \Delta u''_{i-d} \\ \Delta u''_{i-q} \end{bmatrix}_k , \tag{3.19}$$

and the incremental part of the command is computed as:

$$\begin{bmatrix} \Delta u''_{i-d} \\ \Delta u''_{i-q} \end{bmatrix}_k = \boldsymbol{\Gamma}_u^+ \boldsymbol{\Gamma}_w \begin{bmatrix} \Delta w''_d \\ \Delta w''_q \end{bmatrix}_k - \boldsymbol{\Gamma}_u^+ \boldsymbol{\Gamma}_i \begin{bmatrix} \Delta i_{l-d} \\ \Delta i_{l-q} \end{bmatrix}_k - \boldsymbol{\Gamma}_u^+ \boldsymbol{\Phi}_x \Delta \hat{\boldsymbol{x}}[k+2/k]. \tag{3.20}$$

Fig. 3.6 shows the implementation of the SF controller using the incremental approach. In that figure, $\Delta(\cdot)$ stands for the incremental operator and $\Sigma(\cdot)$ stands for the accumulation operator ($\Sigma(\Delta(\vec{u}_i)) = \vec{u}_i$). Addressing the problem in this way the implementation of an anti-windup mechanism becomes trivial because $\Delta\vec{u}''_i[k]$ is added to the command signal only if $\vec{u}''_i[k]$ falls within the operation limits [175].

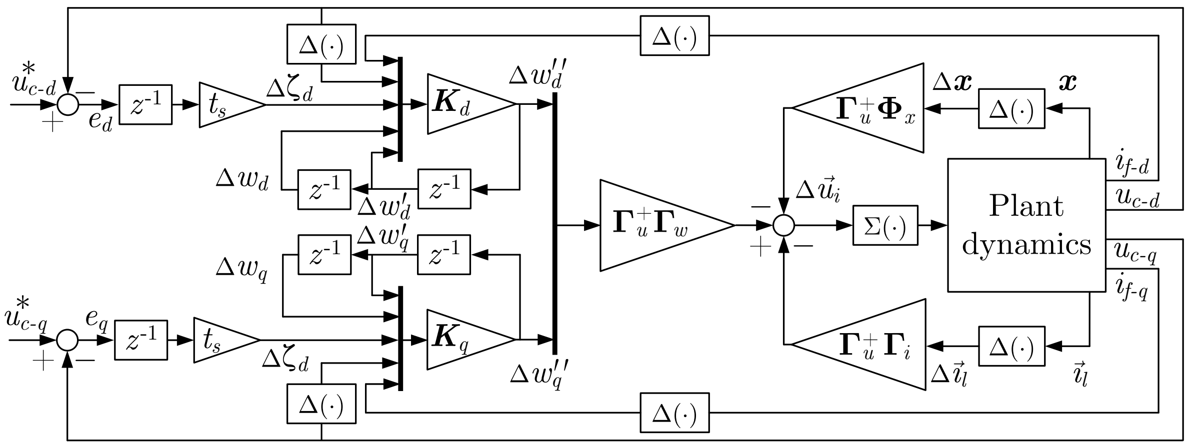

Figure 3.6: Incremental implementation of a SF controller. $\Delta(\cdot)$ stands for the incremental operator and $\Sigma(\cdot)$ stands for the accumulation operator (the state-variable predictions are not shown for simplicity).

3.4 Application of a SF Controller to an SAC

3.4.1 Main Controller Design and Analysis

The schematics of the prototype and the system parameters used in this section can be found in Appendix A. The closed-loop poles (same approach for both axes) have been designed with a dominant real pole placed at 600 Hz ($s = -2\pi 600$ rad/s). The rest of the poles have also been made real and all of them have been placed at 2500 Hz ($s = -2\pi 2500$ rad/s). The gain vectors calculated by the pole-placement algorithm are $\boldsymbol{K}_d$ and $\boldsymbol{K}_q$ in Fig. 3.6. It has been difficult to find a location for the closed-loop poles that results in reasonable stability margins and the high-frequency poles (the ones located at 2500 Hz) greatly modify these margins. The details regarding robustness will be discussed later in Section 3.6. In any case, the closed-loop system can be written as:

$$\begin{bmatrix} U_{c-d}(z) \\ U_{c-q}(z) \end{bmatrix} = \begin{bmatrix} F_p^d(z) & F_p^{dq}(z) \\ F_p^{qd}(z) & F_p^q(z) \end{bmatrix} \begin{bmatrix} U_{c-d}^*(z) \\ U_{c-q}^*(z) \end{bmatrix}. \tag{3.21}$$

Fig. 3.7 (left) shows (grey) the pole-zero diagram of the plant in (3.13) and (black) the frequency response of the closed-loop system, $F_p^d(z)$. The pole-zero diagram contains: (a) the poles related to the LC filter resonance, (b) two poles due to the delays, and (c) a zero due to the sampling process. The closed-loop system has: (d) one dominant pole and (e) 4 high-frequency poles. It has an additional pole (five instead of four) due to the integral term. Fig. 3.7 (right) shows the frequency response of the plant (only the d-axis), (3.14), where $w_d''[k]$ is the input and $u_c[k]$ is the output. The closed-loop plant, $F_p^d(z)$, is also shown in that figure. Clearly, the filter resonance has been damped in closed loop.

Fig. 3.8 shows the frequency response magnitude of the transfer functions in (3.21), with and without the state-variable predictions. For low frequencies both methods provide similar results, but near to the resonance frequency the magnitude of the coupling terms is reduced using predictions. The improvement in the decoupling at high frequency using predictions may be useful when dealing with harmonics.

Fig. 3.9 shows the step response of $F_p^d(z)$ and $F_p^{dq}(z)$ with and without the predictions. The dynamic response is well damped, anyway, and the steady state is reached in almost 2.5 ms. Fig. 3.9 shows that the coupling effects between axes are relatively low. The transient response obtained here is slower than the one obtained by Kim and

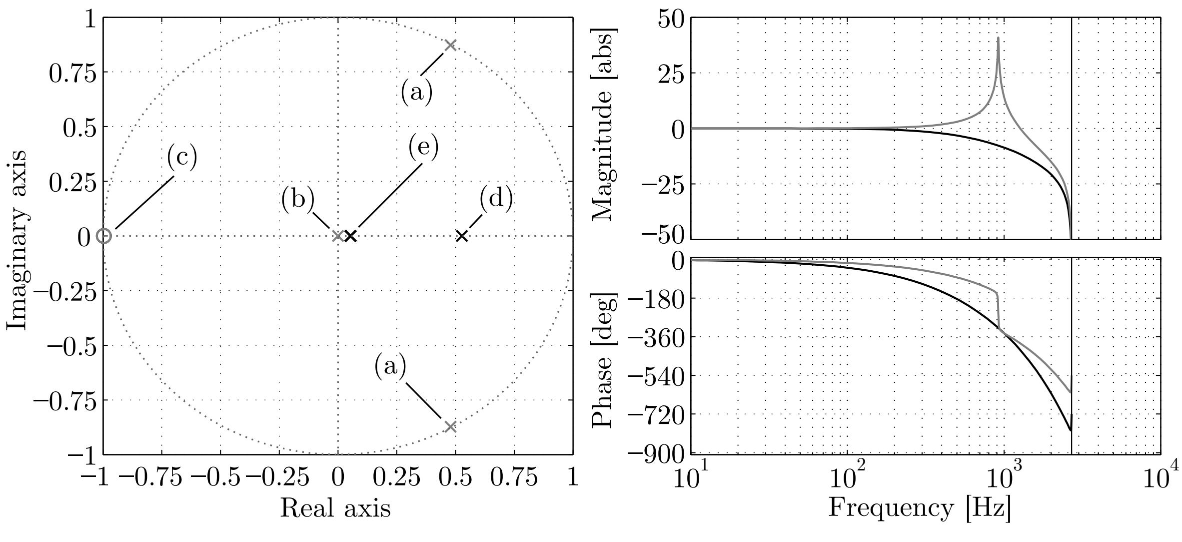

Figure 3.7: (left) Pole-zero diagram of (grey) the uncompensated plant in (3.13) ($w_d''[k]$ is the input and $u_{c-d}[k]$ is the output) and (black) the compensated plant, $F_p^d(z)$. (right) Bode diagram of (grey) the uncompensated plant and (black) the compensated plant.

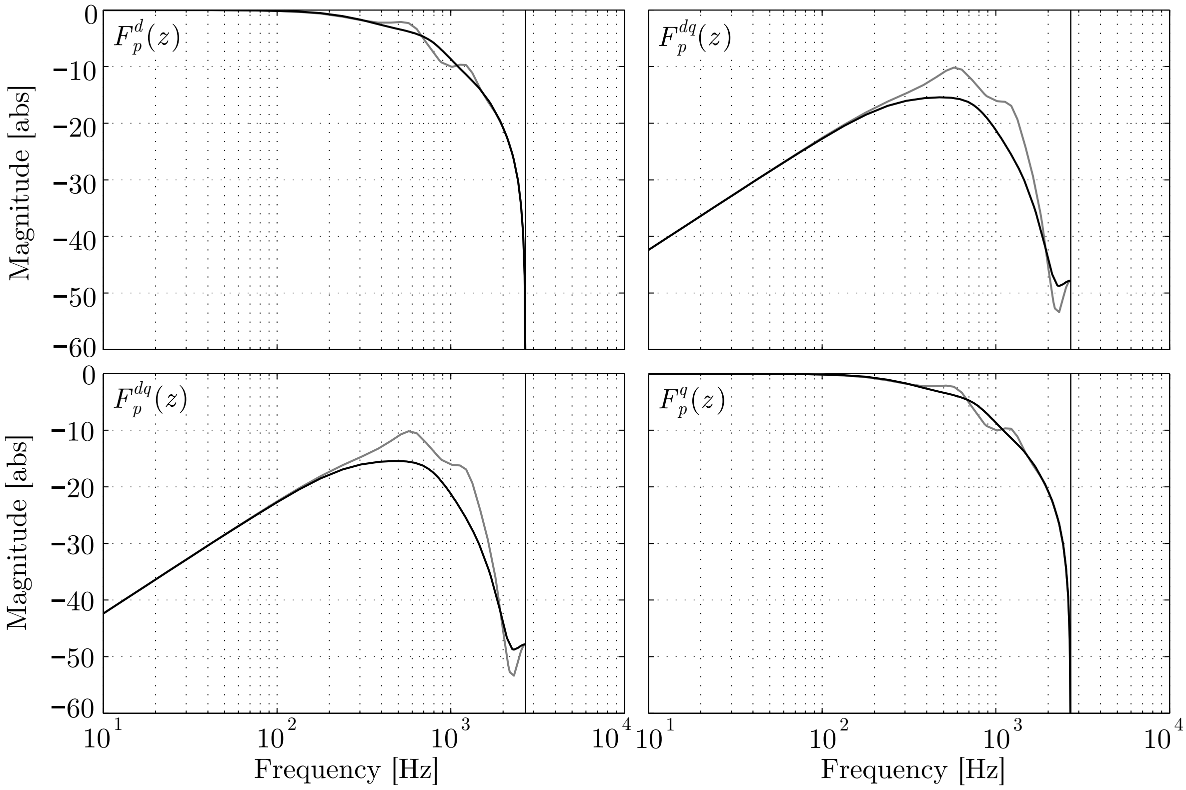

Figure 3.8: Bode plot of $F_p^d(z)$, $F_p^q(z)$, $F_p^{dq}(z)$, and $F_p^{qd}(z)$, (black) with predictions and (grey) without predictions.

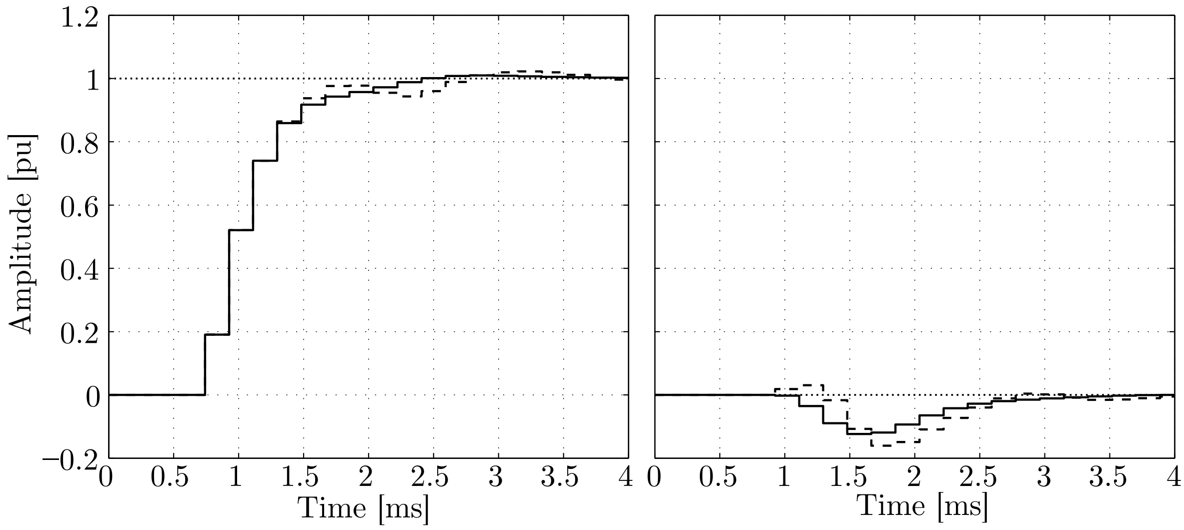

Figure 3.9: Step response of (left) $F_p^d(z)$ and (right) $F_p^{dq}(z)$ (solid) using predictions and (dashed) without predictions.

Sul [129] with a different SF controller. This is probably because the sampling frequency in that paper is 10 kHz (here is 5.4 kHz) and the *LC* filter resonance frequency can be made higher. Therefore, the closed-loop system can be made faster than here.

3.4.2 Performance of the State-Feedback Controller

Compensation of Voltage Sags

To start with, the SAC has been tested under a three-phase voltage sag of 60 % retained voltage (DVR application). Fig. 3.10 shows (a) the grid voltage, (b) the series-injected voltage, (c) the load voltage, (d) the current through the filter inductor, and (g) the load current. The series-injected voltage contains harmonic components due to the

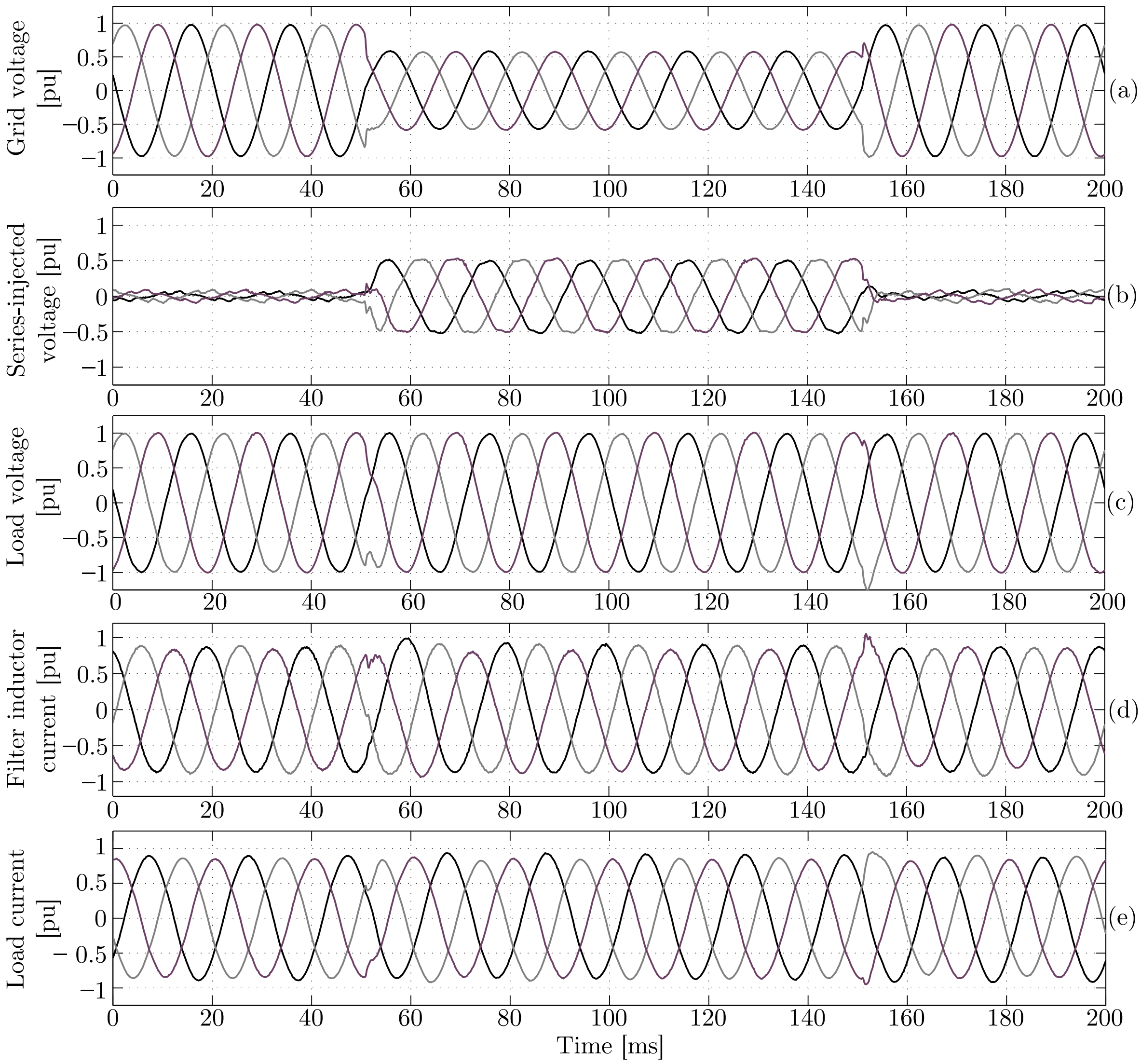

Figure 3.10: Mitigation of a sag (60 % retained voltage) with the SF controller.

PWM process and the non-linearities of the coupling transformer, so the grid voltage THD is 0.3 % and the load voltage THD is 1.4 %. At $t = 50$ ms a sag takes place and the SAC rapidly restores the load voltage. The filter inductor current has a small DC component during the transient, which decays slowly. When the sag ends the SAC rapidly acts and the load voltage remains unaffected.

Fig. 3.11 shows the detailed dq-components of (a and b) the grid voltage, (c and d) the series-injected voltage, and (e and f) the load voltage for the voltage sag in Fig. 3.10. Before the sag the d-axis component of the grid voltage is close to 1 pu because the PLL is forcing the SRF to rotate synchronously with the d-axis of the grid voltage. When the sag takes place, at $t = 4$ ms, the SAC injects the required voltage and, in less than 3 ms, the load voltage is restored. There is an oscillation with a period close to 3 ms in every picture in Fig. 3.11 (e.g. Fig. 3.11 (c)), which corresponds to the harmonics generated by the SAC. Fig. 3.12 shows the results of an FFT applied to the load voltage over 75 cycles (1.5 s). The most important harmonics are 5th (negative sequence) and 7th (positive sequence) ($(6 \pm 1)\omega_g$ in three-phase variables and $6\omega_g$ in dq), which are generated, probably, by the coupling transformer. The component of frequency 100 Hz in dq corresponds to the negative-sequence component in three-phase variables.

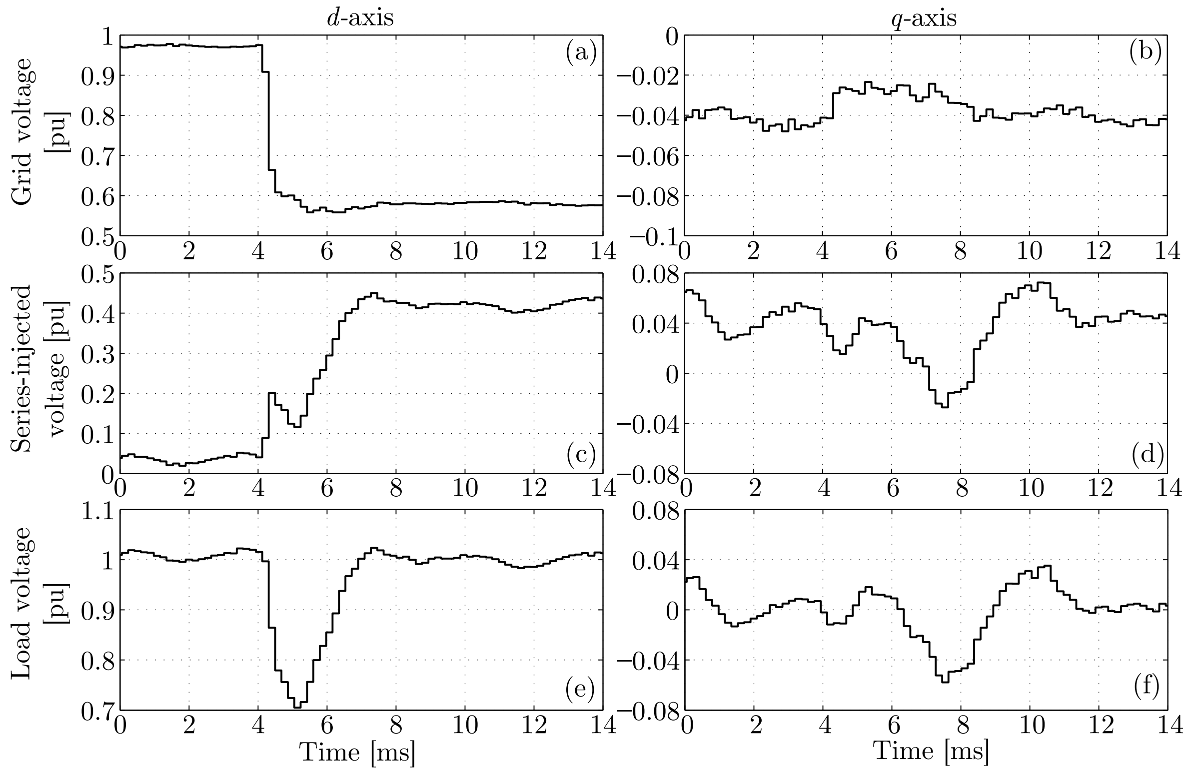

Figure 3.11: Mitigation of a 60 % retained-voltage sag with a SF controller using in-phase compensation (signals referred to a SRF).

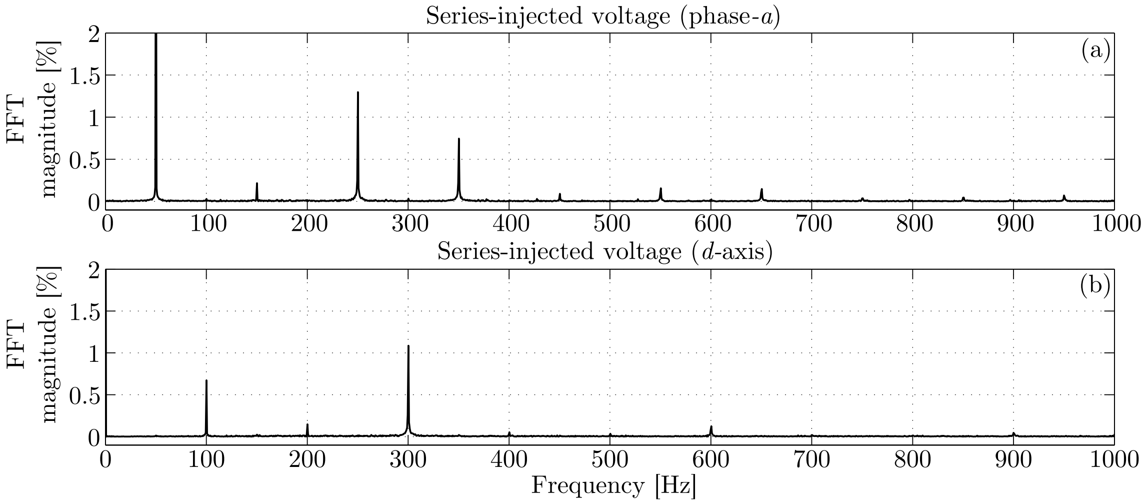

Figure 3.12: FFT modulus of the series-injected voltage: (a) phase-a and (b) d-axis.

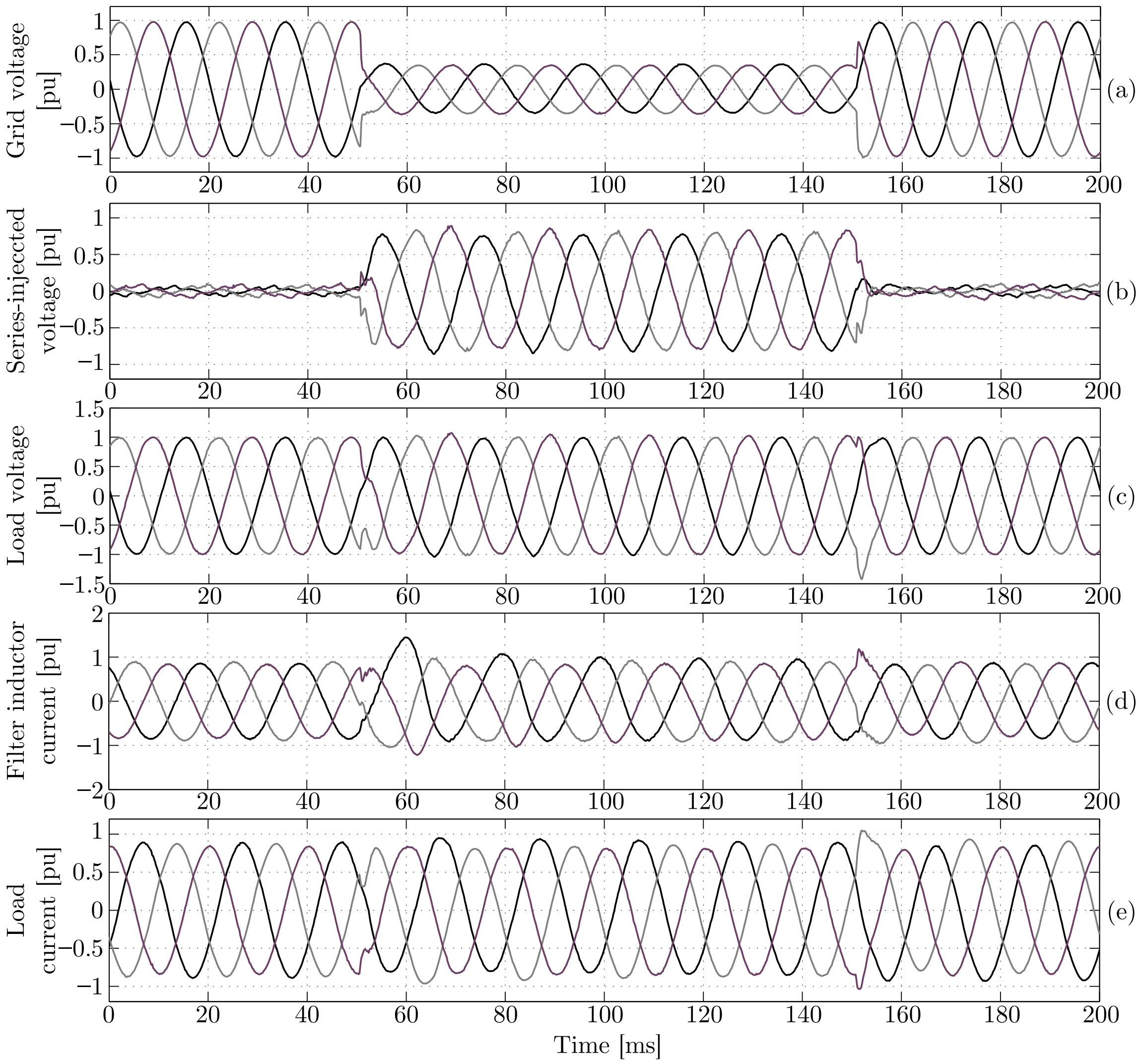

Figure 3.13: Voltage sag compensation (35 % retained voltage) with the SF controller.

Fig. 3.13 shows the SAC performance when compensating a deep voltage sag. Initially, the SAC is connected to the grid and all the variables are in steady-state. At $t = 50$ ms a balanced voltage sag (35 % retained voltage) takes place and the SAC injects the series voltage needed to leave the load voltage undisturbed. One can see a large inrush current in Fig. 3.13 (d) when the compensation starts because the coupling transformer saturates. The current through L_f falls to its previous value after a few cycles, but the load current remains unbalanced. This happens because the load is inductive and the transient requires several cycles to die out.

Fig. 3.14 shows the SAC performance when compensating a sag type D_a (50 % retained voltage) [119]. Notice that the SAC is not able to restore the load voltage because the grid voltage contains negative sequence components (100 Hz in dq). In

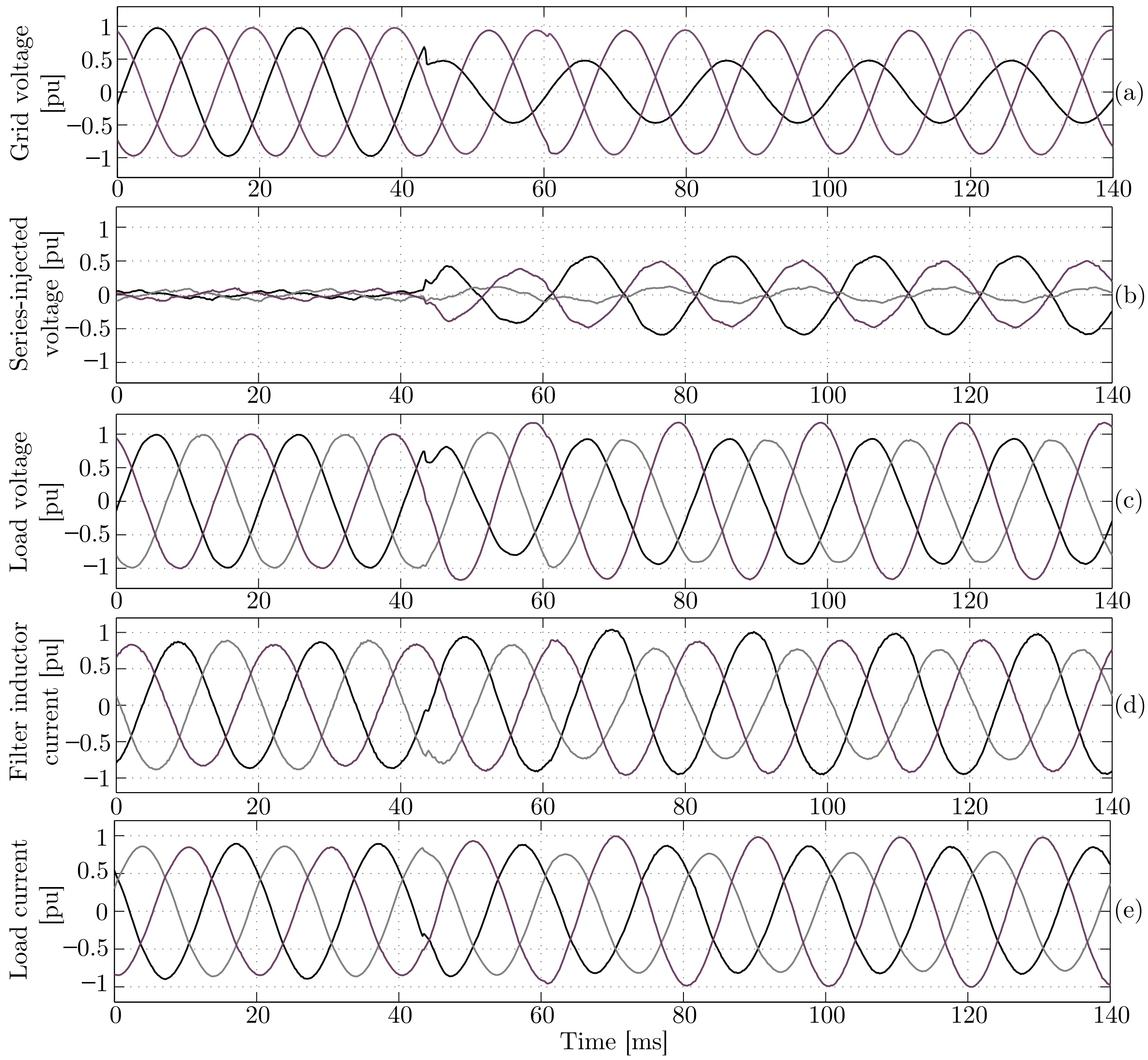

Figure 3.14: Mitigation of a sag type D_a (50 % retained voltage) with the SF controller.

fact, two phases of the load voltage have a voltage magnitude smaller than 1 pu, while another phase has a magnitude higher than 1 pu. One alternative to solve this problem could be, for example, adding a complex resonator tuned at 100 Hz to the state-variable representation, like in Appendix D. This issue will be studied in detail in the following chapters using the harmonic controller mentioned in Section 3.1.

Fig. 3.15 shows the SAC performance compensating a three-phase voltage sag when the grid voltage is polluted with harmonics. The SAC can effectively restore the fundamental component of the load voltage, but it can not compensate the harmonics. Fig. 3.16 shows the FFT of the grid and the load voltages. The SAC amplifies the 5th harmonic, while the rest of them are slightly reduced. The harmonic problem will be thoroughly studied in Chapters 4, 5, and 6.

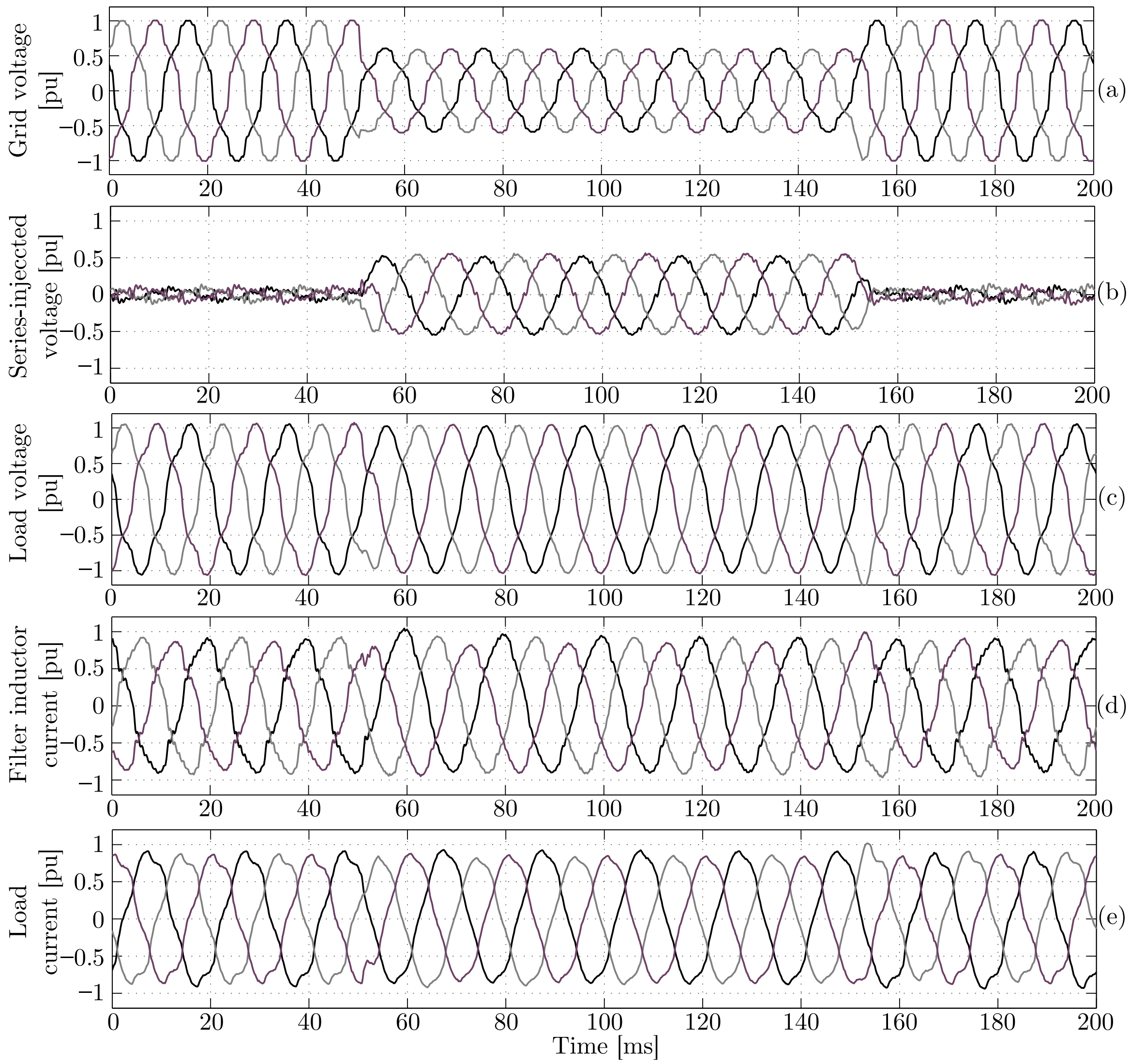

Figure 3.15: Voltage sag compensation (60 % retained) with harmonics in the grid voltage.

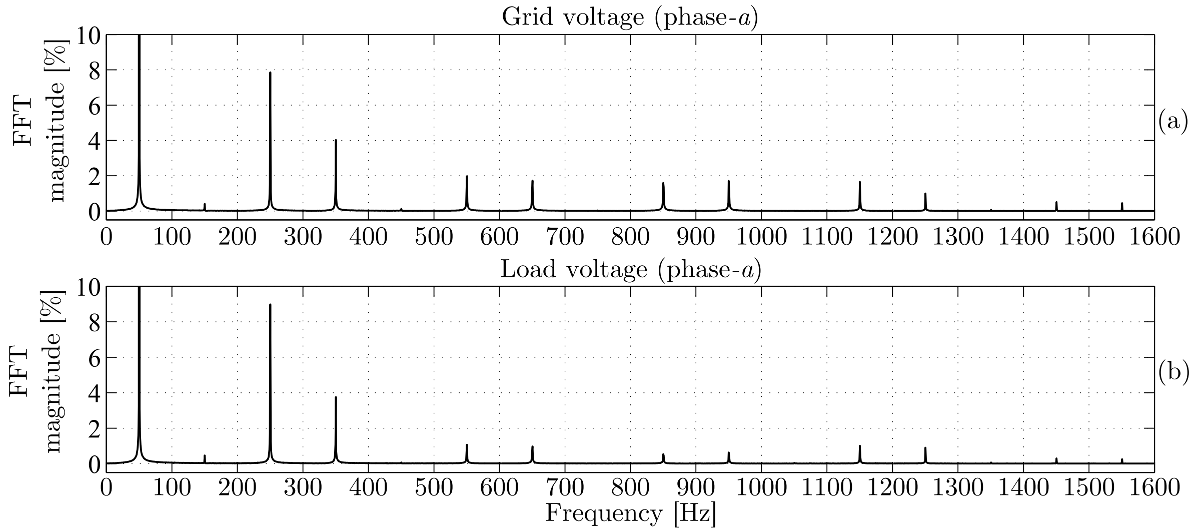

Figure 3.16: FFT magnitudes of (a) the grid and (b) the load voltage when the SAC is in normal operation and the grid is polluted with harmonics.

Fig. 3.17 shows the transient performance of the SAC when the load is a diode bridge with (a) a C-filter (voltage-sourced load) and (b) a L-filter (current-sourced load). For the voltage-sourced load the load voltage becomes highly distorted in steady state (THD is 24.6 %). Fig. 3.17 (e) shows that the grid voltage quality deteriorates as well (THD is 4.6 %). For the current-sourced load (Fig. 3.17, (f to j)) the load voltage THD is 3.2 %, while the grid voltage THD is 3.8 %. As it has been shown, the SAC works better with current-sourced loads than with voltage-sourced loads. This is so because the load voltage is more difficult to control with voltage-sourced loads since, in this case, the load tend to impose the voltage.

Sag Compensation with Phase Rotation

Fig. 3.18 (left) shows a space-vector diagram of the SAC voltages and currents, where $\phi = \varphi + \beta$ is the angle of the impedance if the load is linear. The instantaneous active and reactive powers injected by the SAC can be calculated as follows:

$$p(t) = u_{c-d}(t) i_{l-d}(t) + u_{c-q}(t) i_{l-q}(t), \tag{3.22}$$

$$q(t) = u_{c-q}(t) i_{l-d}(t) - u_{c-d}(t) i_{l-q}(t). \tag{3.23}$$

If (a) the load is balanced and linear, (b) there are no harmonics and, (c) the SAC is working in steady-state: the active power (P) and the reactive power (Q) are constant and $P = p(t)$ and $Q = q(t)$ [14]. Fig. 3.18 (right) shows the active and the reactive power required to compensate a voltage sag of 60 % retained voltage with $\phi = 30$ deg (inductive load). The active power required to compensate the sag varies with φ and

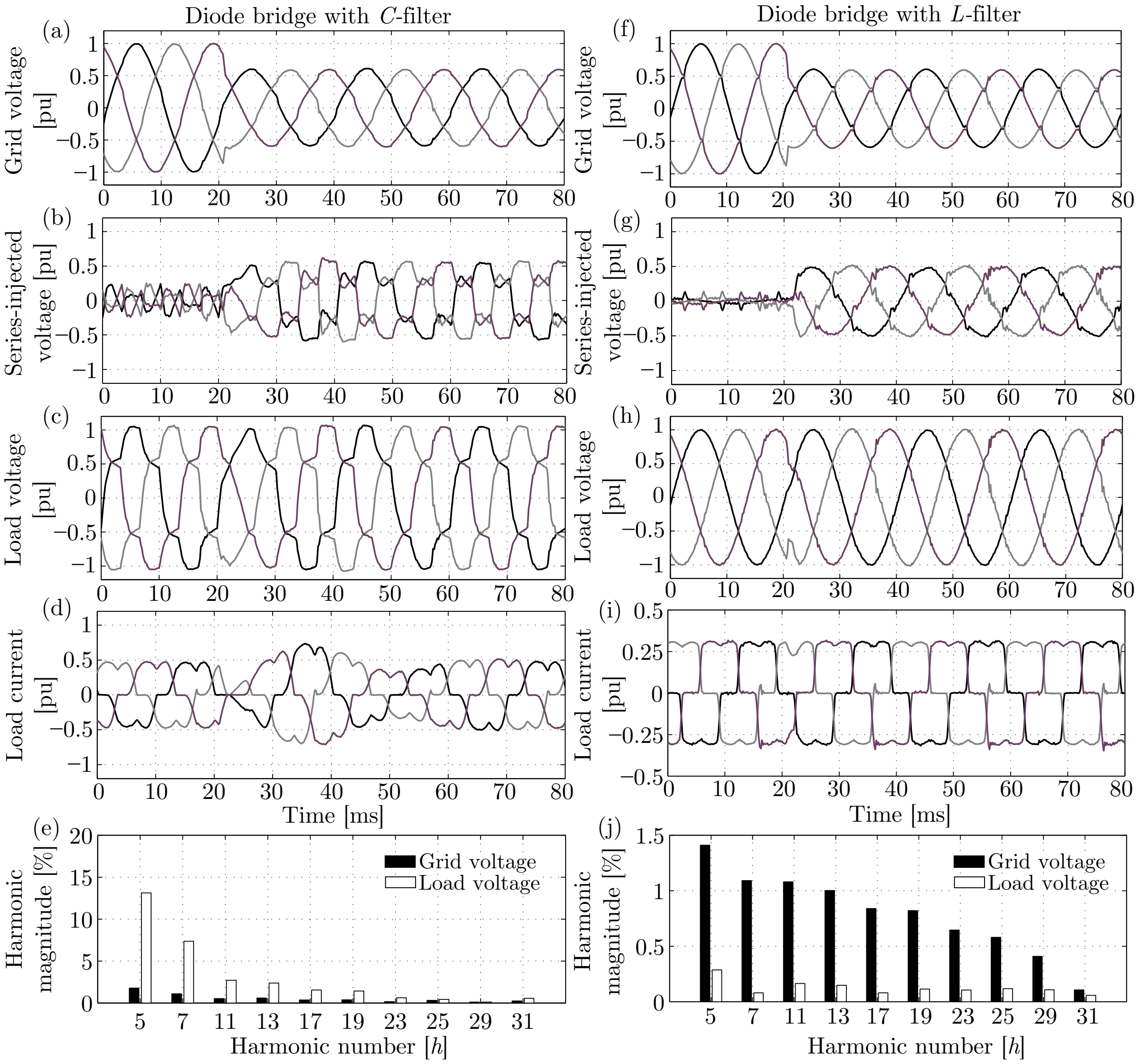

Figure 3.17: Mitigation of a 60 % retained voltage sag when the load is a diode bridge with (a to e) a C-filter and (f to j) an L-filter.

it has a minimum value ($\varphi = 0$, which corresponds to the so-called "minimum-power compensation" [117]). However, when applying this method (a) the load voltage is rotated and (b) the voltage amplitude is very large (see Fig. 3.18).

Fig. 3.19 shows the SAC performance using the minimum-power compensation method. The load voltage is compensated, rapidly, but the phase shift generates an undesired transient in the load current. This happens because the phase shift modifies the flux of the inductive part of the load and, therefore, its current. However, a slow phase rotation might avoid this effect. Fig. 3.19 (f) shows that the SAC injects a huge amount of reactive power (0.6 pu) to compensate the load voltage with the minimum possible power. The oscillations in the powers (active and reactive) are generated by

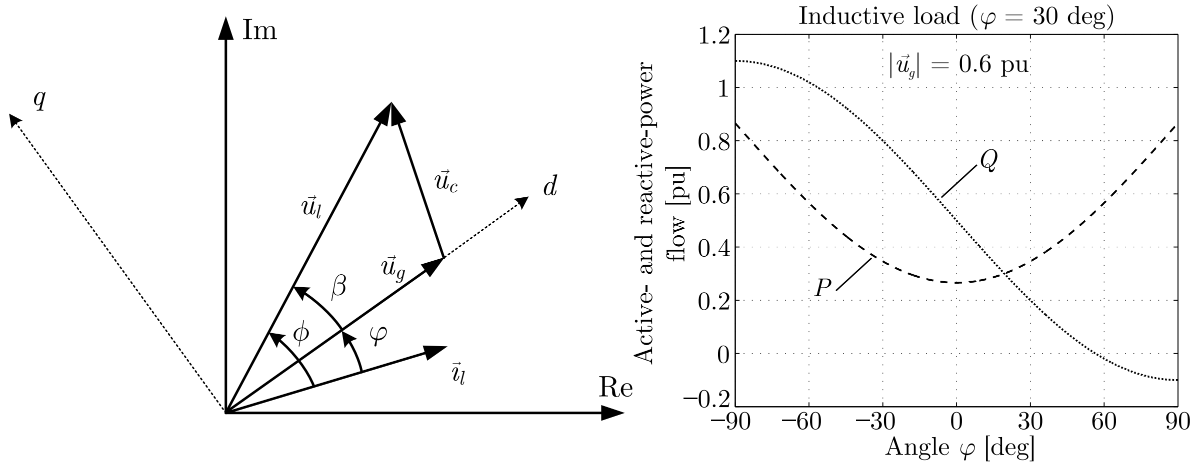

Figure 3.18: (left) Space-vector diagram and (right) active and reactive power required to restore the load voltage (60 % retained voltage and $\phi = 30$ deg).

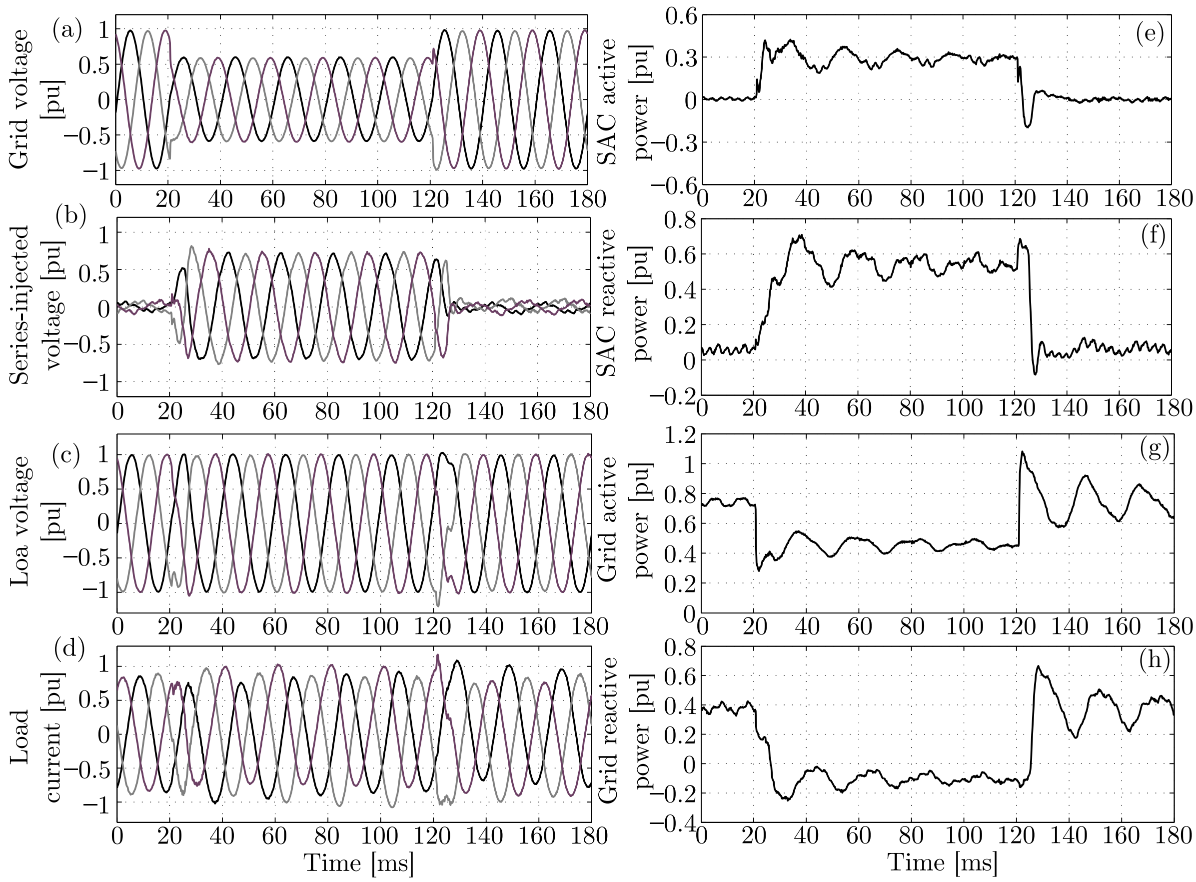

Figure 3.19: Mitigation of a 60 % retained voltage sag using minimum-power compensation. (e and f) Power delivered by the SAC and (g and h) power delivered by the grid. The DC link is maintained constant with the additional rectifier (see Appendix A.)

the transient response of the load current (see Fig. 3.19 (d)). The power flow when compensating voltage sags will be studied in more detail in Chapter 7.

A sensible approach would be to start the compensation using in-phase compensation, thus avoiding disturbing the load. Once the magnitude of the load voltage has been properly restored, the phase can be shifted, slowly. The maximum rate of change for the phase shift is defined as follows:

$$-SR_\beta \leq (\beta[k] - \beta[k-1])/t_s \leq SR_\beta, \tag{3.24}$$

where SR_β is the maximum rate of change of β. When the sag is detected the reference can be rotated multiplying the initial load voltage set-point ($\vec{u}_l^* = 1 + j0$) by $e^{-j\beta}$, where β is limited using (3.24). The algorithm used to detect the voltage sag in order to shift the load voltage is presented in Appendix B.

Fig. 3.20 shows the SAC performance when the speed of the phase rotation is limited. The SAC is in steady-state and the sag starts at $t = 20$ ms. The load voltage is restored using in-phase compensation but, as the sag goes on, the SAC slowly rotates the load-voltage phase and the load remains undisturbed. Fig. 3.20 (e) shows that the active power injection is maximum at the beginning, but decreases while the phase shifts. Meanwhile, the reactive power injected increases (see Fig. 3.20 (f)).

3.4.3 Influence of the Load

The SAC model obtained in Section 3.2 did not take into account the load. The load effects on the SAC performance can be reduced adding the feed-forward of the load current, but this only compensates the low-frequency dynamics. The load can be modelled as an inductor (L_l) and a resistor (R_l) connected in parallel (see Fig. 3.4):

$$\boldsymbol{A} = \begin{bmatrix} -\frac{R_f}{L_f} & -\frac{1}{L_f} & 0 & \omega_g & 0 & 0 \\ \frac{1}{C_f} & 0 & -\frac{1}{C_f} & 0 & \omega_g & 0 \\ \frac{1}{R_l C_f} & \frac{1}{L_l} & -\frac{1}{R_l C_f} & 0 & 0 & \omega_g \\ -\omega_g & 0 & 0 & -\frac{R_f}{L_f} & -\frac{1}{L_f} & 0 \\ 0 & -\omega_g & 0 & \frac{1}{C_f} & 0 & -\frac{1}{C_f} \\ 0 & 0 & -\omega_g & \frac{1}{R_l C_f} & \frac{1}{L_l} & -\frac{1}{R_l C_f} \end{bmatrix}, \quad \boldsymbol{x}(t) = \begin{bmatrix} i_{f-d} \\ u_{c-d} \\ i_{l-d} \\ i_{f-q} \\ u_{c-q} \\ i_{l-q} \end{bmatrix}_t, \tag{3.25}$$

$$\boldsymbol{B} = \begin{bmatrix} \frac{1}{L_f} & 0 \\ 0 & 0 \\ 0 & 0 \\ 0 & \frac{1}{L_f} \\ 0 & 0 \\ 0 & 0 \end{bmatrix}, \quad \boldsymbol{u}(t) = \begin{bmatrix} u_{i-d} \\ u_{i-q} \end{bmatrix}_t. \tag{3.26}$$

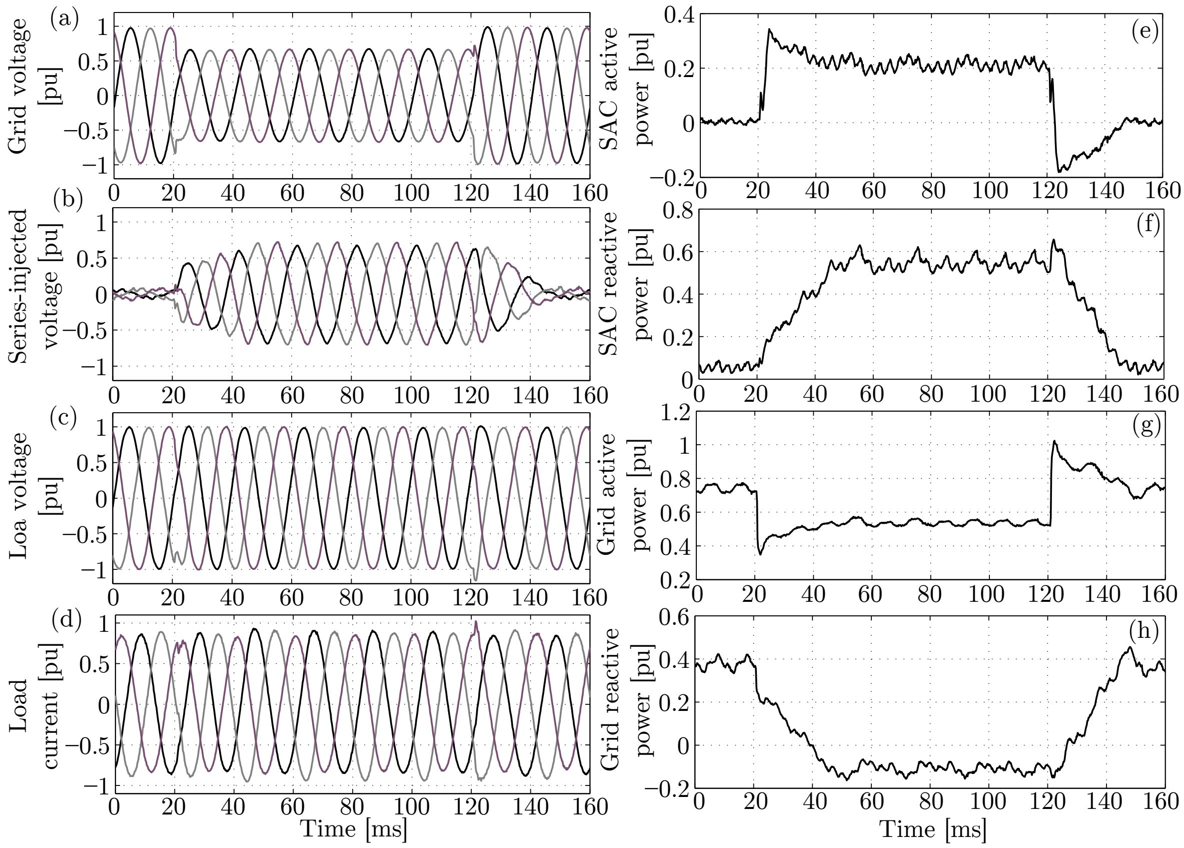

Figure 3.20: Voltage sag compensation (65 % retained voltage) when the speed of the phase rotation is limited using (3.24).

Now, the load current is a state variable. Fig. 3.21 shows the frequency response of the plant ($u_{i-d}(t)$ is the input and $u_{c-d}(t)$ is the output) when adding a load of the rated current with different power factors. The resonance is automatically damped and the lower ϕ is (lower R_l), the lower the resonance peak is. Therefore, the SAC should work better when there is a load connected because the load clearly damps the resonance.

3.5 Alternatives for the Main Controller

The SF controller studied in Section 3.3 gives good results, but it has some considerable drawbacks. First of all, it is not easy to find a location for the closed-loop poles that results in reasonable stability margins and, secondly, the design is not intuitive. In this section, two alternatives for the main controller are proposed and investigated, namely, a PID and a "cascade" controller. These are interesting alternatives because their design is more intuitive and they can be easily retuned in real time.

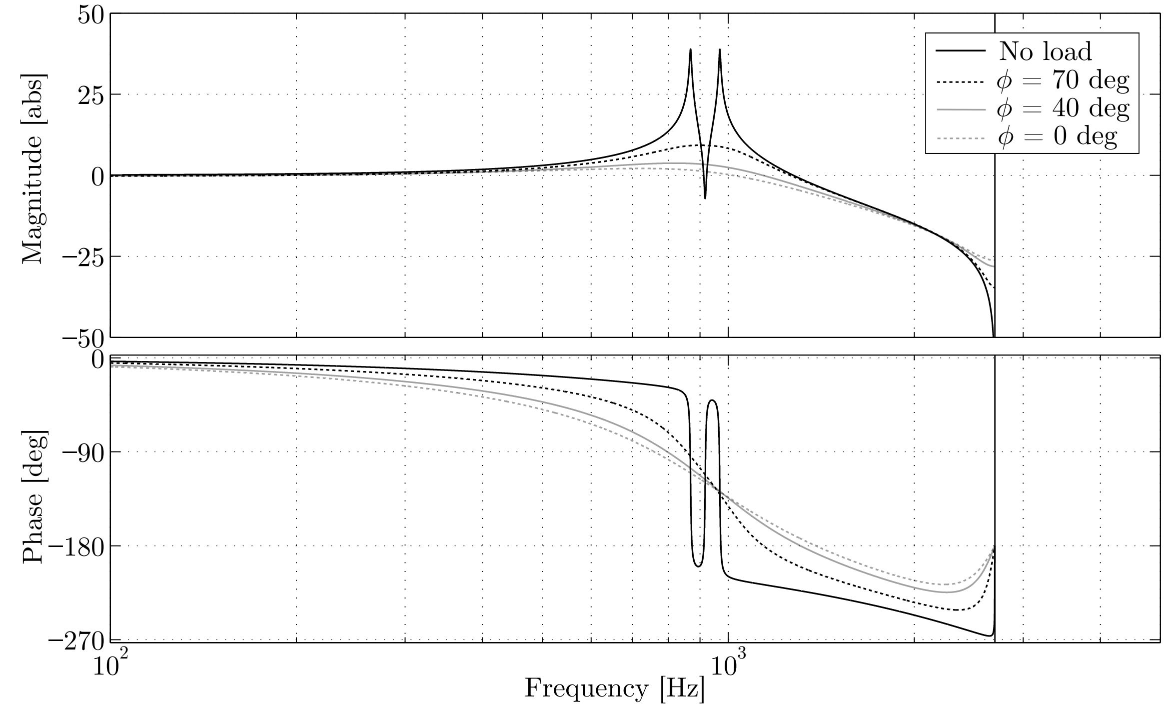

Figure 3.21: Frequency response of the plant when using a parallel RL load, for different values of ϕ (ϕ is the angle of the load impedance). In all cases (except in the one called "no load") the load consumes the nominal current at the rated voltage.

3.5.1 PID Controller

The set of decoupling equations suggested in Section 3.2 can accommodate several controller alternatives. Among them are a typical PID controller and a cascade controller. In this thesis, the following continuous-time PID controller has been used:

$$C'_u(s) = K_p \left(1 + \frac{1}{T_i s} + \frac{T_d s}{(T_d/N_d)s + 1}\right), \tag{3.27}$$

which can be discretized using the backward-Euler method [176], for example. This controller can be designed in continuous time using frequency-response techniques [177]. However, the validity of the design has to be investigated after the discretization analysing the open- and closed-loop characteristics. The model needed to design the controller can be obtained by converting the decoupled state-variable representation in (3.13) into a transfer function [178]. The incremental controller approach can be used to implement this controller, as suggested in Section 3.3.2 for the SF controller.

3.5.2 Cascade Controller

A "cascade" controller consist of two nested control loops, as shown in Fig. 3.22. For an SAC, the inner controller handles the current through L_f, and it is called "inner-

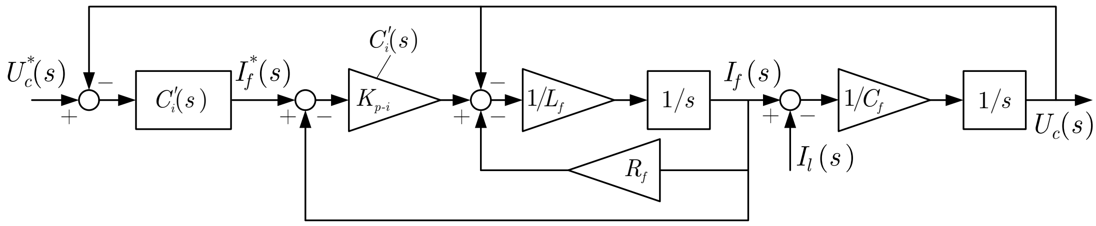

Figure 3.22: Simplified block diagram of an SAC with a cascade controller.

current controller". The outer controller handles the load voltage modifying the current set-point ($i_f^*(t)$), and it is called "outer-voltage controller". A cascade (multi-loop) controller is proposed by Vilathgamuwa et al. [101] for a DVR. However, the controller is implemented in a static RF, so zero steady-state error is not ensured for the fundamental component. This problem is solved by Wang et al. [98] using a cascade controller referred to a SRF. However, neither Vilathgamuwa et al. [101] nor Wang et al. [98] investigated the discrete-time implementation.

The advantages of a cascade controller can be easily understood using a single-phase continuous-time approach. Fig. 3.22 shows the block diagram of the plant with the current and the voltage controllers. The plant seen by the outer-voltage controller can be obtained from Fig. 3.22:

$$F_i'(s) = \frac{U_c(s)}{I_f^*(s)} = \frac{K_{p-i}C_f s}{L_f C_f s^2 + \underbrace{(R_f + K_{p-i})}_{R_v} C_f s + 1}, \tag{3.28}$$

where R_v is called virtual resistance. Clearly, the higher the value of K_{p-i} (R_v) is, the more damped $F_i'(s)$ becomes, so K_{p-i} can be easily designed. Once the value of K_{p-i} has been set, the voltage controller can be designed as a typical PID controller, where the open-loop transfer function is computed as follows:

$$G_p'(s) = C_u'(s)F_i'(s). \tag{3.29}$$

where $C_u'(s)$ is shown in Fig. 3.22. The proposed method seems to simplify the design of the inner controller, but the implementation must be investigated. Fig. 3.23 (a) shows the pole-zero diagram of $F_i'(s)$ modifying the value of K_{p-i}, while Fig. 3.23 (b) shows the pole-zero diagram of $F_i(z)$ (discrete-time equivalent of $F_i'(s)$ taking into account the ZOH and the calculus delay and the anti-aliasing filters). In Fig. 3.23 (b), the discrete-time poles have been moved to the continuous-time plane to simplify the comparison. It can be seen that, even if the closed-loop poles start being stable, they move to the right-hand side of the complex plain when K_{p-i} increases. Therefore, the LC filter resonance can not be damped.

3.6 Main Controller Trade-offs

Fig. 3.24 (left) shows the Nichols chart of $G_p^d(z) = F_p^d(z)/(1-F_p^d(z))$ (open-loop transfer function) for the SF, the PID, and the cascade controllers. All of them have been designed to achieve the same phase margin of 60 deg (first crossing of 0 dB). It is as-

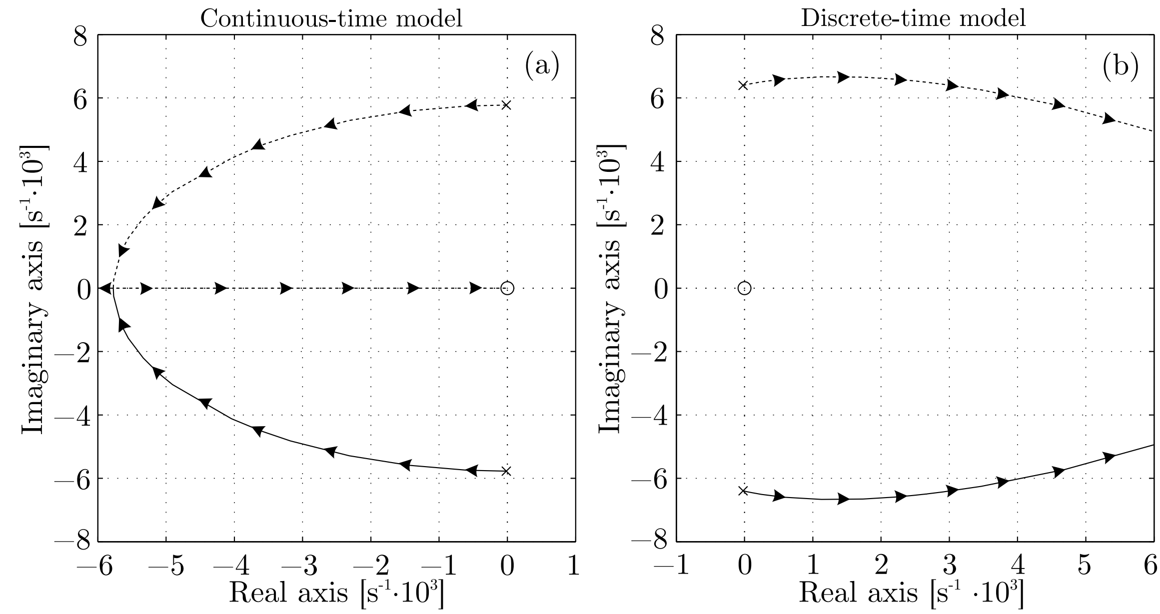

Figure 3.23: Root locus of (a) $F_i'(s)$ and (b) $F_i(z)$, shifting the value of K_{p-i}. The arrows indicate the zero-pole movement when K_{p-i} increases.

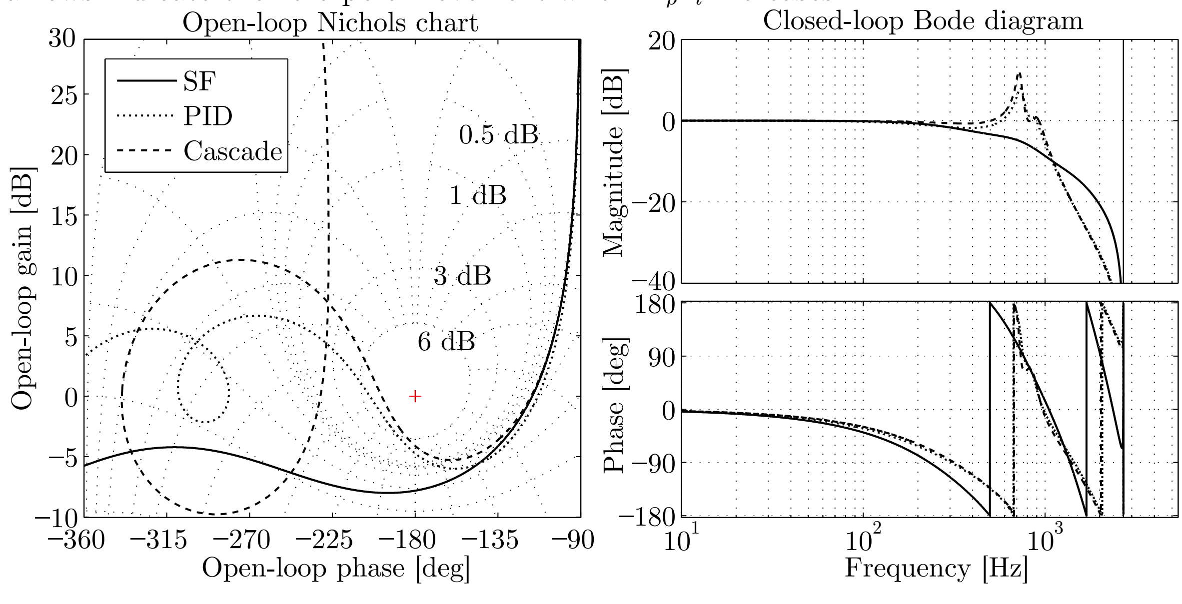

Figure 3.24: (left) Open-loop Nichols chart and (right) closed-loop Bode diagram for (solid) the SF, (dotted) the PID, and (dashed) the cascade controllers.

sumed that the coupling effects between axes are negligible, so closed-loop stability can be assessed using SISO open-loop-based stability margins. The open-loop magnitude greatly increases at high frequency for the PID and the cascade controllers, suggesting that the resonance is not properly damped. In fact, Fig. 3.24 (right) shows that the SF behaves better than the rest of the alternatives. In addition, Fig. 3.24 (right) shows that no one of the controllers presented here is able to track harmonics because at the harmonic frequencies (a) the phase is not zero and (b) the magnitude is not 0 dB.

Fig. 3.25 shows the transient of the SAC compensating a 60% retained voltage sag when (left) there is a load connected downstream the SAC (230 V, 3.7 kW, and 2 kvar) and (right) there is no load. All the alternatives work properly when a load

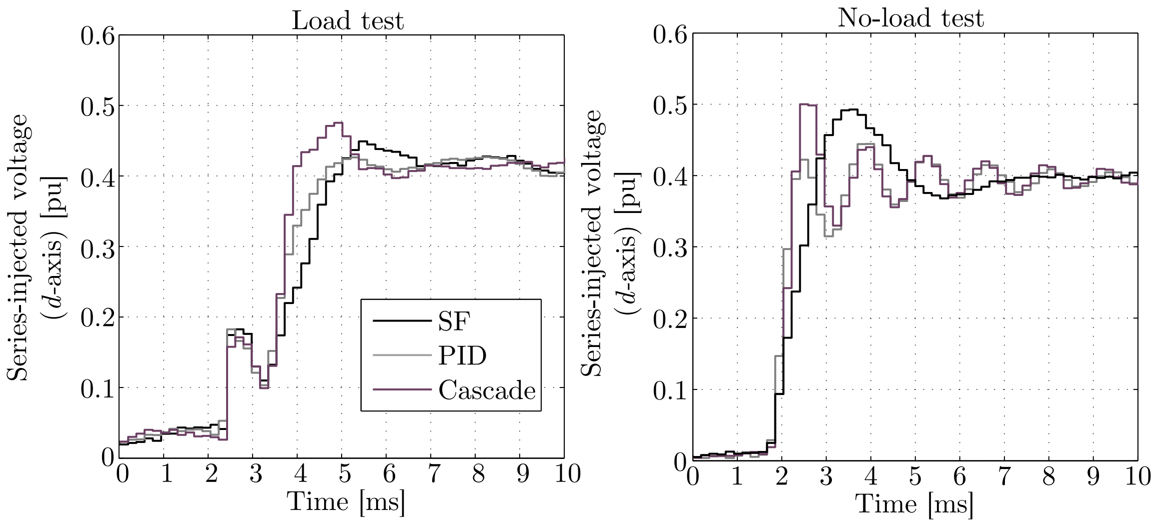

Figure 3.25: d-axis component of the series-injected voltage for the PID, the cascade, and the SF controllers (left) with the load and (right) without the load.

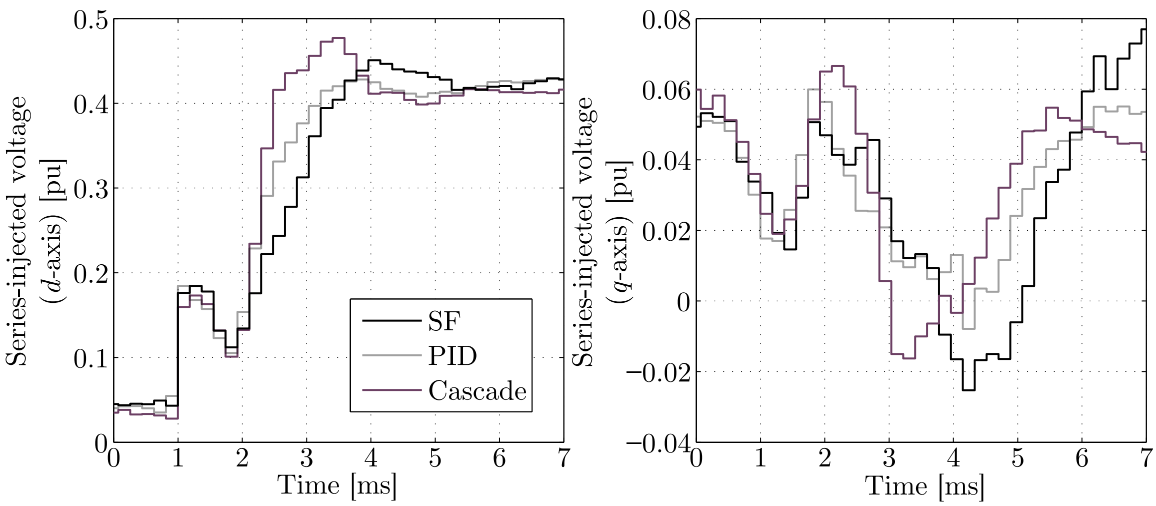

Figure 3.26: dq-axis components of the series-injected voltage for the PID, the cascade, and the SF controllers when the load is connected.

is connected, but only the SF controller damps the resonance when there is no load (observe the oscillations with the PID and the Cascade controller).

Fig. 3.26 shows the experimental results obtained when the SAC compensates a voltage sag of 60 % retained voltage when there is load connected (230 V, 3.7 kW, and 2 kvar). All the alternatives provide a fast transient response with reduced coupling effects and, between them, the cascade controller is the fastest one.

3.7 Model of the Coupling Transformer

3.7.1 Single- and Three-Phase Magnetic Circuit Modelling

Fig. 3.27 shows the electrical model of the SAC in series with the load. The transformer has been modelled using a T equivalent circuit [103] and, for simplicity, the flux equations will be studied in natural magnitudes (abc). The equations that relate the flux linkages of the primary and the secondary windings of the transformer are (only the equations for one phase are shown) [103]:

$$\begin{bmatrix} u_{cf} \\ u_c \end{bmatrix}_t = \begin{bmatrix} R_{t-c} & 0 \\ 0 & R_{t-l} \end{bmatrix} \begin{bmatrix} i_{t-c} \\ i_{t-l} \end{bmatrix}_t + \frac{d}{dt} \begin{bmatrix} \lambda_{t-c} \\ \lambda_{t-l} \end{bmatrix}_t, \tag{3.30}$$

with

$$\begin{bmatrix} \lambda_{t-c} \\ \lambda_{t-l} \end{bmatrix}_t = \begin{bmatrix} L_{t-c} + L_m & L_m \\ L_m & L_{t-l} + L_m \end{bmatrix} \begin{bmatrix} i_{t-c} \\ i_{t-l} \end{bmatrix}_t, \tag{3.31}$$

where $\lambda_{t-c}(t)$ is the flux linkage of the converter-side winding, $\lambda_{t-l}(t)$ is the flux linkage of the load-side winding, and L_m, L_{t-c}, and L_{t-l} are the magnetizing and the leakage inductances, respectively. For simplicity, "flux linkages" will be referred as "fluxes" from now on. Assuming that $u_{cf}(t) \approx u_m(t)$ (leakage flux and windings resistances are neglected), the first row of (3.30) becomes

$$u_{cf}(t) \approx \frac{d\lambda_m(t)}{dt}, \tag{3.32}$$

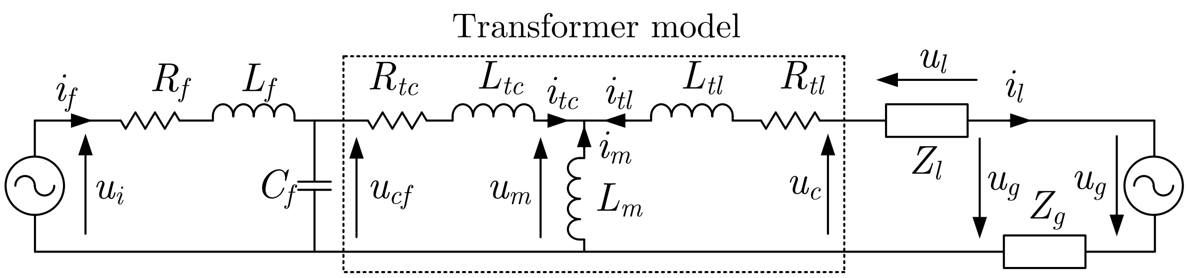

Figure 3.27: Detailed single-phase model of the coupling transformer and the SAC.

where λ_m is the magnetising flux. Furthermore, if $u_{cf}(t) \approx u_c^*(t)$, $u_c^*(t)$ can be modelled as [104]

$$u_{cf}(t) = \begin{cases} 0, & \text{if} \quad t < 0, \\ |u_{cf}| \sin(\omega_g t + \alpha_i), & \text{if} \quad 0 \le t < \infty, \end{cases} \tag{3.33}$$

where α_i is the initial angle and (3.32) yields:

$$\lambda_m(t) = \int_0^t u_{cf}(t)dt = \underbrace{\frac{|u_{cf}|}{\omega_g}\cos(\alpha_i)}_{\text{DC component}} - \underbrace{\frac{|u_{cf}|}{\omega_g}\cos(\omega_g t + \alpha_i)}_{\text{AC component}}. \tag{3.34}$$

Equation (3.34) consist of two terms: a DC component (λ_m^{dc}) and a AC component (λ_m^{ac}). The DC component increases when $|u_{cf}|$ increases and when α_i is close to $\pi/2$ ($-\pi/2$). This DC component can saturate the transformer, thus increasing the current through the converter-side winding [104].

Fig. 3.28 (right) shows the solution of (3.34) when $|u_{cf}| = 1$ pu for (a) $\alpha_i = \pi/2$ and (b) $\alpha_i = 0$. The maximum value of the flux is strongly related to α_i. Fig. 3.28 (left) shows the maximum value of λ_m^{dc} when $|u_{cf}|$ and α_i vary. In the worst case, the flux can be twice that of the AC component. Therefore, saturation can be avoided if the transformer is designed to withstand twice the nominal flux, but this would require a bigger transformer core [105].

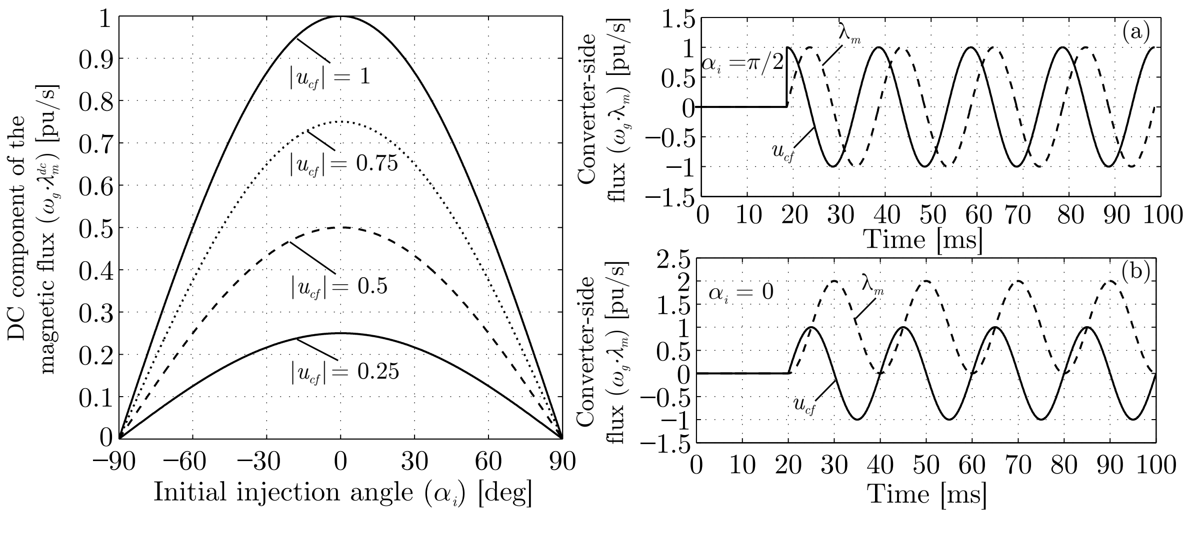

Figure 3.28: (left) DC component of λ_m for different values of $|u_{cf}|$ and (right) transient response of λ_m for (a) $\alpha_i = \pi/2$ and (b) $\alpha_i = 0$.

Model of a Three-Phase Transformer

The flux equations in (3.33) and (3.34) are only valid for three single-phase transformers [103]. However, compact three-phase transformers can also be used for an SAC. In this case, the flux equations should be projected into the $\alpha\beta$ plane, yielding

$$\frac{d}{dt}\begin{bmatrix}\lambda_{m-\alpha}\\ \lambda_{m-\beta}\end{bmatrix}=\begin{bmatrix}u_{m-\alpha}\\ u_{m-\beta}\end{bmatrix}, \tag{3.35}$$

with

$$\begin{bmatrix}\lambda_{m-\alpha}\\ \lambda_{m-\beta}\end{bmatrix}=\begin{bmatrix}L_m-2M_m & 0\\ 0 & L_m-2M_m\end{bmatrix}\begin{bmatrix}i_{m-\alpha}\\ i_{m-\beta}\end{bmatrix}, \tag{3.36}$$

where M_m is the mutual magnetising inductance between two phases. Each axis have independent dynamics because the phase rotation of the transformer has been avoided referring all the measurements to grid-side of the transformer. Therefore, the single-phase analysis is also valid for three-phase transformers in the $\alpha\beta$ plane. Brunke and Frohlich [179, 180] studied the flux equations of a three-phase transformer in three-phase variables, obtaining a similar result. However, the $\alpha\beta$ plane simplifies the study.

3.7.2 Limitation and Control of the Magnetic Flux

The steps to avoid DC-flux in three-phase transformers are:

1. When one axis (α or β) satisfies $\alpha_i = \pm\pi/2$, the SAC should start injecting voltage in that axis.
2. One quarter cycle later the other axis voltage can be applied because it will satisfy $\alpha_i = \pm\pi/2$.

Additionally, the voltage reference can be multiplied by $e^{j\omega_g t_c}$ to compensate the delay caused by the main controller. The value of t_c has been selected by trial and error since the controller can not be modelled, exactly, as a single-period delay.

Fig. 3.29 shows the results when compensating a three-phase (symmetric) voltage sag with 35 % retained voltage. A 4 kW resistive load has been used and the sag is compensated using the in-phase compensation method. The value of t_c has been set to 3.2 ms to compensate the equivalent delay of the main controller. On the left, no method to avoid inrush current is used. Therefore, the series-injected voltage leads to a large inrush current and the transformer saturates. The inrush current is avoided if $\alpha_i = \pm\pi/2$, as shown in Fig. 3.29 (e to h). However, the SAC requires more time to compensate the sag (between a quarter and half cycle). Obviously, the controller is not perfect ($\vec{u}_l^*(t) \approx \vec{u}_l(t)$, but not equal) and, therefore, the DC-component of the flux is reduced, but not completely suppressed (see Fig. 3.29 (h)).

Based on these results, it seems a good idea to remove the coupling transformer. This could be done, for example, using the approach presented by Goharrizi et al. [128]. That paper proposes an SAC with three independently-controlled phases and a high-frequency transformer to isolate each DC-link voltage. Therefore, the AC transformer is not required and a fast transient response can be expected. Another alternative is to

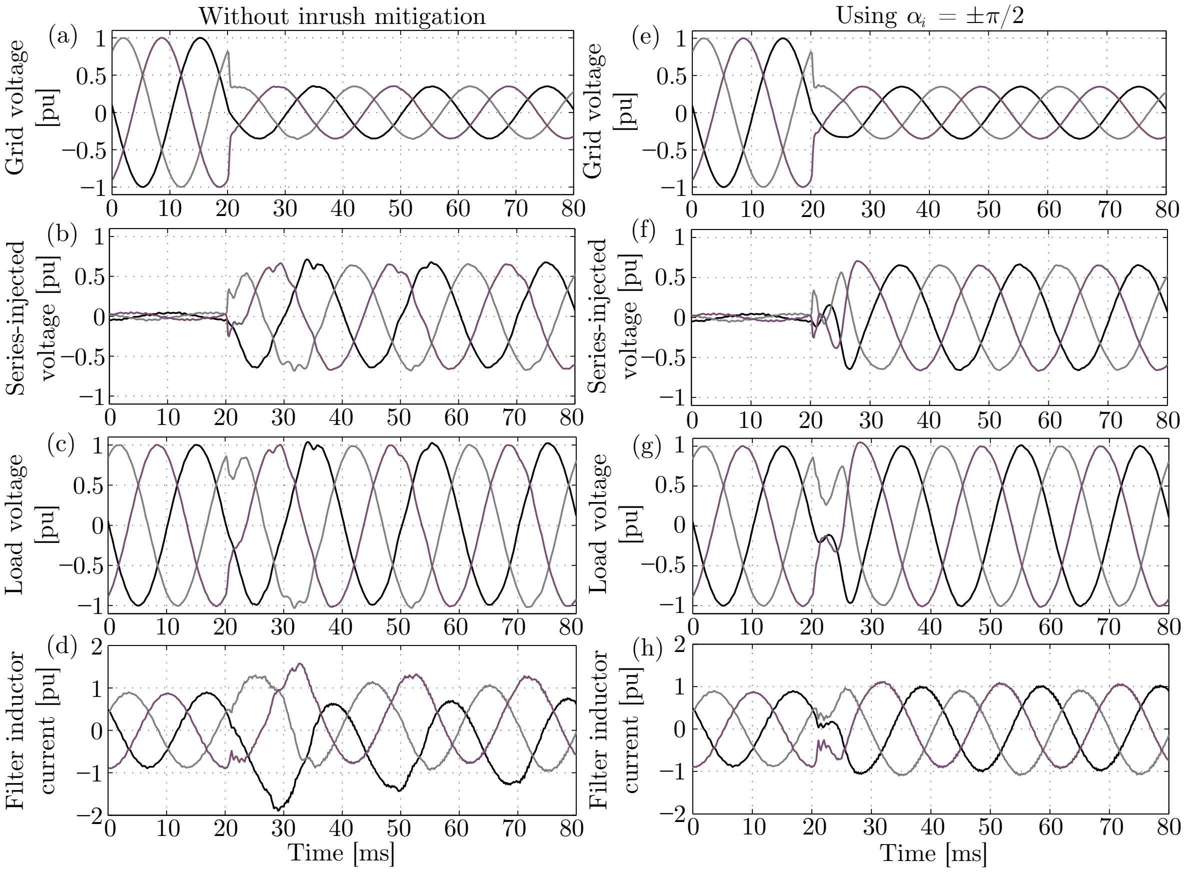

Figure 3.29: Compensation of a 35 % retained voltage sag (a to d) without using any inrush mitigation method and (e to h) using the proposed method.

use a transformer-less SAC, as described in Section 2.3.2. For this topology the effect of sags over the transformer has not been studied and it need to be addressed in detail.

3.8 Chapter Summary

This chapter has shown the first steps towards the control of a three-phase SAC. The SAC has been modelled taking into account the digital implementation effects and three controllers have been applied to the SAC: a SF, a PID, and a cascade controller. The SF controller exhibits an adequate performance, but its design is not intuitive. The PID and the cascade controllers are easier to design and provide a similar transient response but, without a load, only the SF damps the filter resonance. These controllers only address the use of an SAC as a DVR. In addition, a method to improve the application of the minimum-power compensation has been presented, obtaining accurate results.

The coupling transformer has been modelled and its saturation has been investigated. The analysis presented is similar to the one used in the literature for single-phase transformers, but it has been adapted for the three-phase case and the experimental results confirmed the validity of this approach.

Chapter 4

Troubleshooting a Digital Repetitive Controller

This chapter details the implementation of a repetitive controller (RC) for an SAC. Section 4.1 introduces continous- and discrete-time RCs. Closed-loop stability is addressed in Section 4.2 and steady-state performance is studied in Section 4.3. Section 4.4 explains the design procedure for discrete-time RCs, while Section 4.5 is focused on troubleshooting discrete-time implementation problems. A RC is applied to an SAC in Section 4.6. Section 4.7 and Section 4.8 give alternatives to traditional RCs such as odd- and even-harmonic RCs [154], $nk \pm m$-harmonic RCs [157], and high-order RCs [181]. Results obtained with these alternatives are discussed in Section 4.9 and, finally, Section 4.10 summarizes this chapter.

4.1 Repetitive Controller Overview

The internal model principle (IMP) [182] reveals that a controller should contain poles such as $s = \pm jh\omega_g$, with $h = 0, 1, 2, \ldots, \infty$, to track (reject) a periodic signal of period $t_p = 2\pi/\omega_g$, which contains harmonics at frequencies $h\omega_g$ rad/s. A transfer function (using Laplace transform) with poles as required is

$$RC_o\left(s\right) = \frac{e^{-t_p s}}{1 - e^{-t_p s}}. \tag{4.1}$$

Controllers that include a transfer function like (4.1) are usually referred as "repetitive controllers" in the literature [183, 184].

4.1.1 Discrete-Time Formulation

In most applications, RCs are implemented with a sampling period (t_s) so that [26]

$$N = t_p/t_s \in \mathbb{N}. \tag{4.2}$$

In this case, $e^{-t_p s}$ in (4.1) can be replaced by z^{-N} [26] or, in a more general approach that will prove to be useful, by

$$W(z) = z^{-N}L(z). \tag{4.3}$$

The transfer function $L(z)$ is not often used in the literature, but it is included here because it will be used in subsequent sections for frequency adaptation purposes.

Fig. 4.1 shows a typical "plug-in" implementation of a RC, where $RC(z)$ is the discrete-time RC and $G_p(z)$ is the open-loop plant with the main controller. The transfer function $G_x(z)$ and the gain K_x are used to ensure closed-loop stability, while $Q(z)$ limits the bandwidth.

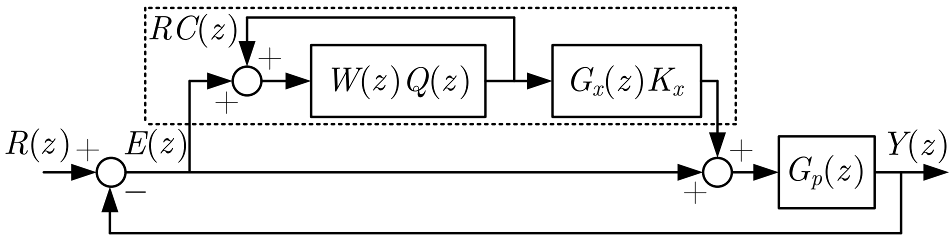

Figure 4.1: Repetitive controller applied in a plug-in structure.

4.2 Stability Analysis

The complete controller in series with $G_p(z)$ in Fig. 4.1 can be written as:

$$C(z) = 1 + RC(z) = 1 + \frac{W(z)Q(z)}{1 - W(z)Q(z)} G_x(z)K_x. \tag{4.4}$$

The closed-system in Fig. 4.1 will be internally stable if [151]:

1. The transfer function $1 + C(z)G_p(z)$ has no zeros with $|z| \geq 1$.
2. There is no unstable pole-zero cancellation when the product $C(z)G_p(z)$ is formed.

The zeros of $1 + C(z)G_p(z)$ are also the roots of:

$$[1 + G_p(z)]\,\{1 - W(z)Q(z)\,[1 - K_x G_x(z) F_p(z)]\} = 0, \tag{4.5}$$

with $F_p(z) = G_p(z)/(1 + G_p(z))$. If the second condition above is satisfied and $F_p(z)$ is stable, a sufficient condition for stability in Fig. 4.1 is [26]:

$$\max\left\{|W(z)Q(z)||1 - K_x G_x(z) F_p(z)|\right\} < 1, \tag{4.6}$$
$$\text{with } z = e^{j\omega t_s} \text{ for all } |\omega| < \pi/t_s.$$

The reference-to-error transfer function of the system depicted in Fig. 4.1 is:

$$F_e(z) = \frac{E(z)}{R(z)} = \frac{1}{1 + G_p(z)} \underbrace{\left[\frac{1 - W(z)Q(z)}{1 - W(z)Q(z)\left[1 - K_x G_x(z) F_p(z)\right]}\right]}_{S(z)}, \tag{4.7}$$

where $S(z)$ is the so-called "Relative Sensitivity Error Transfer Function" or "Modifying Sensitivity Function" [185].

If (a) $\hat{G}_p(z)$ is a model of $G_p(z)$ and (b) $F_p(z)$ contains only minimum-phase zeros, it is recommended to use:

$$G_x(z) = \hat{F}_p^{-1}(z) = (1 + \hat{G}_p(z))/\hat{G}_p(z), \tag{4.8}$$

in order to satisfy (4.6). If $\hat{F}_p(z)$ contains non-minimum phase (NMP) zeros, it can not be inverted since this would lead to an unstable closed-loop system. In this case, $\hat{F}_p(z)$ can be written as

$$\hat{F}_p(z) = \frac{B_x^-(z) B_x^+(z)}{A_x(z)}, \tag{4.9}$$

where $A_x(z)$ includes the poles of $\hat{F}_p(z)$, $B_x^-(z)$ includes the minimum-phase zeros, $B_x^+(z)$ includes the NMP zeros, and $G_x(z)$ can be chosen as [186]

$$G_x(z) = \frac{A_x(z) B_x^+(z^{-1})}{B_x^-(z)(B_x^-(1))^2}. \tag{4.10}$$

The phase of (4.10) exactly matches the phase of $\hat{F}_p^{-1}(z)$ when using (4.10), so stability can be guaranteed [186]. There are other methods to invert $\hat{F}_p(z)$ when it contains NMP zeros. For instance, Longman et al. [187] invert $\hat{F}_p(z)$ using a FIR filter that emulates the phase of $\hat{F}_p^{-1}(z)$. Besides, Doh et al. [188] estimate $\hat{F}_p(z)$ in real time using a recursive least-square estimator. However, if $\hat{F}_p(z)$ is known at the design stage, the best solutions to satisfy (4.6) are (4.8) when $\hat{F}_p(z)$ is invertible and (4.10) when $\hat{F}_p(z)$ can not be inverted. Therefore, these alternatives will be applied from now on.

The filter $Q(z)$ can be designed to have $|Q(z)| \approx 1$ within the bandwidth. Since the model of $F_p(z)$ can not be accurate for all frequencies, $Q(z)$ is also chosen to have $|Q(z)| \approx 0$ in the frequency range where $\hat{F}_p(z)$ is not reliable so that stability is never threatened. The filter $L(z)$ will be designed in Section 4.5.1 to ensure that $|L(e^{j\omega t_s})| = 1 \ \forall\omega$ and, therefore, it will not affect the stability condition. Bearing in mind the considerations above, the stability condition in (4.6) is reduced to [25]

$$|1 - K_x G_x(e^{j\omega t_s}) F_p(e^{j\omega t_s})| < 1, \text{ if } 0 \leq \omega \leq \omega_c, \tag{4.11}$$

where ω_c is the RC bandwidth.

4.3 Steady-State Performance Analysis

4.3.1 RC Sensitivity Function

The transfer function $S(z)$ in (4.7) will be called here "RC sensitivity function", for simplicity, and it is more easily understood assuming that $F_p(z)G_x(z) = 1$ (often the case) and $K_x = 1$, yielding:

$$\hat{S}(z) = 1 - \underbrace{W(z)Q(z)}_{H(z)}, \tag{4.12}$$

where $\hat{S}(z)$ is a simplified version of $S(z)$. The value of $|\hat{S}(e^{j\omega t_s})|$ is periodic with a period of ω_g rad/s in the frequency domain, assuming that $L(e^{j\omega t_s}) = 1$ and $Q(e^{j\omega t_s}) = 1$, which is normally the case within the bandwidth of the RC. Defining $\theta_s = \omega t_s N$, $0 \leq \theta_s \leq 2\pi$ rad corresponds to $0 \leq \omega \leq \omega_g$ rad/s and, in general, $2\pi(h-1) \leq \theta_s \leq 2\pi h$ rad corresponds to $\omega_g(h-1) \leq \omega \leq \omega_g h$ rad/s. Therefore, it will always be enough to study $\hat{S}(z)$ within $0 \leq \omega \leq \omega_g$ (or $0 \leq \theta_s \leq 2\pi$).

Fig. 4.2 (left) shows $|\hat{S}(e^{j\theta_s/N})|$ versus $|H(e^{j\theta_s/N})|$ for different values of θ_s. Notice that $|\hat{S}(e^{j\theta_s/N})|$ is nothing but the magnitude of the frequency response of $\hat{S}(z)$ when

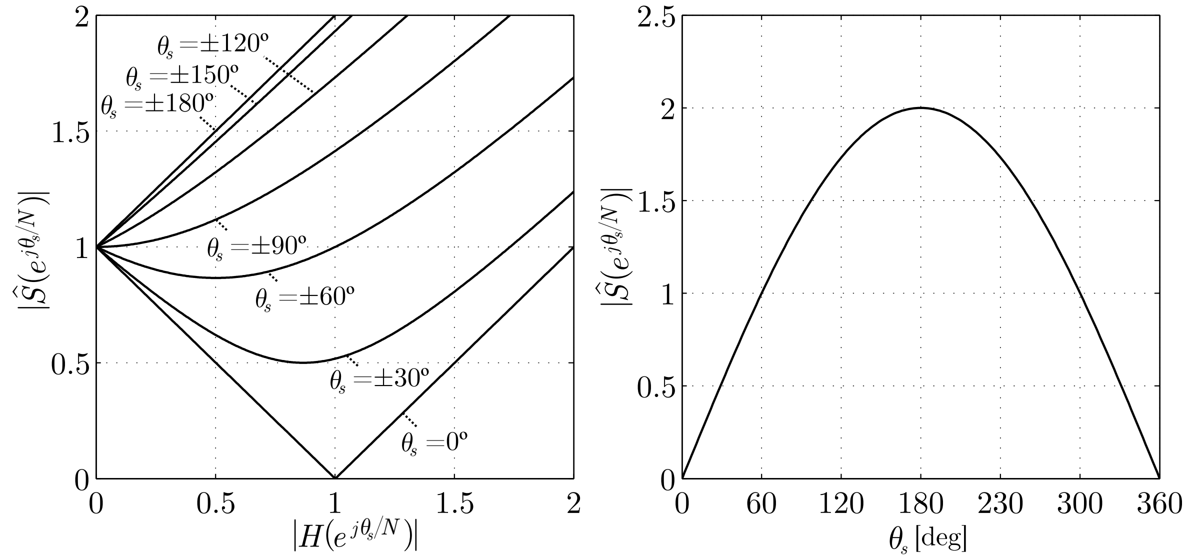

Figure 4.2: (left) $|\hat{S}(e^{j\theta_s/N})|$ versus $|H(e^{j\theta_s/N})|$ for $\theta_s = \pm 30°, \pm 60°, \pm 90°, \pm 120°, \pm 150°$, and $\pm 180°$, where "°" means deg. (right) $|\hat{S}(e^{j\theta_s/N})|$ versus θ_s, with $\left|H(e^{j\theta_s/N})\right| = 1$.

$0 \leq \omega \leq \omega_g$. Inspecting that figure and recalling (4.12), the error becomes zero if $|H(e^{j\theta_s/N})| = 1$. Fig. 4.2 (right) shows $|\hat{S}(e^{j\theta_s/N})|$ assuming $|H(e^{j\omega t_s})| = 1$ (always the case a classical RC). Signals with frequencies that lead to $|\hat{S}(e^{j\theta_s/N})| = 0$ are perfectly eliminated, while those that lead to $|\hat{S}(e^{j\theta_s/N})| > 1$ are amplified. Summarizing:

- The error at a specific harmonic frequency is zero if $|H(e^{j\omega_g h t_s})| = 1$.
- At frequencies where $|S(e^{j\omega t_s})| = 0$ the error is suppressed, while at those where $|S(e^{j\omega t_s})| > 1$ the error is amplified.

4.3.2 Frequency Deviation

If the frequency varies, the resonant poles will not be tuned at the harmonic frequencies, causing steady-state error. This error can be quantified with:

$$\left|F_e(e^{j\omega_g(1+\delta\omega_g)ht_s})\right|, \tag{4.13}$$

where $\delta\omega_g$ is the frequency deviation in per-unit values:

$$\delta\omega_g = \frac{\omega - \omega_g}{\omega_g}. \tag{4.14}$$

It is advised to inspect $|\hat{S}(e^{j\omega_g(1+\delta\omega_g)ht_s})|$ instead of (4.13) to facilitate interpretation. Fig. 4.3 shows that, when the frequency varies, there is a large increase on $|\hat{S}(e^{j\omega_g(1+\delta\omega_g)ht_s})|$, meaning that performance deteriorates. Therefore, it would be useful to search for a RC alternative with improved robustness against frequency variations.

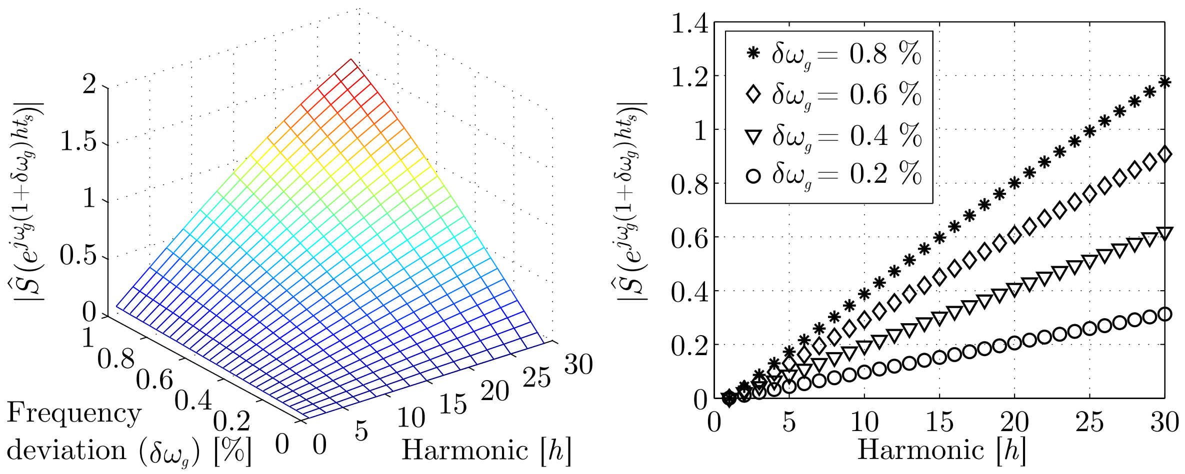

Figure 4.3: RC steady-state performance when the grid frequency deviates. Recall that, ideally, $|\hat{S}(e^{jh\omega_g t_s})| = 0$ for each harmonic h.

4.4 Design Criteria

4.4.1 $Q(z)$ Filter Design

The filter $Q(z)$ limits the bandwidth at high frequency where the model $F_p(z)$ may not be reliable. Stability is not affected if $|Q(e^{j\omega t_s})| \leq 1\ \forall\omega$, so

$$\begin{aligned} &|Q(e^{j\omega t_s})| = 1, \text{ if } 0 \leq \omega \leq \omega_c, \\ &|Q(e^{j\omega t_s})| = 0, \text{ if } \omega_c < \omega < \pi/t_s, \end{aligned} \tag{4.15}$$

Furthermore, the phase delay of $Q(z)$ should be zero in the range of frequencies where $|Q(e^{j\omega t_s})| = 1$ to avoid shifting the resonant poles.

The design of $Q(z)$ has been thoroughly studied by Subramanian and Mishra [189], revealing that performance deteriorates using discretised continuous-time LPFs because the filter requirements in (4.15) are difficult to accomplish. By contrast, zero-phase high-order FIR filters are well suited for this application [26, 190]:

$$Q(z) = \sum_{k=-M/2}^{M/2} a_i z^i, \text{ with } a_{-i} = a_i, \tag{4.16}$$

where $M + 1$ is the number of coefficients, which can be chosen to provide a low-pass response [191, 192]. The design of this filter has been deeply studied for RCs by Ye et al. [193] and by Escobar et al. [194]. The approach used here to implement this filter is not going to be detailed because it is like the one used by Pinzón-Ardila [163], which provides accurate results with a simple formulation.

4.4.2 K_x Design

Influence of K_x on Stability

Modelling errors are defined as $G_e(\omega) = |F_p(e^{j\omega ts})||G_x(e^{j\omega ts})|$ and $\theta_e(\omega) = \angle F_p(e^{j\omega ts}) + \angle G_x(e^{j\omega ts})$. Taking $G_e(\omega)$ and $\theta_e(\omega)$ to (4.11),

$$K_x^2 G_e^2(\omega) - 2K_x G_e(\omega)\cos(\theta_e(\omega)) < \min\left(1/|H(e^{j\omega t_s})|^2 - 1\right). \tag{4.17}$$

Fig. 4.4 shows the surface that results when the left-hand side of (4.17) is evaluated, assuming $|H(e^{j\omega t_s})| = 1$ (always the case for a classical RC). This surface can be interpreted as the frontier between stable and unstable regions of the closed-loop system with modelling errors. The region that is under the surface will produce a stable closed-loop system even if there are modelling errors ("stable region"). The region that is above the surface will produce an unstable closed-loop system ("unstable region").

The interval where K_x leads to a stable system can be solved from (4.17), yielding

$$-\pi/2 < \theta_e(\omega) < \pi/2 \tag{4.18}$$

and

$$\frac{\cos(\theta_e(\omega)) - \lambda_x(\omega)}{G_e(\omega)} < K_x < \frac{\cos(\theta_e(\omega)) + \lambda_x(\omega)}{G_e(\omega)}, \tag{4.19}$$

where

$$\lambda_x(\omega) = \sqrt{\cos^2(\theta_e(\omega)) + \min\left(1/|H(e^{j\omega t_s})|^2 - 1\right)^2}. \tag{4.20}$$

First of all, condition (4.18) limits the phase error to $\pm\pi/2$ in the band-pass frequency region. Secondly, condition (4.19) establishes a relationship between K_x and the modelling errors. For a classical RC, $|H(e^{j\omega t_s})| = 1$ and (4.19) leads to $0 < K_x < 2$. From Fig. 4.4 and the conditions (4.19) and (4.18):

- If there are not modelling errors, the closed-loop is stable if $0 < K_x < 2$.
- The lower K_x is, the more robust the design is.
- Magnitude errors ($G_e(\omega)$) can be compensated tuning K_x. However, phase errors must always be between $\pm\pi/2$ rad.

Influence of K_x on Steady-State Performance

A RC ensures zero steady-state error at the harmonic frequencies regardless of the value of K_x [182], but the value of K_x affects the performance at other frequencies. The impact of K_x on $|S(e^{j\theta_s/N})|$ can be studied assuming $G_x(z) = F_p^{-1}(z)$, $Q(z) = 1$, and $L(z) = 1$, yielding:

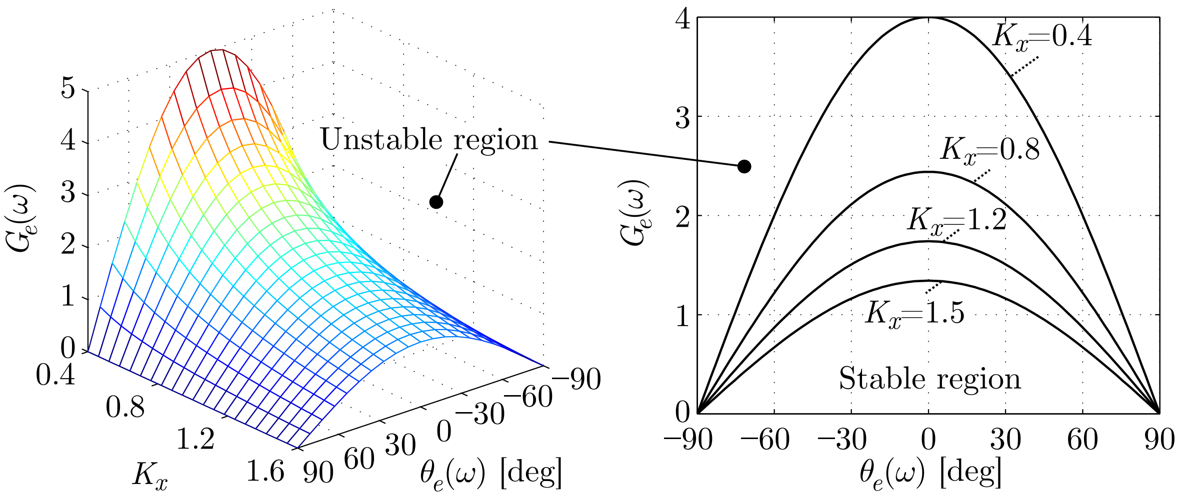

Figure 4.4: (left) Stability regions and (right) particular cases for K_x =0.5, 0.8, 1.2, and 1.5. The region under the surface is stable while that above the surface is unstable.

$$S(z) = \frac{1 - W(z)}{1 - W(z)(1 - K_x)}. \tag{4.21}$$

Fig. 4.5 shows (4.21) varying K_x. The value of $|S(e^{j\theta_s/N})|$ becomes zero, always, when $\theta_s = 0$ or $\theta_s = 2\pi$. Meanwhile, the value of $|S(e^{j\theta_s/N})|$ is modified at inter-harmonic frequencies if K_x changes. From Fig. 4.5:

- The value of K_x has a small impact on the performance close to the harmonic frequencies.
- The value of K_x has a big impact on inter-harmonics (noise). The higher K_x is, the higher the noise amplification is.

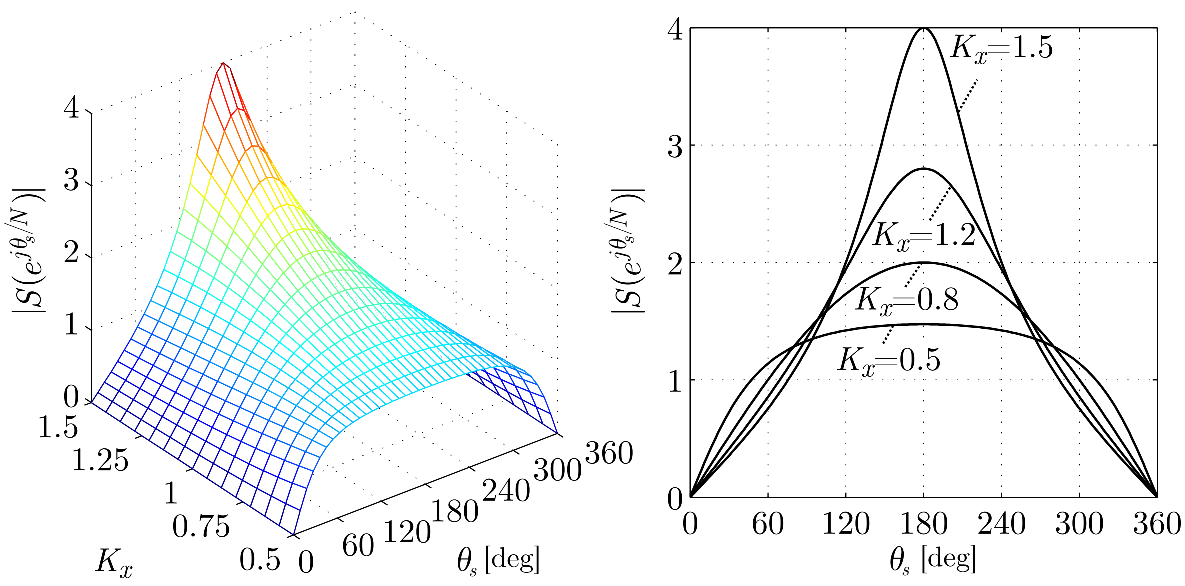

Figure 4.5: $|S(e^{j\theta_s/N})|$ versus θ_s for $K_x = 0.5,\ 0.8,\ 1.2$, and 1.5.

Influence of K_x on Transient Performance

The transient response of a system driven by a RC can be assessed with the poles of the sensitivity function. Considering $Q(z) = 1$ and $L(z) = 1$, for clarity:

$$S(z) = \frac{1 - W(z)}{1 - (1 - K_x)W(z)}, \tag{4.22}$$

and, if the plant dynamics are neglected ($F_p(z) \approx 1$), (4.22) has poles at

$$z = \sqrt[N]{1 - K_x} \cdot e^{\pm j2\pi h/N}, \text{ with } h = 1, 2, \ldots, N/2. \tag{4.23}$$

To facilitate interpretation (4.23) can be transformed to the continuous-time domain:

$$s = \frac{\log(1 - K_x)}{Nt_s} \pm j\frac{2\pi h}{Nt_s}, \tag{4.24}$$

where the pole with the smallest modulus is obtained for $h = 0$, yielding:

$$s = \log(1 - K_x)/Nt_s. \tag{4.25}$$

Fig. 4.6 (left) shows the modulus of the smallest pole for different values of K_x. If $1 < K_x < 2$, the pole for $h = 0$ in (4.24) splits into a pair of complex poles and the step response has overshoot (see Fig. 4.6 (right)). If $0 < K_x < 1$, the response becomes slower and overdamped. If $K_x = 1$, there is a zero-pole cancellation in (4.22) and the closed-loop system has a dead-beat behaviour. Concluding:

- The fastest transient response occurs when $K_x = 1$ (dead-beat).
- If $0 < K_x < 1$, the transient response is overdamped and slower than with $K_x = 1$.
- If $1 < K_x < 2$, the transient response is underdamped and slower than with $K_x = 1$. Therefore, it is recommended to use $0 < K_x \leq 1$.

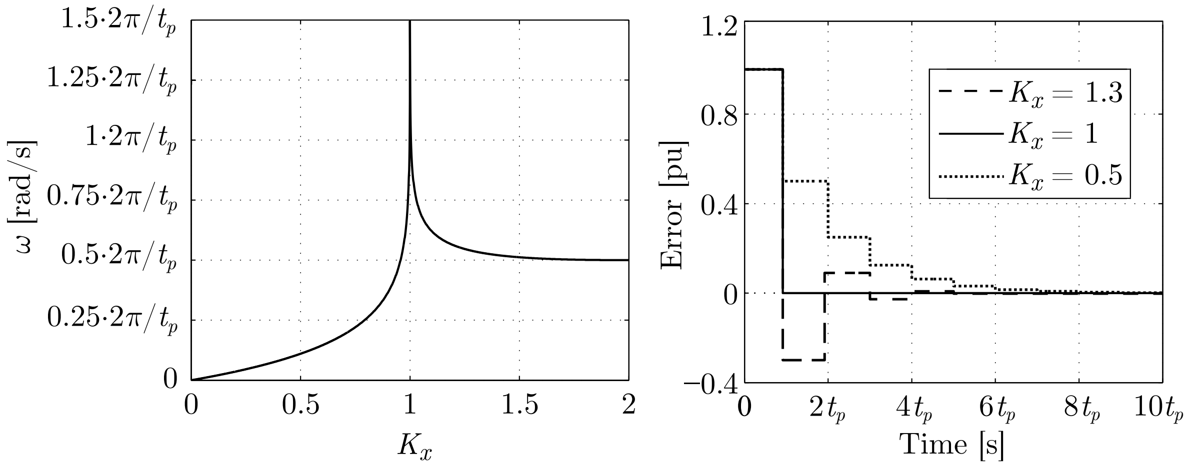

Figure 4.6: (left) Modulus (ω) of the smallest pole (continuous-time domain), varying K_x, and (right) transient response of $S(z)$ for different values of K_x.

4.5 Troubleshooting RCs Implementation

4.5.1 Frequency Deviation

Frequency-Adaptive Repetitive Controller: Adapting N

The disturbance period (t_p) can be split into

$$t_p = Nt_s + \varepsilon t_s, \tag{4.26}$$

where $N \in \mathbb{N}$ and $-1/2 < \varepsilon < 1/2$. A RC can be implemented updating N to the one calculated with (4.26) using the frequency estimated by the PLL ($\hat{\omega}_g$) [195]. Fig. 4.7 shows the steady-state performance of a RC (see Section 4.3.1) when the frequency deviates for N equal 100 and 200, respectively. When $N = 200$, the maximum error is relatively low, but for $N = 100$ the performance is poorer. Hence, for applications where N is large enough the frequency-deviation problem may be tackled with this method [196]. However, a large value of N (small t_s) may be impossible to attain in PE applications because the computational burden would increase beyond acceptable limits and the switching period may have to be limited. Accordingly, novel methods not requiring such a small sampling period have been investigated in this thesis. RCs stability when N varies has been studied by Olm et al. [196]. However, in this thesis N will be changed slowly, so the stability condition in (4.11) remains fully applicable.

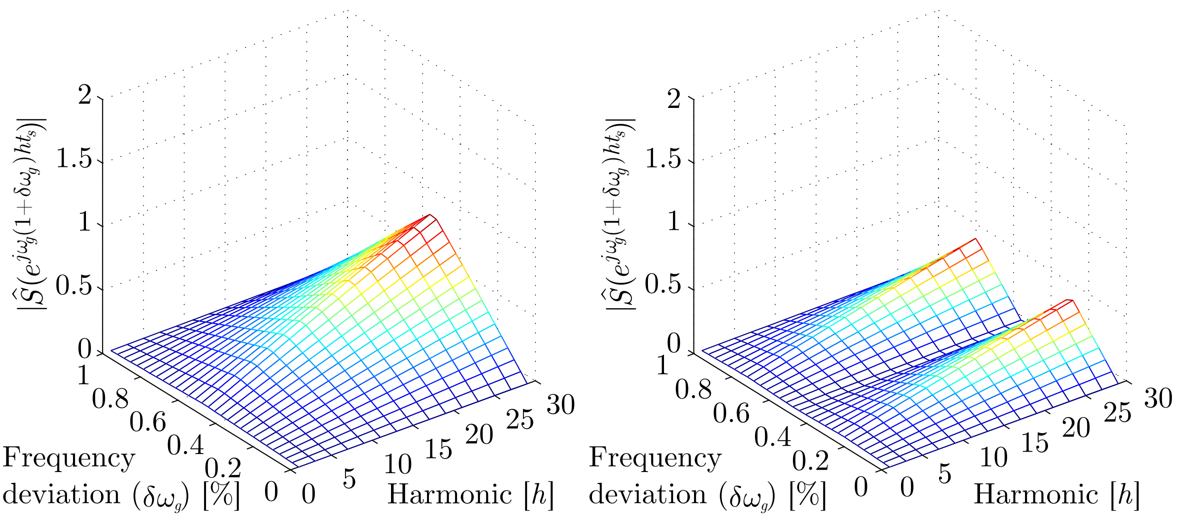

Figure 4.7: $\hat{S}(z)$ updating N to the nearest integer value with (left) $t_s = 1/5000$ s ($N = 100$ for $\omega_g = 2\pi 50$ rad/s) and (right) $t_s = 1/10000$ s ($N = 200$).

Frequency-Adaptive Repetitive Controller: a Simple Approximation

In a general case in which (4.2) is not satisfied t_p can be split into

$$t_p = Nt_s + l_e t_s, \tag{4.27}$$

where $N \in \mathbb{N}$ and $l_e \in [0, 1)$. If the grid frequency is estimated ($\hat{\omega}_g$), l_e and N can be calculated and the RC core in (4.1) can be written as

$$RC_o\left(s\right) = \frac{e^{-Nt_s s}e^{-l_e t_s s}}{1 - e^{-Nt_s s}e^{-l_e t_s s}}. \tag{4.28}$$

The discretization of (4.28) can be carried out in two steps:

1. $e^{-Nt_s s}$ can be represented, exactly, by z^{-N}.
2. The rest of the delay in (4.28) can be approximated by an nth-order Padé approximation [177]:

$$e^{-t_s l_e s} \approx \frac{1 - \frac{t_s l_e}{2}s + \frac{t_s^2 l_e^2}{8}s^2 + \cdots + \frac{\left(-\frac{l_e t_s}{2}s\right)^n}{n!}}{1 + \frac{t_s l_e}{2}s + \frac{t_s^2 l_e^2}{8}s^2 + \cdots + \frac{\left(\frac{l_e t_s}{2}s\right)^n}{n!}}. \tag{4.29}$$

To start with, a first-order approximation can be used:

$$e^{-l_e t_s s} \approx \frac{1 - \frac{t_s l_e}{2}s}{1 + \frac{t_s l_e}{2}s}, \tag{4.30}$$

which can be discretized using Tustin's transformation, yielding

$$L(z) = \frac{\left(1 - l_e\right) + \left(1 + l_e\right)z^{-1}}{\left(1 + l_e\right) + \left(1 - l_e\right)z^{-1}}. \tag{4.31}$$

The filter $L(z)$ has the structure of a first-order all-pass filter with unity gain [197]. A filter similar to $L(z)$ is proposed by Tammy [198], but that alternative does not preserve stability. Chen et al. [157] propose interpolation with a formulation that preserves stability, but performance deteriorates for high-frequency harmonics. The approach proposed here works with a single sampling period and the stability condition in (4.6) is not modified because $|L(e^{j\omega t_s})| = 1 \ \forall\omega$. This is one important contribution of the proposed method. From now on, the version of $L(z)$ based on a Padé's approximation will be called "Padé filter".

Fig 4.8 (a) shows the phase of (4.31) for $l_e = 0.7$ and for different filter orders. The first-order filter gives the best results, so it will be used in the rest of the thesis. Fig. 4.9 shows $|\hat{S}(e^{j\omega_g(1+\delta\omega_g)ht_s})|$ when the frequency deviates using $t_s = 1/5000$ s ($N = 100$ for $\omega_g = 2\pi 50$ rad/s) and $t_s = 1/10000$ s ($N = 200$). Notice that the scale of $|\hat{S}(e^{j\omega_g(1+\delta\omega_g)ht_s})|$ in Fig. 4.9 has been divided by five when compared with Fig. 4.7.

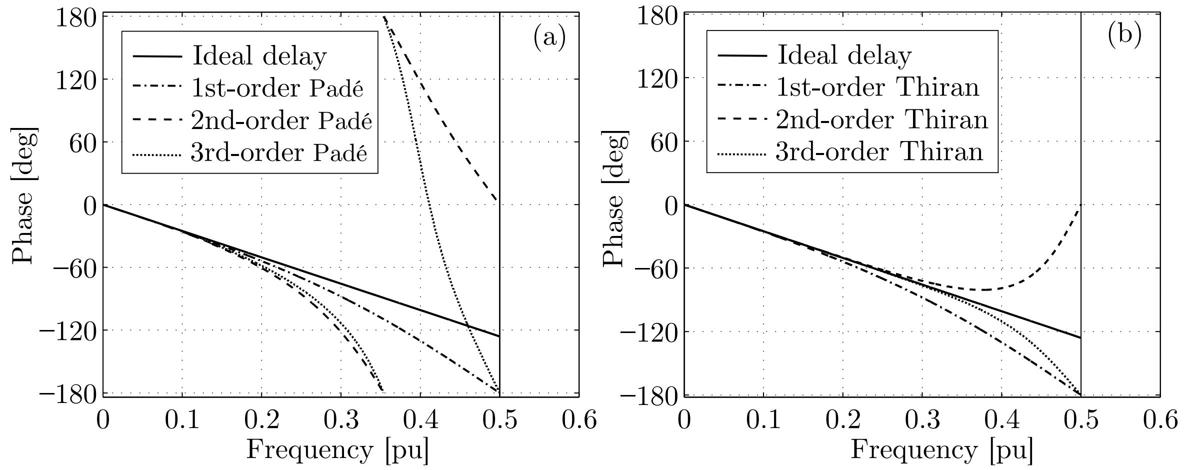

Figure 4.8: Fractional delay approximation using (a) a Padé filter and (b) a Thiran filter when $l_e = 0.7$ (the base frequency is the sampling frequency).

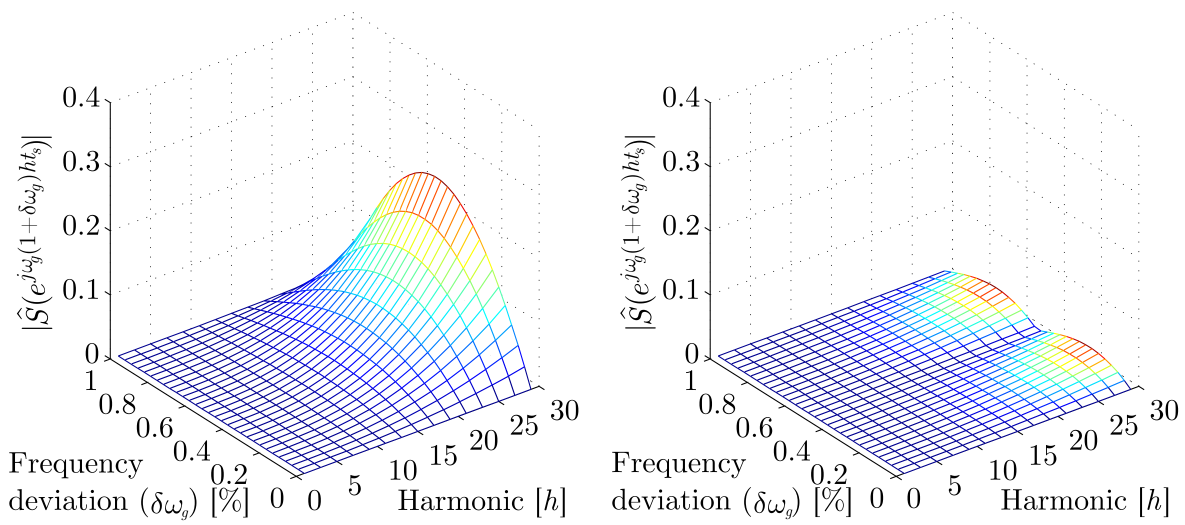

Figure 4.9: $\hat{S}(z)$ for the RC updating N and l_e in $L(z)$ (first order Padé) (left) with $t_s = 1/5000$ s ($N = 100$) and (right) with $t_s = 1/10000$ s ($N = 200$)

Frequency-Adaptive Repetitive Controller: an Accurate Solution

Fractional-delay approximations based on digital filters have been thoroughly studied in the digital-signal-processing field [197]. For a RC, an approximation using an all-pass filter is welcome since this type of filter provides constant gain for all frequencies and, therefore, the stability condition in (4.6) would remain unchanged. In particular, Thiran's all-pass filters approximate a fractional delay with maximally-flat phase delay at $\omega = 0$ [72, 197, 199]. Accordingly, this filter can replace the Padé filter proposed before. A Thiran filter has the structure of an nth-order all-pass filter:

$$L(z) = \frac{\sum_{i=0}^{n} a_{n-i} z^{-i}}{\sum_{i=0}^{n} a_i z^{-i}}. \tag{4.32}$$

If $a_0 = 1$ in (4.32), the filter has unity gain. The rest of the coefficients that approximate a given delay Dt_s are [197]

$$a_k = (-1)^k \binom{n}{k} \prod_{i=0}^{n} \frac{D-n+i}{D-n+k+i}, \text{ for } k = 1, 2, \ldots, n, \tag{4.33}$$

with

$$\binom{n}{k} = \frac{n!}{k!(n-k)!}. \tag{4.34}$$

Parameter D can not be defined along the lines of ε or l_e, as it was done previously, because stability problems might arise [197]. Instead, D is defined as

$$D = L + l_e, \tag{4.35}$$

with $0 < l_e < 1$ and $L \in \mathbb{N}$. As noticed by Laakso et al. [197], if L is large enough, stability of the Thiran filter is guaranteed. For an nth-order filter stability is guaranteed if $L = n - 1$, yielding

$$D = n - 1 + l_e. \tag{4.36}$$

Fig. 4.8 (b) shows the phase-delay (only the fractional part) provided by a Thiran filter for different filter orders. Fig. 4.8 shows that a Thiran filter improves the results when compared with a Padé filter. Moreover, the higher the order is, the better the approximation is. Fig. 4.10 shows $|\hat{S}(e^{\omega_g(1+\delta\omega_g)ht_s})|$ with $t_s = 1/5000$ s ($N = 100$) using a first-, a second-, a third-order Thiran filter, and a Padé filter. The error is much smaller when applying Thiran filters and it is reduced when the filter order increases. Notice that a first-order Padé filter and a first-order Thiran filter give similar results.

4.5.2 Providing Internal Stability

Problems with internal stability when using a RC in an SAC were explained in Chapter 2, Section 2.7. The key point here is how to avoid the cancellation of the zero in the system transfer function caused by the coupling transformer (at $s = 0$) by the unstable pole of the RC. This problem has been tackled as follows.

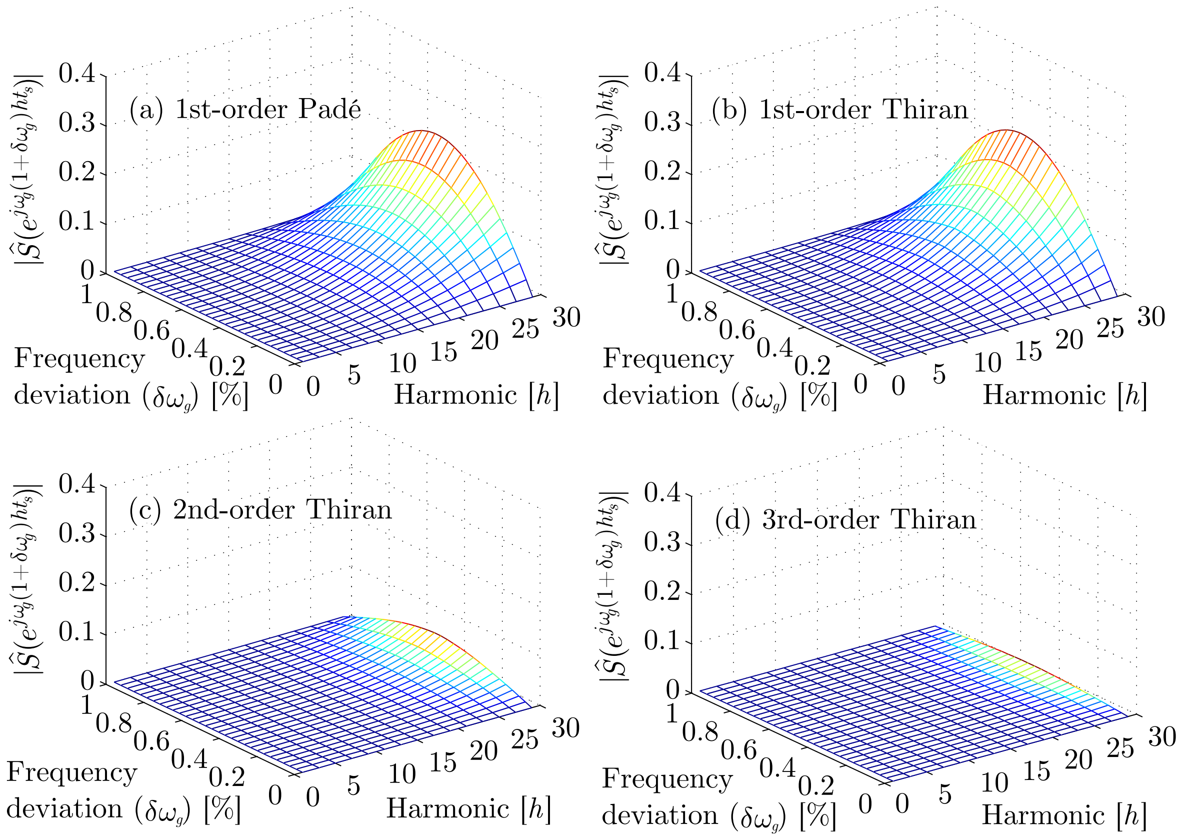

Figure 4.10: $\hat{S}(z)$ with $L(z)$ using (a) a first-order Padé filter, (b) a first-, (c) a second-, and (d) a third-order Thiran filter.

Internal Stability in a Stationary Reference Frame

Park's transformation is commonly used to synchronize VSCs with the grid because the main controller is easier to implement. However, the application of a RC has often been proposed in a stationary RF or using three-phase variables, as in Roncero-Sánchez et al. [15, 37], and this will be the alternative to be applied first.

The filter $Q(z)$ in Fig. 4.1 can be split into a low-pass filter, called $Q_{lp}(z)$, and a high-pass filter, called $Q_{hp}(z)$, to include a DC-removal system within the RC and make close-loop stability possible without affecting the performance:

$$Q(z) = Q_{lp}(z)Q_{hp}(z). \tag{4.37}$$

The filter $Q_{lp}(z)$ is designed as a FIR zero-phase low-pass filter [163], while $Q_{hp}(z)$ is designed as [198]

$$Q_{hp}(z) = \frac{1+\lambda_r}{2}\frac{z-1}{z-\lambda_r}, \text{with } \lambda_r \in (0,1), \tag{4.38}$$

where λ_r is intended to modify the filter bandwidth.

If a SRF is used in the main controller, a RC could still be applied in a stationary RF where a high-pass filter can easily be built in the RC formulation, as shown before. The output of the RC can be transformed into a SRF to be used together with the main controller. The implementation of this strategy is depicted in Fig. 4.11.

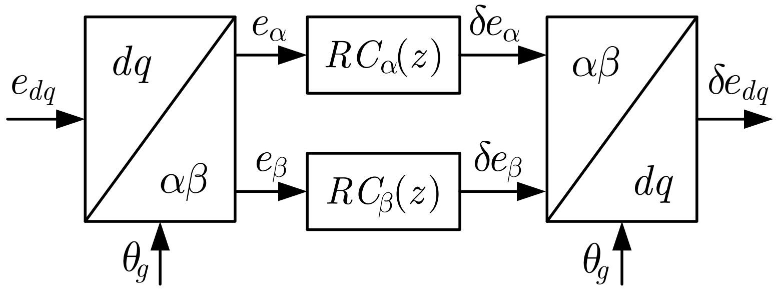

Figure 4.11: Application of a RC in a stationary RF.

Internal Stability in a Synchronous Reference Frame

In a SRF, DC signals are seen as components of frequency ω_g and the magnetizing inductance of the transformer would now appear to block this frequency (zeros at $s = \pm j\omega_g$). Meanwhile, a RC also has unstable poles at $s = \pm j\omega_g$ that would cancel the zeros of the transformer, so the internal-stability problem still appears. Removing the RC poles with a narrow-band filter $Q(z)$ emulating the solution using a stationary RF is not easy. In this thesis, the internal stability problem is tackled in a SRF using the following RC core:

$$RC_o\left(s\right) = \frac{e^{-Nt_s s}}{1 - K_s e^{-Nt_s s}}, \tag{4.39}$$

with $0 < K_s < 1$. If K_s is selected close to 1, a RC will produce a high (but-not-infinite) gain for all the harmonic frequencies, including ω_g, making it possible to apply a RC in a SRF. The closed-loop system will be internally stable because the controller does not cancel any zero of the plant with unstable poles and, as shown in the experiments in Section 4.6, good results are obtained.

The problem with the internal stability is more clearly shown when offsets are present in the measurements. Now, the solutions proposed to make the system internally stable would keep all signals bounded in spite of any possible offset going into the loop. Nevertheless, it goes without saying that looking after offsets in the sensor chain is of paramount importance, anyway.

4.5.3 RC Implementation

The implementation of some of the transfer functions within the RC in Fig. 4.1 is not possible because $G_x(z)$ is not proper and $Q(z)$ is often chosen to be a non-casual filter to avoid delays [26]. Fortunately, the number of delays needed in the RC (N) is large and some of these delays can be used to make these transfer functions proper. If $z^{-C}G_x(z)$, $z^{-M}Q(z)$, and $L(z)$ are proper transfer functions and $N > M + C$ (always the case in practice), the RC can be easily implemented as in Fig. 4.12. A PLL is used to estimate the grid frequency ($\hat{\omega}_g$), which is filtered with a LPF ($\hat{\omega}_g^f$) to avoid fast changes in the controller parameters. The filtered frequency is used to calculate the value of l_e and N to be updated in the RC. As long as changes in the RC (N and l_e) are made slowly, the stability analysis in (4.6) is still valid.

The coefficients of $L(z)$ ($a_0, a_1, \ldots, a_n$) are first computed manually according to the fractional-delay parameter (l_e or D) and, in the real-time application, these coefficients are computed and updated in the filter. For the Padé filter $a_1 = 1 - l_e$ and $a_0 = 1 + l_e$, while for Thiran filters Table 4.1 summarizes the coefficients to be used.

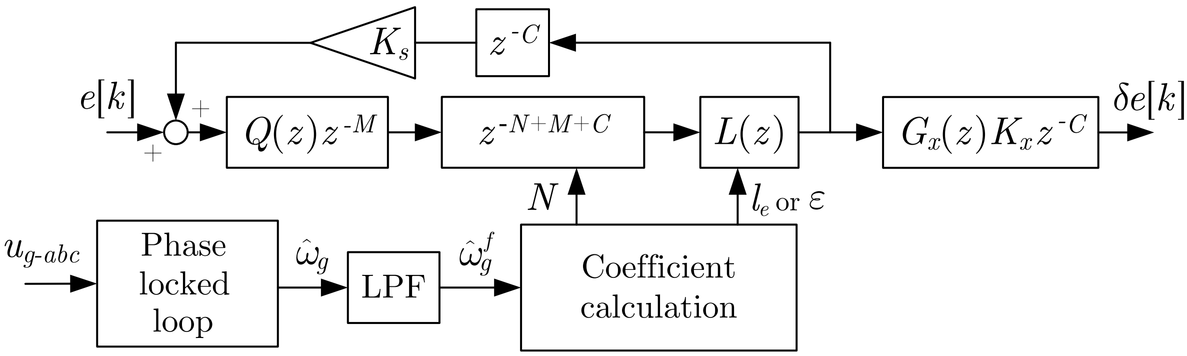

Figure 4.12: Implementation of a frequency-adaptive RC for one axis.

n	a_0	a_1	a_2	a_3
1	1	$-\frac{D-1}{D+1}$	-	-
2	1	$\frac{-2(D-2)}{(D+1)}$	$\frac{(D-1)(D-2)}{(D+1)(D+2)}$	-
3	1	$\frac{-3(D-3)}{(D+1)}$	$\frac{3(D-2)(D-3)}{(D+1)(D+2)}$	$\frac{-(D-1)(D-2)(D-3)}{(D+1)(D+2)(D+3)}$

Table 4.1: Coefficients for an nth order Thiran filter.

4.6 Application of a RC to an SAC

Fig. 4.13 depicts how the RC was placed within the control system of the three-phase SAC described in Appendix A. The SAC is synchronized with the grid using a PLL and the main controller provides the required decoupling between axes, so two independent RCs can be applied. In that figure, $\boldsymbol{K}_d$ and $\boldsymbol{K}_q$ are the gain vectors calculated by the pole-placement algorithm applied to the main controller. The poles of the main controller have been made equal for both axes: a dominant real pole is placed at 600 Hz ($s = -2\pi 600$ rad/s), while the rest of the poles have been also made real and placed at 2500 Hz ($s = -2\pi 2500$ rad/s). Table 4.2 summarizes the SAC parameters (see Appendix A for more details). The switching period is t_{sw}, while P_l and Q_l are the active and the reactive power consumed by the load, respectively.

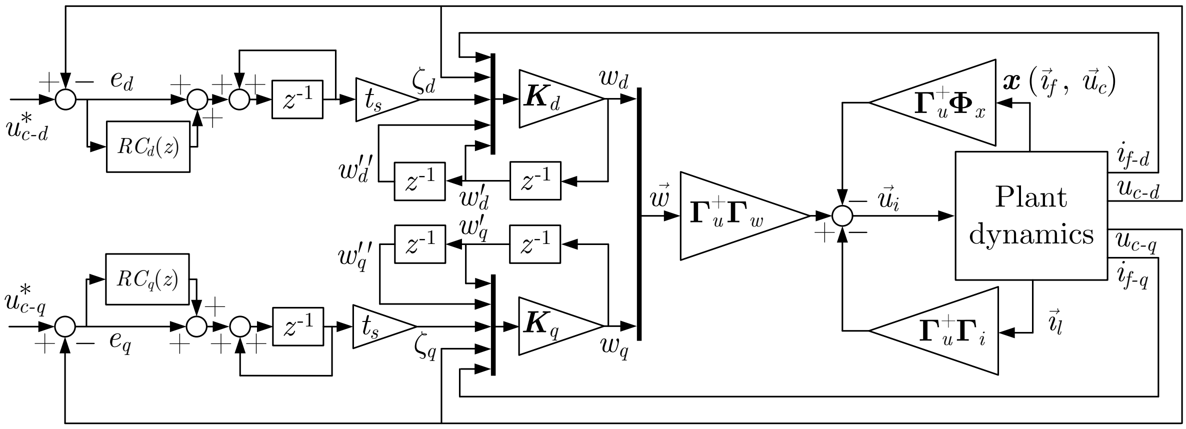

Figure 4.13: Control scheme of an SAC showing the main and the harmonic controller.

L_f	1.5 mH	P_l	4 kW	ω_g	$2\pi 50$ rad/s
L_t	3 mH	Q_l	3 kvar	t_s	1/5400 s
C_f	20 μF	S_n	5 kVA	t_{sw}	1/5400 s
C_{dc}	1.3 mF	V_n	230 V	L_g	700 μH

Table 4.2: Parameters to carry out the RC tests (see Appendix A for more delails).

The RC bandwidth has been set to 1350 Hz with $Q(z)$ using a 25th-order filter ($M = 12$). Such design provides almost perfect tracking up to the 24th harmonic (1200 Hz) in the dq RF, which correspond to the 23th harmonic (negative sequence) and to the 25th harmonic (positive sequence) in abc, as shown Fig. 4.14. The value of K_x has been set to 0.5. Fig. 4.15 (left) shows $|S(e^{j\theta_s/N})|$, revealing that noise amplification is relatively low.

Stability regions can be studied with (4.17), yielding

$$2\cos\left(\theta_e\left(\omega\right)\right) - K_x G_e(\omega) > 0. \tag{4.40}$$

Stable and unstable regions are depicted in Fig. 4.15 (right). If there are not magnitude errors ($G_e(\omega) = 1$), the closed-loop system will be stable if the phase error is smaller than 75.4 deg $\forall\omega$ (black dots in Fig. 4.15 (right)). The transfer-function $G_x(z)$ can be chosen as $\hat{F}_p^{-1}(z)$ because the closed-loop plant does not have NMP zeros (see Chapter 3, Section 3.4.1). The transient performance can be studied using (4.23), yielding a dominant pole of 34.65 rad/s (time constant of 28 ms for $K_x = 0.5$).

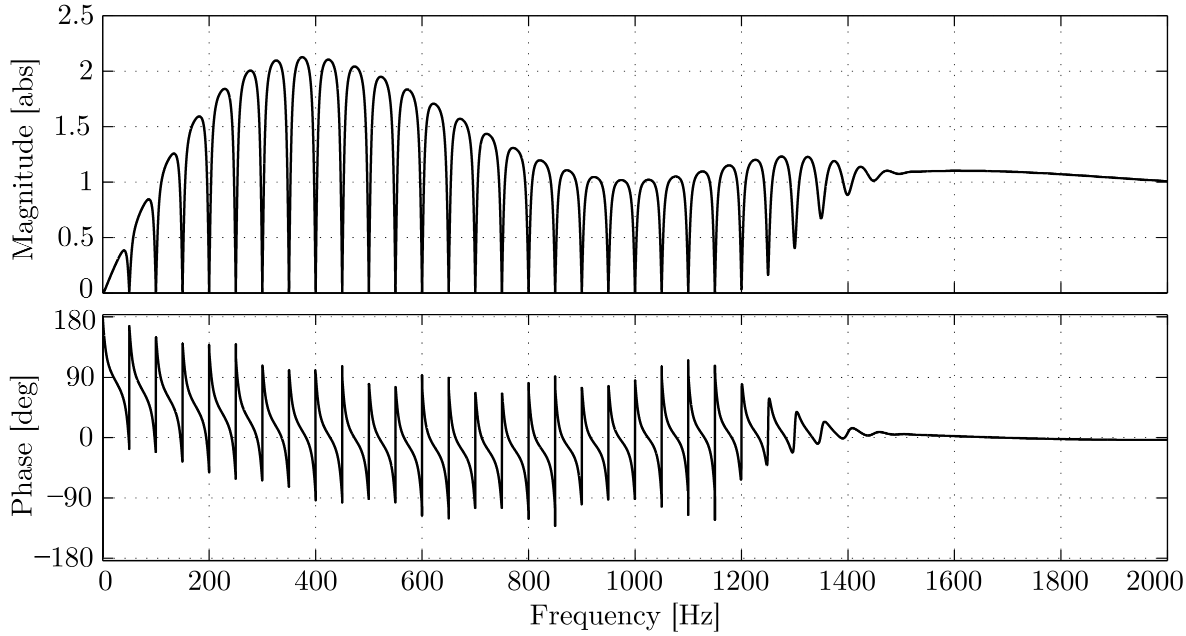

Figure 4.14: Frequency response of $F_e(z)$. The bandwidth of $Q(z)$ is 1350 Hz.

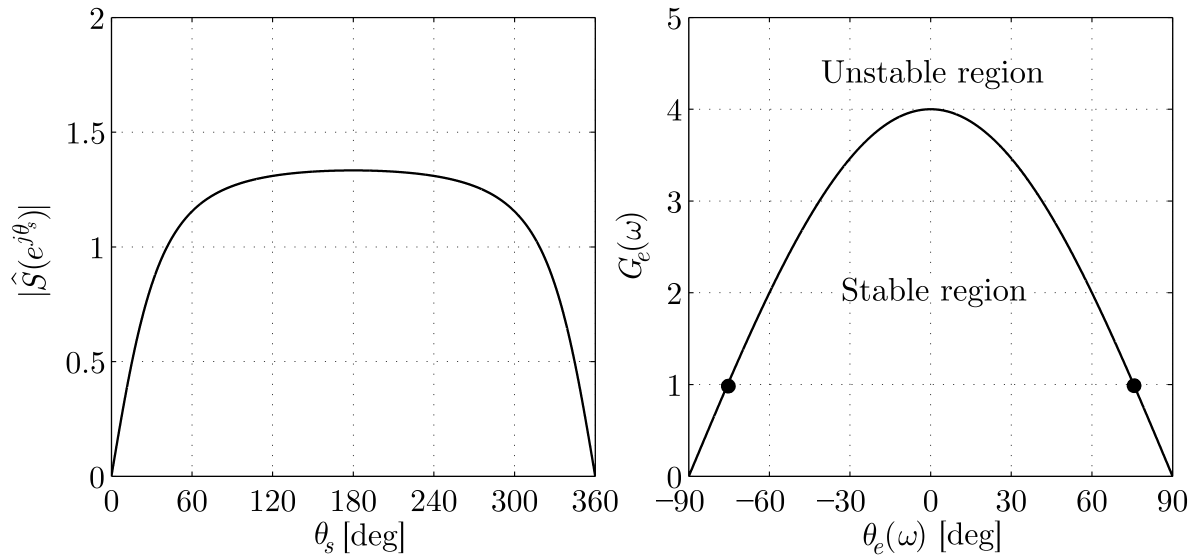

Figure 4.15: (left) $|\hat{S}(e^{j\theta_s/N})|$ for $K_x = 0.5$ and (right) RC stability regions.

Achieving Internal Stability

The need for a DC-removal system when using a RC for an SAC can be easily illustrated with a simple test in the prototype. Fig. 4.16 shows (a) the filter inductor current and (b) the controller error signal after turning the RC on without a DC-removal system. Although the current seems to be constant at first, it goes out of control, eventually. This effect would not be apparent if a short-time test is run. It should be pointed out that high-pass filters were used in all the measurements trying to reduce sensor offsets for all the experiments reported in this chapter.

The two methods proposed to avoid the internal instability problem have been implemented in the prototype. When running the RC in a stationary RF, the value of λ_r in (4.38) has been set to 0.9995. For the strategy suggested in (4.39), the value of K_s has been set to 0.99. Both methods result in a stable closed-loop system with similar performance. Therefore, the second method is preferred (at least for this application) because the RC is easier to implement.

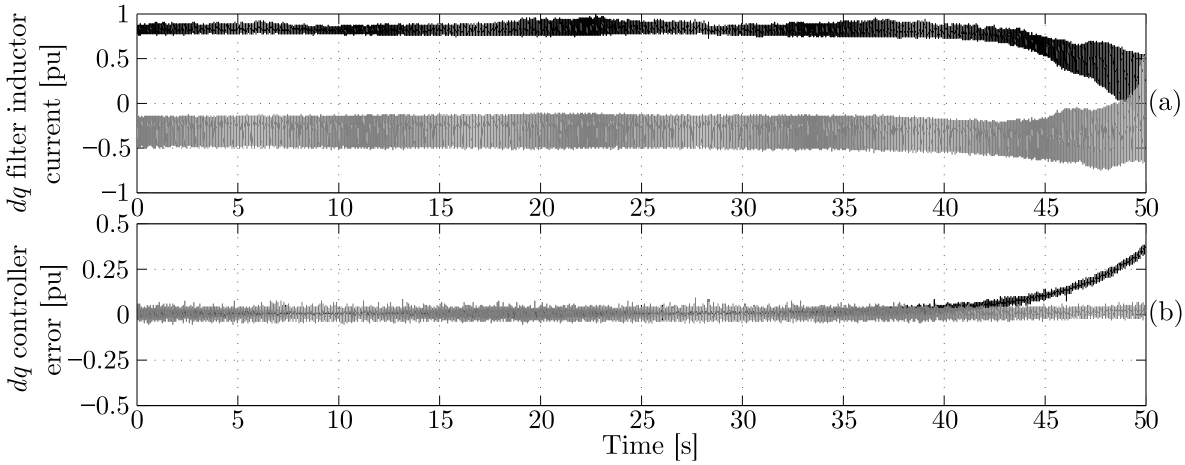

Figure 4.16: Error and transformer current when an unstable RC is applied to the SAC.

Steady-State and Transient Performance

Fig. 4.17 (a) shows the line-to-neutral voltage at the PCC when the grid voltage is polluted with harmonics and $\delta\omega_g = 0.47$ % ($N = 108$ and $l_e = 0.5$). Fig 4.17 (b) and (c) show the line-to-neutral load voltages using a RC without and with $L(z)$ based on a first-order Padé approximation, respectively. The results of a FFT applied to these waveforms are depicted in Fig. 4.18 for key harmonics. The THD of the PCC voltage is 11.6 %, which clearly exceed the IEC limits (2 %) [200]. Using a classical RC the THD is reduced to 5.2 %, exceeding the limits as well. When using the proposed frequency-adaptation method, the THD is drastically reduced to 0.9 %. Clearly, steady-state performance improves using $L(z)$ when the grid frequency deviates. Thiran filters have also been implemented for orders one, two, and three, and the results (load-voltage THDs) are shown in Table 4.3. The higher the filter order is, the lower the load-voltage THD is. This effect is more important when the grid frequency leads to $l_e = 0.5$ ($\delta\omega_g \approx 0.47$ %), as already shown in Fig. 4.10.

Fig. 4.19 shows the d- and q-axis load voltages when the RC is turned on at $t = 0.17$ s. It shows that, after 0.1 seconds (at $t = 0.27$ s), most of the harmonic pollution has been rejected. The transient behaviour is as fast as expected because, for $K_x = 0.5$, steady-state is reached in about $5t_p$ (100 ms) (see Fig. 4.6).

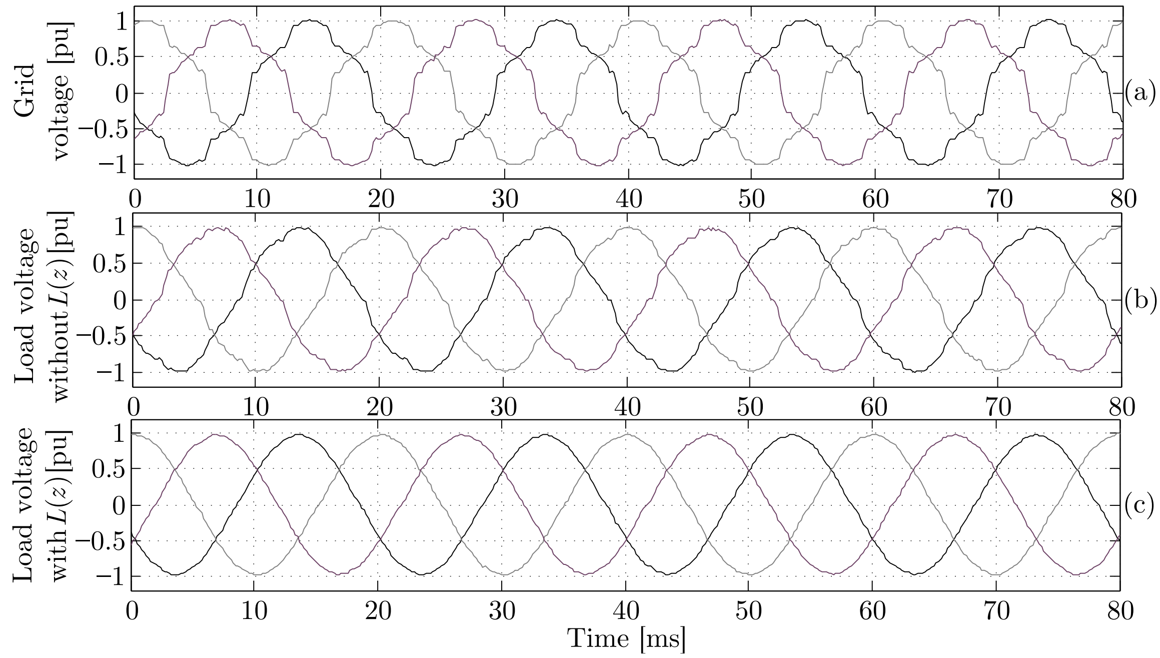

Figure 4.17: (a) Grid voltage and load voltage (b) without and (c) with the Padé filter.

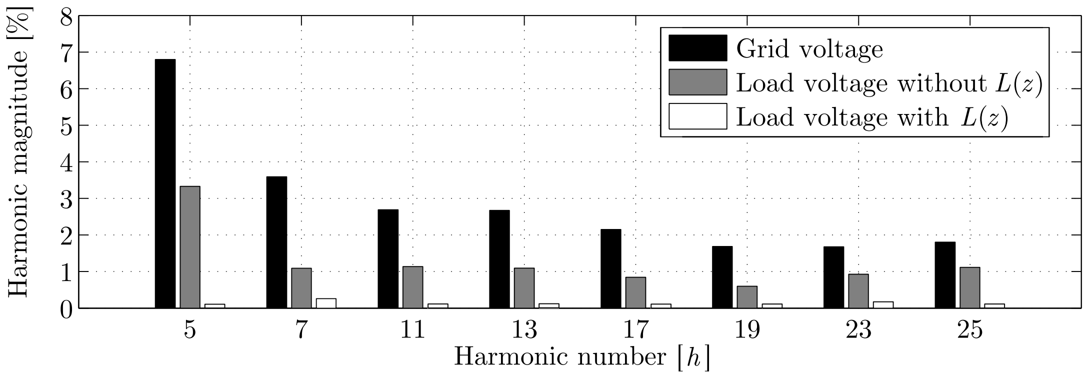

Figure 4.18: FFT results at key frequencies of (a) the grid voltage and the load voltage (b) without and (c) with the Padé filter.

	$\delta\omega_g = 0$ %	$\delta\omega_g = 0.1$ %	$\delta\omega_g = 0.5$ %
$n = 1$	0.71	0.82	0.93
$n = 2$	0.71	0.75	0.81
$n = 3$	0.71	0.71	0.72

Table 4.3: Load voltage THD using a first-, a second-, and a third-order Thiran filter.

Fig. 4.20 shows the transient behaviour when the grid frequency changes from 49.95 Hz to 50.2 Hz at $t = 0.15$ s. A sharp frequency change has been used for demonstration purposes, although it is not realistic. The estimated frequency is filtered with a fourth-order LPF with a 3 Hz cut-off frequency and, to avoid zero-pole cancellations, the value

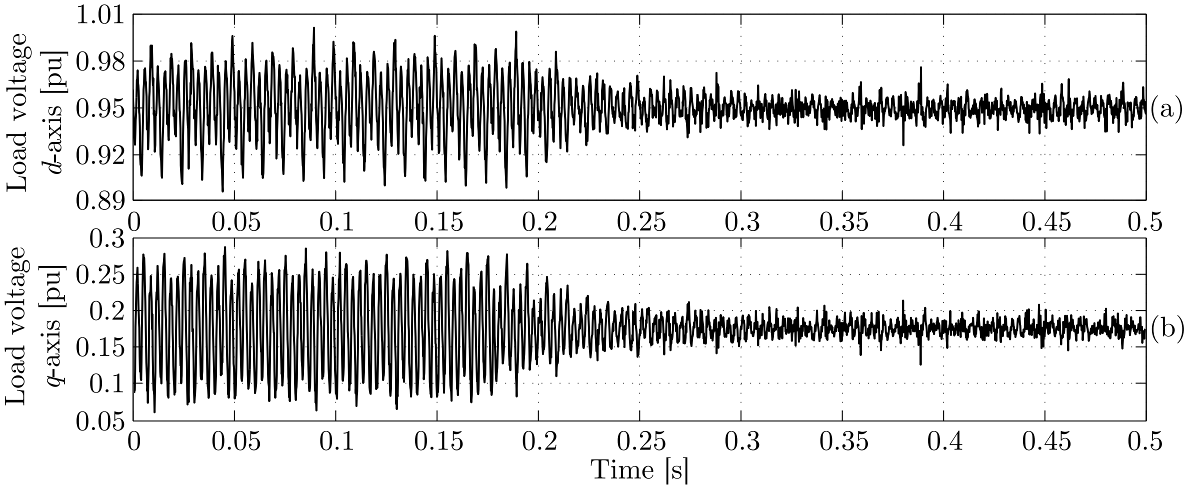

Figure 4.19: Transient of the load voltage when the RC is turned on.

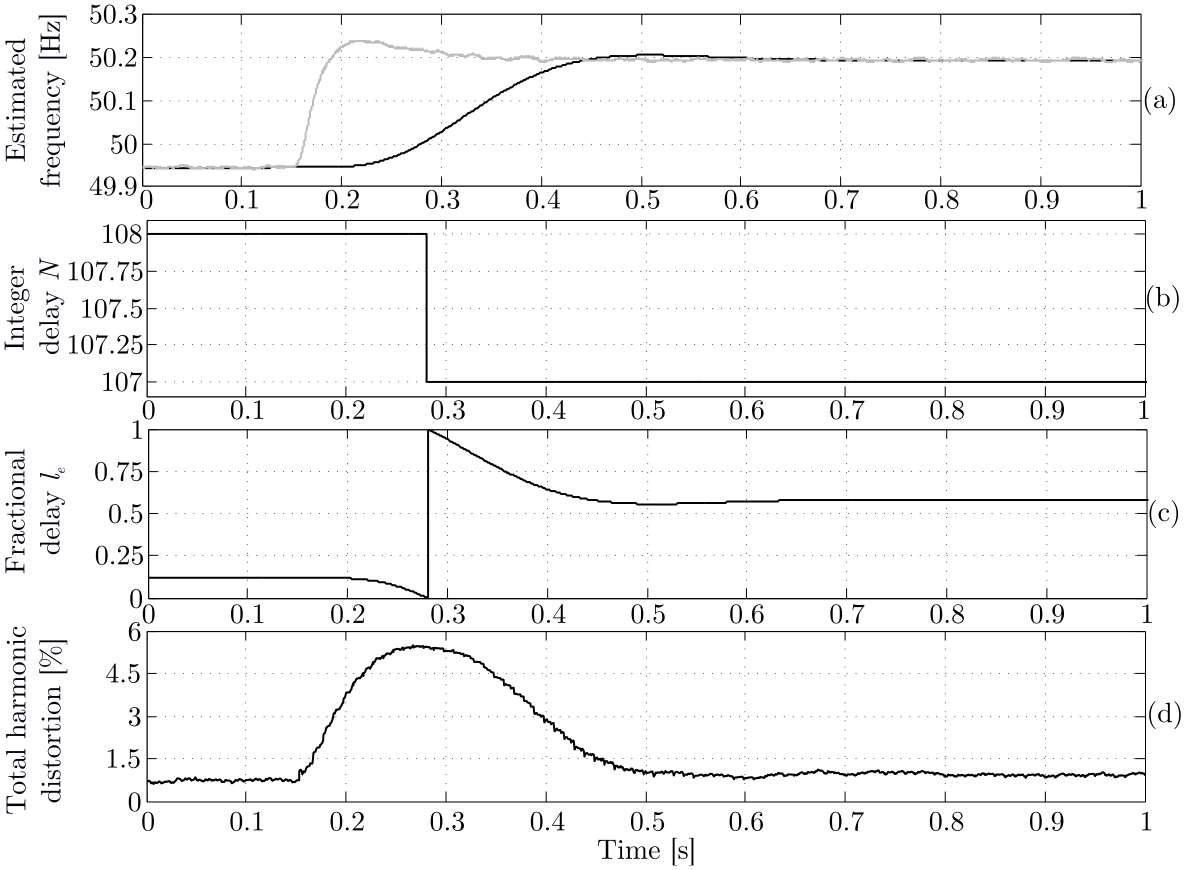

Figure 4.20: SAC performance when the grid frequency suddenly changes. (a) (grey) Estimated frequency and (black) filtered frequency, (b) value of N, (c) value of l_e, and (d) THD of the load voltage.

of l_e is limited to $0.0001 < l_e < 0.9999$. Fig. 4.20 (a) shows (grey) the frequency estimated by the PLL and (black) the filtered frequency. The filtered frequency is used to calculate the value of N and l_e, which are shown in Fig. 4.20 (b) and (c), respectively. Fig. 4.20 (d) shows the load voltage THD during the adaptation. To start with, the grid frequency is 49.95 Hz, yielding $N = 108$ and $l_e = 0.11$. In that case, the THD is 0.7 %. When the grid frequency changes the THD of the load voltage increase up to 5 %. When the grid frequency is correctly estimated and filtered $N = 107$ and $l_e = 0.58$, so the transient dies out and the THD reaches 0.9 %. Nevertheless, only THD values in steady state make sense.

Fig. 4.21 shows how the device compensates a three-phase (symmetric) voltage sag. Initially, the SAC is in steady-state, compensating the supply-voltage harmonics. When the sag starts, at $t = 50$ ms, the SAC rapidly compensates it. As mentioned in Section 3, the current through the filter inductor contains a small decaying DC component due to the transformer magnetisation. The SAC compensates the fundamental component and the harmonics of the load voltage when the grid voltage is low and, when the sag ends, it reduces the injected voltage and the load voltage returns to its previous state. When the sag takes place, the SAC requires a few cycles to eliminate the harmonics.

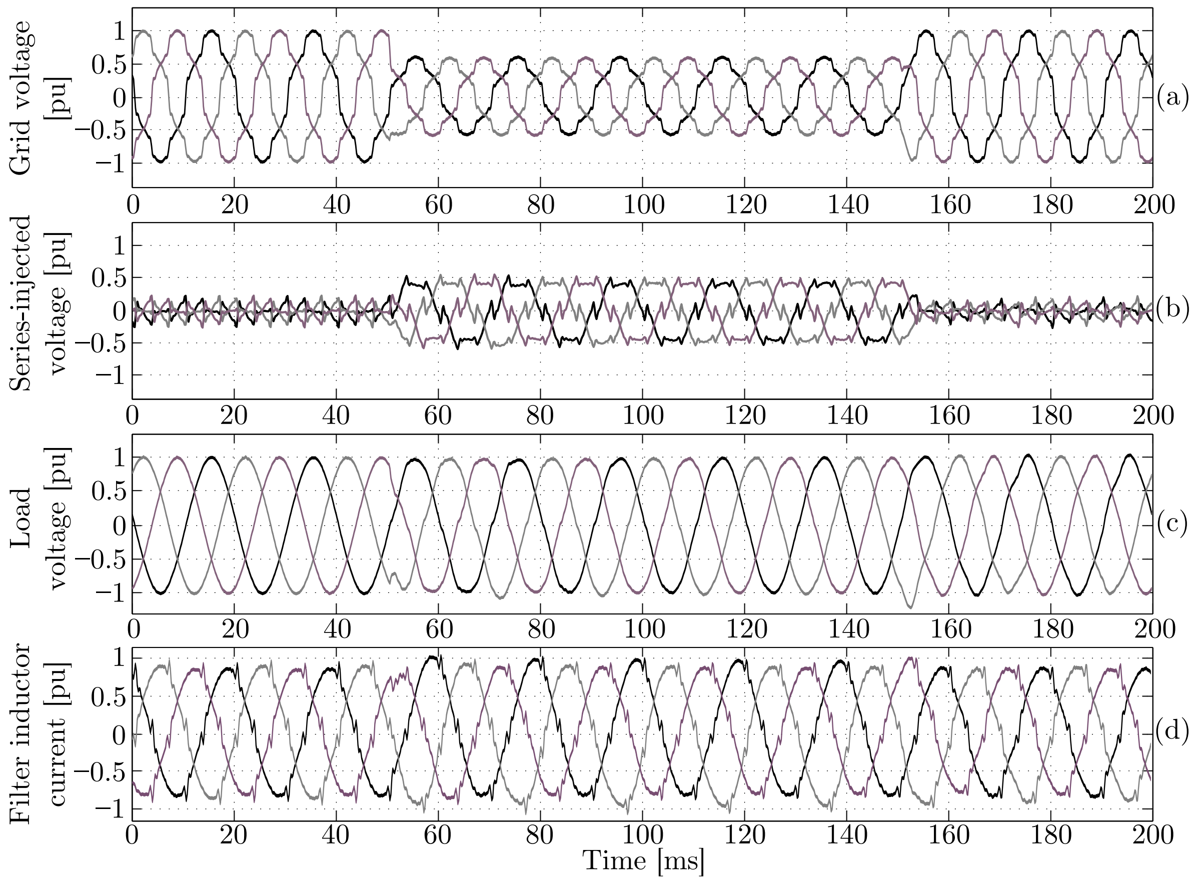

Figure 4.21: Compensation of a three-phase sag with harmonics using a RC+$L(z)$.

Fig. 4.22 shows how the SAC compensates an unbalanced voltage sag (type D_a, 50 % retained voltage). When the sag takes place the SAC restores the load voltage, but the unbalanced components of the grid voltage can not be compensated by the main controller. After a few cycles, the RC eliminates the unbalanced components.

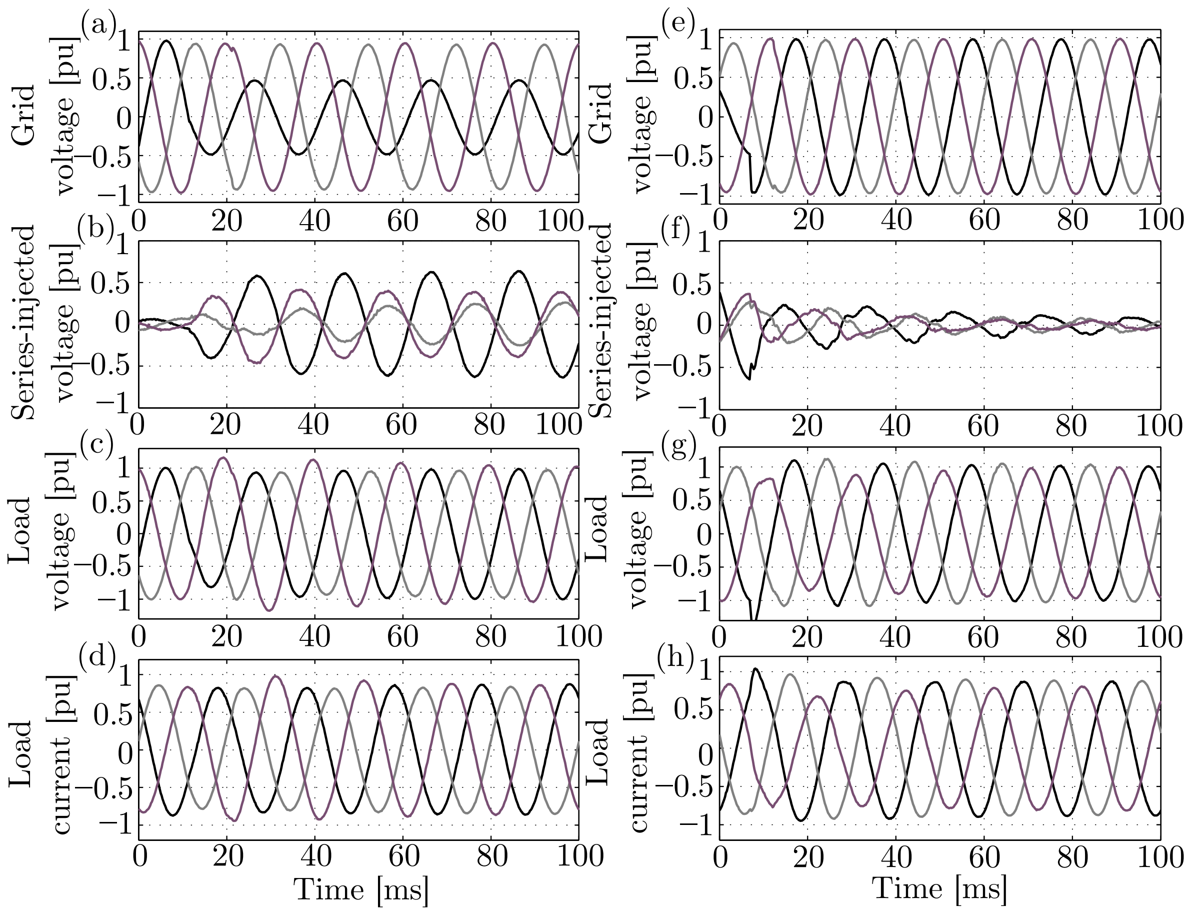

Figure 4.22: Compensation of an unbalanced voltage sag. (a and e) Grid voltage, (b and f) series-injected voltage, (c and g) load voltage, and (d and h) load current.

Protecting Non-Linear Loads

In this section the load is a diode rectifier with a filter capacitor and a resistive load at the DC side (see Appendix A for more details). For this test the grid voltage does not contain harmonics, but the non-linear load produces harmonic voltage drops across the SAC. Fig. 4.23 (left) shows the steady-state performance when the RC is not applied (only the main controller is active). Accordingly, the quality of the load voltage is poor, but the current harmonics consumed by the load are low. Therefore, as the PCC is upstream, its voltage is not polluted with harmonics. Fig. 4.23 (right) shows the SAC performance with the RC. Clearly, the load voltage quality improves, but the PCC voltage quality deteriortates due to the harmonic currents.

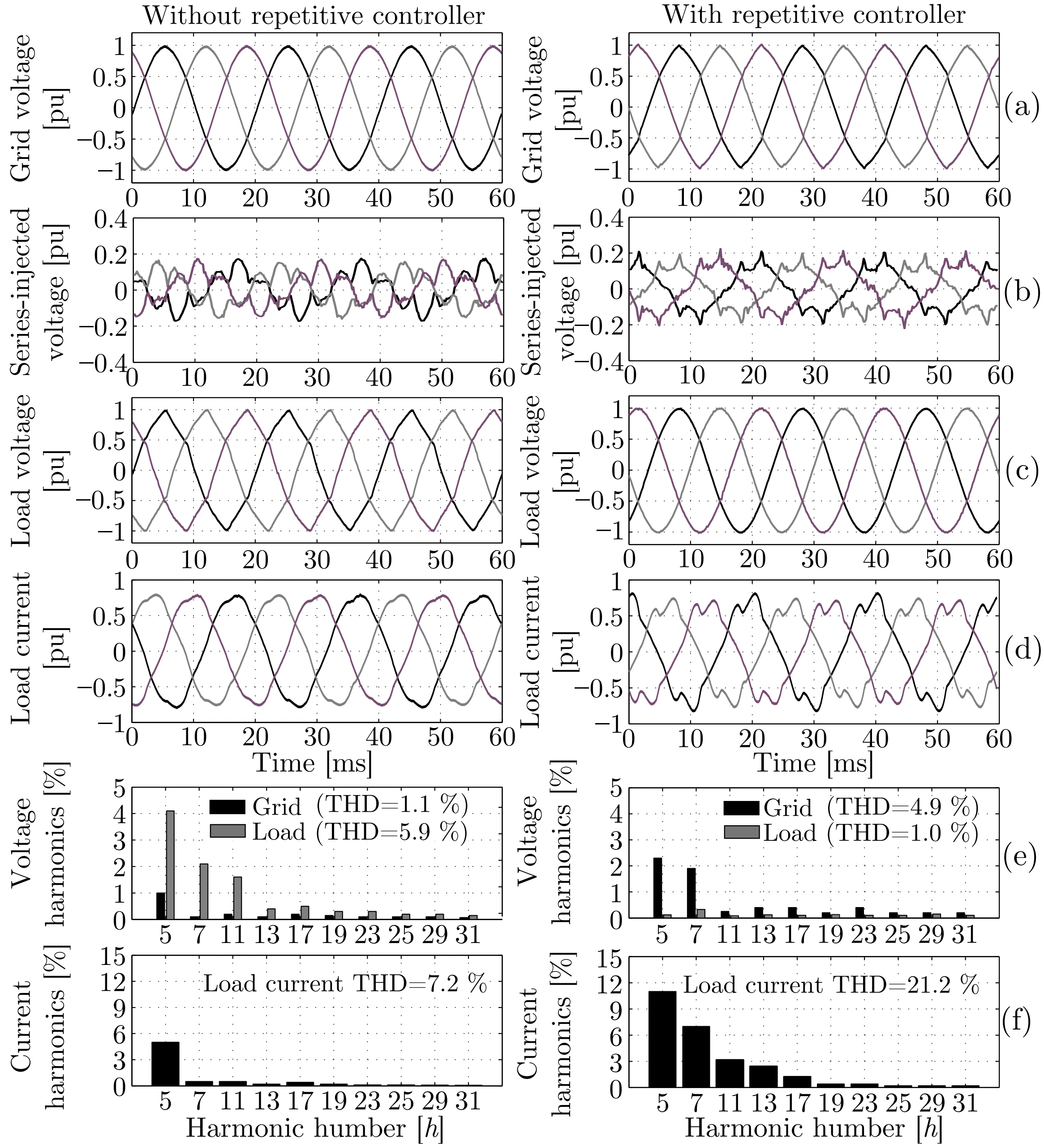

Figure 4.23: Nonlinear load: (a) Grid voltage, (b) series-injected voltage, (c) load voltage, (d) load current, (e) voltage harmonics, and (f) current harmonics (left) with and (right) without a RC.

4.7 Repetitive Controller Alternatives

This section describes odd-harmonic RCs (ODD-RCs), buffer-reduction techniques, and a RC alternative that tracks $nk \pm m$ harmonics, only ($nk \pm m$-RC). Another alternative, called high-order RC (HORC), will be studied separately in Section 4.8.

4.7.1 Odd-Harmonic Repetitive Controller

The core of an ODD-RC is

$$RC_o(z) = -\frac{z^{-N/2}}{1 + z^{-N/2}}, \tag{4.41}$$

which has infinite gain for odd harmonics ($h = 1, 3, 5, \ldots, N/2 - 1$). Therefore, this alternative is interesting to be applied in a stationary RF because the error signal does not contain even harmonics if (a) the error is periodic and (b) it has half-wave symmetry. An ODD-RC requires half the storage capacity when compared to a classical RC. Furthermore, it does not contain an integral action (pole at $s = 0$ in continuous time), so internal stability is guaranteed in a stationary RF.

RCs formulae can be accommodated for ODD-RCs using

$$W(z) = -z^{-N/2} L(z), \tag{4.42}$$

and replacing $h = 0, 1, 2, \ldots, N/2$ by $h = 1, 3, 5, \ldots, N/2 - 1$ (N even) or by $h = 1, 3, 5, \ldots, N/2$ (N odd). The stability condition is also valid because $|W(e^{j\omega t_s})| = 1\ \forall \omega$.

The simplified sensitivity function for an ODD-RC is

$$\hat{S}(z) = 1 + z^{-N/2} L(z). \tag{4.43}$$

Fig. 4.24 shows $|\hat{S}(e^{j\omega_g(1+\delta\omega_g)ht_s})|$ for an ODD-RC ($L(z) = 1$). It behaves better than a classical RC under frequency variations because the surface in Fig. 4.24 (left) is flatter when compared to the one generated by a classical RC. In any case, the frequency-adaptive techniques presented in Section 4.5.1 can be applied to ODD-RCs if

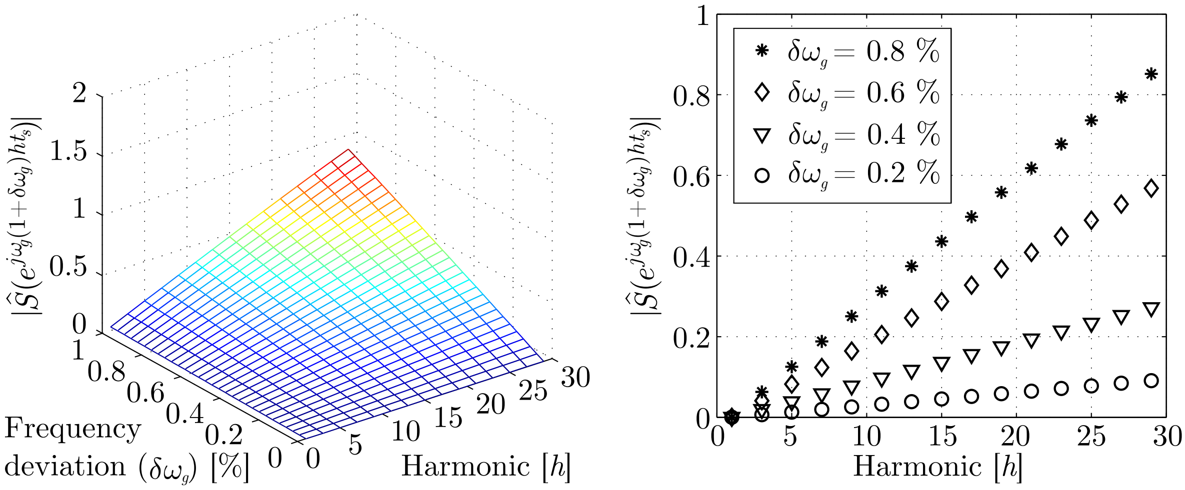

Figure 4.24: Steady-state performance of a ODD-RC when the grid frequency deviates (only odd harmonics).

$$t_p = (N/2)t_s + l_e t_s, \tag{4.44}$$

where $N/2 \in \mathbb{N}$ and $0 < l_e < 1$.

The closed-loop analysis for RCs provided in Section 4.4.2 can also be applied to ODD-RCs. Assuming $F_p(z) \approx 1$, the closed-loop poles are

$$z = \sqrt[N/2]{1 - K_x} \cdot e^{\pm j2\pi h/N} \text{ , with } h = 1, 3, \ldots, N/2 - 1 \text{ (}N\text{ even)}. \tag{4.45}$$

The dominant pole in (4.45) has twice the modulus of that of a RC. Therefore, the transient response here is twice as fast as that of a RC.

4.7.2 Reducing the Buffer Size

The size of the buffer can be reduced if not all the harmonics need to be eliminated. For instance, a RC embarked on a SRF can eliminate $h = 6k \pm 1$ ($k = 1, 2, \ldots$) harmonics in *abc* ($\pm 6k$ in *dq*) if

$$W(z) = z^{-N/6}. \tag{4.46}$$

Another alternative that tracks even harmonics is obtained if $W(z) = z^{-N/2}$ (EVEN-RC). If an EVEN-RC is embarked in a SRF, it would not contain poles at $s = \pm j\omega_g$ and, therefore, internal stability is guaranteed. There are several ways to use the buffer-reduction techniques (e.g. triple harmonics with $W(z) = z^{-N/3}$, etc.), but these alternatives do not need an additional analysis since (a) all of them have similar stability properties and (b) the frequency (modulus) of the dominant pole is inversely proportional to the buffer size (the smaller the buffer is, the faster the transient is).

4.7.3 $nk \pm m$ Repetitive Controller

Lu et al. [156] proposes the following RC alternative to track $nk \pm m$ harmonics:

$$RC_o(z) = \frac{\cos(2\pi m/n) z^{N/n} - 1}{z^{2N/n} - 2\cos(2\pi m/n) z^{N/n} + 1}, \text{with } N/n \in \mathbb{N} \text{ and } n > m > -n. \tag{4.47}$$

The RC core in (4.47) can be rewritten as follows:

$$RC_o(z) = \frac{\cos(2\pi m/n) z^{N/n} - 1}{\left(z^{N/n} - e^{j2\pi m/n}\right)\left(z^{N/n} - e^{-j2\pi m/n}\right)}, \tag{4.48}$$

which has poles at $s = \pm j(nk \pm m)\omega_g$. Fig. 4.25 (left) shows the bode diagram of (4.48) for $n = 6$ and $m = 1$ ($6k \pm 1$ harmonics). Fig. 4.25 (right) shows a detail of the frequency response of (4.48) for $n = 6$, varying m. Notice that m can be a non-integer number and, therefore, an $nk \pm m$-RC can be used to eliminate, for instance, inter-harmonics. For the scope of this thesis this property is not relevant, but it could be useful for other applications. To study an $nk \pm m$-RC,

$$W(z) = z^{-N/n} L(z), \text{ with } N/n \in \mathbb{N}. \tag{4.49}$$

The RC stability condition in (4.11) is valid for an $nk \pm m$-RC [156], so $G_x(z)$ and K_x can be chosen as described in Section 4.4.

Fig. 4.26 shows the implementation of an $nk \pm m$-RC. It requires three buffers with a length of N/n samples each, which is half the memory storage when compared with a RC. However, $Q(z)$ is applied three times. The modulus of the dominant pole is $m+1$ times larger than the one of a RC [156] (for $n = 6$ and $m = 1$ the transient response is twice as fast as that of a RC). If $m \neq 0$, the controller does not include a pole equivalent to $s = 0$ and, therefore, internal stability is guaranteed in a stationary RF. In addition, if $n - m \neq 1$, it does not include a pole equivalent to $s = \pm j\omega_g$, so it can be applied in a SRF.

An $nk \pm m$-RC can be seen as a generalisation of RCs. First of all, if $n = 1$ and $m = 0$, it becomes a RC. Secondly, if $n = 2$ and $m = 1$, it becomes an ODD-RC. Furthermore, RCs with a reduced buffer correspond to $m = 0$ and n equal to the buffer reduction (e.g. $n = 2$ and $m = 0$ yields an EVEN-RC). Another RC alternative published by Escobar et al. [201], which tracks $6k \pm 1$ harmonics, corresponds to $n = 6$ and $m = 1$ ($6k \pm 1$).

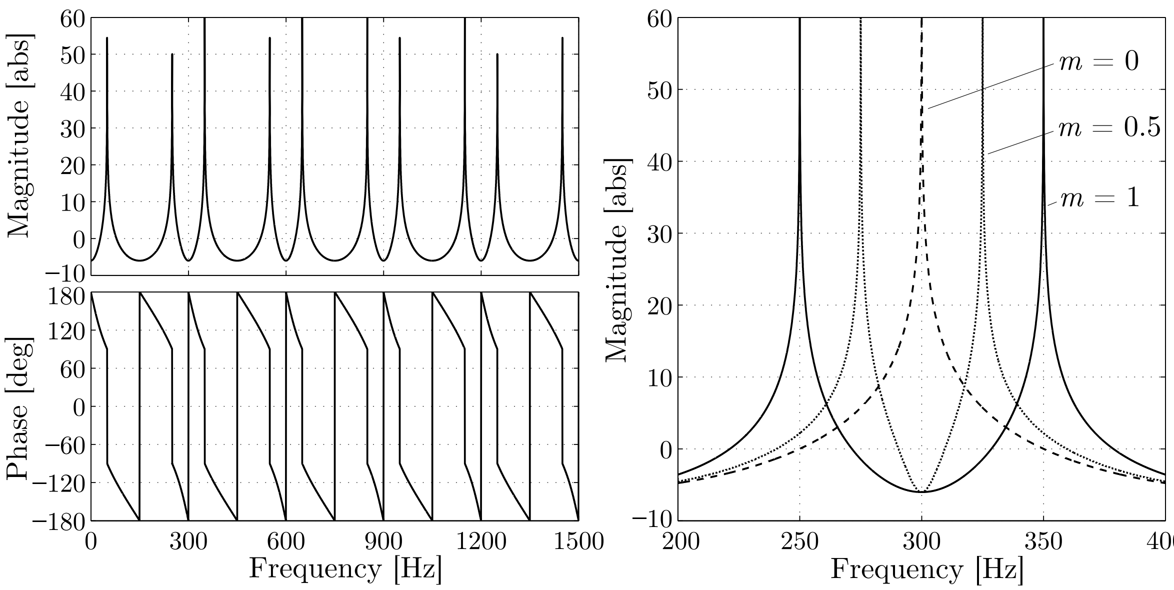

Figure 4.25: Bode diagram of the $nk \pm m$-RC for (left) $n = 6$ and $m = 1$ and (right) for (solid) $m = 1$, (dotted) $m = 0.5$, and (dashed) $m = 0$.

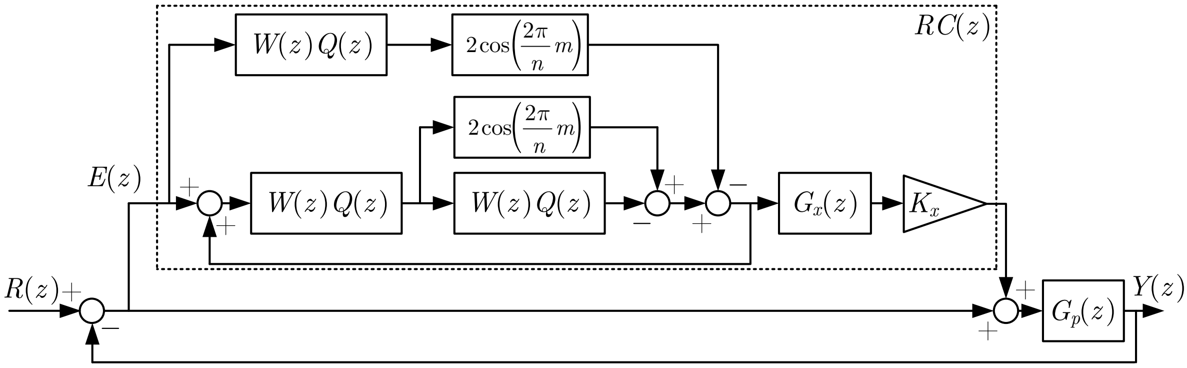

Figure 4.26: Schematics of an $nk \pm m$ repetitive controller.

4.7.4 Other Repetitive Controller Alternatives

Escobar et al. [202] and Loh et al. [203] present a RC with feed-forward action. This alternative has an improved inter-harmonic behaviour but, unfortunately, it can not be applied to plants with a phase-delay larger than 90 deg, as shown by Costa-Castelló et al. [204]. Another alternative based on a repetitive disturbance observer was presented by Chen and Tomizuka [190] and by Na et al. [205]. This alternative improves the performance when the plant is constantly perturbed with non-periodic disturbances, which is not the SAC case.

If two (or more) RCs are plugged in parallel, the controller will contain the poles of each of the RCs. Therefore, parallel RCs can be used to track harmonics of two (or more) fundamental frequencies. In this case, the core is defined as follows [206]:

$$RC_o(z) = \sum_{i}^{n} k_{x-i} \frac{W_i(z)Q_i(z)}{1 - W_i(z)Q_i(z)}, \tag{4.50}$$

where k_{x-i} is the gain of each individual RC and $0 \leq \sum_{i=1}^{n} k_{x-i} \leq 2$ [158]. RCs can be plugged in parallel using different SRFs if they are applied to space-vector based plants. Chen et al. [157] use three RCs in parallel with different SRFs. In this case, the transient response can be made faster because the RC that deals with the most relevant harmonics (the ones related to $6k \pm 1$ harmonics in *abc*) is designed with a high value of k_{x-i}, while the rest of the RCs are designed with a smaller k_{x-i}.

4.8 High-Order Repetitive Controller

HORCs use not only the information from the previous cycle to compute the command (like a RC) but also older information. All the information is weighted using the so-called weighting coefficients, which can be chosen to improve the controller performance when the frequency varies [185] or to reduce noise amplification [207]. The core of an

HORC is [185]:

$$RC_o(z) = \frac{\sum_{i=1}^{n} W_i z^{-Ni}}{1 - \sum_{i=1}^{n} W_i z^{-Ni}}, \tag{4.51}$$

where W_i are the weighting coefficients. The controller in (4.51) is called RC if $i = 1$, otherwise is called HORC. Fig. 4.27 shows the block-diagram for an HORC. To accommodate RCs formulae to HORCs,

$$W(z) = \sum_{i=1}^{n} W_i L^i(z) z^{-Ni}. \tag{4.52}$$

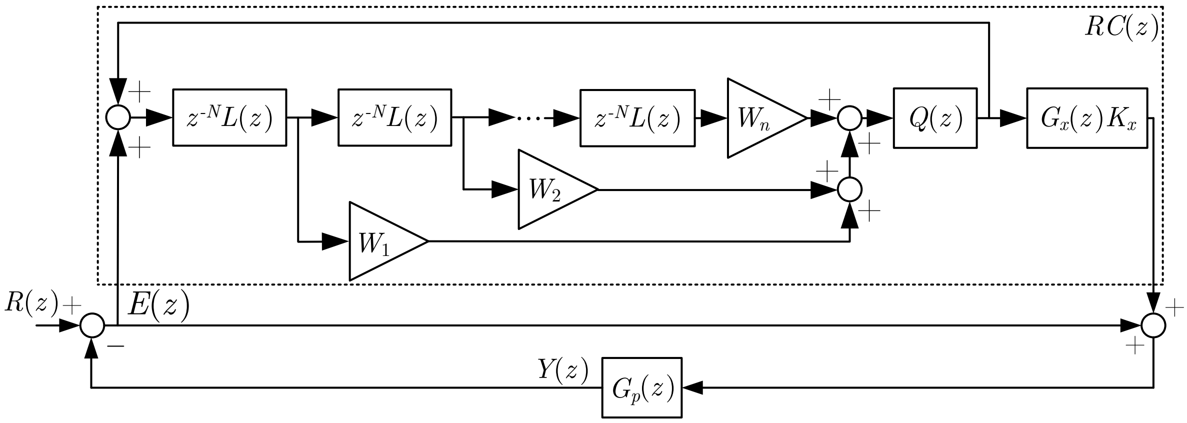

Figure 4.27: Block diagram of a high-order repetitive controller (HORC).

4.8.1 Constrains of the Weighting Coefficients

Performance-Based Constraint

The value of $H(e^{j\theta_s/N})$ should be one at the harmonic frequencies to ensure perfect tracking of periodic signals (Section 4.3). Assuming that $Q(z) = 1$ and $L(z) = 1$:

$$H(e^{j\theta_s/N}) = \sum_{i=1}^{n} W_i e^{j\theta_s/Ni}, \tag{4.53}$$

and, for $\theta_s = 0$, (4.53) should equal one:

$$\sum_{i=1}^{n} W_i = 1. \tag{4.54}$$

Stability-Based Constraint

For a RC, $|H(e^{j\omega t_s})| = 1 \ \forall\omega$ (if $Q(z) = L(z) = 1$). Therefore, the stability condition in (4.11) is not affected by $H(e^{j\omega t_s})$. For an HORC, the weighting coefficients affect both the phase and the magnitude of $H(e^{j\omega t_s})$. So, the condition to ensure that $|H(e^{j\omega t_s})| \leq 1 \ \forall\omega$ is (see Appendix C, Section C.1.1 for the proof):

$$\sum_{i=1}^{n} |W_i| \leq 1. \tag{4.55}$$

From (4.55):

- The filter $L(z)$ does not affect stability when applied to a HORC.
- If the sum of the modulus of the weighting coefficients is less than or equal to one, the simplified stability condition in (4.11) is still an upper-bound for the stability condition in (4.6).
- If the sum of the modulus of the weighting coefficients is higher than one, stability must be checked with (4.6) instead of with (4.11), and stability margins are likely to deteriorate.

4.8.2 Selection of the Weighting Coefficients

The selection of the weighting coefficients depends on the application. For instance, Steinbuch [185] gives a solution that minimises frequency-deviation effects on the steady-state performance (period-robust RC, PR-RC). On the contrary, Chang et al. [208] give a solution that ensures maximum noise attenuation (noise-robust RC, NR-RC). In a general approach, Pipeleers et al. [209, 210] give a solution where the weighting coefficients are chosen based on an optimization problem.

Period-Robust Configuration

For an mth-order PR-RC, the equations to obtain the weighting coefficients are (see Appendix C, Section C.1.2 for the proof):

$$\sum_{i=1}^{k} W_i i^{(k-1)} = 0, \text{ for } k = 2, 3, \ldots, m, \tag{4.56}$$

and the performance-based constraint in (4.54).

Noise-Robust Configuration

The problem to obtain the coefficients in this case can be formulated as:

$$\min_{W_i}\left(\max_{0<\theta_s<2\pi}|\hat{S}(e^{j\theta_s/N})|\right), \quad \text{with } \sum_{i=1}^{m}|W_i| = 1, \tag{4.57}$$

which includes both the stability- and the performance-based constraints [208]. There is no analytical solution for (4.57), but practical experience has shown that the weighting coefficients that fulfil (4.57) are [208]

$$W_i = (m - i + 1) \,/ \sum_{k=1}^{m} k, \tag{4.58}$$

and the solutions are summarized in Table 4.4 for different controller orders.

	PR_2-RC	PR_3-RC	PR_4-RC	NR_2-RC	NR_3-RC	NR_4-RC
W_1	2	3	4	2/3	3/6	4/10
W_2	-1	-3	-6	1/3	2/6	3/10
W_3	-	1	4	-	1/6	2/10
W_4	-	-	-1	-	-	1/10

Table 4.4: Weighting coefficients for a second-, a third-, and a fourth-order PR-RC and for a second-, a third-, and a fourth-order NR-RC. The sub-index means “order”.

Noise-Robust Alternative Formulation

Inoue [207] gives an alternative solution to minimise noise and inter harmonics. The criteria in this case is

$$\min_{W_i}\left(\int_0^{\pi}|\hat{S}(e^{j\theta_s/N})|^2 d\theta_s\right), \quad \text{with } \sum_{i=1}^{m}|W_i| = 1, \tag{4.59}$$

which is equivalent to minimise the power of white-noise amplification and leads to $W_i = 1/m$. This formulation is very similar to the one presented above, so it will not be studied here.

4.8.3 Comparison of HORCs

HORCs Stability

The values of K_x to have a stable closed-loop system have to be calculate for HORCs and can be done as follows: $\min(1/|H(e^{j\omega t_s})|^2 - 1)$ is computed, first, and the result is replaced in the limits of K_x, in (4.19). Table 4.5 summarizes the interval from which K_x can be chosen for different HORCs. For NR-RCs the interval remains constant, but for PR-RCs the interval is reduced when the order increases.

	RC	NR_2-RC	NR_3-RC	NR_4-RC	PR_2-RC	PR_3-RC	PR_4-RC
$\min K_x$	0	0	0	0	2/3	6/7	14/15
$\max K_x$	2	2	2	2	4/3	8/7	16/15

Table 4.5: Range of K_x for different weighting-coefficient configurations.

Steady-State and Transient Performance of HORCs

Fig. 4.28 (left) shows $|\hat{S}(e^{j\theta_s/N})|$ for a RC, a second-, and a third-order PR-RC. If the order increases, $|\hat{S}(e^{j\theta_s/N})|$ remains close to zero in the surroundings of $\theta_s = 0$ and $\theta_s = 2\pi$. Therefore, robustness against frequency deviation improves when the order increases but, unfortunately, the peak value of $|\hat{S}(e^{j\theta_s/N})|$ indicates that noise is greatly amplified. Fig. 4.28 (right) shows $|\hat{S}(e^{j\theta_s/N})|$ for a RC, a second-, and a third-order NR-RC: the higher the order is, the lower noise amplification is.

Fig. 4.29 (left) shows the performance of (a) a second- and (b) a third order NR-RC, revealing that NR-RCs are very sensitive to frequency variations. Fig. 4.29 (right) shows the steady-state performance of (c) a second- and (d) a third-order PR-RC. PR-RCs are robust against small frequency variations, but their performance deteriorates for large variations.

The transient performance of HORCs can be studied with the poles of $F_e(z)$, yielding:

$$\sum_{i=1}^{m} W_i z^{-iN} = (1 - K_x)^{-1}\,. \tag{4.60}$$

These poles depend on the weighting coefficients and are not easy to obtain. However, the transient performance can be studied if $K_x = 1$ because, in that case, there is a pole-zero cancellation and the transient has a dead-beat behaviour that is m times slower than the transient response of a RC.

4.9 Applying RC Alternatives

Based on Section 4.7 and Section 4.8, the following RC alternatives have been tested experimentally:

1. An EVEN-RC in a SRF to eliminate even harmonics in *dq* (positive- and negative-sequence odd harmonics in *abc*), without jeopardizing internal stability.
2. An ODD-RC in a stationary ($\alpha\beta$) RF, which is similar to an EVEN-RC in a SRF. The design parameters for the EVEN- and the ODD-RC presented above are similar to those presented in Section 4.6 for a RC.
3. A RC in a SRF with a buffer length of $N/6$ (called “$6k$-RC”). This alternative can eliminate $6k \pm 1$ harmonics in *abc* and internal stability is guaranteed.

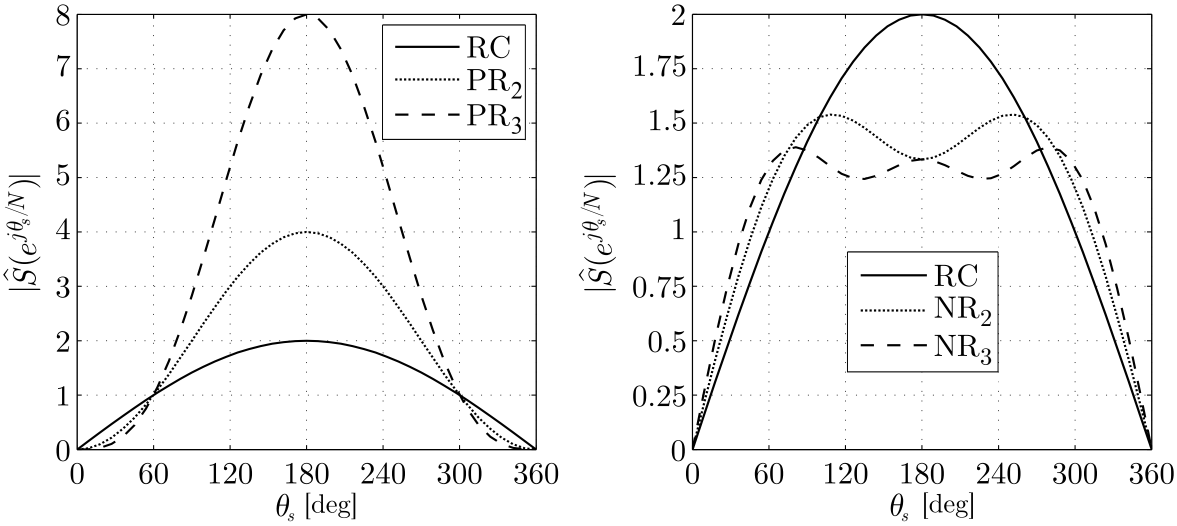

Figure 4.28: (left) $|\hat{S}(e^{j\theta_s/N})|$ for a second- and a third-order PR-RC and (right) for a second- and a third- order NR-RC.

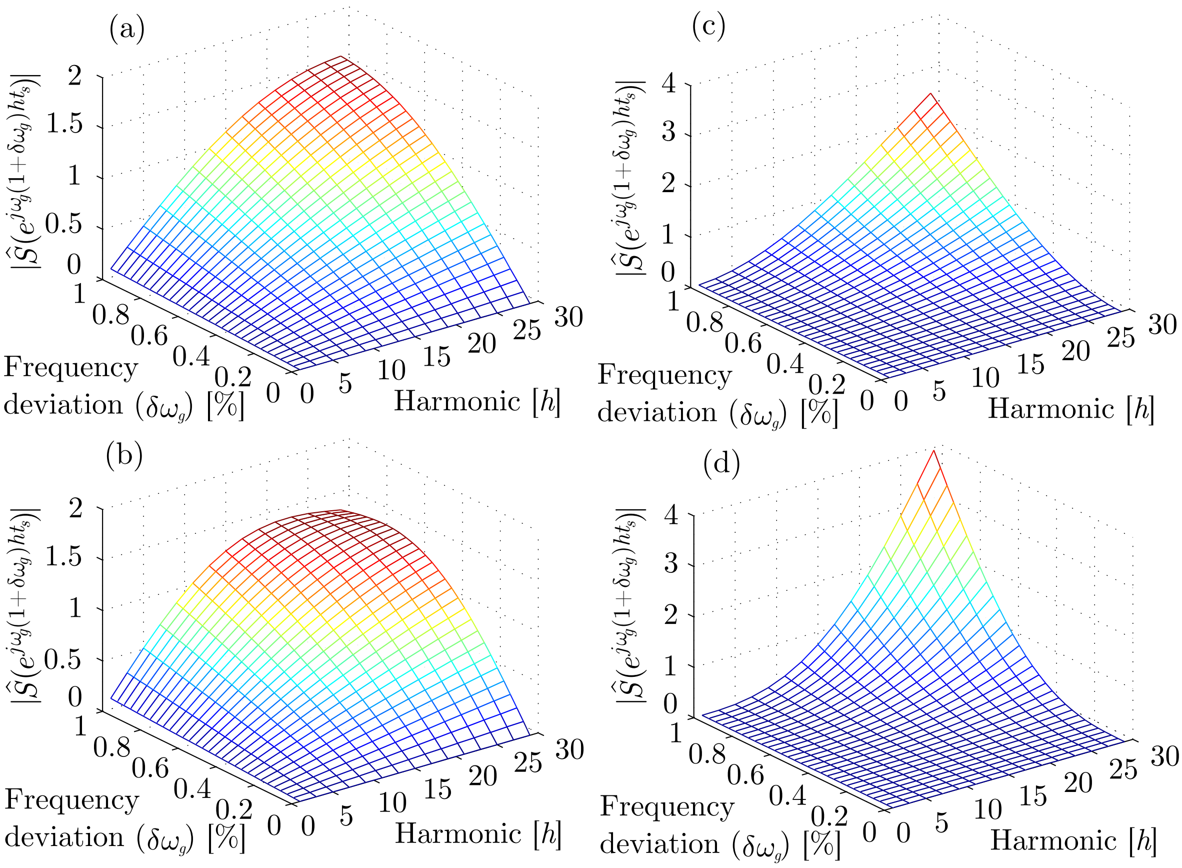

Figure 4.29: $|\hat{S}(e^{j\theta_s/N})|$ for (a) a second-order NR-RC, (b) a third-order NR-RC, (c) a second-order PR-RC, and (d) a third-order PR-RC. Notice that the vertical scales are different. PR means PR-RC and NR means NR-RC.

4. A $nk \pm m$-RC in $\alpha\beta$ with $n = 6$ and $m = 1$ ($6k \pm 1$ harmonics in abc). $Q(z)$ is selected with $M = 10$ and $\omega_c = 1200$ Hz to ensure that all the transfer functions are proper ($N/n > M + C + L$).

5. A second-order PR-RC with $K_x = 0.8$ (which is within the limits provided in Table 4.5), while the rest of the parameters are similar to those of the RC.

6. A second-order NR-RC with similar design parameters of those of the RC.

RC Alternatives Performance

Fig. 4.30 shows the steady-state performance when applying the proposed RC alternatives with and without $L(z)$ (first-order Padé in all cases) and $\delta\omega_g = 0.5$ %. The EVEN- and the ODD-RC lead to similar results with and without frequency deviation and both behave better than a classical RC when the frequency deviates (THD = 4.7 % compared to THD = 5.6 %). If $L(z)$ is applied, both alternatives provide similar results (THD = 0.9 %).

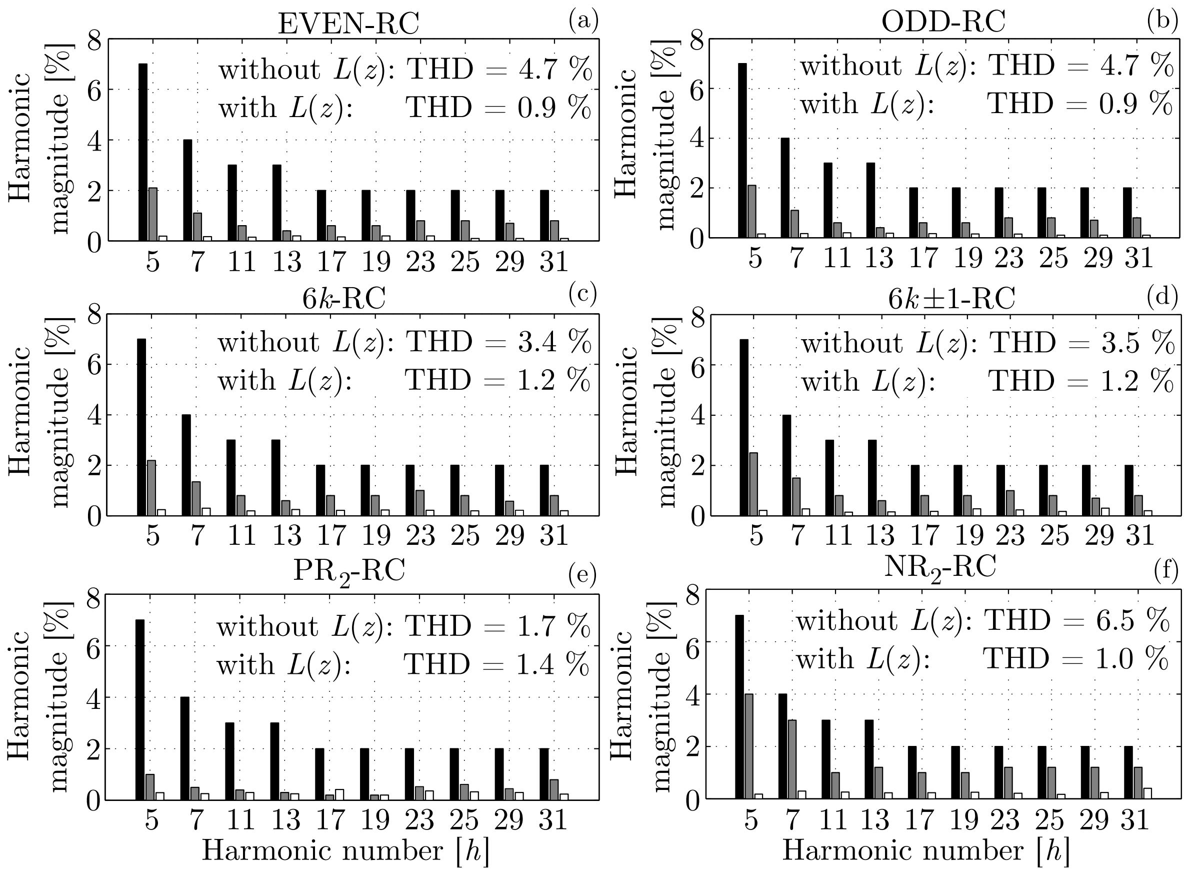

Figure 4.30: Harmonic magnitudes for the RC alternatives. (black) Grid voltage, (grey) load voltage without $L(z)$ and (white) load voltage with $L(z)$. $\delta\omega_g = 0.5$ %.

With the $6k$-RC and the $6k \pm 1$-RC the harmonics are reduced (THD = 1.2 % using $L(z)$), but less than with the RC because not all positive an negative sequences of the harmonics are eliminated. For instance, only the negative sequence of the 5th harmonic is eliminated, but not the positive sequence.

The PR-RC results are also displayed in Fig. 4.30. The performance is reasonable without $L(z)$, and improves when $L(z)$ is used. However, the THD is 1.4 % because noise is amplified. The NR-RC performance is very poor when there are frequency variations and, if $L(z)$ is applied, the harmonic attenuation is worse than with any of the other alternatives (THD = 1 %), but still within IEC limits.

Fig. 4.31 illustrate the transient responses when RCs are switched on. The ODD- and the EVEN-RC behave similarly and harmonics are rejected in $t = 0.05$ s. The transient of the $6k \pm 1$-RC is faster than those of the ODD- and the EVEN-RC ($t = 0.05$ s). However, the $6k$-RC is the fastest alternative ($t = 0.02$ s). The PR-RC is fast, but very oscillating and it, clearly, amplifies noise. Finally, the transient response of the NR-RC is the slowest one ($t = 0.2$ s).

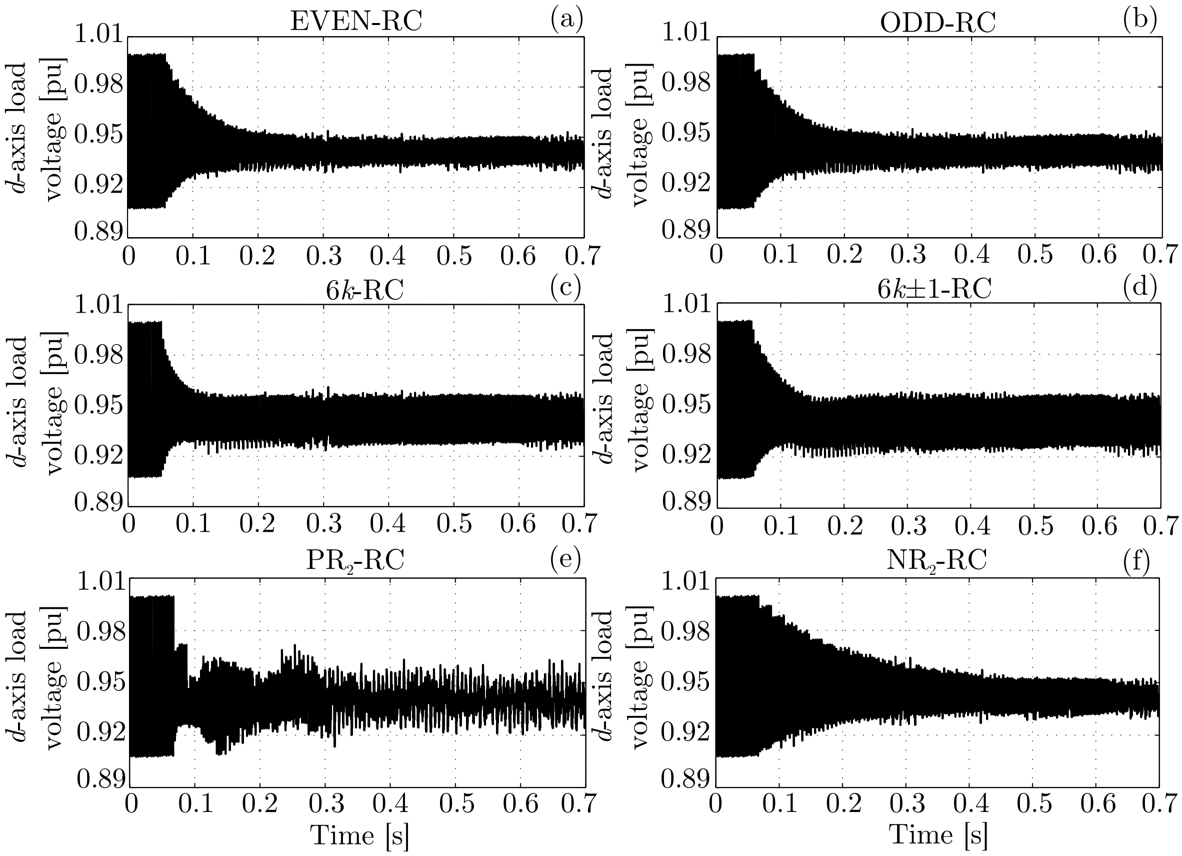

Figure 4.31: d-axis load voltage when RCa are turned on using an ODD-RC, an EVEN-RC, a $6k$-RC, a $6k \pm 1$-RC, a PR_2-RC, and a NR_2-RC.

4.10 Chapter Summary

This chapter has presented the application of a RC to an SAC. First of all, a detailed analysis of RCs has been developed. Secondly, digital implementation problems of RCs have been solved: this is the main contribution of this chapter. Frequency deviation is solved using a novel strategy that greatly improves RCs performance without jeopardizing stability. Meanwhile, internal instability when RCs are applied to systems that filter out DC signals has been studied and solved. All the contributions were tested in the SAC prototype, showing excellent performance. The results presented in this chapter show that an SAC can compensate voltage sags, voltage imbalances, and voltage harmonics at the same time with a fast transient response.

In the second part of this chapter several RC alternatives were designed and tested in the prototype. This part shows the versatility of the tools developed in the first part of this chapter because they can be used to analyse any type of RC. All the RC alternatives were tested in the prototype for analysis and comparison.

Chapter 5

Revisiting Proportional-Resonant Controllers

This chapter revisits the application of proportional-resonant controllers (PRCs) for PE devices. Section 5.1 explains PRCs basics and Section 5.2 presents a new method to design high-performance PRCs. Section 5.3 analyses the steady-state error caused by frequency variations, while Section 5.3.3 proposes an innovative method to adapt PRCs when the grid frequency varies slightly. Section 5.4 gives a number of experimental results and Section 5.5 deals with large grid-frequency variations. Section 5.6 investigates the connection between PRCs and repetitive controllers (RCs) and, finally, Section 5.7 summarises the main results of this chapter.

5.1 Proportional-Resonant Controllers Overview

The application of the IMP reveals that a controller should contain poles at $s = \pm j\omega_g h$ to track (reject) a sinusoidal signal of frequency $h\omega_g$ [182]. A transfer function that contains the required poles (using Laplace transform) is [163]:

$$PR'_h(s) = K_h \frac{N'_h(s)}{s^2 + (\omega_g h)^2}, \tag{5.1}$$

where $N'_h(s)$ is a compensator and K_h is a constant number. For a general periodic signal of period t_p, the controller should include poles at all the harmonic frequencies. This can be done paralleling many transfer functions like (5.1):

$$PR'(s) = \sum_{h=1}^{\infty} PR'_h(s) = \sum_{h=1}^{\infty} K_h \frac{N'_h(s)}{s^2 + (\omega_g h)^2}. \tag{5.2}$$

This type of controllers are usually referred as “proportional-resonant controllers” (PRCs) in the literature or, alternatively, “selective controllers”. The DC component

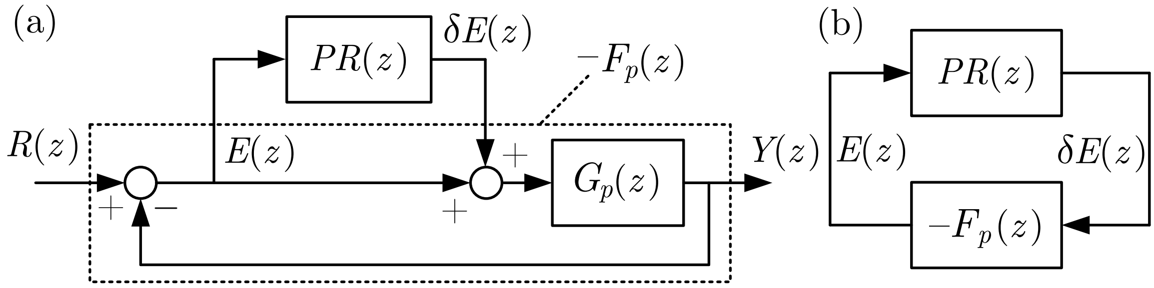

Figure 5.1: (a) Implementation of PRCs as a plug-in and (b) equivalent system to study closed-loop stability.

of the generic periodic signal has not been included in (5.2) because it is usually addressed using a PI controller, directly. For discrete-time systems the poles of (5.2) are transformed into its z-domain equivalent, yielding

$$PR(z) = \sum_{h=1}^{\infty} PR_h(z) = \sum_{h=1}^{\infty} K_h \frac{N_h(z)}{z^2 - 2\cos(\omega_g h t_s)z + 1}. \tag{5.3}$$

Generally, PRCs should not be discretised using classical methods (e.g. Tustin) because precision may deteriorate and closed-loop stability might be threatened [24].

5.1.1 Stability Assessment with PRCs

Fig 5.1 (a) shows the block diagram of a typical closed-loop system with PRCs applied in a plug-in configuration. From now on, PRCs are applied using this configuration due to the reasons that will be clarified through the rest of the chapter. If $R(z) = 0$, this block diagram can be simplified to the one in Fig. 5.1 (b), so stability can be studied with the following open-loop transfer function:

$$G(z) = PR(z)F_p(z), \tag{5.4}$$

with $F_p(z) = G_p(z)/(1 + G_p(z))$. Fig. 5.2 (a) shows the Nyquist diagram of $G'(s)$ assuming $h = 1$, $N_1'(s) = \omega_g s$, and $F_p'(s) = 1$ (continuous-time equivalents of $G(z)$, $N_1(z)$, and $F_p(z)$). In this case, there are two phase-margins, namely, ϕ_m^+ and ϕ_m^-, and both are equal to $\pi/2$ rad. Fig. 5.2 (b) shows the Nyquist diagram when $F_p'(s) = e^{j\phi_h^p}$ (constant phase-delay). It shows that ϕ_m^+ increases while ϕ_m^- decreases as the plant phase (ϕ_h^p) approaches to $-\pi/2$ rad. Therefore, the phase lag produced by the open-loop transfer function should always be compensated to ensure good stability margins.

If $F_p(z)$ has no unstable poles, closed-loop stability can be fully assessed with the stability margins of $G_p(z)$. This condition is always fulfilled here because $F_p(z)$ is a closed-loop stable system. Fig. 5.3 shows the open-loop frequency response of a plant with PRCs in plug-in configuration. The phase margins (ϕ_m^h) are obtained when

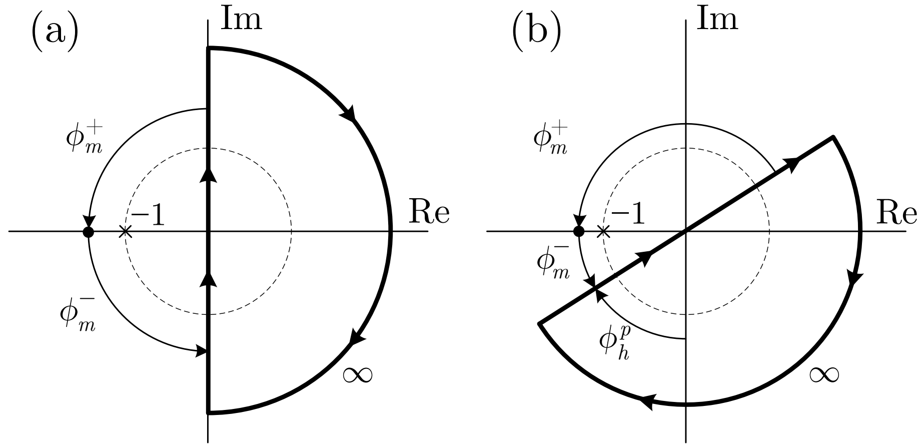

Figure 5.2: Nyquist diagram of a PRC (a) with $h = 1$, $N_1'(s) = s\omega_g$, and $F_p'(s) = 1$, and (b) with $F_p'(s) = e^{j\phi_h^p}$ (constant delay).

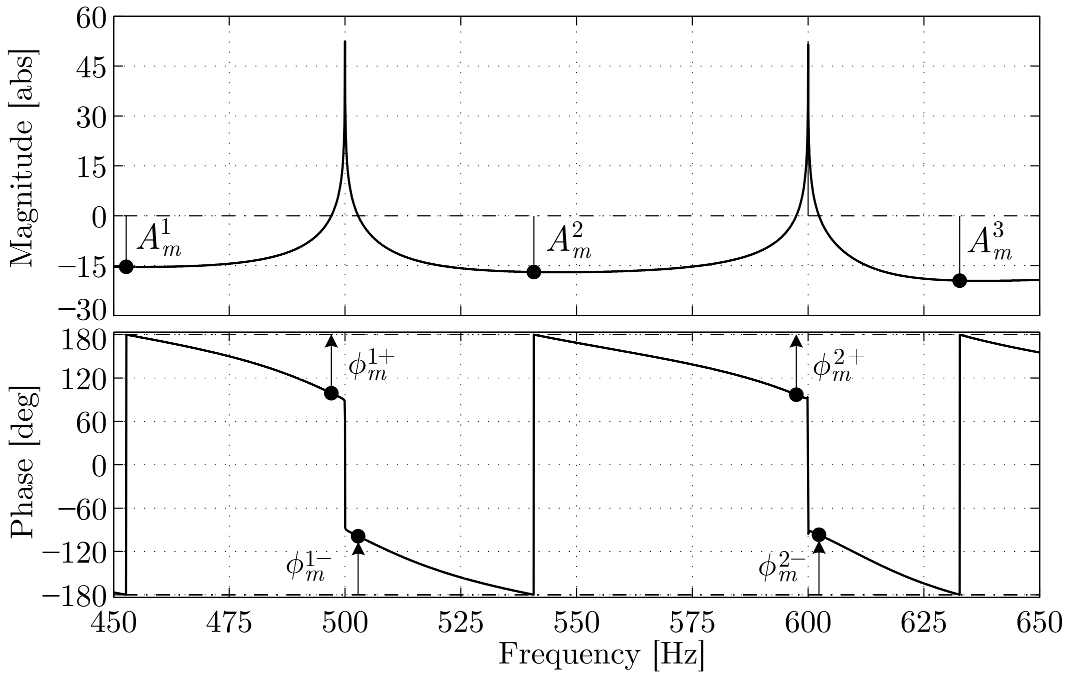

Figure 5.3: Bode diagram of the open-loop transfer function of a system with PRCs. The phase margins are ϕ_m^{h+} and ϕ_m^{h-}, while the gain margins are A_m^h in dB.

$|G(e^{j\omega t_s})| = 1$ (see phase plot), while the gain margins (A_m^h) are computed making $\angle G(e^{j\omega t_s}) = \pm\pi$ rad (see the magnitude plot). A system with PRCs may have several stability margins, as shown in Fig. 5.3, and stability is assessed with the worst one.

Generally, the design of each single PRC is carried out without taking into account the rest of PRCs because $N_h'(s)$ in (5.1) is typically designed to have almost zero magnitude for all frequencies except close to its own resonant frequency [163]. Therefore, the open-loop transfer function to be investigated can be rewritten as follows:

$$G(z) = \sum_{h=1}^{n} G_h(z) = \sum_{h=1}^{n} PR_h(z) F_p(z), \tag{5.5}$$

where $G_h(z)$ is the individual open-loop transfer-function of a PRC in series with $F_p(z)$. The compensator $N_h(z)$ in (5.3) is designed to ensure zero phase at the resonance frequency. In other words, $N_h(z)$ compensates the phase of $G_h(z)$ at the resonant frequency. Therefore, the 180-degree phase jump generated by the complex poles will take place between 90 and -90 degrees (see Fig. 5.3) and $\phi_m^+ \approx \phi_m^-$. Besides, the gain margins have to be tuned adjusting the values of K_h although, in this case, each PRC can not be studied separately because gain margins are typically found in frequencies in between resonant poles. Therefore, each gain margin may be affected by several PRCs.

5.2 A New Proposal to Design Discrete-Time PRCs

5.2.1 Overview of the Design Method

First of all, the PRC core has to be selected. A derivative term and a normalisation factor (η_h) can be added to the core to achieve a band-pass effect:

$$PR_h^r(z) = \frac{\eta_h(z-1)}{z^2 - 2\cos(\omega_g h t_s) z + 1}, \tag{5.6}$$

and a compensator, called $PR_h^c(z)$, can be also added to (5.6), yielding

$$PR_h(z) = PR_h^c(z) PR_h^r(z) = \underbrace{\beta_h(\alpha_h z + 1)}_{PR_h^c(z)} PR_h^r(z). \tag{5.7}$$

The compensator parameters (α_h and β_h) will be calculated in subsequent sections taking into account the frequency response of $F_p(z)$ and, as will be shown, the open-loop phase lead at the resonant frequency can be set arbitrarily. Furthermore, the design of the harmonic controller can be simplified to a single parameter if the PRCs are designed to compensate not only the phase of $F_p(z)$ but also its magnitude.

5.2.2 Core Normalisation

If the core is selected like in (5.6), η_h can be calculated so that all PRCs produce the same amplification in the surroundings of their resonant frequency. A non-ideal core can be written as:

$$PR_h^r(z) = \frac{\eta_h(z-1)}{z^2 - 2a\cos(\omega_g h t_s) z + a^2}, \tag{5.8}$$

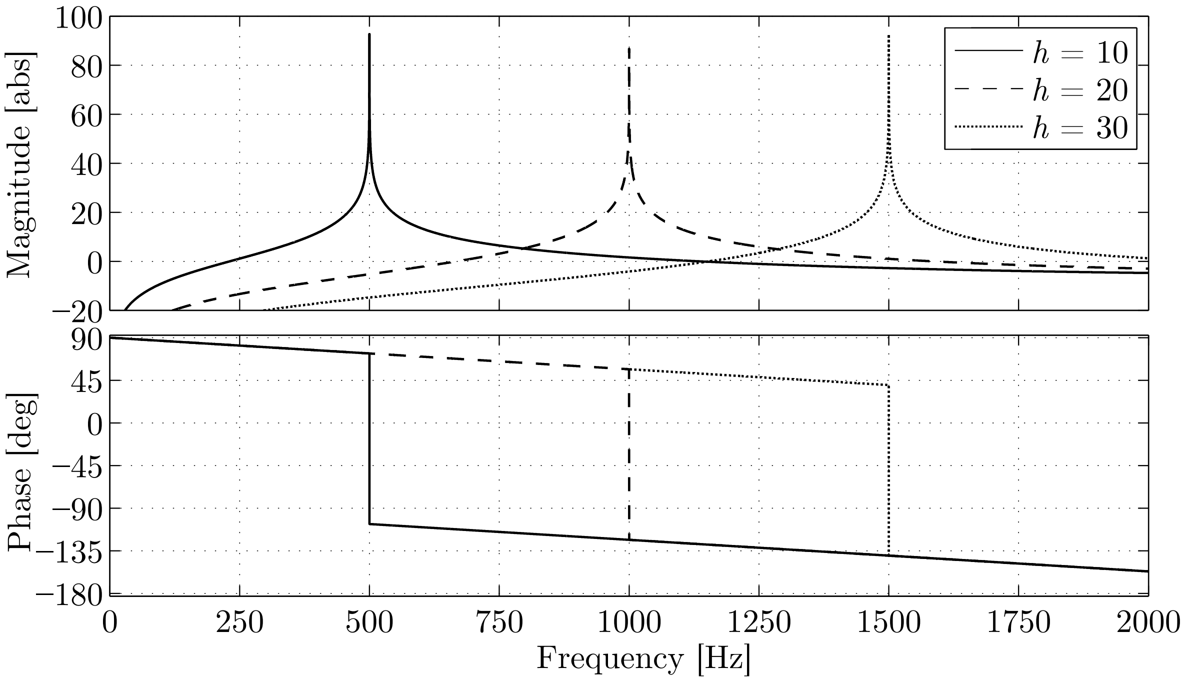

Figure 5.4: Frequency response of (5.6) for $\omega_g = 2\pi 50$ rad/s, $t_s = 1/5400$ s and $h = 10$, 20, and 30 ($a = 1$).

where a is the damping coefficient ($0 < a < 1$). The frequency response of (5.8) at $\omega_g h$ is

$$PR_h^r(e^{j\omega_g h t_s}) = \left(\frac{1}{1-a}\right)\frac{\eta_h \sin(\omega_g h t_s/2)}{\cos(2\omega_g h t_s) - a + j\sin(2\omega_g h t_s)}. \tag{5.9}$$

If $a \approx 1$ in (5.9), $\cos(2\omega_g h t_s) - a \approx \cos(2\omega_g h t_s) - 1$ and (5.9) can be simplified to

$$\left|PR_h^r(e^{j\omega_g h t_s})\right| \approx \left(\frac{1}{1-a}\right)\frac{\eta_h \sin(\omega_g h t_s/2)}{2\sin(\omega_g h t_s)} = \left(\frac{1}{1-a}\right)\eta_h \frac{1}{4\cos(\omega_g h t_s/2)}. \tag{5.10}$$

Therefore, the value of η_h that provides a similar amplification for each one of the PRCs at their resonant frequency is

$$\eta_h = 4\cos(\omega_g h t_s/2), \text{ which implies that } \left|PR_h^r(e^{j\omega_g h t_s})\right| = \left(\frac{1}{1-a}\right). \tag{5.11}$$

Fig. 5.4 shows the frequency response of three PRCs like (5.6) with $\eta_h = 4\cos(\omega_g h t_s/2)$. The PRCs are tuned at $h = 10$, 20, and 30, with $\omega_g = 2\pi 50$ rad/s and $t_s = 1/5400$ s. Notice that the controller amplification close to $h\omega_g$ does not depend on h anymore.

5.2.3 Parametrization and Design Conditions

The harmonic controller is written as

$$PR(z) = \sum_{h=1}^{n} PR_h(z) = \sum_{h=1}^{n} \frac{K_h \eta_h \beta_h (\alpha_h z + 1)(z-1)}{z^2 - 2\cos(\omega_g h t_s) z + 1}, \tag{5.12}$$

where n is the highest harmonic to be eliminated. Hence, the open-loop frequency-response of $G_h(z)$ at the resonance frequency is

$$\underbrace{(A_h^g e^{j\phi_h^g})}_{G_h(e^{j\omega_g h t_s})} = \underbrace{(A_h^c e^{j\phi_h^c})}_{PR_h^c(e^{j\omega_g h t_s})} \cdot \underbrace{(A_h^r e^{j\phi_h^r})}_{PR_h^r(e^{j\omega_g h t_s})} \cdot \underbrace{(A_h^p e^{j\phi_h^p})}_{F_p(e^{j\omega_g h t_s})} . \tag{5.13}$$

From (5.13):

$$\phi_h^g = \phi_h^c + \phi_h^r + \phi_h^p. \tag{5.14}$$

Consequently, ϕ_h^c at $\omega_g h$ can be chosen adjusting α_h and β_h in (5.7) to modify the phase of the open-loop transfer function (ϕ_h^g).

5.2.4 Designing the Compensator Parameters

Assuming $0 < a < 1$, the phase-delay of $PR_h^r(z)$ at $\omega_g h$ is

$$\phi_h^r = -\omega_g h t_s/2. \tag{5.15}$$

If $F_p(z)$ is stable (always the case for a plug-in implementation), making the phase of the open-loop transfer function equal zero for $\omega_g h$ seems to be a good choice because, in this case, $\phi_m^- \approx \phi_m^+$:

$$0 = \phi_h^p + \phi_h^c - \omega_g h t_s/2, \text{ which implies that } \phi_h^c = -\phi_h^p + \omega_g h t_s/2. \tag{5.16}$$

The value of α_h and β_h in $PR_h^c(z)$ must be computed for each harmonic to satisfy the design conditions (ϕ_h^c and A_h^c). Therefore, the following equality can be written:

$$A_h^c e^{j\phi_h^c} = \beta_h \left(\alpha_h e^{j\omega_g h t_s} + 1\right), \tag{5.17}$$

and solving for α_h and β_h:

$$\alpha_h = \frac{\sin(\phi_h^c)}{\sin(\omega_g h t_s - \phi_h^c)}, \quad \beta_h = A_h^c \frac{\sin(\omega_g h t_s - \phi_h^c)}{\sin(\omega_g h t_s)}. \tag{5.18}$$

Taking ϕ_h^c to (5.18) and forcing $A_h^c = 1$ the compensator provides a phase delay of ϕ_h^c at $\omega_g h$, but without modifying the amplification of the controller. This approach provide a phase lead equal to the one proposed by Yepes et al. [24] but, in this case, the magnitude of the compensator can be chosen. A coherent approach is to compensate not only the phase delay of $F_p(z)$ but also the magnitude by setting $A_h^c = 1/A_h^p$ (see (5.13)). Therefore, the compensator provides a single-point approximation of the inverse frequency-response of the plant. These two alternatives (with and without magnitude inversion) will be discussed in detail in the following subsections and they are characterised as follows:

$$\beta_h^1 = \frac{\sin\left(\omega_g h t_s - \phi_h^c\right)}{\sin\left(\omega_g h t_s\right)},\ \beta_h^2 = \frac{1}{A_h^p}\frac{\sin\left(\omega_g h t_s - \phi_h^c\right)}{\sin\left(\omega_g h t_s\right)}. \tag{5.19}$$

Finally, the value of K_h in each PRC may be tuned independently to improve either performance or stability margins. The following sections will show that the same value of K_h in each PRC ($K_h = K,\ \forall h$) produces high-performance controllers, thus reducing the whole design process to the selection of a single value.

5.2.5 Singular Values of the Compensator Parameters

As noticed by Yepes et al. [24], a discrete-time compensator might have singular solutions where the plant phase delay can not be compensated. For the proposed compensator, singular values can be calculated analysing (5.18). The value of α_h becomes singular when $\phi_h^c = 0$, $\phi_h^c = \pi$ ($\alpha_h = 0$), or when

$$\sin(\omega_g h t_s - \phi_h^p) = 0,\ \text{which implies that}\ \phi_h^c = \omega_g h t_s\ \text{and forces}\ \alpha_h = \infty. \tag{5.20}$$

The value of β_h also becomes singular when (5.20) is met and when $\omega_g h t_s = 0$ or $\omega_g h t_s = \pi$. The last two cases correspond to zero and Nyquist frequency, respectively, and they can be ignored. In any case, the open-loop phase delay can not be exactly compensated if the phase yields a singular solution. To avoid these cases one can (a) select the sampling period (t_s) to avoid them, which may be impossible if t_s is imposed, or (b) do not compensate the plant phase delay exactly in these cases using $\phi_h^c + \epsilon$, where ϵ is a small value. As long as the phase margins will be close to $\pi/2$ rad a small variation in the open-loop phase will be negligible and, consequently, strategy the second option above is more interesting because it is simpler.

5.3 Grid-Frequency Changes

5.3.1 Steady-State Error when the Grid-Frequency Changes

The denominator of each PRC contains the term $2\cos(\omega_g h t_s)$ in the z-domain, which gives a resonant frequency of $\omega_g h$ in the time domain. If the grid frequency deviates from its nominal value the PRCs will not be tuned to the harmonic frequencies causing a steady-state error. One can write the z-domain reference-to-error transfer function in 5.1 to quantify this effect:

$$F_e(z) = \frac{1}{1+G_p(z)} \underbrace{\frac{1}{1+PR(z)F_p(z)}}_{S(z)}, \tag{5.21}$$

When the frequency deviates the error is $|F_e(e^{j\omega_g(1+\delta\omega_g)ht_s})|$, where $\delta\omega_g$ is the frequency deviation in per-unit values and, ideally, $|F_e(e^{j\omega_g(1+\delta\omega_g)ht_s})| = 0\ \forall h$. Alternatively, the error can be assessed with $|S(e^{j\omega_g(1+\delta\omega_g)ht_s})|$. In this case, the effects of $G_p(z)$ on the error are not included and the contribution of the PRCs can be understood more easily.

5.3.2 Using Taylor Polynomials to Adapt the Controller

A different value of $2\cos(\omega_g h t_s)$ has to be used in each controller with the actual value of the frequency to eliminate the steady-state errors. This is computationally expensive because trigonometric functions are required. Look-up tables can be used as well, but in this case a lot of coefficients have to stored since precision is a key issue when computing $2\cos(\omega_g h t_s)$. To overcome this problem, Yepes et al. [211] uses Taylor polynomials:

$$\cos(\omega_g h t_s) = 1 - C_h, \tag{5.22}$$

with

$$C_h = \frac{2}{t_s^2} \sum_{i=1}^{m/2} \frac{(-1)^{i+1}(h\omega_g t_s)^{2i}}{(2i)!}, \tag{5.23}$$

where m is the order of the Taylor polynomial that should be selected depending on the application and the order of the harmonic to be tackled. For low-frequency applications $m = 4$ is normally enough, but for higher-order harmonics 6th- or 8th-order polynomials may be needed.

5.3.3 Application of Chebishov Polynomials

Chebishov polynomials can be used as an alternative to Taylor polynomials. An interesting property of the first-kind Chebishov polynomials is [212]:

$$T_h\left(\cos\left(\omega_g t_s\right)\right) = \cos\left(\omega_g h t_s\right)\ \forall h \in \mathbb{N}, \tag{5.24}$$

where $T_h(x)$ stands for the hth-order first-kind Chebyshov polynomial. So, if $\cos\left(\omega_g t_s\right)$ is known, $\cos\left(\omega_g h t_s\right)$ can be computed with (5.24).

The polynomial coefficients need to be calculated beforehand and stored in the DSP memory to apply (5.24). Nevertheless, the recursive form of Chebishev polynomials is very convenient to simplify this task because [212]

$$T_h(x) = 2xT_{h-1}(x) - T_{h-2}(x), \tag{5.25}$$

with $T_0(x) = 1$ and $T_1(x) = x$. If $x = \cos(\omega_g t_s)$ is taken to (5.25),

$$T_h(\cos(\omega_g t_s)) = 2\cos(\omega_g t_s)\, T_{h-1}(\cos(\omega_g t_s)) - T_{h-2}(\cos(\omega_g t_s)). \tag{5.26}$$

Therefore, $\cos(\omega_g h t_s)$ can be computed recursively if the value $\cos(\omega_g(h-1)t_s)$ and $\cos(\omega_g(h-2)t_s)$ were computed in previous iterations. For the initial iteration $h = 2$, giving $T_0(x) = 1$ and $T_1(x) = \cos(\omega_g t_s)$. For power electronics applications synchronised to the grid, $\cos(\omega_g t_s)$ is known in advance if the PLL is implemented using an oscillator. Therefore, no additional trigonometric functions are required. If $2\cos(\omega_g t_s)$ in (5.26) is computed only in the first iteration, the computation of each new cosine requires only 1 multiplication and 1 sum. Thereby, the number of operations is:

$$NC = 1 + 2n, \tag{5.27}$$

where NC is the total number of operations and n is the highest-order harmonic to be addressed.

5.3.4 Nesting Property of Chebyshov Polynomials

The nesting property of Chebishov polynomials can be applied to reduce even more the computational burden if not all the cosines are required (e.g. only odd or even numbers required, only multiples of 6 required, etc.) [212],

$$T_h(x) = T_{i \cdot m}(x) = T_i(T_m(x)). \tag{5.28}$$

First of all, $T_m(x)$ is computed. Secondly, (5.25) is replaced in (5.28), yielding

$$T_i(T_m(x)) = 2T_m(x) \cdot T_{i-1}(T_m(x)) - T_{i-2}(T_m(x)), \tag{5.29}$$

with $x = \cos(\omega_g t_s)$. To illustrate the procedure, consider that one needs to compute $\cos(\omega_g h t_s)$ for even values of h $(2, 4, 6, \ldots)$ up to n. First of all, one can set $m = 2$ and $i = 2, 3, \ldots, n/2$. Secondly, $T_{m=2}(\cos(\omega_g t_s))$ is computed using (5.25) and, subsequently, (5.29) can be used to compute the rest of the cosines. The iterative process in (5.29) starts with $i = 2$, yielding $T_0(T_m(\cos(\omega_g t_s))) = 1$ and $T_1(T_m(\cos(\omega_g h t_s))) = T_m(\cos(\omega_g t_s))$.

The computational burden required to compute all the cosines is

$$NC = m + 2n/m. \tag{5.30}$$

If n is large enough, the number of operations is approximately divided by m. Fig 5.5 (b) shows the implementation of the example above.

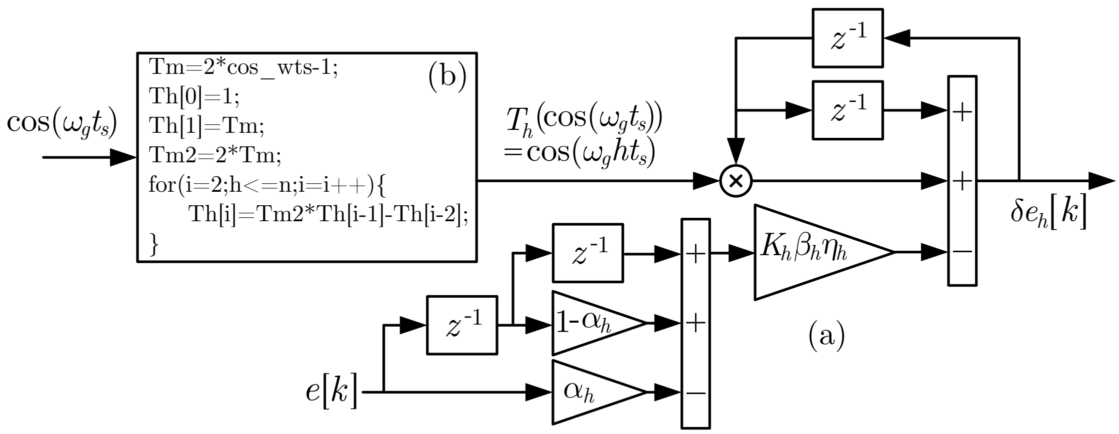

Figure 5.5: PRC implementation: (a) resonator and (b) frequency-adaptive mechanism.

5.4 Application of PRCs to an SAC

The control scheme used here is similar to the one in Fig. 4.13 (Chapter 4), but $RC(z)$ is replaced by $PR(z)$. The system parameters are in Appendix A. In this example, the SAC has been designed to compensate voltage sags, together with balanced and unbalanced harmonics of the supply, which are of frequencies $(2h \pm 1)\omega_g$ (in a three-phase description abc). Therefore, $PR(z)$ includes PRCs for even harmonics in dq-axis up to the 30th. Fig. 5.6 and Fig. 5.7 show the frequency response of $G(z)$ in (5.5) when the PRCs are designed using the two alternatives (β_h^1 and β_h^2) in (5.19). In both cases $K_h = K\ \forall h$ and the value of K has been set manually to have the smallest gain margin equal to 17 dB. Fig. 5.6 shows that the open-loop gain is affected by the frequency response of the plant. Therefore, for high-frequency PRCs the amplification is smaller, yielding higher gain margins. This strategy may be of interest if the model of the plant is not reliable at high frequency and the magnitude of the closed-loop frequency response decreases monotonically as frequency increases. This is clearly satisfied because $F_p(z)$ is the closed-loop transfer function of the plant with the main controller in place. On the contrary, Fig. 5.7 shows that the magnitude of the open-loop frequency response is hardly affected by the frequency response of the plant.

Fig 5.5 (a) shows the implementation of a PRC and Fig 5.5 (b) shows a brief C-code that has been used to compute the cosines. The value of $\cos(\omega_g t_s)$ is taken from the PLL and filtered with a second-order LPF with a cut-off frequency of 3 Hz.

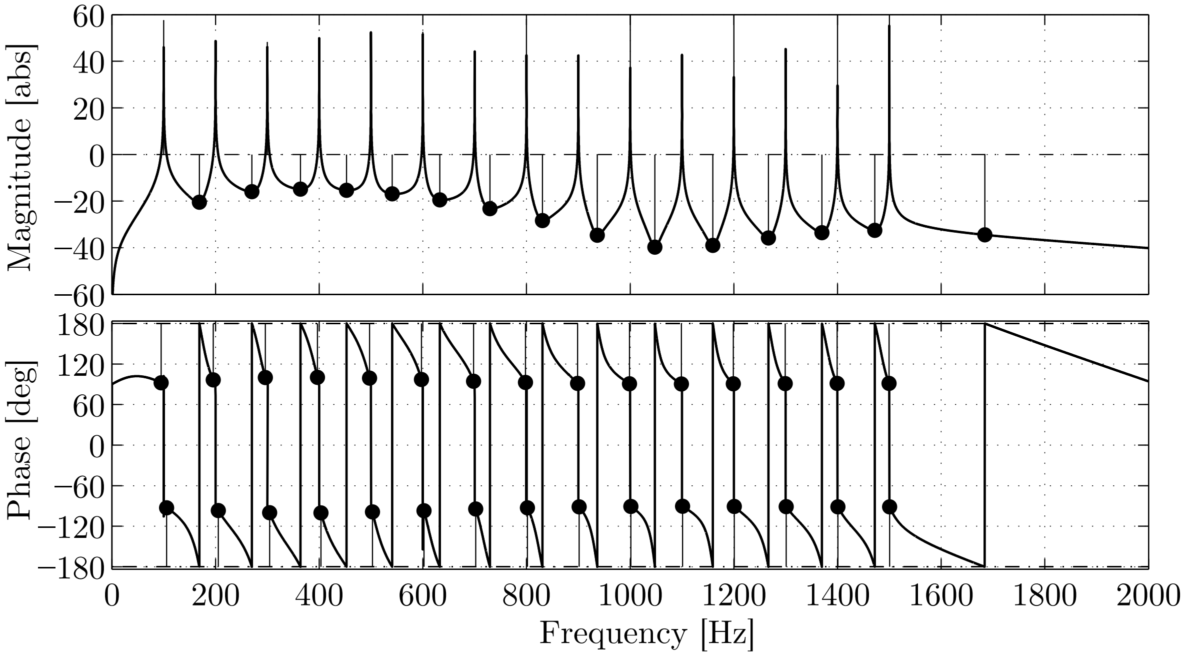

Figure 5.6: Frequency response of $G(z)$ with alternative β_h^1 and $K_h = K \; \forall \; h$.

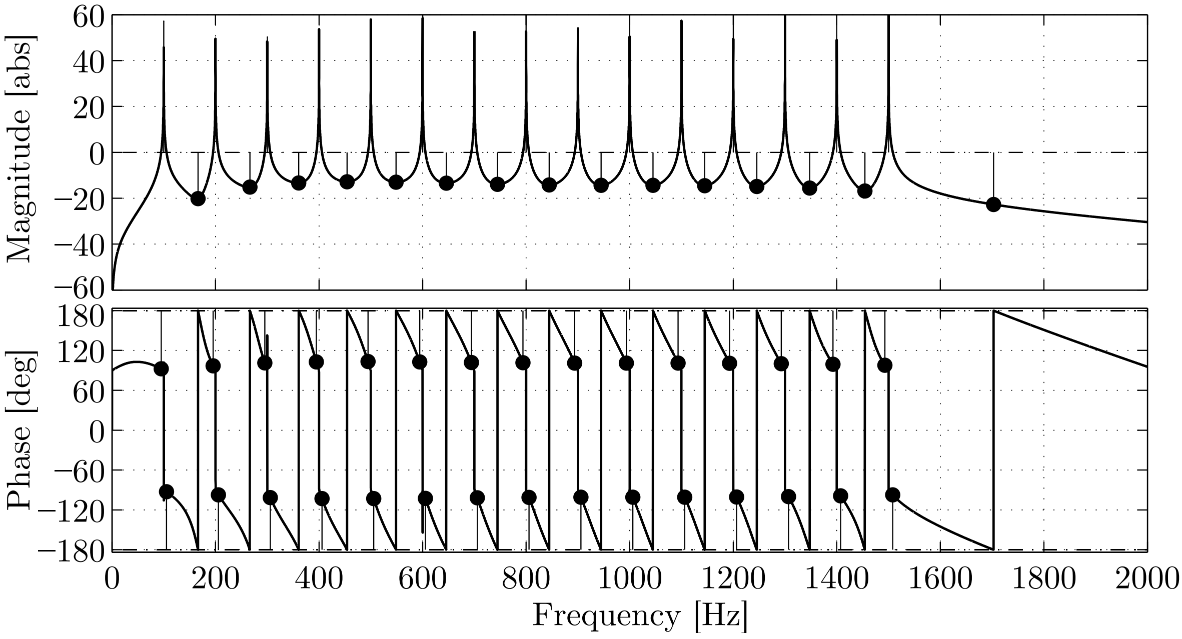

Figure 5.7: Frequency response of $G(z)$ with alternative β_h^2 and $K_h = K \; \forall \; h$.

Fig. 5.8 shows the frequency response of $G(z)$ when the design is carried out with β_h^1 and several values of K_{20} are used. The magnitude of the open-loop frequency response close to 1000 Hz greatly increases when K_{20} changes, while the magnitude at other frequencies is only modified slightly. Besides, only the gain margins related to that specific PRC are modified significantly.

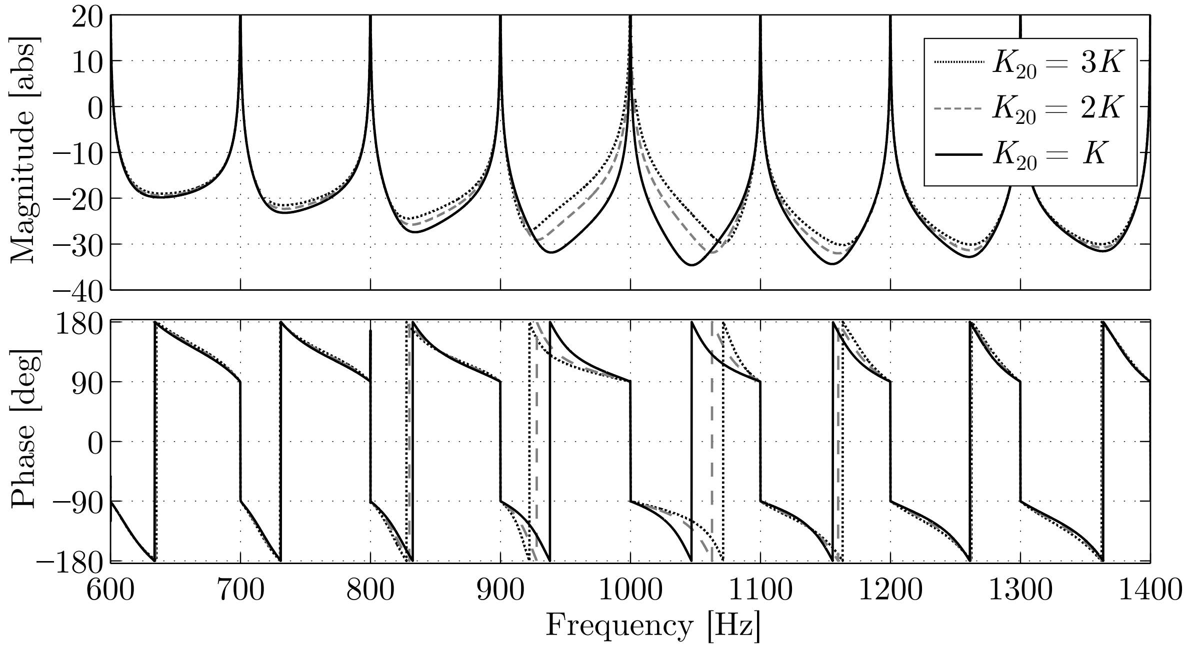

Figure 5.8: Frequency response of $G(z)$ when $K_{20} = K$, $K_{20} = 2K$, and $K_{20} = 3K$ (20th harmonic corresponds to 1000 Hz).

Transient and Steady-State Performance

Fig. 5.9 shows the d-axis error ($e_d(t)$) when the PRCs are switched on at $t = 0.2$ s using (a) β_h^1 and (b) β_h^2. The grid voltage has been contaminated with a number of harmonics. Both designs give a similar transient performance, although the design with β_h^2 is slightly faster because the gains obtained with this design are higher, especially for the high-frequency harmonics. All the results shown in this section and the following ones come from the experimental platform.

Fig. 5.10 shows the experimental results obtained when the SAC compensates a three-phase voltage sag and the PRCs are designed using β_h^1. At $t = 0$ ms the SAC is in steady-state, providing a clean load voltage. The voltage sag takes place at $t = 50$ ms. The SAC can compensate both the fundamental component and the harmonic components of the supply voltage. When the sag ends the SAC goes back to its initial state.

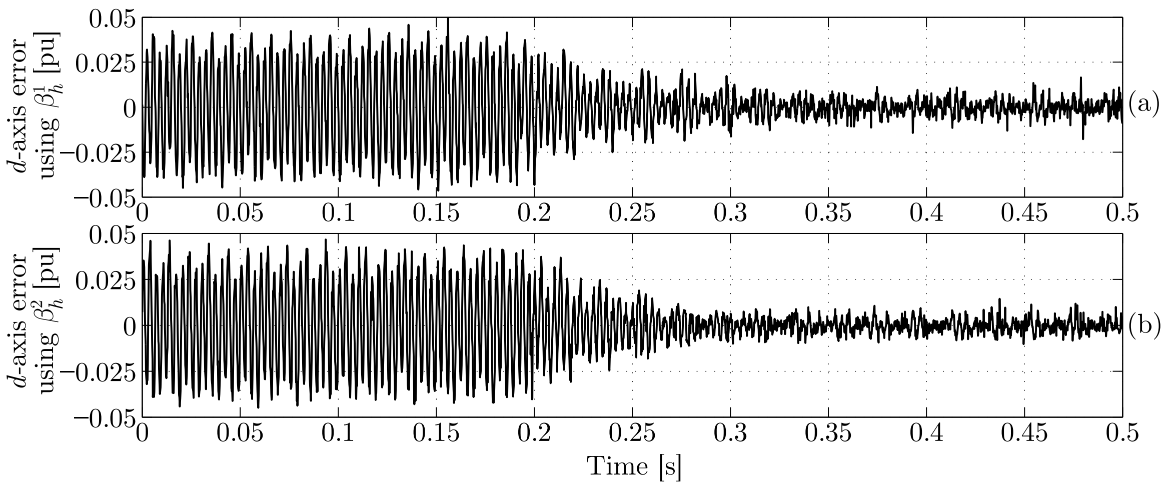

Figure 5.9: d-axis error when PRCs are turned on using (a) β_h^1 and (b) β_h^2.

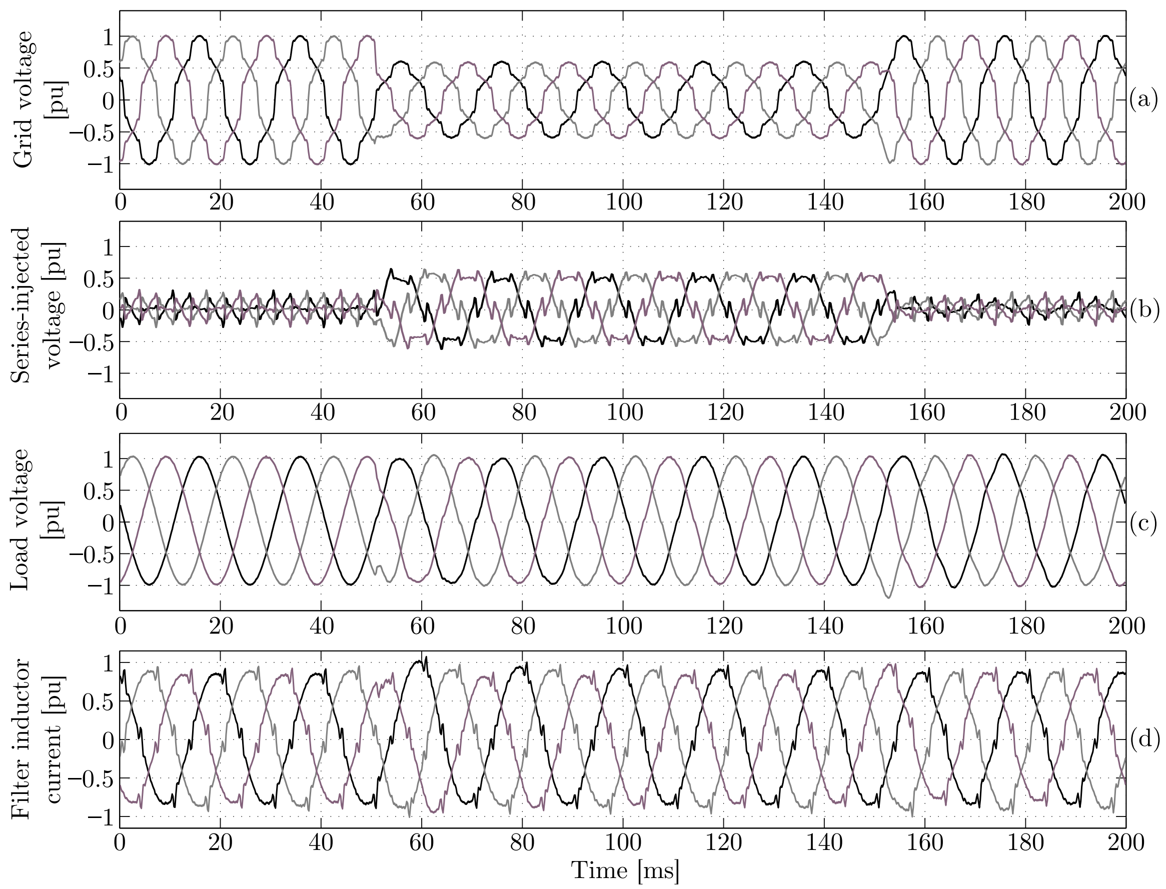

Figure 5.10: Sag and harmonic mitigation using PRCs (auxiliary) and a SF (main) controller.

Fig. 5.11 (left) shows the FFT of the grid and the load voltage at key frequencies in steady-state. For both designs the steady-state performance is similar and the THD of the load voltage is 0.71 %.

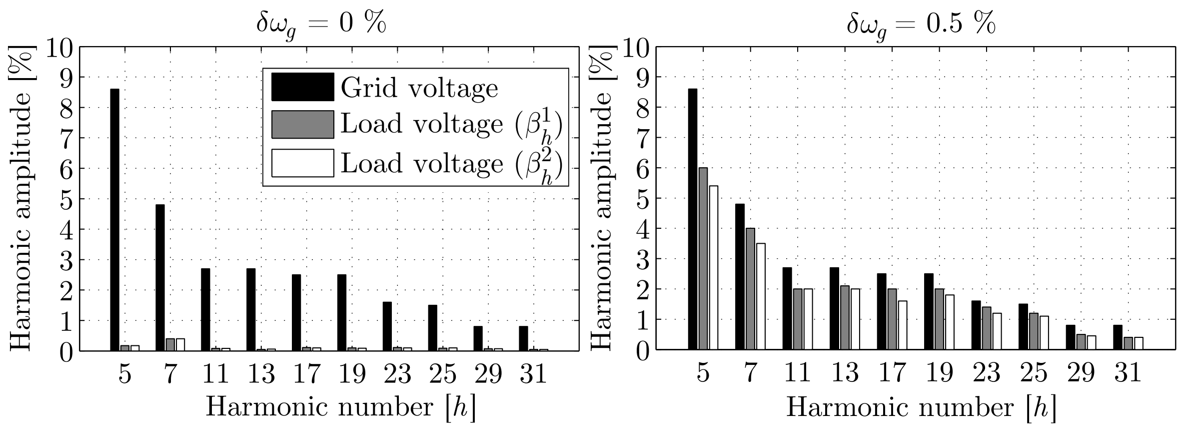

Figure 5.11: FFT of (black) the grid voltage and the load voltage using (grey) β_h^1 and (white) β_h^2. (left) No frequency deviation and (right) $\delta\omega_g = 0.5$ %.

Performance with Frequency Variations in the Grid Voltage

Fig. 5.12 shows $|S(e^{j\omega_g(1+\delta\omega_g)t_s})|$ for the design carried out with (a) β_h^1 and the one with (b) β_h^2. For low-order harmonics both designs lead to similar results, but the error rapidly increases for high-order harmonics when using β_h^1. Fig. 5.11 (right) shows the FFT of the load and the grid voltages calculated at key frequencies. The design accomplished using β_h^2 gives better results for small frequency variations. Summarising: the higher the gain is, the better the performance is, but stability margins deteriorate.

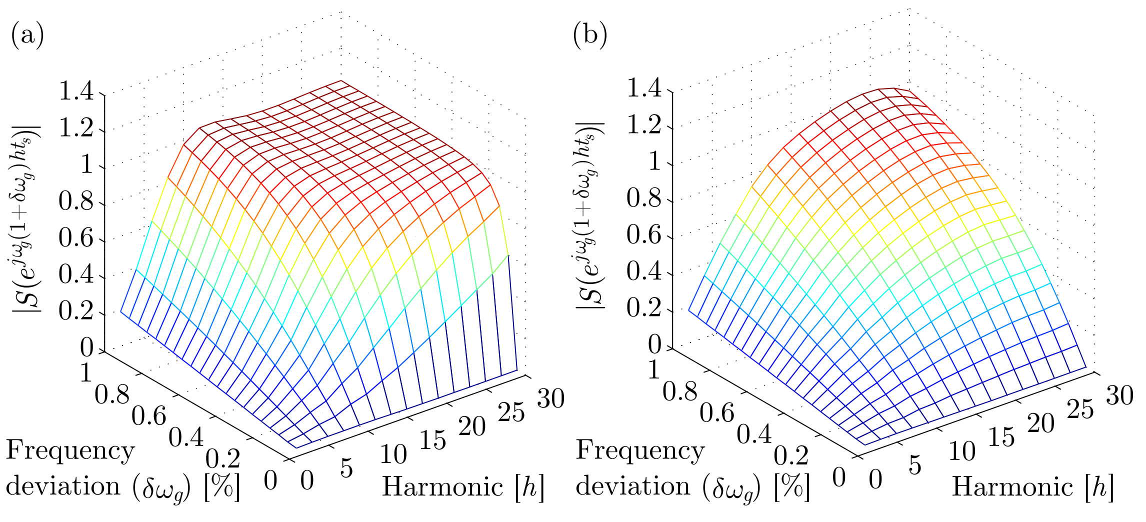

Figure 5.12: $|S(e^{j\omega_g(1+\delta\omega_g)ht_s})|$ with (a) β_h^1 and (b) β_h^2.

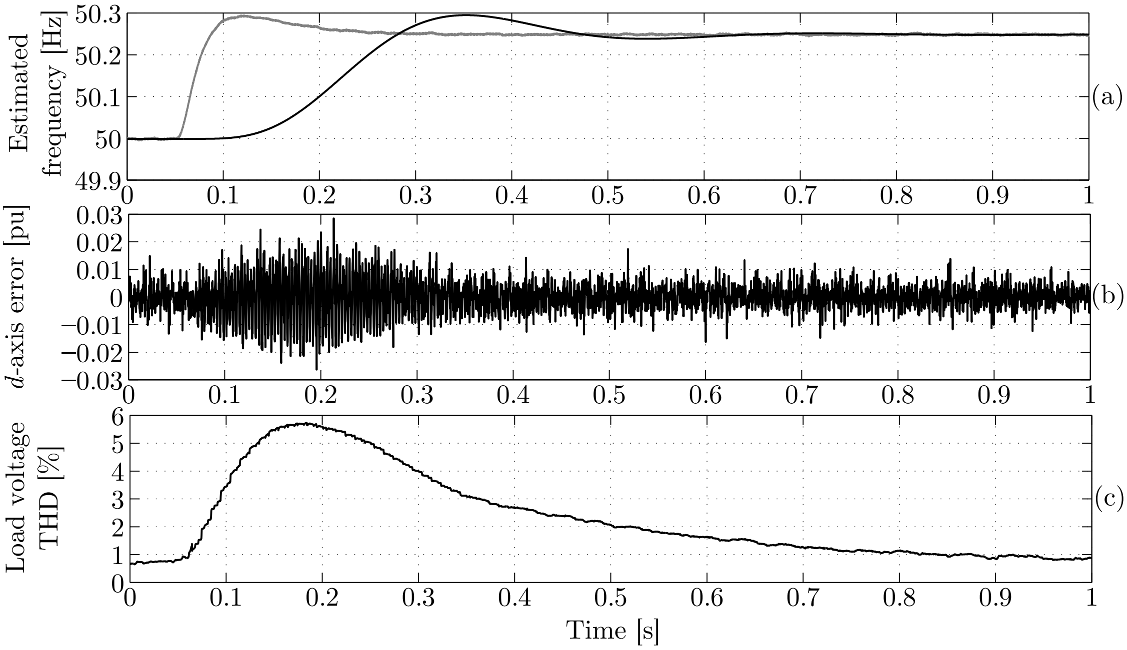

Figure 5.13: (a) (grey) PLL frequency and (black) filtered version of the PLL frequency, (b) d-axis error, and (c) load voltage THD for a step change in the grid frequency.

Fig. 5.13 shows the transient performance of the SAC when there is an abrupt change in the grid frequency. Initially, the THD of the load voltage deteriorates, but it returns to 0.7 % when the frequency is correctly estimated an updated in the PRCs.

Table. 5.1 shows the execution time (see Appendix A for more details) and the load voltage THD for the frequency-adaptive methods that have been tested with PRCs. Meanwhile, Fig. 5.14 shows the harmonic amplitudes recorded in a laboratory session. The base design (case (a), β_h^1) has a good performance when the design frequency exactly matches the grid frequency, but the performance deteriorates rapidly for small frequency variations. The PRCs based on a 2nd-order Taylor approximation of the cosine functions (case (d)) are not effective, even for low-order harmonics. Performance improves with higher-order approximations (4th, 6th, and 8th) but, unfortunately, computational burden also increases.

5.5 Performance with Large Frequency Variations

With the design approach explained in Section 5.3.3, the compensator is not modified when the grid frequency varies. Therefore, if there are large frequency fluctuations the proposed method to adapt the PRCs could lead to an unstable system. For instance, Fig. 5.15 shows the open-loop frequency response when $\delta\omega_g = 10$ % and the resonant poles are updated as previously mentioned. For low-order harmonics the phase-margins

PRC type	Ex. time	$THD_{0\%}$	$THD_{0.5\%}$	$THD_{1\%}$	$THD_{3\%}$
(a) Non-adaptive (β_h^1)	3.3 μs	0.7	5.6	7.2	7.0
(b) Chebishov ($m = 1$)	4.0 μs	0.7	0.7	0.7	0.7
(c) Chebishov ($m = 2$)	3.6 μs	0.7	0.7	0.7	0.7
(d) 2nd-order Taylor	3.8 μs	1.5	7.1	-	-
(e) 4th-order Taylor	5.0 μs	1.2	2.6	2.9	-
(f) 6th-order Taylor	6.2 μs	0.9	1.2	1.4	1.4
(g) 8th-order Taylor	7.3 μs	0.7	0.7	0.8	0.8

Table 5.1: Computational burden and THD using different RC adaptive mechanisms, for $\delta\omega_g = 0$, 0.5, 1, and 3 %. "-" means "unstable".

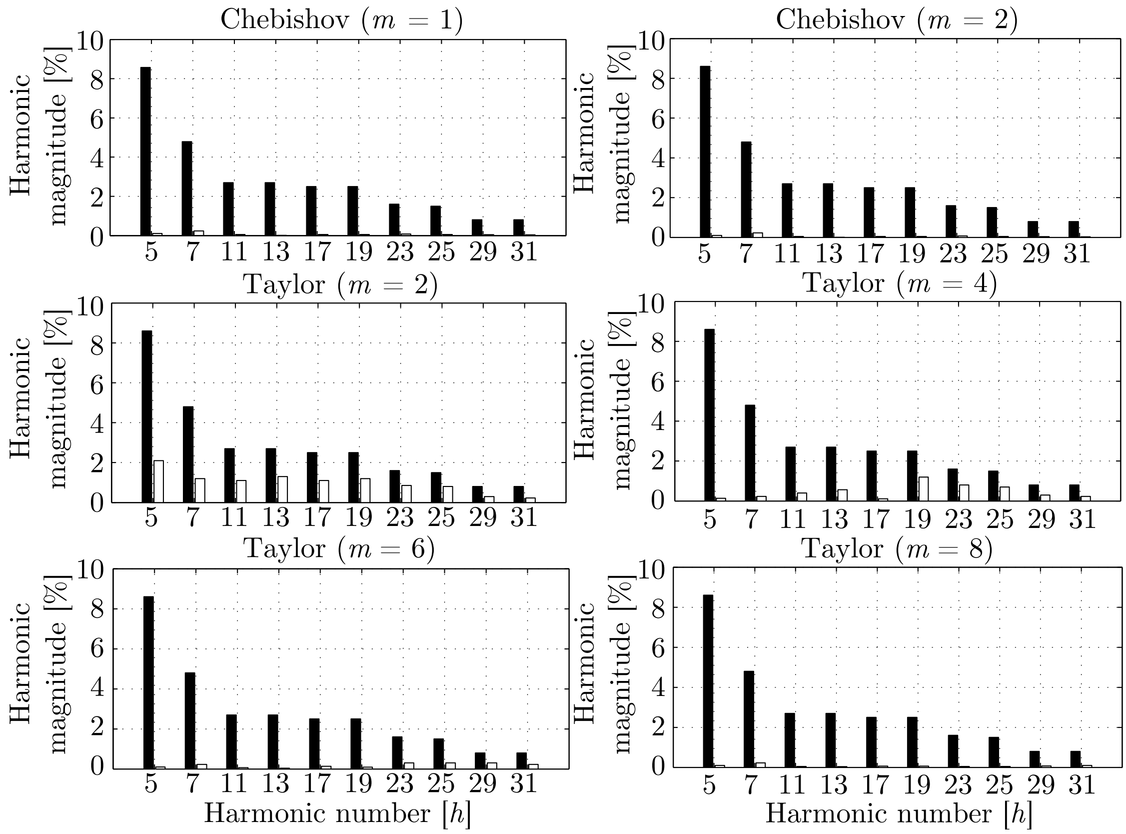

Figure 5.14: Load voltage FFT depicted at key frequencies for different frequency-adaptive methods (β_h^1). (black) Grid voltage and (white) load voltage.

are similar, but they deteriorate for the high-order harmonics. To avoid this effect, the terms α_h and β_h can be updated in each PRC when the frequency deviates, but this would require the computation of α_h and β_h in real-time.

Fig. 5.16 shows the SAC transient performance when there is a sudden frequency variation from 54 Hz to 55.5 Hz, which is unrealistic, but interesting for academic purposes. Initially, the system is stable and the SAC gives a clean load voltage. When the frequency step takes place, $\cos(\omega_g h t_s)$ is updated in each PRC, but α_h and β_h are not modified: the system becomes out of control.

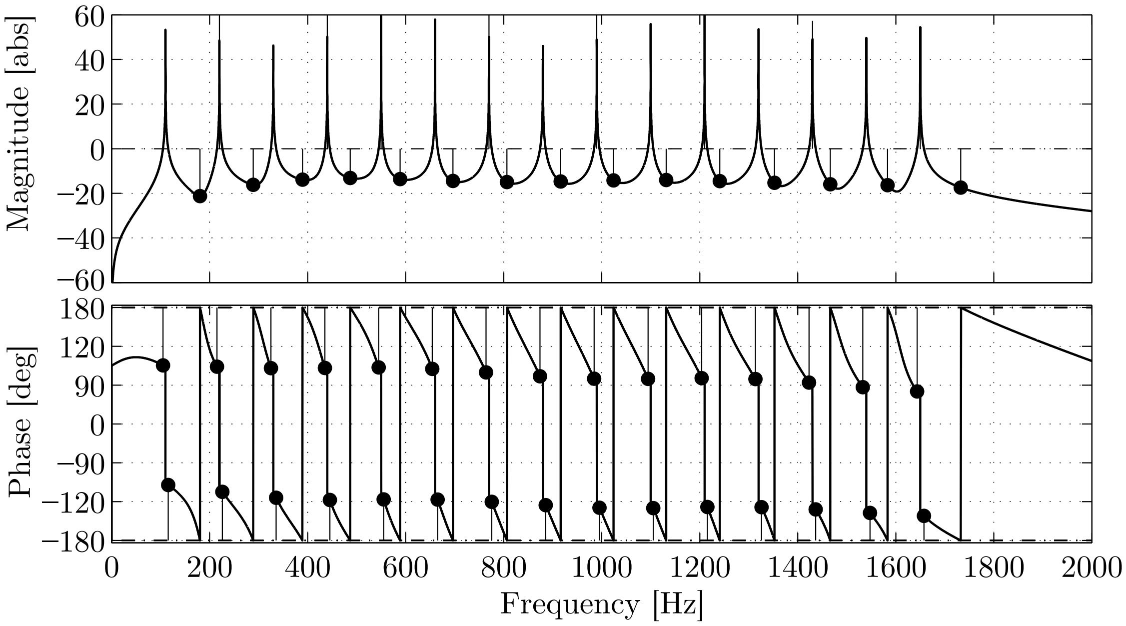

Figure 5.15: Bode diagram of the plant with the PRCs when there is a frequency deviation of $\delta\omega_g = 10$ % and the resonant poles are updated in the controllers.

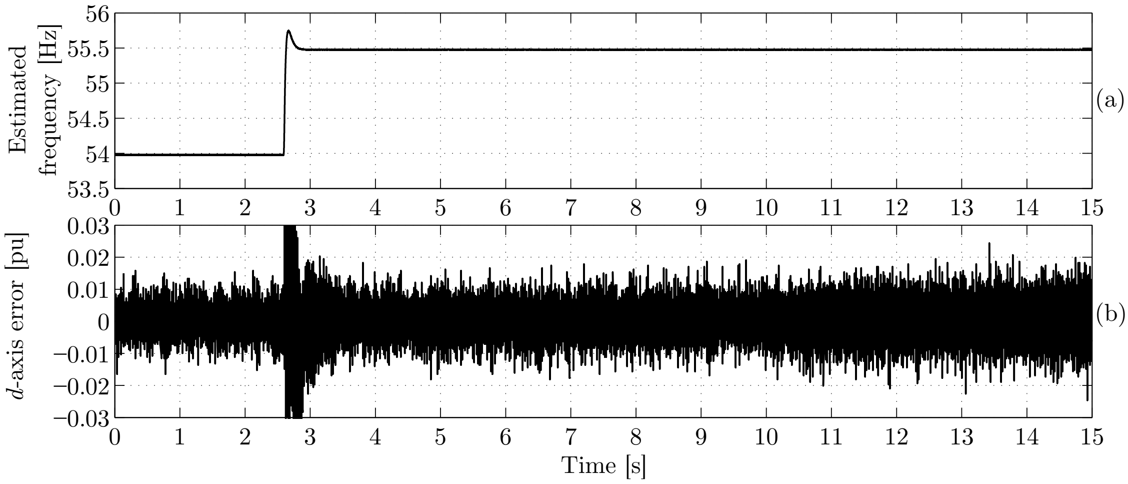

Figure 5.16: Abrupt change in the grid frequency from $\delta\omega_g = 8$ % to $\delta\omega_g = 12$ %.

5.6 From Repetitive to Resonant Controllers

Although resonant and repetitive controllers are usually studied separately, Escobar et al. [202] show that a RC has an equivalent PRC form. Consider a RC core:

$$RC_o(s) = \frac{e^{-st_p}}{1-e^{-st_p}} = -\frac{1}{2} + \frac{1}{2}\left(\frac{1+e^{-st_p}}{1-e^{-st_p}}\right) = -\frac{1}{2} + \frac{1}{2}\coth\left(st_p/2\right). \tag{5.31}$$

Recalling that $\omega_g = 2\pi t_p$, $\coth(st_p/2)$ can be expanded as follows [213]:

$$\coth(st_p/2) = \frac{2}{st_p} + \sum_{h=1}^{\infty} \frac{t_p(2/t_p)^2 hs}{s^2 + (2\pi h/t_p)^2} = \frac{1}{\pi}\left(\frac{\omega_g}{s} + 2\sum_{h=1}^{\infty}\frac{\omega_g hs}{s^2+(\omega_g h)^2}\right), \tag{5.32}$$

equation (5.31) can be written as:

$$RC_o(s) = -\frac{1}{2} + \frac{1}{t_p}\left(\frac{1}{s} + 2\sum_{h=1}^{\infty}\frac{hs}{s^2+(\omega_g h)^2}\right). \tag{5.33}$$

Finally, the continuous-time RC core in (5.33) can be discretised as

$$RC_o(z) = \frac{z^{-N}}{1-z^{-N}} = -\frac{1}{2} + \frac{t_s}{t_p}\frac{z}{z-1} + 2\frac{t_s}{t_p}\sum_{h=1}^{N/2}\frac{(z-1)}{z^2 - 2\cos(\omega_g h t_s)z + 1}. \tag{5.34}$$

Notice that (5.34) contains a proportional gain, an integral action, and the resonators, but only the resonators in (5.34) are required to compensate harmonics. The PRCs described in this chapter are similar to those in (5.34), although neither integral action nor proportional gain were included before. The phase of $RC_o(z)$ is linear and the phase jump due to the resonators always takes place between +90 and −90 degrees. The RC core is multiplied by $G_x(z) = \hat{F}_p^{-1}(z)$ to guarantee closed-loop stability, but this is impossible for PRCs because the controller would not have a proper transfer function. However, the inverse model of the plant can be approximated around $\omega_g h$ with the compensator:

$$G_x(e^{j\omega t_s}) = \hat{F}_p^{-1}(e^{j\omega t_s}) \approx \beta_h^2(\alpha_h e^{j\omega t_s} + 1), \text{ if } \omega \approx \omega_g h. \tag{5.35}$$

The core used in this chapter adds some delay to the open-loop (see Fig. 5.4). Accordingly, the phase jump does not occur between +90 and −90 deg. Therefore, the phase delay produced by the resonator has been compensated to overcome this problem, as suggested in Section 5.2.

5.7 Chapter Summary

This chapter revisits the application of PRCs to deal with harmonics in PE applications. First of all, PRCs basics has been explained and a novel method to tackle the design of PRCs has been developed. This method takes into account the delay of the open-loop transfer function and the controller is adjusted automatically. The core has been selected with a derivative term to ease independent tuning of PRCs for each harmonic frequency.

This chapter has shown once more that, if the controller is not adapted when the grid frequency changes, the performance deteriorates. This problem has been solved applying Chebishov polynomials, thus providing perfect harmonic compensation in spite of frequency fluctuations. This method is well suited for real-time applications because its computational burden is moderate. It is, certainly, a better alternative than using the Taylor approximation previously proposed in the literature for the same purpose.

Chapter 6

Steady-State Space-Vector-Based Harmonic Controller

This chapter presents an algorithm to deal with harmonics in PE devices that will be called here "steady-state space-vector-based harmonic controller" or, alternatively, SVB controller. Section 6.1 presents an overview of the SVB controller and Section 6.2 explains how to obtain a steady-state model of the plant. Section 6.3 describes a method to design the SVB controller and Section 6.4 analyses the stability of the closed-loop system when applying the proposed controller. An adaptive version of the controller is proposed in Section 6.5, while the controller is applied to suppress harmonics in (a) an SAC and (b) a CSeAPF in Section 6.6. Finally, Section 6.7 summarises the findings and conclusions of this chapter.

6.1 Overview of the Proposed Controller

Fig. 6.1 portrays the block diagram of the SVB controller. The controller has two sampling periods: a fast one and a slow one. The fast one is similar to the one used for the other control algorithms already presented in this thesis and will be called t_s. The slow one is an integer multiple of the fast one and it is equal to a period of the algorithm used to estimate the harmonic components of the signals involved (e.g. discrete Fourier transform, Kalman filter, etc.). If the plant is in steady-state, each harmonic can be represented, exactly, with a space vector of constant components that will be called steady-state space vector in this thesis. In Fig. 6.1, the variables sampled with a slow sampling period ($t_s^{\triangledown}$) bear the superscript "$\triangledown$". In the rest of the chapter, the z variable related to t_s is called z, while the z variable related to $t_s^{\triangledown}$ is called $z^{\triangledown}$. A harmonic estimation (HE) algorithm is applied to the error signal, called $\vec{e}[k]$, giving two components (d and q) for each harmonic (h). The real part is called $e^{c\triangledown}_{(h)-d}$, while the imaginary part is called $e^{c\triangledown}_{(h)-q}$. This pair of numbers can be treated as DC error signals, which can be eliminated, completely, with PI controllers (included in $\mathbf{C}^{\triangledown}_{(h)}$). However, each component of the command signal ($u^{\triangledown}_{(h)-d}$ and $u^{\triangledown}_{(h)-q}$) affect both the real and imaginary part of the error ($e^{c\triangledown}_{(h)-d}$ and $e^{c\triangledown}_{(h)-q}$). Therefore, the controller $\mathbf{C}^{\triangledown}_{(h)}$ can not be implemented as two independent controllers (as shown in Fig. 6.1) unless the cross-coupling between the real and imaginary parts is compensated. Each error signal (with two components, namely, $e^{c\triangledown}_{(h)-d}$ and $e^{c\triangledown}_{(h)-q}$) is multiplied by a matrix, called $\mathbf{X}^{\triangledown}_{(h)}$, which ensures that $e^{\triangledown}_{(h)-d}$ is only related to $u^{\triangledown}_{(h)-d}$ and $e^{\triangledown}_{(h)-q}$ is only related to $u^{\triangledown}_{(h)-q}$. Finally, the output signal of each controller is transformed back to the time domain to reconstruct the command signal, $\vec{u}[k]$. Notice that samples for the HE algorithm have to be taken with a fast sampling period (t_s) to include several samples within a period of the highest-order harmonic to be tackled. Consequently, the same fast sampling period has to be used for the command reconstruction (CR). However, the PI controllers applied to the HE outputs and the decoupling matrix ($\mathbf{X}^{\triangledown}_{(h)}$) can run with the slow sampling period ($t^{\triangledown}_s$), thus reducing the computational burden.

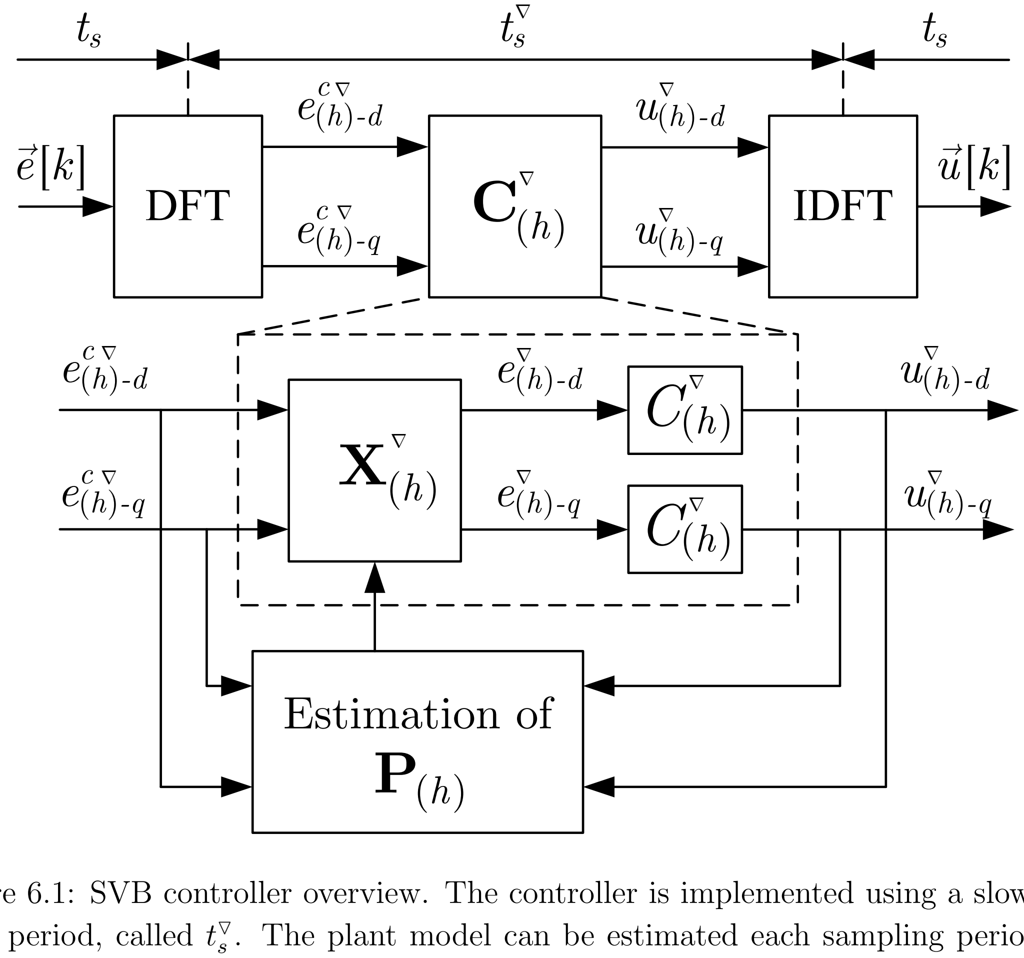

Figure 6.1: SVB controller overview. The controller is implemented using a slow sampling period, called $t^{\triangledown}_s$. The plant model can be estimated each sampling period ($t^{\triangledown}_s$) and updated in $\mathbf{X}^{\triangledown}_{(h)}$

6.1.1 Adaptive Version of the SVB Controller

The matrix that provides the required decoupling between the components of the error is the inverse frequency-response of the plant at the harmonic frequency addressed ($\mathbf{X}^{\triangledown}_{(h)} = \mathbf{P}^{-1}_{(h)}$), as will be shown in this chapter. Unfortunately, the closed-loop system may become unstable if the estimated model of the plant does not describe the actual plant, accurately. This problem is solved in this thesis estimating the frequency response of the plant every sampling period (of period $t_s^{\triangledown}$), as shown in Fig. 6.1. If $t_s^{\triangledown}$ is slow enough, the plant becomes a steady-state relationship (a complex gain, called $\mathbf{P}_{(h)}$, multiplied by a delay). In that case, the model of $\mathbf{P}_{(h)}$, to be called $\hat{\mathbf{P}}_{(h)}$, can be easily estimated each sampling period and updated in the control system.

6.2 Steady-State Modelling and Decoupling

6.2.1 Steady-State Modelling Equations

The relation between the z-domain space vector of the plant input ($\vec{U}(z)$) and the z-domain space vector of the plant output ($\vec{Y}(z)$) is

$$\vec{Y}\left(z\right) = \vec{P}\left(z\right)\vec{U}\left(z\right) + \vec{D}\left(z\right), \tag{6.1}$$

where $\vec{P}(z)$ is the complex transfer function of the plant and $\vec{D}(z)$ is a disturbance. Assuming unity feedback gain and neglecting $\vec{D}(z)$, the input-to-error relationship is

$$\vec{E}\left(z\right) = -\vec{P}\left(z\right)\vec{U}\left(z\right). \tag{6.2}$$

In steady-state, the complex number that relates $\vec{E}(z)$ with $\vec{U}(z)$ at any harmonic frequency (h) can be know from the frequency response of $\vec{P}(z)$. Therefore,

$$e^c_{(h)-d} + je^c_{(h)-q} = -\vec{P}_{(h)}(u_{(h)-d} + ju_{(h)-q}), \tag{6.3}$$

where $\vec{P}_{(h)} = \vec{P}\left(z = e^{jh\omega_g t_s}\right)$ [176]. Using matrix notation, (6.3) can be written as

$$\underbrace{\begin{bmatrix} e^c_{(h)-d} \\ e^c_{(h)-q} \end{bmatrix}}_{\mathbf{E}^c_{(h)}} = -\underbrace{\begin{bmatrix} \mathrm{Re}\left\{\vec{P}_{(h)}\right\} & -\mathrm{Im}\left\{\vec{P}_{(h)}\right\} \\ \mathrm{Im}\left\{\vec{P}_{(h)}\right\} & \mathrm{Re}\left\{\vec{P}_{(h)}\right\} \end{bmatrix}}_{\mathbf{P}_{(h)}} \underbrace{\begin{bmatrix} u_{(h)-d} \\ u_{(h)-q} \end{bmatrix}}_{\mathbf{U}_{(h)}}, \tag{6.4}$$

where superscript "c" stands for "coupled". In (6.4), $\mathbf{P}_{(h)}$ is the steady-state relationship between the input ($\mathbf{U}_{(h)}$) and the error ($\mathbf{E}^c_{(h)}$) for a specific harmonic frequency (h).

6.2.2 Plant Modelling Using a Slow Sampling Period

The SVB controller is implemented using a slow sampling period ($t_s^\triangledown$), which is an integer multiple of the fast sampling period (t_s). Therefore,

$$t_s^\triangledown = N t_s, \text{ with } N \in \mathbb{N}. \tag{6.5}$$

If the plant reaches the steady-state in one sampling period (of period $t_s^\triangledown$), the plant can be roughly approximated by a one-sample-period delay plus the steady-state relationship derived in (6.4):

$$\underbrace{\begin{bmatrix} e^{c\triangledown}_{(h)-d} \\ e^{c\triangledown}_{(h)-q} \end{bmatrix}}_{\mathbf{E}^{c\triangledown}_{(h)}} \approx -\underbrace{\begin{bmatrix} \mathrm{Re}\left\{\vec{P}_{(h)}\right\} & -\mathrm{Im}\left\{\vec{P}_{(h)}\right\} \\ \mathrm{Im}\left\{\vec{P}_{(h)}\right\} & \mathrm{Re}\left\{\vec{P}_{(h)}\right\} \end{bmatrix}}_{\mathbf{P}_{(h)}} \underbrace{\begin{bmatrix} 1/z^\triangledown & 0 \\ 0 & 1/z^\triangledown \end{bmatrix}}_{\mathbf{Z}^\triangledown(z^\triangledown)} \underbrace{\begin{bmatrix} u^\triangledown_{(h)-d} \\ u^\triangledown_{(h)-q} \end{bmatrix}}_{\mathbf{U}^\triangledown_{(h)}}. \tag{6.6}$$

6.2.3 Steady-State Decoupling Equations

Unsurprisingly, (6.6) shows that changes in the d-axis component of $\mathbf{U}^\triangledown_{(h)}$ will produce changes in both the d- and the q-axis components of the error signal, $\mathbf{E}^{c\triangledown}_{(h)}$. One can define a new error signal to avoid this cross-coupling between both axis dynamics:

$$\mathbf{E}^\triangledown_{(h)} = \mathbf{X}^\triangledown_{(h)} \mathbf{E}^{\triangledown c}_{(h)}, \tag{6.7}$$

where $\mathbf{X}^\triangledown_{(h)}$ is a matrix of the appropriate size (see Fig. 6.2). Taking (6.7) to (6.6),

$$\mathbf{E}^\triangledown_{(h)} = -\mathbf{X}^\triangledown_{(h)} \mathbf{P}_{(h)} \mathbf{Z}^\triangledown(z^\triangledown) \mathbf{U}^\triangledown_{(h)}. \tag{6.8}$$

If the cross-coupling terms in (6.8) are to be avoided, $\mathbf{X}^\triangledown_{(h)} \mathbf{P}_{(h)} \mathbf{Z}^\triangledown(z^\triangledown)$ must be a diagonal matrix. Furthermore, $\mathbf{X}^\triangledown_{(h)}$ can be selected to satisfy $\mathbf{X}^\triangledown_{(h)} \mathbf{P}_{(h)} = \mathbf{I}$, yielding

$$\mathbf{X}^\triangledown_{(h)} = \hat{\mathbf{P}}^{-1}_{(h)}, \tag{6.9}$$

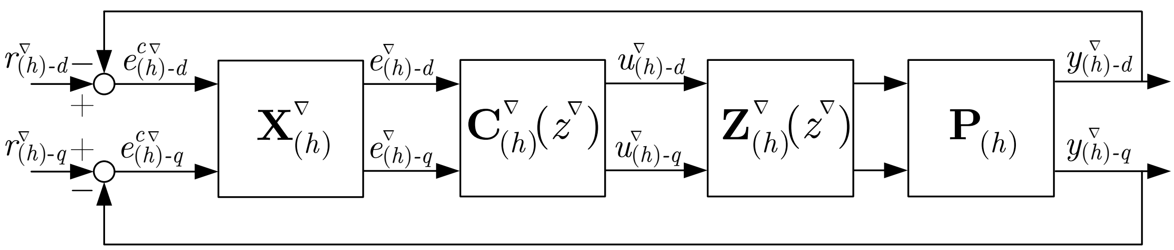

Figure 6.2: System model using the slow sampling period.

where $\hat{\mathbf{P}}_{(h)}$ is the estimated frequency response of the complex plant at the frequency $h\omega_g$. If the decoupling matrix is selected as shown in (6.9), the relationship between the decoupled error and the plant command becomes

$$\underbrace{\begin{bmatrix} e^{\triangledown}_{(h)-d} \\ e^{\triangledown}_{(h)-q} \end{bmatrix}}_{\mathbf{E}^{\triangledown}_{(h)}} \approx - \underbrace{\begin{bmatrix} 1/z^{\triangledown} & 0 \\ 0 & 1/z^{\triangledown} \end{bmatrix}}_{\mathbf{Z}^{\triangledown}_{(h)}(z^{\triangledown})} \underbrace{\begin{bmatrix} u^{\triangledown}_{(h)-d} \\ u^{\triangledown}_{(h)-q} \end{bmatrix}}_{\mathbf{U}^{\triangledown}_{(h)}}. \tag{6.10}$$

6.3 Steady-State Controller Design

The decoupled plant in (6.10) can be controlled in closed-loop and an integral controller has to be applied to each of the error components (d and q) to ensure zero steady-state error at each of the harmonic frequencies:

$$\mathbf{C}^{\triangledown}_{(h)}(z^{\triangledown}) = \begin{bmatrix} \dfrac{(1-\alpha_d)\, z^{\triangledown}}{z^{\triangledown}-1} & 0 \\ 0 & \dfrac{(1-\alpha_d)\, z^{\triangledown}}{z^{\triangledown}-1} \end{bmatrix}, \tag{6.11}$$

with $0 < \alpha_d < 1$. The closed loop transfer function is

$$\mathbf{F}^{\triangledown}_{(h)}(z^{\triangledown}) = \mathbf{Z}^{\triangledown}_{(h)}(z^{\triangledown})\mathbf{C}_{(h)}(z^{\triangledown})(\mathbf{I} + \mathbf{Z}^{\triangledown}_{(h)}(z^{\triangledown})\mathbf{C}^{\triangledown}_{(h)}(z^{\triangledown}))^{-1}, \tag{6.12}$$

where $\mathbf{I}$ is a identity matrix of the appropriate size. Simplifying (6.12):

$$\mathbf{F}^{\triangledown}_{(h)}(z^{\triangledown}) = \begin{bmatrix} \dfrac{1-\alpha_d}{(z^{\triangledown}-\alpha_d)} & 0 \\ 0 & \dfrac{1-\alpha_d}{(z^{\triangledown}-\alpha_d)} \end{bmatrix}, \tag{6.13}$$

if $\mathbf{X}^{\triangledown}_{(h)} = \hat{\mathbf{P}}^{-1}_{(h)}$. As shown in (6.13), α_d modifies the closed-loop transient performance. The smaller α_d is, the faster the closed-loop transient response becomes. Unfortunately, stability deteriorates using small values of α_d, as will be shown shortly. Notice that (6.13) has unity DC gain regardless the value of α_d.

6.4 Stability Analysis

Decoupling of d- and q-axis dynamics will not be perfect if the plant model does not describe the plant dynamics, accurately. This uncertainty can be modelled with a square matrix, to be called $\mathbf{\Delta}^{\triangledown}_{(h)}$, connected in series with $\mathbf{P}^{\triangledown}_{(h)}$ (see Fig. 6.3):

$$\mathbf{\Delta}^{\triangledown}_{(h)} = \delta_{(h)} \begin{bmatrix} \cos\phi_{(h)} & \sin\phi_{(h)} \\ -\sin\phi_{(h)} & \cos\phi_{(h)} \end{bmatrix}, \tag{6.14}$$

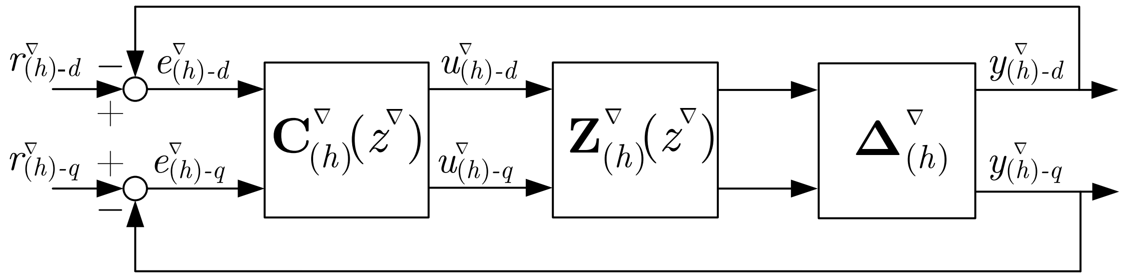

Figure 6.3: Control system diagram adding the uncertainty model ($\boldsymbol{\Delta}^{\nabla}_{(h)}$).

where $\delta_{(h)}$ and $\phi_{(h)}$ are the modulus and the angle uncertainty for each harmonic (h) vector, respectively. For the sake of simplicity, subscript (h) in $\delta_{(h)}$ and $\phi_{(h)}$ will be omitted in the rest of this section. The closed-loop system taking into account $\boldsymbol{\Delta}^{\nabla}_{(h)}$ is

$$\mathbf{F}^{\nabla}_{(h)}(z^{\nabla}) = \boldsymbol{\Delta}^{\nabla}_{(h)}\mathbf{Z}^{\nabla}_{(h)}(z^{\nabla})\mathbf{C}^{\nabla}_{(h)}(z^{\nabla})(\mathbf{I} + \boldsymbol{\Delta}^{\nabla}_{(h)}\mathbf{Z}^{\nabla}_{(h)}(z^{\nabla})\mathbf{C}^{\nabla}_{(h)}(z^{\nabla}))^{-1}, \tag{6.15}$$

which yields

$$\mathbf{F}^{\nabla}_{(h)}(z) = F_{(h)} \begin{bmatrix} (1-\alpha_d)\,\delta + (z^{\nabla}-1)\cos\phi & (z^{\nabla}-1)\sin\phi \\ -(z^{\nabla}-1)\sin\phi & (1-\alpha_d)\delta + (z^{\nabla}-1)\cos\phi \end{bmatrix}, \tag{6.16}$$

where

$$F_{(h)} = \frac{(1-\alpha_d)\,\delta}{((1-\alpha_d)\delta\cos\phi + (z^{\nabla}-1))^2 + ((1-\alpha_d)\delta\sin\phi)^2}. \tag{6.17}$$

One can easily prove that forcing $\phi = 0$ and $\delta = 1$, (6.16) equals the closed-loop transfer function without modelling errors, (6.13). The poles of (6.16) are

$$p = \delta(1-\alpha_d)\,(1 - \cos\phi \pm j\sin\phi)\,. \tag{6.18}$$

The module of the closed-loop poles should be strictly less than one to ensure a stable closed-loop system. Therefore:

$$\cos\phi > \frac{\delta(1-\alpha_d)}{2}, \tag{6.19}$$

which implies that:

- Errors in the magnitude ($\delta_{(h)}$) can be compensated tuning α_d.
- The phase error should be less than $\pi/2$ ($-\pi/2 < \phi_{(h)} < \pi/2$); otherwise the system would become unstable because (6.19) can not be satisfied.
- Stability margins deteriorate for small values of α_d (fast closed-loop system).

6.5 Adaptive SVB Controller

6.5.1 Plant Model Identification

The closed-loop system could become unstable if the plant model is not accurately known at the design stage, as shown in Section 6.4. Unfortunately, the plant model might be difficult to know beforehand in the SAC because the load modifies the system dynamics. Therefore, it is convenient to develop an adaptive mechanism to ensure closed-loop stability when the plant model is unknown.

The SVB controller is based on a steady-state approach, so

$$\hat{\mathbf{P}}_{(h)} \begin{bmatrix} u_{(h)-d} \\ u_{(h)-q} \end{bmatrix}_{k-1} = - \begin{bmatrix} e^c_{(h)-d} \\ e^c_{(h)-q} \end{bmatrix}_k - \begin{bmatrix} d_{(h)-d} \\ d_{(h)-q} \end{bmatrix}_k, \tag{6.20}$$

where $d_{(h)-d}$ and $d_{(h)-q}$ are the real and imaginary part of the disturbance at each harmonic frequency, respectively. Disturbances can be approximated, roughly, as a constant number for each harmonic component ($d_{(h)-d}$ and $d_{(h)-q}$ are constant values). Accordingly, if the incremental operator $\Delta(\cdot)$ is applied to (6.20):

$$\hat{\mathbf{P}}_{(h)} \begin{bmatrix} \Delta u_{(h)-d} \\ \Delta u_{(h)-q} \end{bmatrix}_{k-1} = - \begin{bmatrix} \Delta e^c_{(h)-d} \\ \Delta e^c_{(h)-q} \end{bmatrix}_k - \underbrace{\begin{bmatrix} \Delta d_{(h)-d} \\ \Delta d_{(h)-q} \end{bmatrix}_k}_{0}, \tag{6.21}$$

where $\Delta d_{(h)-d}$ and $\Delta d_{(h)-q}$ are zero. Reorganizing (6.21), the estimated real and imaginary part of the plant can be calculated, giving

$$\begin{bmatrix} \mathrm{Re}\left\{\hat{P}_{(h)}\right\} \\ \mathrm{Im}\left\{\hat{P}_{(h)}\right\} \end{bmatrix} = \begin{bmatrix} -\Delta u_{(h)-d} & \Delta u_{(h)-q} \\ -\Delta u_{(h)-q} & -\Delta u_{(h)-d} \end{bmatrix}^{-1}_{k-1} \begin{bmatrix} \Delta e^c_{(h)-d} \\ \Delta e^c_{(h)-q} \end{bmatrix}_k, \tag{6.22}$$

where $\hat{P}_{(h)}$ is the estimated complex plant for the harmonic h.

6.5.2 Remarks on Plant Identification

The plant model can only be estimated accurately if variations in the command signal are large, otherwise noise and disturbances would spoil the estimation. A small value of α_d leads to larger oscillations in the command signal that are useful for estimation purposes. Accordingly, a value of α_d close to zero seems to be the right choice. Summarizing:

- If the controller is used without plant estimation, α_d should be large enough to ensure closed-loop stability if the load changes.

- If the controller is used in its adaptive form, α_d should be small enough to provide an accurate estimation of the plant.

- If the controller is used to estimate the plant each sampling period, the estimation must be deactivated when steady-state is reached.

The proposed adaptive mechanism provides a kind of "self-stabilising" mechanism to the closed-loop system. When the plant is unknown, the closed-loop system would become unstable and, therefore, the amplitude of the command signal will increase. In that case, the plant can be accurately estimated since the command variations will be large and (6.22) would provide a good approximation of the plant. Therefore, the closed-loop system would become stable.

6.6 Application of the Steady-State SVB Controller

The SVB controller has been applied to the SAC using the control scheme in Fig. 4.13 (Chapter 4), but $CR(z)$ is replaced by the SVB controller. Two different applications are depicted in Fig. 6.4. Fig. 6.4(a) shows how an SAC can be used to supply a clean voltage to a sensitive load while Fig. 6.4(b) shows how an SAC can block current harmonics generated by non-linear loads and prevent them from reaching the grid. In (b), the load-voltage waveform must be distorted to eliminate current harmonics and the way in which this may affect the load will have to be assessed in each application. In both cases, a state-feedback (SF) controller has been used for the main controller (see Chapter 3).

6.6.1 Controller Implementation

The implementation of the controller proposed in this chapter is depicted in Fig. 6.5. The steady-state space vectors of the error are calculated using the multiple reference frame (MRF) theory [214]. The trigonometric functions required to perform transformations are obtained using the recursive formulation proposed by Ochoa et al. [214, 215] to reduce the computational burden. The inverse transformation in Fig. 6.5 (c) is performed using the MRF theory as well. The harmonics are extracted from the measured signals using third-order Butterworth low-pass filters with a cut-off frequency of 40 Hz (see Fig. 6.5 (a)). The fast sampling period has been set to $t_s = 1/5400$ s and $N = 108$ ($t_s^{\triangledown} = 20$ ms). Unless otherwise stated, α_d is zero in the rest of this chapter. The plant estimation if stopped if the command signal is smaller than 0.0005 pu. This value was adjusted by trial and error. The SVB controller includes integral terms to tackle from the 2nd to the 30th harmonic in the dq-RF.

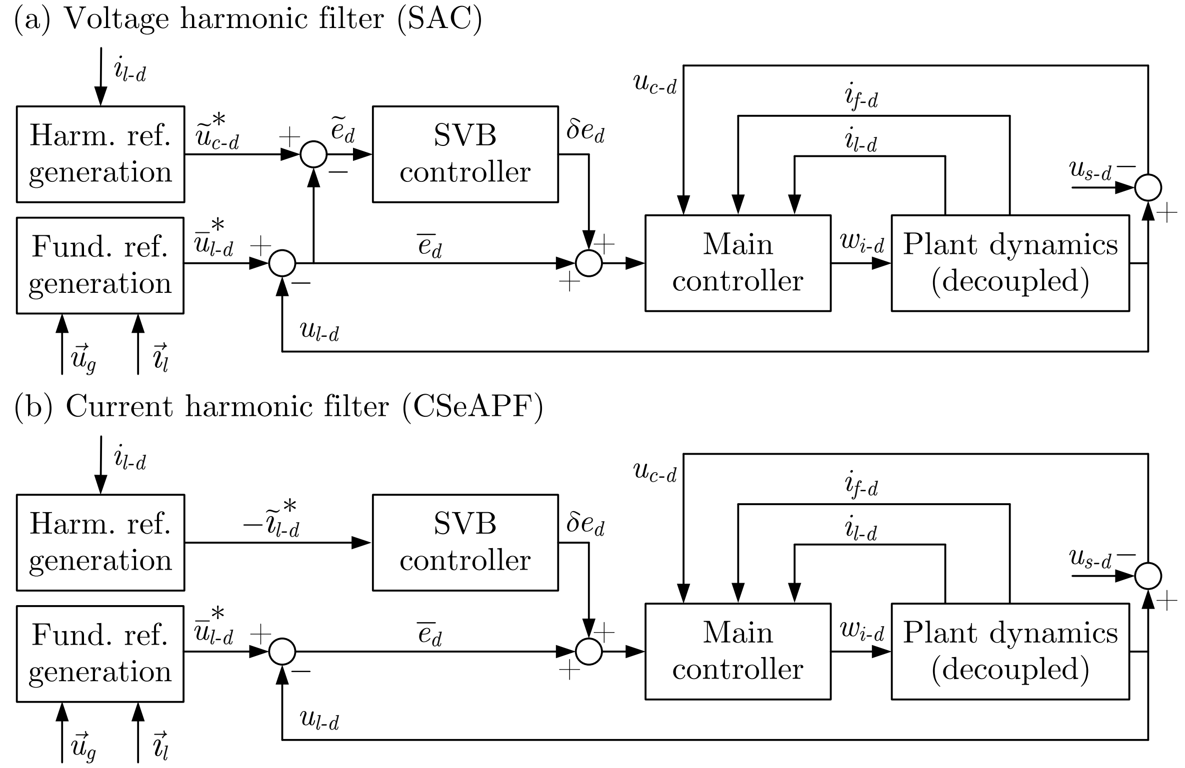

Figure 6.4: Control schemes to be tested. (a) Voltage-harmonic filter (SAC) and (b) current-harmonic filter (CSeAPF).

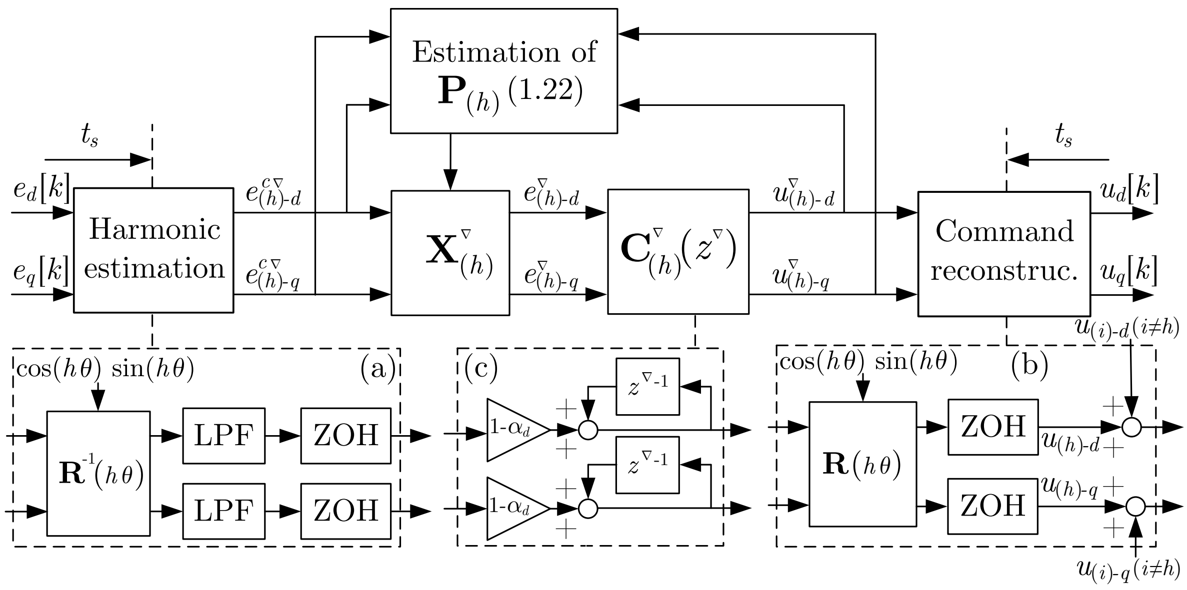

Figure 6.5: Practical implementation of the steady-state SVB controller. (a) Harmonic identification, (b) command reconstruction, and (c) slow sampling period controller.

6.6.2 Series Active Conditioner (SAC)

Transient Performance

Fig. 6.6 shows the results when the SVB controller is applied to eliminate voltage harmonics. Initially, the SAC is working in closed-loop only with the main controller. At t = 5 ms, the SVB controller is switched on and, after 20 ms (a period of the slow sampling period), the SAC perturbs the load voltage with some voltage harmonics because the initial model of the plant is incorrect. One cycle later, at t = 45 ms, the plant has been identified and the SVB controller can successfully eliminate harmonics. Notice that the transient response is quite fast, even thought the SVB controller is implemented using a slow sampling period.

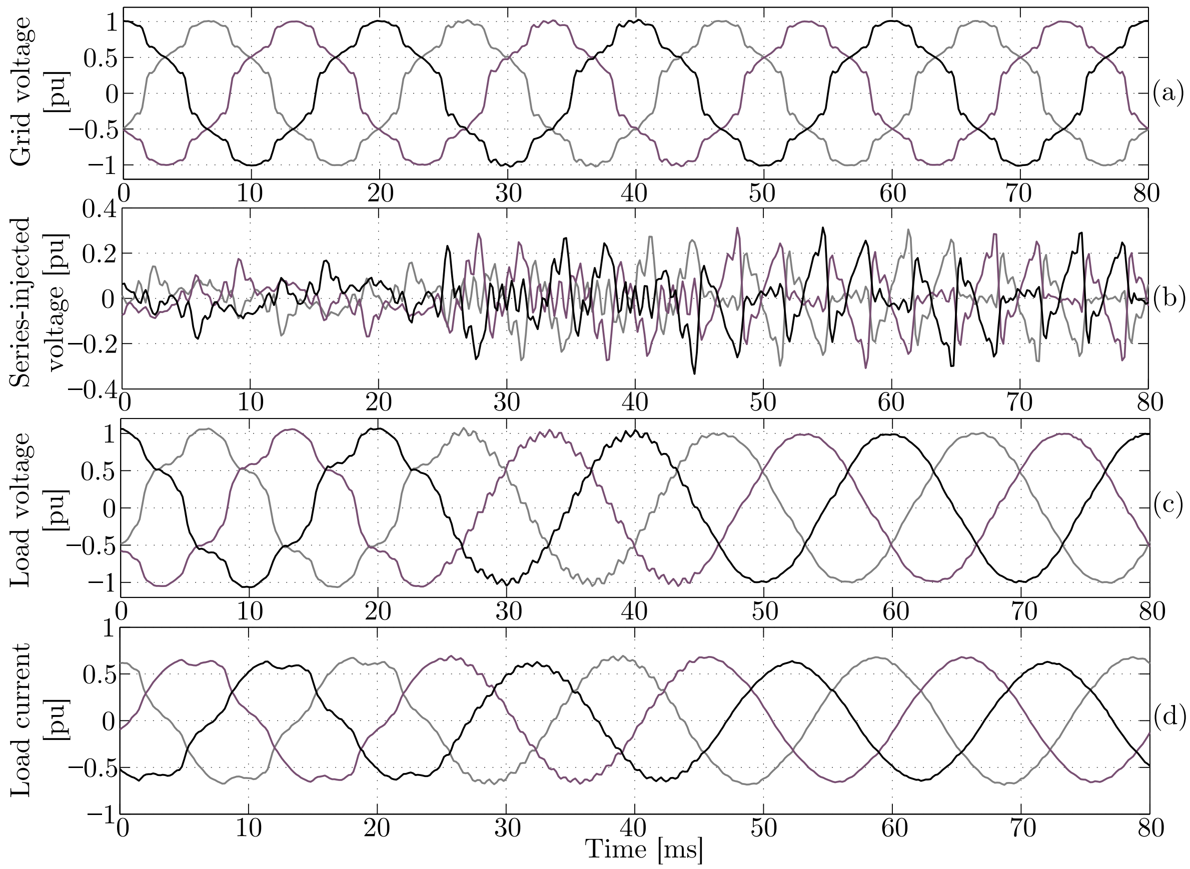

Figure 6.6: SAC transient performance using the SVB controller when the load is linear. (a) Grid voltage, (b) series-injected voltage, (c) load voltage, and (d) load current.

Fig. 6.7 shows the SAC performance when the grid voltage is polluted with harmonics and a voltage sag takes place. Initially, the SAC is in steady-state cleaning the load voltage. At t = 20 ms a voltage sag takes place and the SAC compensates the fundamental component of the load voltage, rapidly. However, the SVB controller requires several cycles to remove the harmonics form the load voltage. At $t = 100$ ms the load-voltage harmonics are almost fully suppressed. The compensation of a voltage sag with the SVB controller is not as fast as it was when using other controllers (repetitive or resonant) because the SVB controller requires several cycles to estimate the plant model when a voltage sag takes place. This happens because the controller cannot distinguish between a disturbance step and a set-point step. Therefore, if the grid voltage changes, the SVB controller will immediately try to identify the plant model. In fact, the adaptation process should be stopped in this case.

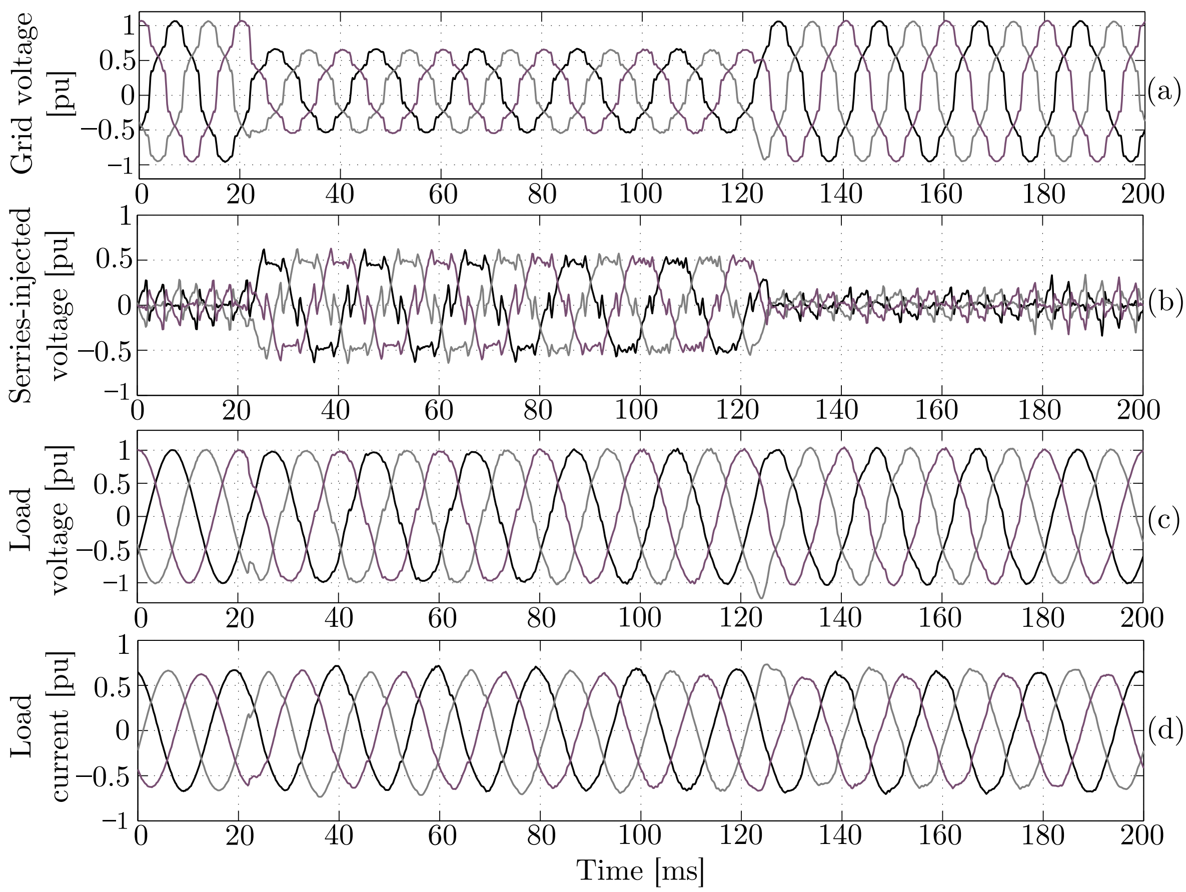

Figure 6.7: Voltage sag compensation when applying the SVB controller to an SAC. (a) Grid voltage, (b) series-injected voltage, (c) load voltage, and (d) load current.

Fig. 6.8 (b) shows d-axis error signal when the grid frequency suddenly changes from 50 Hz to 50.25 Hz. Initially, the SAC is in steady-state and, when the frequency step takes place, the THD rapidly returns to its previous value. However, at $t = 0.25$ s the controller suddenly perturbs the load voltage because $\mathbf{P}_{(h)}$ is modified when ω_g varies. Again, the controller tries to adapt himself.

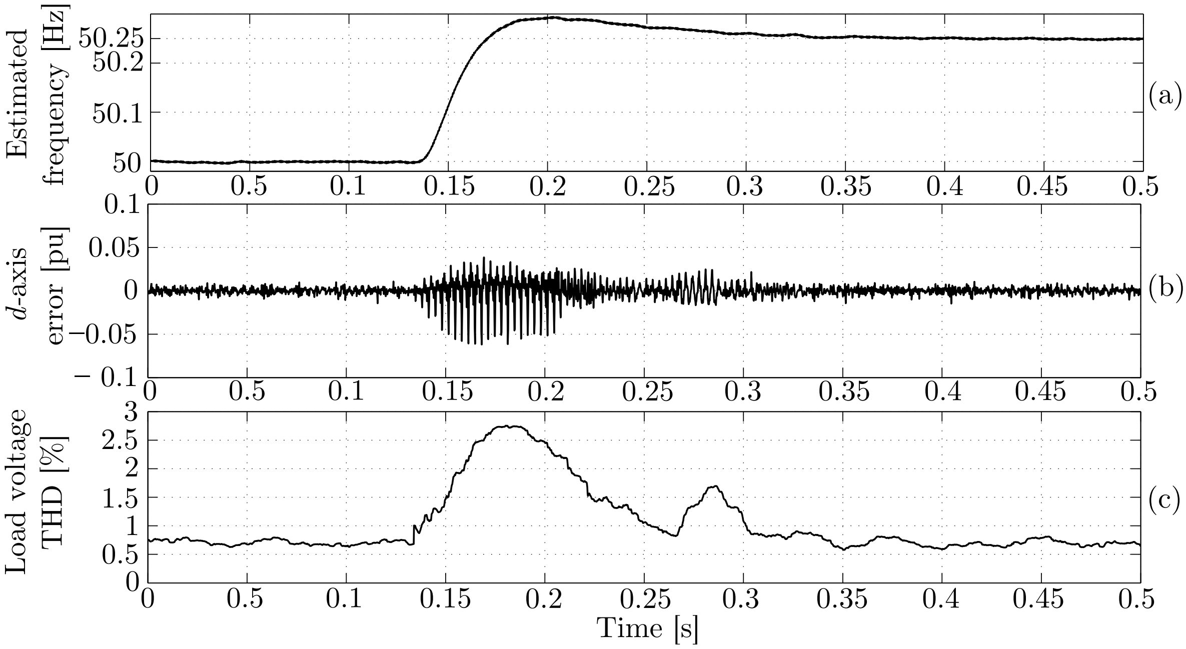

Figure 6.8: (a) Frequency estimated by the PLL, (b) d-axis error, and (c) load voltage THD when the grid frequency suddenly changes from 50 Hz to 50.25 Hz.

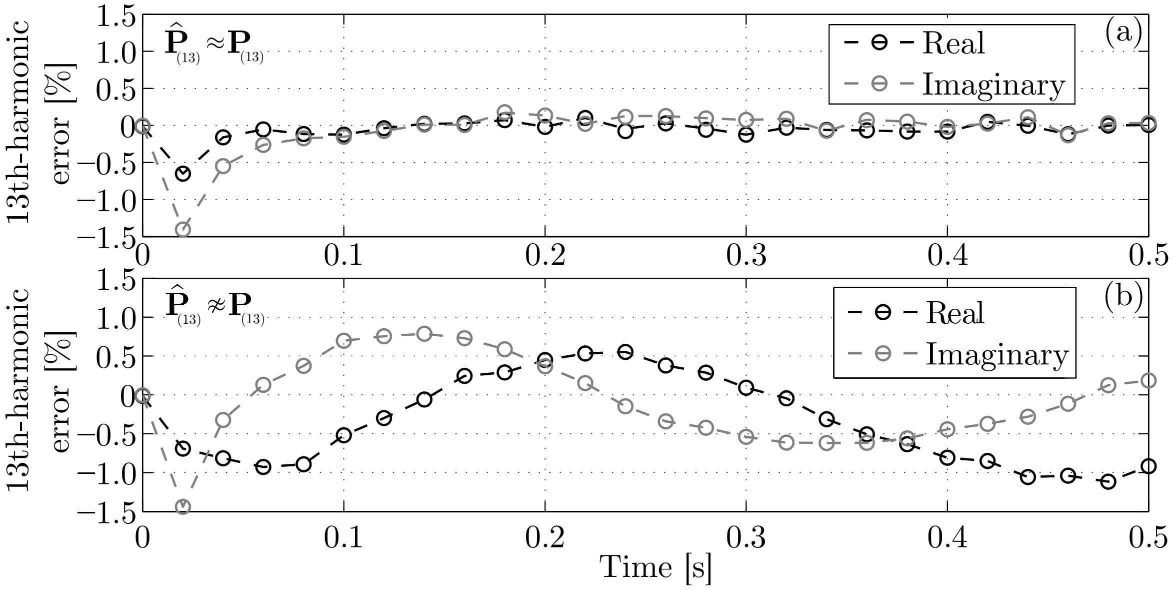

Figure 6.9: Real and imaginary part of the error for the 13th harmonic using $\alpha_d = 0.2$ when (a) $\hat{\mathbf{P}}_{(13)} \approx \mathbf{P}_{(13)}$ and (b) $\hat{\mathbf{P}}_{(13)} \not\approx \mathbf{P}_{(13)}$ (90 degrees mismatch).

Evaluating Stability

The conclusions in Section 6.4 about stability can also be validated in the prototype. The grid voltage has been contaminated only with the 13th harmonic and two experiments have been carried out: (a) the plant model is well known and (b) the plant model is known with errors. The value of α_d for these tests has been set to 0.2. In the first case $\hat{\mathbf{P}}_{(13)} \approx \mathbf{P}_{(13)}$. Fig. 6.9 (a) shows that the 13th harmonic components are eliminated, quickly. In the second case, Fig. 6.9 (b), the plant model has been modified and the phase of $\hat{\mathbf{P}}_{(13)}$ differs approximately 90 degrees from that of the actual plant. Fig. 6.9 (b) shows that the error signal oscillates because the system stability has deteriorated. These results are similar to the ones obtained by Le Roux et al. [133], where a DFT-based controller was proposed to compensate harmonics.

6.6.3 Current SeAPF (CSeAPF)

A CSeAPF will be used to prevent the current harmonics of a non-linear load from reaching the grid. The load consists of a three-phase diode rectifier with a large smoothing capacitor at the DC (see Appendix A). The CSeAPF objectives are (a) to filter the current harmonics generated by the non-linear load and (b) to provide a constant load voltage.

Resonant Controllers to Eliminate Current Harmonics

Fig. 6.10 shows a first attempt to block the current harmonics generated by the non-linear load using PRCs (even harmonics in dq from 2 to 30, see Chapter 5). Initially, only the state-feedback controller is working. At $t = 0.2$ s the PRCs are switched on and the load-current harmonics are reduced (see Fig. 6.10(b)). However, the closed-loop system becomes unstable soon. It seems that the application of harmonic-control

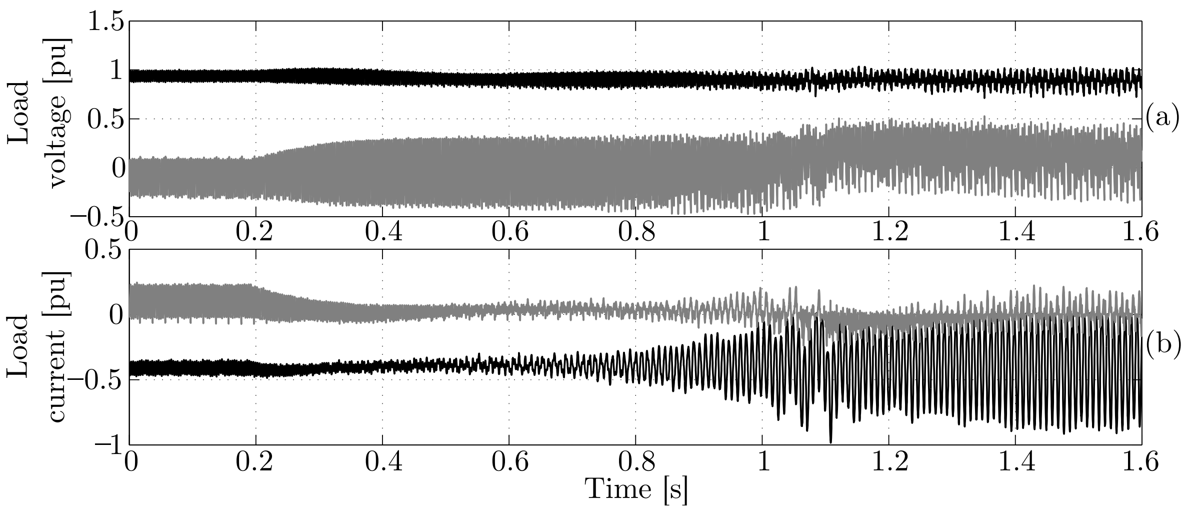

Figure 6.10: First attempt to eliminate current harmonics with PRCs in a CSeAPF. (a) dq-axis components of the load voltage and (b) dq-axis components of the load current.

algorithms that require a plant model at the design stage is not a good choice in this case. This problem can be solved using the adaptive version of the SVB controller.

Performance of the SVB Controller

Fig. 6.11 shows the transient performance of the CSeAPF when the SVB controller is switched on. Initially, the CSeAPF is in steady-state and the power-flow controller sets the fundamental component of the load voltage while $u_{dc} = 400$ V (see Chapter 7). The voltage across the load is highly distorted because the non-linear load is of the so-called voltage-sourced type. At $t = 10$ ms the SVB controller is switched on and, at that time, the SVB controller had no information of the plant. One cycle later, the command signal changes and, therefore, the load current changes. As shown in Fig.

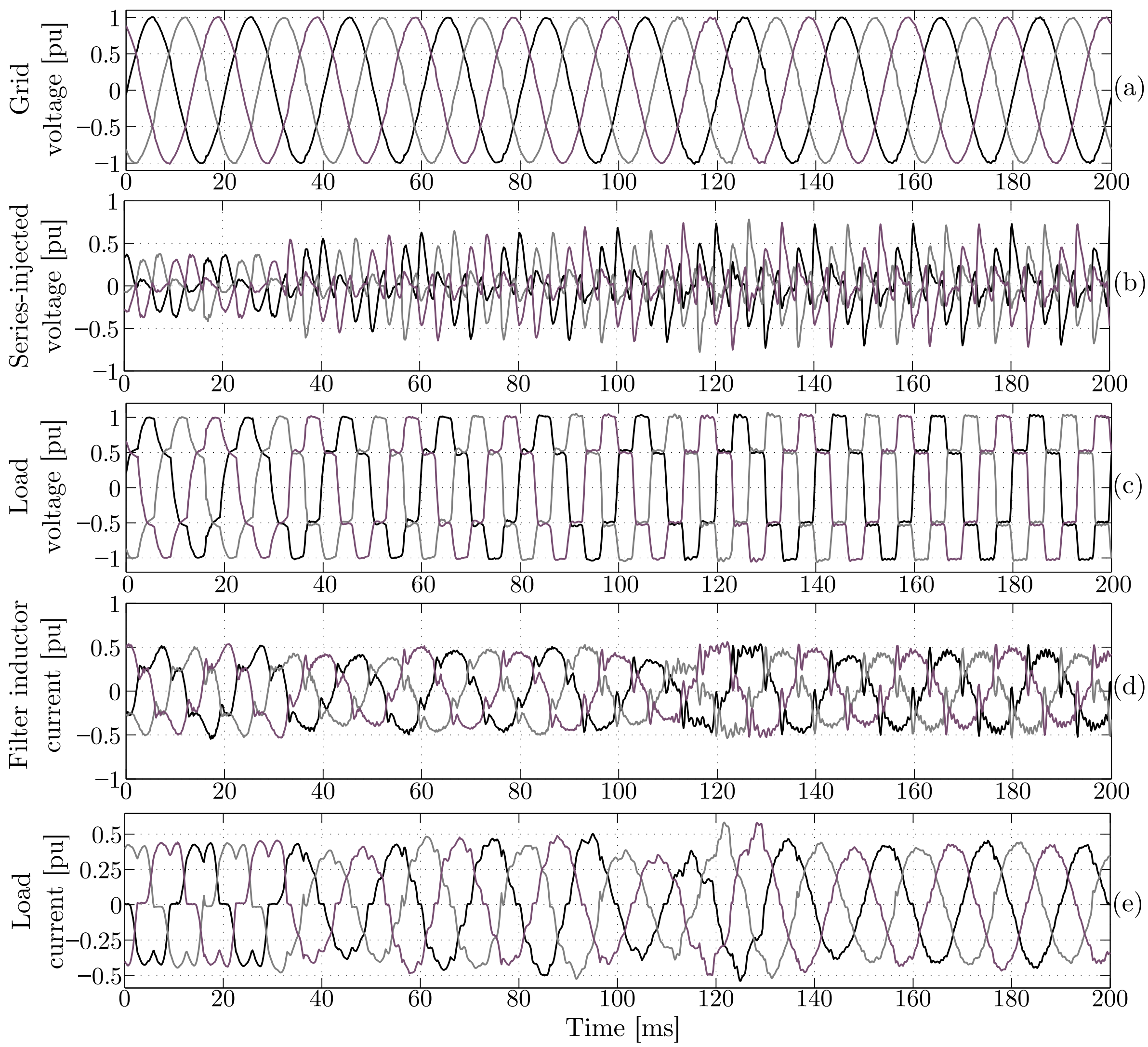

Figure 6.11: CSeAPF transient response. (a) Grid voltage, (b) series-injected voltage, (c) load voltage, (d) filter inductor current, and (e) load current.

6.11(e), the SVB controller requires several cycles to remove all the harmonic currents poured by the non-linear load. Furthermore, one could expect that the controller could tackle all the harmonics in one cycle because $\alpha_d = 0$. However, the load is non-linear and $\mathbf{P}_{(h)}$ may change if the operating point of the load changes.

Fig. 6.12 shows the steady-state performance of the system. The CSeAPF is injecting a highly-distorted voltage to compensate the current harmonics. Meanwhile, the current consumed by the non-linear load is almost sinusoidal. The harmonic content of the current with and without the SVB controller has been depicted in Fig. 6.12(d). The load current previous to the application of the SVB controller is shown in Fig. 6.11(e) at $t = 0$ ms. The grid-current harmonics have been greatly reduced (particularly the 5th and 7th components) and the load current is almost sinusoidal (from a THD of 22.3 % to 3.9 %). Thanks to the application of the CSeAPF the grid voltage THD is reduced from 2.8 % to 0.9 % because the suppressed current harmonics do not produce any voltage drop in the grid short circuit impedance.

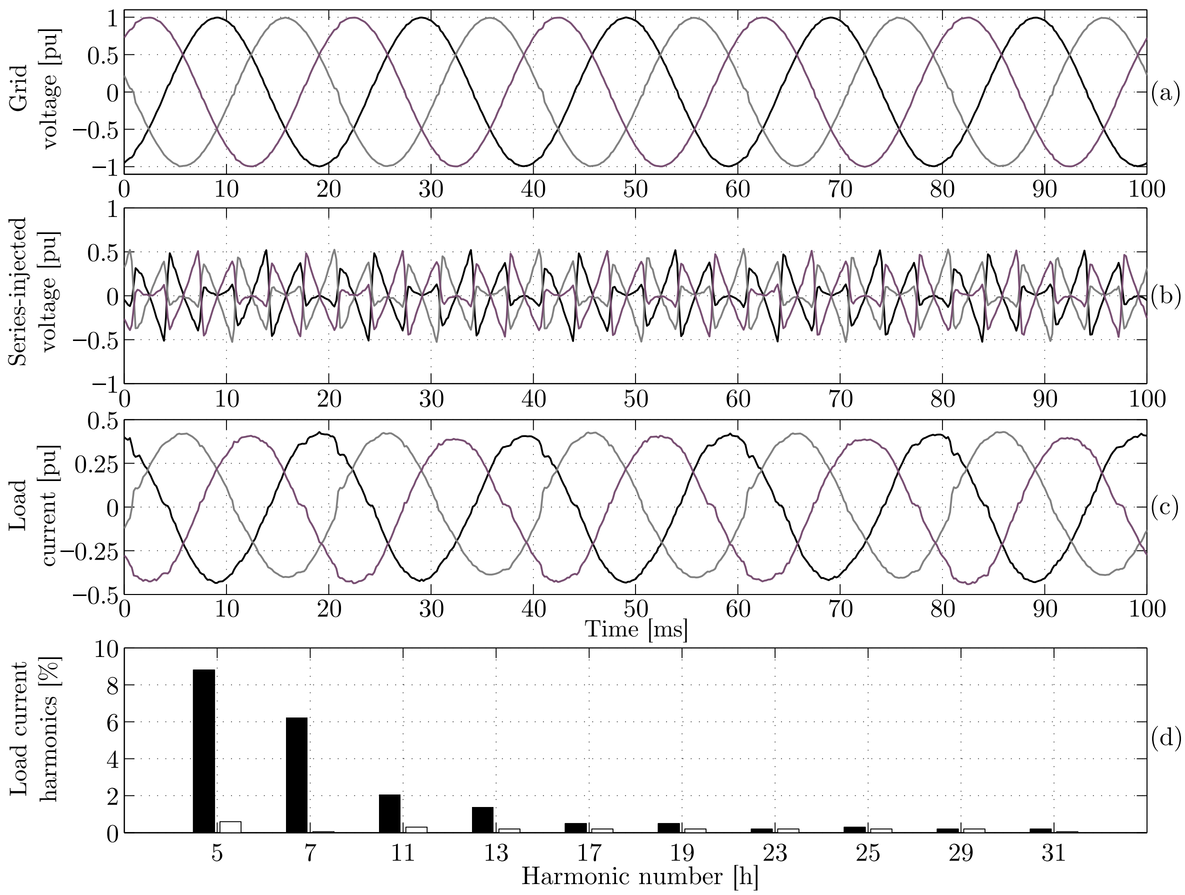

Figure 6.12: Steady-state performance of the CSeAPF using the steady-state SVB controller. (a) Grid voltage, (b) series-injected voltage, (c) load current, and (d) harmonic components (black) before and (white) after the application of the controller.

Fig. 6.13 and Fig. 6.14 shows the CSeAPF performance when a three-phase voltage sag takes place (75 % retained voltage). The initial part of the sag is shown in Fig. 6.13, while the end of the sag is shown in Fig. 6.14. As shown in Fig. 6.13, previous to the voltage sag the CSeAPF is injecting a voltage in series with the line that forces a sinusoidal current. When the sag takes place, the CSeAPF rapidly restores the load voltage, but the load current has widespread amplitude fluctuations because the load behaves like a voltage source.

Fig. 6.14 shows the CSeAPF performance when the voltage sag ends. In this case, the load voltage suddenly increases forcing a large current peak (see Fig. 6.14 (e)). After several cycles (at $t = 120$ ms) the load current returns to the pre-sag value.

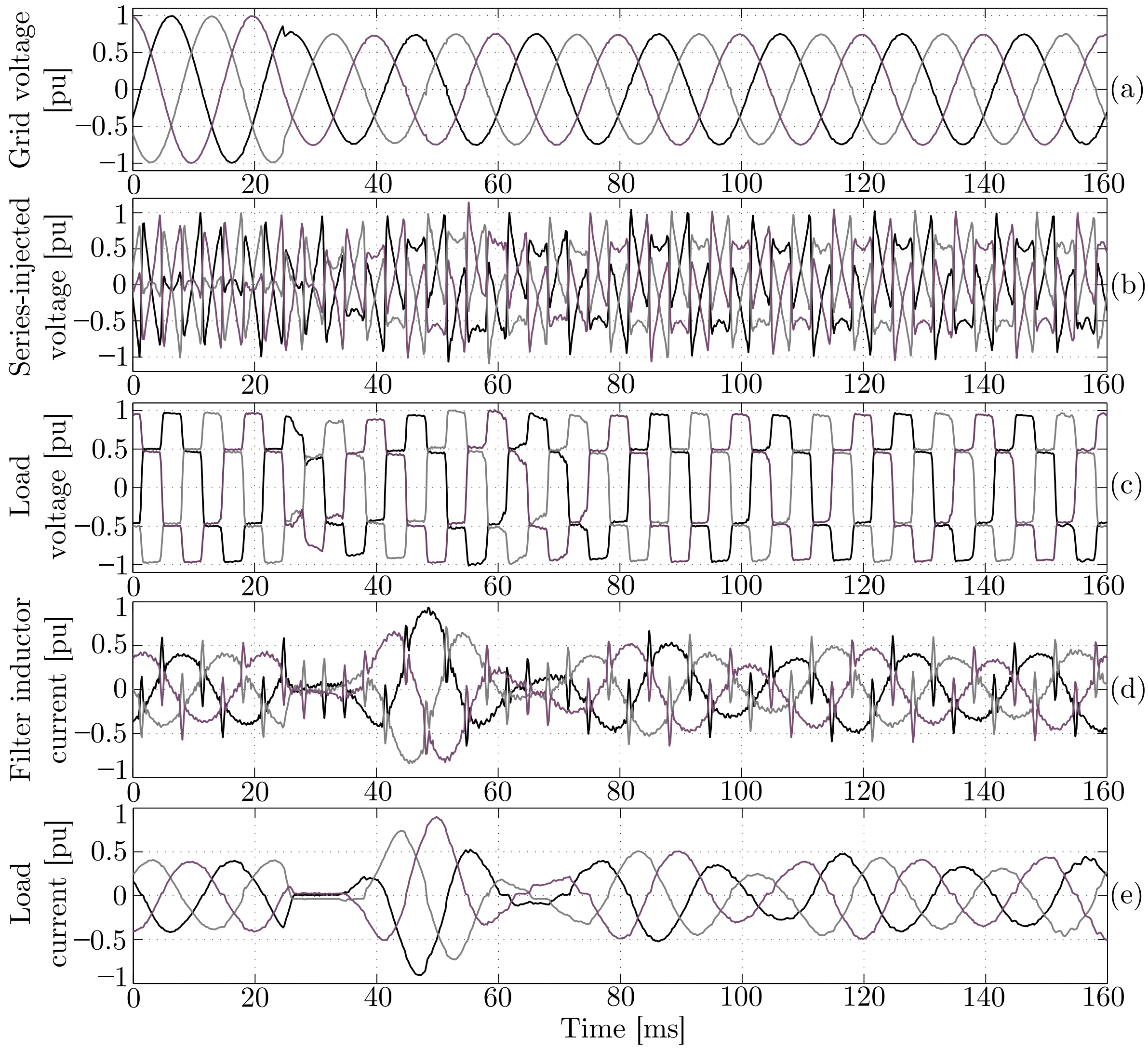

Figure 6.13: Compensation of a three-phase voltage sag (75 % retained voltage) when the CSeAPF is protecting a voltage-sourced non-linear load. (a) Grid voltage, (b) series-injected voltage, (c) load voltage, (d) filter inductor current, and (e) load current.

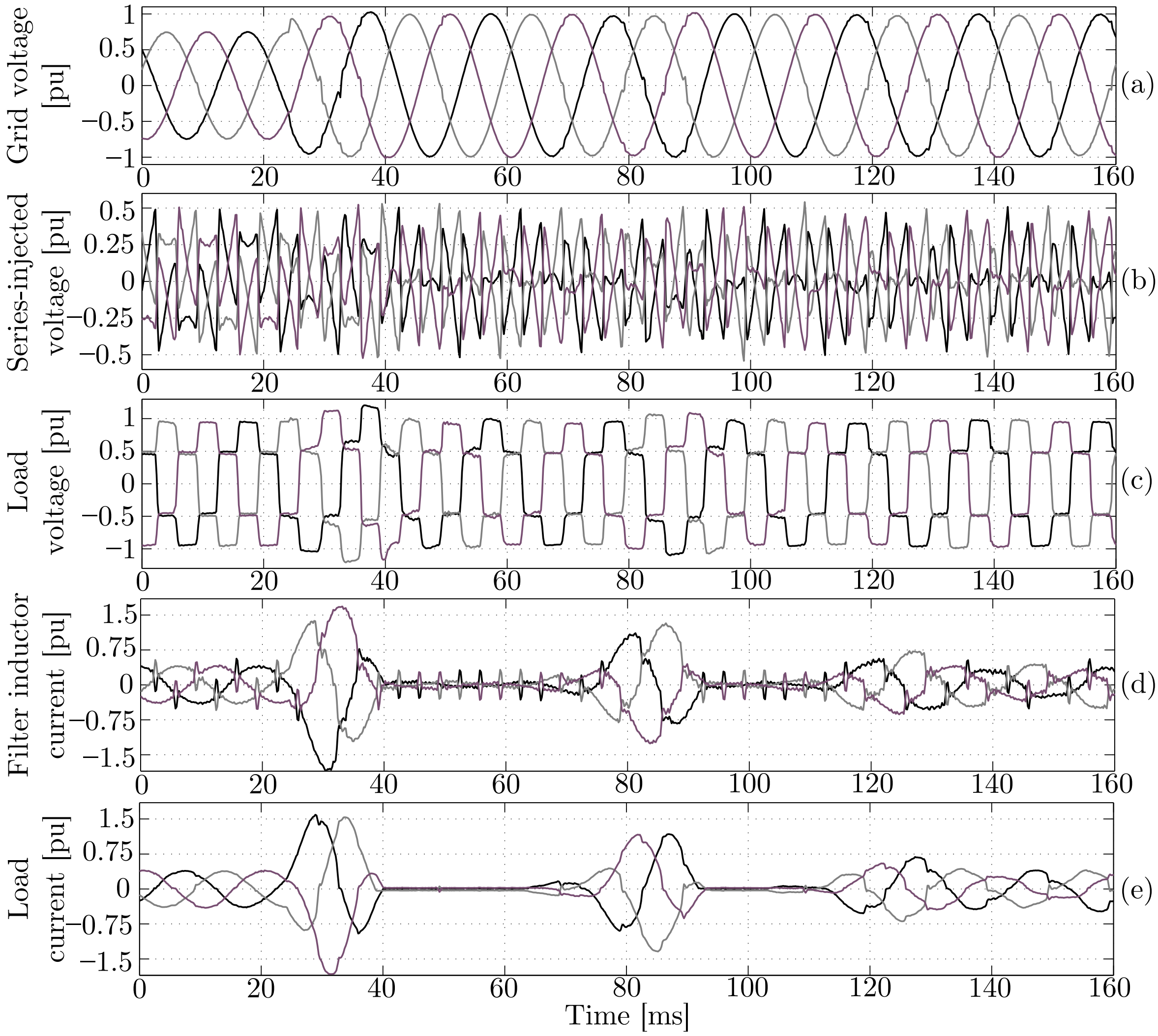

Figure 6.14: Compensation of a three-phase voltage sag (75 % retained voltage) when the CSeAPF is protecting a voltage-sourced non-linear load. (a) Grid voltage, (b) series-injected voltage, (c) load voltage, (d) filter inductor current, and (e) load current.

6.7 Chapter Summary

This chapter has shown a steady-state approach to deal with voltage or current harmonics using series compensators. This controller can compensate harmonics even if the plant model is unknown beforehand. The SVB controller has been applied to eliminate harmonics in two quite different situations: an SAC and a CSeAPF. In both cases the SVB controller has shown an excellent performance even thought some aspects, such as the controller adaptation, need further research.

Chapter 7

Power Flow Analysis and Control

This chapter proposes a control framework where active and reactive power consumed by series devices can be analysed and controlled in a wide variety of applications. The background on power control and the outline of the proposed method are described in Section 7.1. Synchronisation with the load current to simplify active- and reactive-power calculations is explained in Section 7.2. Section 7.3 and Section 7.4 describe load-voltage constraints. Section 7.5 deals with the application of the load-voltage constraints to control active and reactive power. Results are discussed in detail in Section 7.6 and, finally, Section 7.7 gives the conclusions of this chapter.

7.1 Power-Flow Controller Overview

Fig. 7.1 shows an outline of an SAC with its controller. The series-injected voltage ($\vec{u}_c$) is controlled in closed loop with the AC-voltage controller, comparing $\vec{u}_c$ with the reference voltage ($\vec{u}_c^*$). In this chapter, $\vec{u}_c^*$ is generated to ensure that load-voltage requirements are satisfied and, if possible, active- and reactive-power commands (p^* and q^*) are met. The active-power command is calculated to maintain the voltage of the DC capacitor (u_{dc}) at its rated value (u_{dc}^*) using a DC voltage controller, while the reactive-power command can be set arbitrarily. However, active- and reactive-power commands are not always achievable because the load voltage ($\vec{u}_l$) must be maintained within certain limits where loads can operate properly: active- and reactive-power commands and load-voltage limits must always be coordinated.

The AC-voltage controller in Fig. 7.1 has been implemented using a reference frame (RF) synchronized with the d-axis component of the grid voltage (voltage-synchronised reference frame, VSRF), which is a typical choice in PE applications [26]. However, the reference-generation block uses another RF synchronized with the d-axis component of the load current (current-synchronised reference frame, CSRF). As shown in this chapter, the CSRF greatly simplifies the conversion from power requirements to voltage commands. Furthermore, the proposed control strategy will also ease the application of the load-voltage constraints within the reference-generation block.

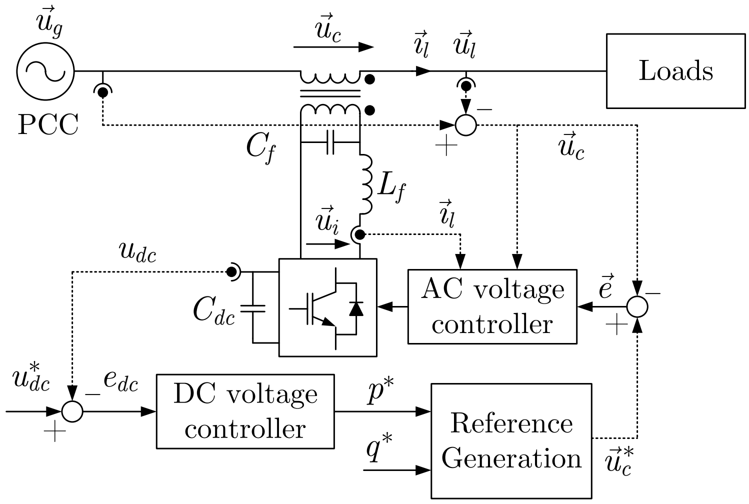

Figure 7.1: SAC setup with the proposed decoupled power controller.

7.2 Synchronisation with the Load Current

Fig. 7.2 shows a vector diagram where two reference frames are depicted. The one with axes named d and q is the VSRF ($\vec{u}_g$ is the grid voltage), while the one with axes named d' and q' is the CSRF ($\vec{\imath}_l$ is the load current). From Fig. 7.2:

$$\vec{u}_l = \vec{u}_g + \vec{u}_c \tag{7.1}$$

with

$$\begin{bmatrix} u_{l-d} \\ u_{l-q} \end{bmatrix} = |Z_l| \begin{bmatrix} \cos\phi & -\sin\phi \\ \sin\phi & \cos\phi \end{bmatrix} \begin{bmatrix} i_{l-d} \\ i_{l-q} \end{bmatrix}, \tag{7.2}$$

where $|Z_l|$ and ϕ are the magnitude and the angle of the load impedance, respectively, while subscripts d and q are used to signal d and q components of space vectors.

Fig. 7.2 (right) shows an equivalent electrical circuit to study the power flow of an SAC. In that figure, $p(t)$ and $q(t)$ are the instantaneous active and reactive power injected ($p, q > 0$) or consumed by the SAC. The instantaneous active and reactive power delivered by the grid are $p_g(t)$ and $q_g(t)$, while the active and reactive power consumed by the load are $p_l(t)$ and $q_l(t)$. For simplicity, the time dependence of signals will be omitted in the rest of the chapter.

The power injected by the SAC in any RF is

$$p = u_{c-d}i_{l-d} + u_{c-q}i_{l-q}, \quad q = u_{c-q}i_{l-d} - u_{c-d}i_{l-q}. \tag{7.3}$$

The CSRF angle is selected to set the q' component of the load current to zero ($i'_{l-q} = 0$):

$$p = u'_{c-d} i'_{l-d}, \quad q = u'_{c-q} i'_{l-d}. \tag{7.4}$$

The transformation that relates space vectors in the VSRF with space vectors in the CSRF is

$$\begin{bmatrix} i'_{l-d} \\ i'_{l-q} \end{bmatrix} = \underbrace{\begin{bmatrix} \cos\varphi & -\sin\varphi \\ \sin\varphi & \cos\varphi \end{bmatrix}}_{\boldsymbol{R}(\varphi)} \begin{bmatrix} i_{l-d} \\ i_{i-q} \end{bmatrix}. \tag{7.5}$$

From the second row of (7.5) and forcing $i'_{l-q} = 0$:

$$i_{l-d} \sin\varphi + i_{l-q} \cos\varphi = i'_{l-q} = 0 \tag{7.6}$$

where,

$$\cos\varphi = \frac{i_{l-d}}{\sqrt{i_{l-d}^2 + i_{l-q}^2}}, \quad \sin\varphi = -\frac{i_{l-q}}{\sqrt{i_{l-d}^2 + i_{l-q}^2}}. \tag{7.7}$$

In the rest of the chapter the angle φ is called "current synchronisation angle". If required, i'_{l-d} can be computed as

$$i'_{l-d} = |\vec{i}_l| = \sqrt{i_{l-d}^2 + i_{l-q}^2}, \tag{7.8}$$

because $i'_{l-q} = 0$.

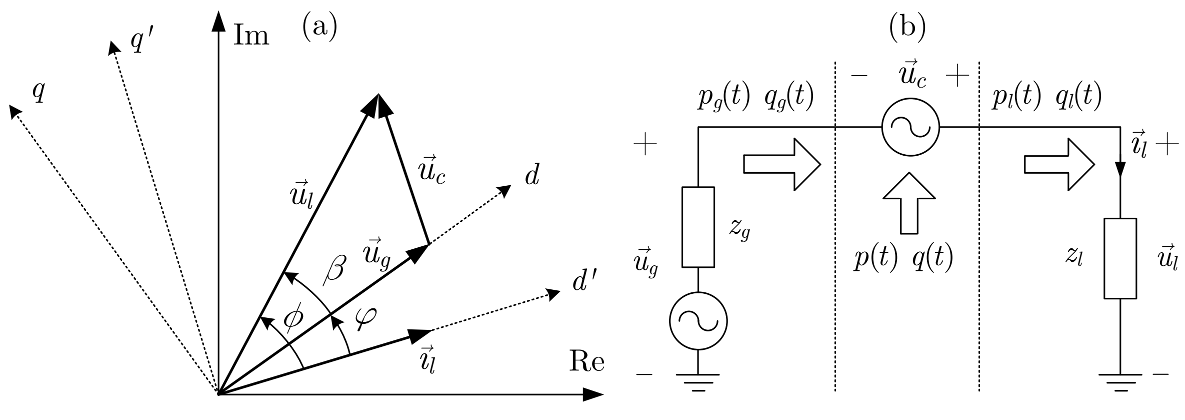

Figure 7.2: (a) Space-vector diagram of the VSRF (dq) and the CSRF ($d'q'$) and (b) equivalent circuit to study the power flow thought an SAC.

7.3 Application of the Load-Voltage Constraints

The load voltage should be maintained within certain limits to ensure proper operation of loads connected downstream the SAC. Calling u_l^+ and u_l^- the maximum and minimum load voltage limits, respectively:

$$u_l^- \leq |\vec{u}_l| \leq u_l^+, \tag{7.9}$$

where,

$$|\vec{u}_l| = \sqrt{(u'_{c-d} + u'_{g-d})^2 + (u'_{c-q} + u'_{g-q})^2}. \tag{7.10}$$

Since $\vec{u}_g$ is an exogenous variable, the challenge is to find the limits of u'_{c-d} and u'_{c-q} to satisfy (7.9). From (7.2), recalling that $i'_{l-q} = 0$:

$$u'_{l-q} = u'_{c-q} + u'_{g-q} = |z_l| i'_{l-d} \sin\phi, \tag{7.11}$$

which can be taken to (7.10), yielding

$$|\vec{u}_l| = \sqrt{(u'_{c-d} + u'_{g-d})^2 + (|z_l||\vec{i}_l| \sin\phi)^2}. \tag{7.12}$$

If the VSRF ensures that $u_{g-q} = 0$, then

$$u'_{g-d} = u_{g-d} \cos\varphi - \underbrace{u_{g-q} \sin\varphi}_{0} = |\vec{u}_g| \cos\varphi. \tag{7.13}$$

Finally, taking (7.13) to (7.12) and solving for u'_{c-d}:

$$u'_{c-d} = |\vec{u}_l| \cos\phi - |\vec{u}_g| \cos\varphi. \tag{7.14}$$

Notice that (7.14) defines u'_{c-d} according to the value of $\cos\varphi$ and a number of exogenous variables. Similarly, u'_{c-q} can be written as:

$$u'_{c-q} = |\vec{u}_l| \sin\phi - |\vec{u}_g| \sin\varphi. \tag{7.15}$$

Taking u_l^+ (or u_l^-) to (7.14) and (7.15) one obtains the values of u'_{c-q} and u'_{c-d} that yields u_l^+ (or u_l^-). These equations will be used in the following sections to calculate the active- and reactive-power limits according to the load-voltage limits.

7.4 Consequences of Load-Voltage Constraints

The load voltage constraints mentioned in Section 7.3 limit the active- and reactive-power injection. Taking (7.14) and (7.15) to (7.4) the active- and reactive-power for an SAC become

$$p = \frac{|\vec{u}_l|}{|Z_l|}\overbrace{(|\vec{u}_l|\cos\phi - |\vec{u}_g|\cos\varphi)}^{u'_{c-d}}, \quad q = \frac{|\vec{u}_l|}{|Z_l|}\overbrace{(|\vec{u}_l|\sin\phi - |\vec{u}_g|\sin\varphi)}^{u'_{c-q}}. \tag{7.16}$$

For example, Fig. 7.3 (left) shows the active-power-injection capability of an SAC versus the current synchronisation angle (φ) when $|\vec{u}_l| = 1$ pu and the load is linear with $|Z_l| = 1$ pu and $\phi = 30$ degrees (inductive load). Two different values have been used for the grid voltage, namely, 1 pu and 0.8 pu. The active-power-exchange capability is greatly affected by the magnitude of the grid voltage. For example, power absorption ($p < 0$) is impossible when $|\vec{u}_g| = 0.8$ pu. Furthermore, the power equations in (7.16) show that an SAC can absorb active power from the grid only if $|\vec{u}_g| > |\vec{u}_l|\cos\phi$ ($\cos\varphi = 1$), which becomes a necessary condition to maintain the DC-link voltage constant without an auxiliary energy supply. Fig. 7.3 (right) shows the reactive-power-injection capability of an SAC for the same grid conditions. An SAC can inject a large amount of reactive power ($q > 0$) when the load is inductive, but reactive-power consumption ($q < 0$) is more restricted. Moreover, Figs. 7.3 (left) and (right) show that, for the values of φ where the SAC can absorb power (and then, operate without auxiliary energy), reactive-power injection can be easily achieved and power factor correction is feasible.

Taking u_l^+ (or u_l^-) to (7.16) one obtains the limits of active and reactive power p^+ and q^+, respectively (p^- and q^-).

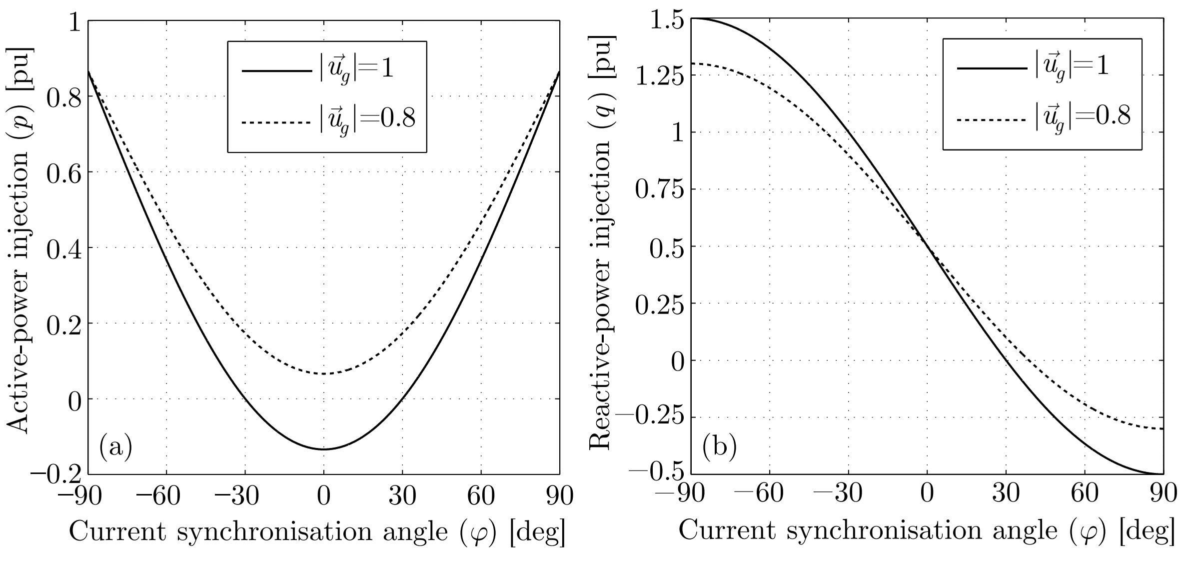

Figure 7.3: (left) Active- and (right) reactive-power injection capability of the SAC when (solid) $|\vec{u}_g| = 1$ and (dashed) $|\vec{u}_g| = 0.8$.

7.5 Power-Flow Controller With Voltage Constraints

7.5.1 Reference Voltage Calculation

The power flow equations in (7.4) can be used for control purposes. To this end, it is assumed that the power injected by the SAC (p) is modified with u'_{c-d}, while the reactive power (q) is modified with u'_{c-q}. If the active- and reactive-power commands are p^* and q^*, respectively, the process can be spelt out as follows:

1. The voltage commands in the CSRF are u'^*_{c-d} and u'^*_{c-q} and can be calculated as

$$\begin{bmatrix} u'^*_{c-d} \\ u'^*_{c-q} \end{bmatrix} = \frac{1}{\sqrt{i^2_{l-d} + i^2_{l-q}}} \begin{bmatrix} q^* \\ p^* \end{bmatrix}. \tag{7.17}$$

2. Once the voltage commands have been computed in the CSRF, they can be referred to the VSRF, in which the control of the SAC is carried out. This transformation is done applying $\mathbf{R}^{-1}(\varphi)$ to the voltage set-point, yielding

$$\begin{bmatrix} u^*_{c-d} \\ u^*_{c-q} \end{bmatrix} = \frac{1}{\sqrt{i^2_{l-d} + i^2_{l-q}}} \begin{bmatrix} i_{l-d} & -i_{l-q} \\ i_{l-q} & i_{l-d} \end{bmatrix} \begin{bmatrix} u'^*_{c-d} \\ u'^*_{c-q} \end{bmatrix}. \tag{7.18}$$

Direct conversion between power commands and reference voltages can also be done merging (7.17) and (7.18):

$$\begin{bmatrix} u^*_{c-d} \\ u^*_{c-q} \end{bmatrix} = \frac{1}{i^2_{l-d} + i^2_{l-q}} \begin{bmatrix} i_{l-d} & -i_{l-q} \\ i_{l-q} & i_{l-d} \end{bmatrix} \begin{bmatrix} p^* \\ q^* \end{bmatrix}, \tag{7.19}$$

but the two-step method based in (7.17) and (7.18) is very advantageous to implement the load-voltage constraints calculated in Section 7.3.

7.5.2 Implementation of the Load-Voltage Constraints

The DC-link voltage of an SAC should be maintained constant during normal operation. This implies that the active-power command should take priority over that of the reactive power. Therefore, limits of the voltage component related to active power (u'^*_{c-d}) should be studied first and limits of the voltage component related to reactive power (u'^*_{c-q}) should be studied in the second place. The maximum value of u'_{c-d} in (7.14) is obtained with $\cos\varphi = 0$ and $|\vec{u}_l| = u^+_l$, while its minimum value is obtained with $\cos\varphi = 1$ and $|\vec{u}_l| = u^-_l$:

$$\begin{aligned} u'^+_{c-d} &= u^+_l \cos\phi, \\ u'^-_{c-d} &= u^-_l \cos\phi - |\vec{u}_g|. \end{aligned} \tag{7.20}$$

The implementation of the procedure described above has been depicted in Fig. 7.4 (top), where u'_{c-d} is saturated using (7.20). Once the reference value for the d'-axis voltage (u'^*_{c-d}) is set either within the limits or at the closest possible limit, the availability of u'^*_{c-q} has to be investigated. Solving $\cos\varphi$ from (7.14) and recalling that $\sin^2\varphi + \cos^2\varphi = 1$, one can find the following solution for $\sin\varphi$:

$$\sin\varphi = \frac{\pm\sqrt{|\vec{u}_g|^2 - \left(|\vec{u}_l|\cos\phi - u'^*_{c-d}\right)^2}}{|\vec{u}_g|}. \tag{7.21}$$

If (7.21) is taken to (7.15), the limits of u'_{c-q} which ensure that the load voltage will be within u_l^- and u_l^+ are

$$\begin{aligned} u'^+_{c-q} &= u_l^+ \sin\phi \mp \sqrt{|\vec{u}_g|^2 - \left(u_l^+\cos\phi - u'^*_{c-d}\right)^2}, \\ u'^-_{c-q} &= u_l^- \sin\phi \mp \sqrt{|\vec{u}_g|^2 - \left(u_l^-\cos\phi - u'^*_{c-d}\right)^2}. \end{aligned} \tag{7.22}$$

Assuming $\cos\varphi > 0$, (7.22) has two possible solutions for each limit: one for $\varphi > 0$ and the other one for $\varphi < 0$. Fig. 7.5 shows the two possible solutions with $|\vec{u}_l| = u_l^+ = u_l^-$. The solution for $\varphi > 0$ is shown in red and the solution for $\varphi < 0$ is shown in green. For inductive loads the series-injected voltage is smaller for $\varphi > 0$, while for capacitive loads $|\vec{u}_c|$ is smaller for $\varphi < 0$. Inductive load is assumed and, therefore, only positive values of φ are considered. Fig. 7.4 (bottom) details the implementation of the constraints for u'^*_{c-q}.

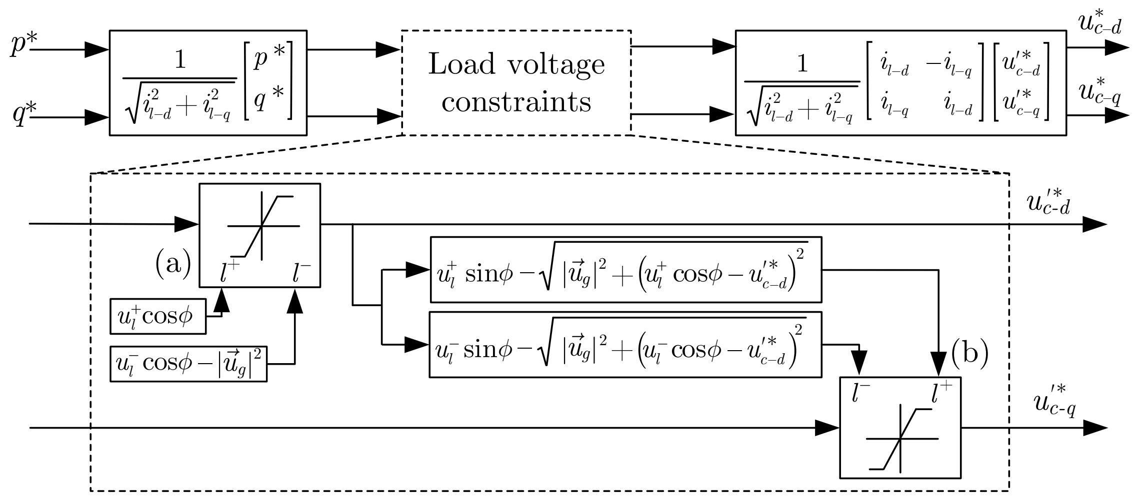

Figure 7.4: Load voltage constraint implementation. Active power is modified with u'_{c-d}, while u'_{c-q} modifies reactive power. Load-voltage constraints imposes limits on both u'_{c-d} and u'_{c-q}. Active power is taken care of first and the remaining voltage-injection capability may be used for reactive-power compensation.

If $|\vec{u}_l| = u_l^+ = u_l^-$, the range for u'_{c-d} is reduced to

$$u'^+_{c-d} = |\vec{u}_l| \cos\phi, \quad u'^-_{c-d} = |\vec{u}_l| \cos\phi - |\vec{u}_g|, \tag{7.23}$$

while u'_{c-q} is fixed because there is no degree of freedom to compensate reactive power:

$$u'^+_{c-q} = u'^-_{c-q} = |\vec{u}_l| \sin\phi \mp \sqrt{|\vec{u}_g|^2 - \left(|\vec{u}_l| \cos\phi - u'^*_{c-d}\right)^2}. \tag{7.24}$$

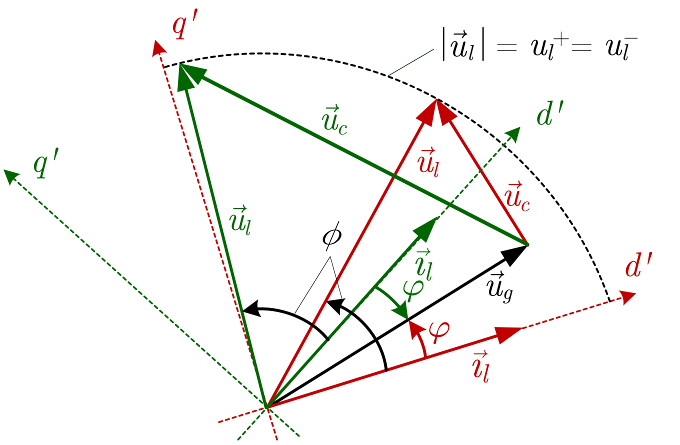

Figure 7.5: Possible solutions for $\vec{u}_c$ with $|\vec{u}_l| = u_l^- = u_l^+$ when the load is inductive.

7.5.3 Minimum Power Compensation of Voltage Sags

Fig. 7.6 shows the power-flow controller implementation with load voltage constraints. The load current ($\vec{i}_l$) and $|\vec{u}_g|$ are filtered with low-pass filters (LPFs) to avoid fast transients and to reject harmonic components. If required, notch filters at specific frequencies may be used (e.g. 100 Hz for negative sequence components).

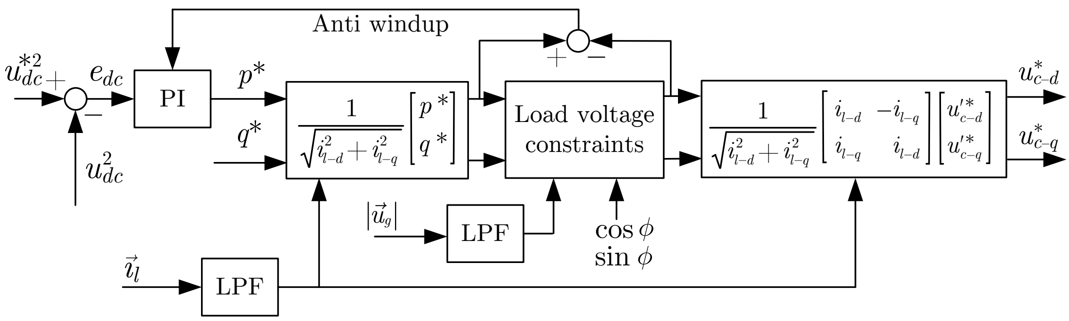

Figure 7.6: Power-flow controller implementation.

The active-power reference (p^*) is calculated with a PI controller applied to the square of the DC-link voltage. Notice that, when a voltage sag takes place, the power required to compensate the load voltage will increase and, accordingly, it will be impossible to maintain the DC-link voltage constant without auxiliary energy. At this point, the PI controller should be deactivated using an anti wind-up mechanism to avoid the failure of the DC-link voltage controller (see Fig. 7.6). Equation (7.20) shows that, if the grid voltage (u_g) falls, u'^{-}_{c-d} increases. When a voltage sag takes place, u'_{c-d} should decrease to maintain the DC-link voltage constant because the active power exchanged by the SAC with the grid is proportional to u'_{c-d}. Therefore, the PI controller will decrease the value of p^* (u'_{c-d}) trying to recover the DC voltage until the anti wind-up mechanism trips. When this happens, the limit of u'^{-}_{c-d} in (7.20) is activated: $u'_{c-d} = u'^{-}_{c-d}$, so $\cos\varphi = 1$. In this case, the active power injected by the SAC will be at its minimum. In other words, minimum-power compensation of the voltage sag will take place.

7.5.4 Load Impedance Identification

The load model must be known beforehand to apply the power-flow formulae presented in Section 7.2 but, in real applications, the load may be unknown or non-linear. Recalling the power-flow formulae, only the load impedance (fundamental-component steady-state characteristic) is required to apply the power controller and it can be estimated as follows

$$Z_l^e \approx \frac{\vec{u}_l^f}{\vec{i}_l^f} = Z_l^f, \tag{7.25}$$

where superscript f stands for "filtered" and superscript e stands for "estimated". If the power related to the harmonic components of the load is zero, (7.25) is fully applicable [14]. For an SAC this condition is always satisfied because, even if the load is non-linear and the grid voltage is polluted with harmonics, the SAC suppress the load-voltage harmonics. Therefore, the power related to harmonic components of the load current will be zero and (7.25) can be applied. The method proposed in this section is simple, but still valid since only the steady-state characteristic of the load is required. The impedance estimation should be carried out in matrix form:

$$|Z_l^e| \begin{bmatrix} \cos\phi^e \\ \sin\phi^e \end{bmatrix} = \frac{1}{i_{l-d}^2 + i_{l-d}^2} \begin{bmatrix} i_{l-d} & i_{l-q} \\ -i_{l-q} & i_{l-d} \end{bmatrix} \begin{bmatrix} u_{l-d} \\ u_{l-q} \end{bmatrix}, \tag{7.26}$$

where the real and imaginary parts of the impedance should be filtered out with LPFs.

7.5.5 Tips for the Controller Implementation

The controller implementation requires:

1. *Signal filtering:* All measurements are filtered to avoid fast transients and harmonic noise. In the prototype, the load-current components (i_{l-d} and i_{l-q}) and

the grid voltage $|\vec{u}_g|$ are filtered with second-order low-pass Butterworth filters (20-Hz cut-off frequency) together with a notch filter tuned at 100 Hz. The latter is used to reject negative sequence components. Besides, if the SAC is to be used together with non-linear loads, notch filters should be added at specific frequencies (e.g. $6k \pm 1$).

2. *Implementation of u'_{c-q} constraints:* Instead of calculating the limits of u'_{c-q} with (7.22), it is better to calculate $\sin\varphi$, first, using (7.21), and then use (7.15) to calculate u'^{+}_{c-q} and u'^{-}_{c-q}. With this procedure $\sin\varphi$ can be limited to ensure that $-1 < \sin\varphi < 1$. If $\sin\varphi$ is not limited, (7.22) may lead to incoherent results during transients.

7.6 Application of the Power Controller

The prototype description can be found in Appendix A. In the experiments reported in this section, the load is balanced, star-connected, and consumes 3.7 kW and 2 kvar at rated voltage. The switching frequency and the sampling frequency have been made equal to 5.4 kHz. A SF controller has been used for the AC voltage controller in Fig. 7.1 and an auxiliary repetitive controller has been added in parallel with the main controller to suppress harmonic components (see Chapter 4).

7.6.1 Experimental Results

Changing the Reference Voltage of the DC-Link

Fig. 7.7 shows the SAC performance when the DC-link reference voltage (u^*_{dc}) is modified and the load voltage constraints are equal ($u_l^- = u_l^+ = 1$ pu). To start with, the system is in steady-state and the DC voltage equals 400 V. This forces the SAC to absorb active power from the grid to compensate losses. The reactive-power command is always zero, as shown in Fig. 7.7 (d) but, initially, 0.25 pu of reactive power is required ($q^+ = q^- = 0.25$ pu) to satisfy the load voltage constraints (1 pu in Fig. 7.7 (f)). After a few milliseconds, the DC-link reference voltage changes to 450 V. As shown in Fig. 7.7 (c), the active power absorbed increases from -0.07 pu to a value close to -0.12 pu. Accordingly, the DC voltage increases. During 0.2 seconds the value of p is almost constant and equal to p^- because the DC-link voltage controller is demanding the maximum power (the controller is saturated). Fig. 7.7 (d) shows that some amount of reactive-power injection is also required during the charge of the DC capacitor to ensure that the load voltage falls within its limits (Fig. 7.7 (f)). In this case, $u'^{-}_{c-q} = u'^{+}_{c-q}$ because $u_l^- = u_l^+$ and the reactive power injected is always imposed by the active-power command. When the DC-link voltage is equal to the reference voltage, p

and q return to their previous value. At $t = 1.1$ s, approximately, the DC-link reference voltage is put back to the initial value (400 V) and, as shown in Fig. 7.7 (c), the active power consumed by the SAC decreases, rapidly. Notice that the discharge of the DC capacitor is faster than the charge because the active-power-injection capability of the SAC is much higher than the absorption capability. Therefore, no limit is reached during the discharging. Fig. 7.7 (g) and (h) verifies that active and reactive powers are proportional to u'_{c-d} and u'_{c-q}, respectively.

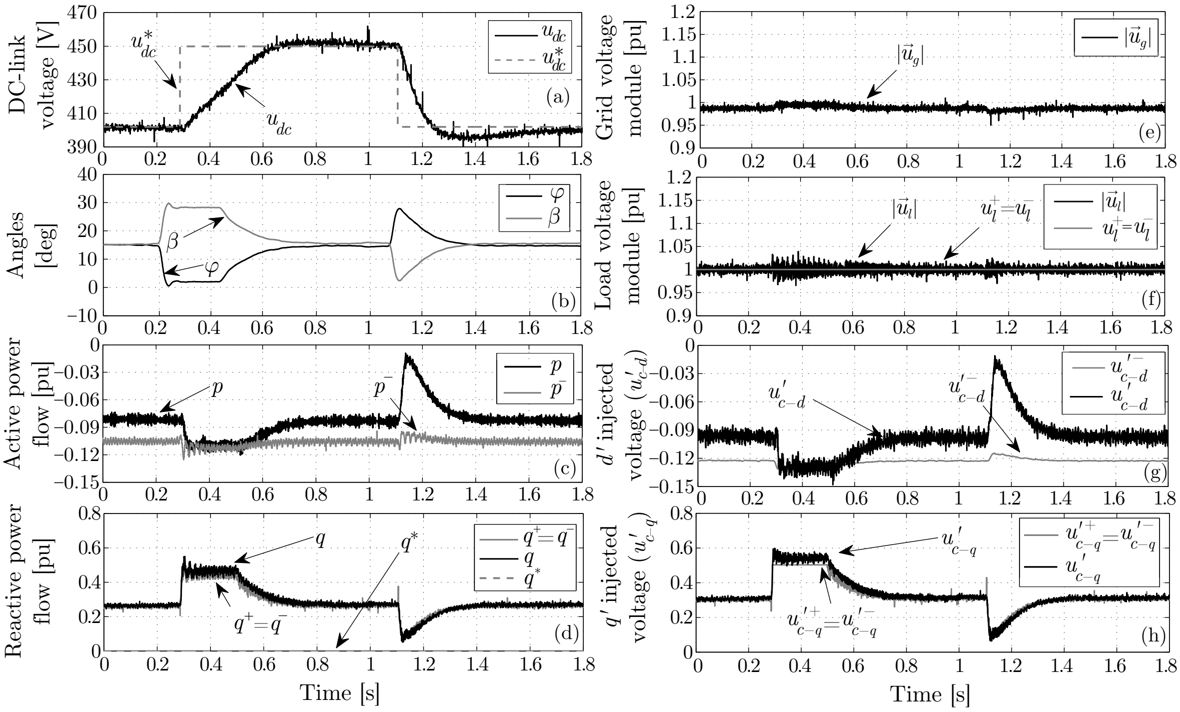

Figure 7.7: (a) DC-link voltage, (b) power controller angles, (c) active power exchange, (d) reactive power exchange, (e) grid voltage module, (f) load voltage module, (g) d'-axis series-injected voltage, and (h) q'-axis series-injected voltage for a step in u^*_{dc}.

Compensating the Reactive Power Consumed by the Load

Fig. 7.8 shows the SAC behaviour when the reactive-power command is changed. In this case, the load-voltage limits are set to $u_l^- = 0.95$ pu and $u_l^+ = 1.1$ pu because, if reactive-power compensation is required, the load voltage limits must be flexible. First of all, the SAC is in steady-state and the DC-link voltage is constant. As shown in Fig. 7.8 (c), the required power to compensate the losses is around -0.07 pu. The reactive-power command 0 pu, initially, but some reactive power is injected to satisfy the load-voltage constraints. When $t = 0.2$ s, the reactive-power command (q^*) is changed from 0 to 0.5 pu, as shown in Fig. 7.8 (d). The reactive power injected rapidly changes and reaches the reference value. Fig. 7.8 (f) shows how the reactive power injected increases the load voltage module from 0.95 pu to 1.03 pu and the lower bound of the load-voltage constraints is no longer active. The reactive-power injection produce extra losses (Fig. 7.8 (c)) and the DC-link voltage changes. The DC-voltage controller modifies the active power to compensate the extra losses, so the DC-link voltage remains constant. Figs. 7.8 (g) and (h) show, again, that u'_{c-d} is proportional to p and u'_{c-q} is proportional to q.

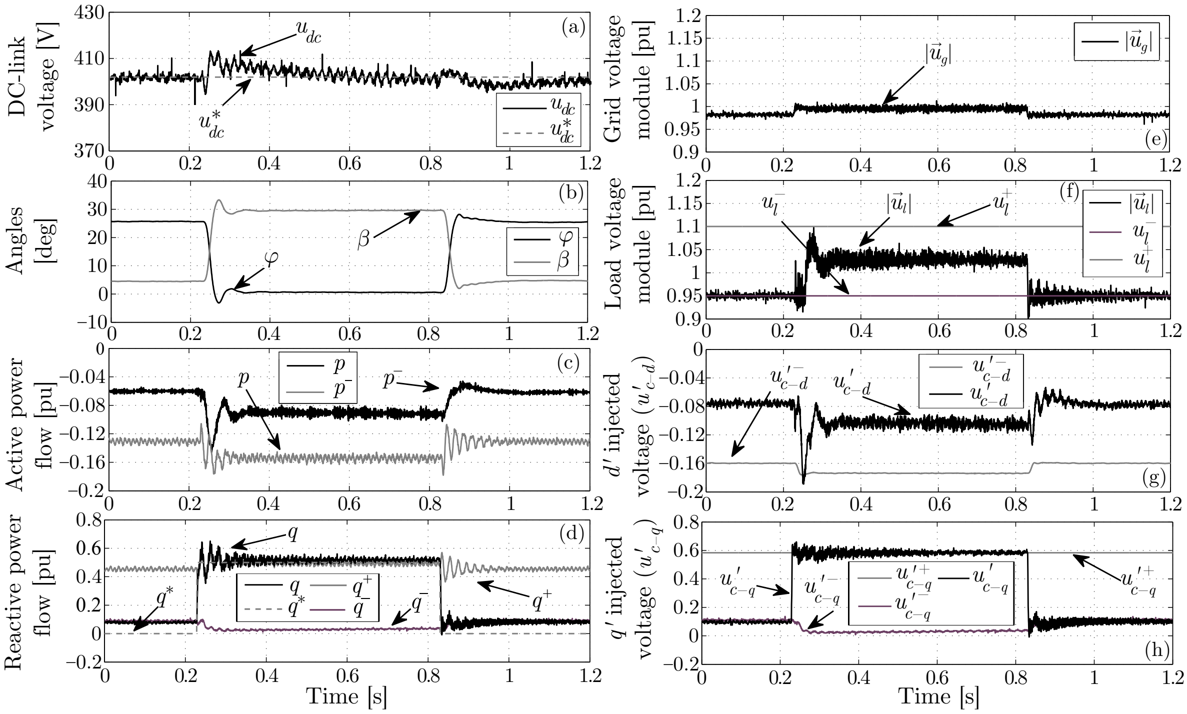

Figure 7.8: (a) DC-link voltage, (b) power controller angles, (c) active power exchange, (d) reactive power exchange, (e) grid voltage module, (f) load voltage module, (g) d'-axis series-injected voltage, and (h) q'-axis series-injected voltage for a step in q^*.

Voltage-Sag Mitigation With Minimum Power Compensation

Fig. 7.9 shows the SAC behaviour when a three-phase voltage sag (60 % retained voltage) takes place. In this case, the load voltage limits have been set to $u_l^- = 0.95$ pu and $u_l^+ = 1.1$ pu. When the voltage sag takes place (Fig. 7.9 (e)), the load voltage is rapidly taken between the load-voltage constraints (Fig. 7.9 (f)). Fig. 7.9 (c) and (d) show the active- and reactive-power injection during the sag, respectively. When the sag takes place, the lower bound for the active-power injection is reached ($p = p^-$) and, therefore, $\varphi = 0$ (Fig. 7.9 (b)). This means that the voltage sag is being restored using the minimum possible power. Since $p^- > 0$ during the sag, the DC-link voltage decreases (Fig. 7.9 (a)) until the DC-link voltage reaches 300 V, where the auxiliary power supply starts working. When the voltage sag ends at $t = 0.7$ s, the DC-link voltage is low, so the SAC absorbs the required power (Fig. 7.9 (c)) to increase the DC-link voltage up to u_{dc}^{*}.

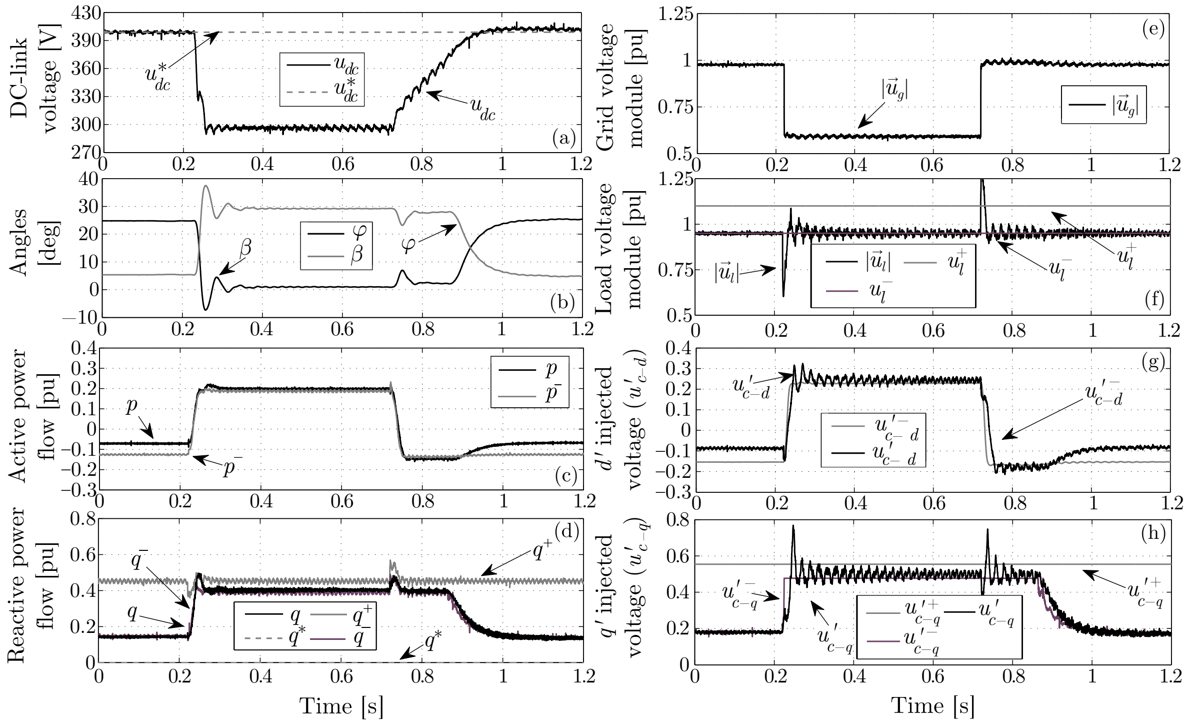

Figure 7.9: (a) DC-link voltage, (b) power-controller angles, (c) active-power exchange, (d) reactive-power exchange, (e) grid-voltage module, (f) load-voltage module, (g) d'-axis series-injected voltage, and (h) q'-axis series-injected voltage for a voltage sag.

Compensation of Voltage Sags, Voltage Harmonics, and Reactive-Power

Fig. 7.10 shows the SAC performance when a voltage sag takes place and the grid voltage is polluted with harmonics. Prior to the voltage sag the SAC injects the required voltage to give a clean load voltage (Fig. 7.10 (a), (b), and (c)). Fig. 7.10 (d) shows the harmonic contents of the grid and load voltages at key frequencies in steady state. Clearly, voltage harmonics present in the grid voltage have been greatly reduced in the load. Figs. 7.10 (f), (g), and (h) show the power flow through the SAC, the power consumed by the load, and the power delivered by the grid, respectively. Prior to the voltage sag, the SAC is compensating the reactive power of the load, so the reactive power delivered by the grid is zero. Meanwhile, the active power delivered by the grid is the power consumed by the load plus the power consumed by the SAC.

When the voltage sag takes place, the SAC rapidly restores the load voltage using the minimum power compensation. Therefore, $p = p^{-}$ in Fig. 7.10 (f). During the sag, the DC-link voltage decreases down to 300 V and the auxiliary power supply starts working. When the voltage sag ends, the SAC starts absorbing active power to increase the DC-link voltage ($t = 150$ ms). During the whole process the reactive power consumed form the grid is almost zero and the load is hardly disturbed.

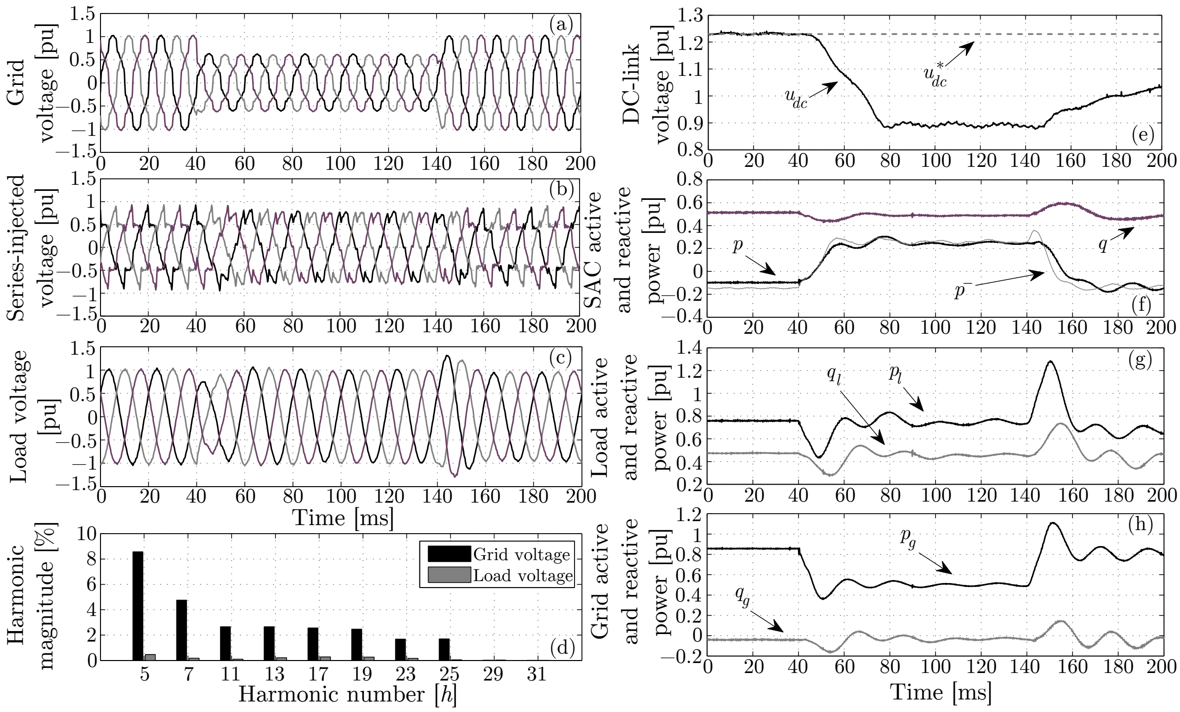

Figure 7.10: (a) Grid voltage, (b) series-injected voltage, (c) load voltage, (d) harmonics magnitude before the voltage sag, (e) DC-link voltage, (f) SAC power flow, (g) power consumed by the load, and (h) power delivered by the grid when the grid voltage is polluted with harmonics and a voltage sag takes place.

7.7 Chapter Summary

This chapter provides a detailed insight into the active- and reactive-power consumption of an SAC in a electrical distribution system. The AC output voltage controller is implemented using a SRF synchronized with the d component of the grid voltage, while the power set-point is calculated in a SRF synchronized with the d component of the load current. Within certain limits, it is possible to independently control the active and reactive power exchanged by the device. Moreover, load-voltage constraints can be easily implemented to be taken into account while controlling active and reactive power. Moreover, minimum-power compensation of voltage sags is easily achieved with the proposed implementation.

Chapter 8

Conclusions and Suggestions for Further Research

The objective of this thesis is to investigate the control system and the applications of a Series Active Conditioner (SAC) in electric power systems. In order to have a very versatile performance, the control system has been divided in two parts: a main controller and an auxiliary controller. The former provides a fast transient response to compensate voltage sags. Meanwhile, the auxiliary controller prevents grid-voltage harmonics from reaching sensitive loads. It was the auxiliary controller the one that drew most of the attention and work of this thesis. Three alternatives have been tested for the auxiliary controller: a repetitive (RC), a proportional-resonant (PRC), and a steady-state space-vector-based (SVB) controller. In the three of them, a number of original contributions have been proposed and validated. In addition to the main and the auxiliary controller, the power-flow limits of SACs have been investigated. All the contributions in this thesis have been validated on a prototype.

8.1 Summary and Conclusions

1. *Series Active Compensation: State of the Art*

   Chapter 2 provides the background on series active compensation and summarizes the state of the art of this type of devices. First of all, the topology of an SAC was detailed: the converter, the transformer, the battery, and the AC filter. Secondly, the basics of series active compensation were explained: voltage-sag compensation strategies, harmonic and unbalance compensation, etc. Finally, several possibilities for the control algorithms for an SAC were reviewed and explained in detail, with special attention to voltage harmonic controllers.

2. *First Steps Towards the Control of an SAC:*

   Chapter 3 spells out the first steps towards the control of an SAC. First of all, a mathematical model is proposed and the control system structure is discussed. The control system proposed in this thesis is divided into a main and an auxiliary controller to facilitate its design and implementation.

   Three alternatives have been investigated for the main controller: a state feedback (SF), a PID, and a cascade controller. The SF controller is not intuitive, but its design is very straightforward. The PID and the cascade controllers exhibit good performance but, when there is no load connected downstream the SAC, only the SF controller is able to damp the LC filter resonance, properly. In any case, none of these controllers is able to tackle either unbalanced voltage sags or voltage harmonics, and this deficiency motivated the rest of the thesis.

   During the work on this topic, it was soon clear that the saturation of the series-injection transformer was a problem for fast transients. This problem has been studied in detail and a solution has been proposed for three-phase transformers. It has been shown that flux-reduction techniques can accurately reduce the DC component of the flux, although the transient performance deteriorates, anyway.

3. *Troubleshooting a Digital Repetitive Controller:*

   Chapter 4 deals with most aspects of the application of a RC to an SAC. Examples of the application of RC to custom power devices can be found in the literature, but mainly in shunt active power filters for harmonic current compensation. The variation of the grid frequency was already detected as an important problem in the applications described so far. In addition, its application to an SAC generates several new problems that were not addressed previously. Probably the most important issue was that the application of a classical RC to an SAC produces a closed-loop system that is not internally stable because the RC cancels the zero of the coupling transformer ($s = 0$) with an unstable pole.

   This thesis has proposed solutions to the problems mentioned above and their viability has been demonstrated in a prototype. The frequency deviation problem has been tackled dividing the RC delay into a fractional part and an integer part, which are calculated based on an estimation of the grid frequency. The integer part has been discretized as a constant delay, while the fractional part has been discretized using an approximation. Two methods to approximate the fractional delay have been tested: one based on a Padé approximation and another one based on a Thiran all-pass filter. Both methods have shown excellent performance for the proposed application. Very recently, Rodríguez-Monter [216] has borrowed this technique for current controllers of VSCs connected to the grid.

The internal instability problem has been solved using two methods. The first one uses a high-pass filter in the RC core to eliminate the RC pole at $s = 0$. The second method uses a gain inside the RC core that limits the controller amplification at all frequencies. Both methods provide similar results and make the RC internally stable when applied to an SAC.

In addition, several alternatives to the classical RC have been investigated, explained, and tested on the prototype: ODD-RCs, EVEN-RCs, $6k$-RCs, $6k\pm1$-RCs, PR-RCs, and NR-RCs. The analysis tools and the implementation solutions developed for the classical RC are also valid for these alternatives. All the alternatives mentioned before have been compared, showing their advantages and drawbacks.

4. *Revisiting Proportional-Resonant Controllers:*

   This chapter revisits the design and the implementation of proportional-resonant controllers (PRCs). Although this type of controllers have been often described in the literature, a novel method to design PRCs has been proposed. This method is directly posed in discrete time and it greatly simplifies the design procedure. Moreover, it leads to high-performance PRCs.

   This chapter also deals with the frequency deviation problem in PRCs. Similarly to the RC case, the performance of PRCs deteriorates with slight frequency variations. It is difficult to adapt PRCs continuously because this increases the computational burden. This chapter proposes a novel method to adapt PRCs that it is easy to implement and it requires less calculations than other methods already proposed in the literature.

   Finally, this chapter highlights the similarities between RCs and PRCs, providing a connection between Chapter 4 and Chapter 5.

5. *Steady-State Space-Vector-Based Harmonic Controller*

   The application of harmonic-compensation algorithms requires previous knowledge of the plant dynamics to ensure closed-loop stability. This makes the application of RCs and PRCs difficult in many PE devices since the model of the plant might vary or be unknown beforehand.

   Chapter 6 proposes a steady-state space-vector-based (SVB) controller to track harmonics. It is implemented using a slow sampling period that makes it possible to use of a very simple MIMO plant model, which consists of a matrix gain and a one-sampling-period delay. This model can be estimated and updated easily each sampling period and closed-loop stability can be guaranteed. The SVB controller has been applied to the prototype, showing its viability. It has been shown that this controller can be used to compensate voltage harmonics (SAC case) or current harmonics (CSeAPF case) and knowledge of the plant dynamics is not required at the design stage. In spite of its apparent limitations, the transient response is reasonably fast.

6. *Power Flow Analysis and Control in an SAC:*

   Active- and reactive-power flow in SACs have been studied in Chapter 7. Active-power flow has drawn much attention in the literature. However, reactive-power flow has been seldom studied because the load voltage constraints made it impossible to manage active and reactive power at the same time.

   This chapter proposes a reference frame for modelling purposes that greatly simplifies the understanding and control of the power flow in an SAC. This reference frame is synchronized with the d-axis component of the load current. It has been shown that adding some flexibility to the load voltage limits (e.g. ± 5 %) the DC-link voltage can be controlled (controlling the active-power flow) while the reactive power consumed by the load can be compensated (controlling the reactive-power flow). The proposed controller has been implemented in the SAC prototype, obtaining good results.

7. *Prototype Description:*

   All the algorithms presented in this thesis have been tested on a dedicated prototype especially built for this purpose. This prototype is versatile and made it possible to test the SAC under several situations.

   There were several types of loads available: resistive, inductive, and non-linear. A programmable three-phase AC voltage source was used to test the SAC under different conditions: voltage sags, voltage harmonics, unbalances, etc. Control systems have been implemented in a *dSpace* platform.

8. *Final Remarks*

   The work carried out in this thesis has demonstrated that SACs can easily play the role of Dynamic Voltage Restorers (DVRs) together with the one of Series Active Power Filters (SeAPF) if a versatile and comprehensive control algorithm is used. Although the actual application of this type of device may still need more work to adjust to every scenario, the work and results presented here show that power electronics can, undoubtedly, contribute to the voltage quality of modern electric power systems.

8.2 Suggestions for Further Research

1. The state-feedback controller presented in Chapter 3 can damp the existing resonance properly. However, the design process is not straightforward because it

is not easy to find the pole-placement position that gives acceptable stability margins. Therefore, it would interesting to develop a tool to asses closed-system stability for state-feedback controllers.

2. All the algorithms presented here have been applied to a three-phase three-wire SAC. However, in some cases voltage sags contain homopolar components that a three-wire SAC can not compensate. Therefore, it would be interesting to apply all the developments of this thesis to a four-wire SAC.

3. Some implementation aspects of RCs have been thoroughly studied during this thesis. However, changes in the plant model has not been studied and they could threaten the system stability. Therefore, further research is needed to provide an adaptive mechanism for RCs when the plant changes.

4. The PRCs presented in this thesis were adapted when the grid frequency varied. However, they can not cope properly with large frequency variations. The performance of PRCs under this circumstance could be greatly improved if changes in the plant model are taken into account, although one should bear in mind that large frequency variations in present electric grids are unlikely. In any case, the use of trigonometric functions should be avoided.

5. The steady-state SVB harmonic controller presented in Chapter 6 provided good results. Moreover, some tips are given to make a good selection of the adaptive gain (α_d). However, there are some aspects that can be studied further:

   - The effects of non-linearities on the system stability. For example, it would be interesting to study the control system behaviour when two harmonics are coupled.
   - The criteria to adapt the controller. In this thesis (a) the plant model was updated if the command signal was above a certain value and (b) the plant was estimated using only the information from the last sampling period. Further research is needed to asses (a) if more information could improve the estimation and (b) to provide a systematic design of the threshold value.

6. The power flow controller presented in Chapter 7 exhibits good results. However, the controller required some time to estimate the reference frame synchronized with the load current and the transient response when compensating voltage sags is slower than the response using other methods presented in this thesis. Further research could improve this transient response.

   The power-flow controller presented in this thesis is only valid when it is applied to a series-connected device. The application of this approach might be also useful in other applications like shunt-series compensators, but this proposals has yet to be investigated.

Bibliography

[1] E. F. Fuchs and M. A. S. Masoum, *Power Quality in Power Systems and Electrical Machines*. Elsevier Academic Press, 2008.

[2] R. C. Dugan, M. F. McGranaghan, S. Santoso, and H. W. Beaty, *Electrical Power Systems Quality*. McGraw-Hill, 2003.

[3] J. Pedra, F. Córcoles, L. Sainz, and R. López, "Harmonic nonlinear transformer modeling," *IEEE Transactions on Power Delivery*, vol. 19, no. 2, pp. 884–890, 2004.

[4] J. Arrillaga and N. R. Watson, *Power System Harmonics*. Wiley, 2004.

[5] E. Acha and M. Madrigal, *Power Systems Harmonics: Computer Modelling and Analysis*, ser. Wiley series in software design patterns. Wiley, 2001.

[6] A. Yazdani and R. Iravani, *Voltage-Sourced Converters in Power Systems*. Wiley, 2010.

[7] M. Bollen, "Voltage sags: effects, mitigation and prediction," *Power Engineering Journal*, vol. 10, no. 3, pp. 129–135, 1996.

[8] R. Carle, "UPS applications: a mill perspective," *IEEE Industry Applications Magazine*, vol. 1, no. 6, pp. 12–17, 1995.

[9] S. Vlahinic, D. Brnobic, and N. Stojkovic, "Indices for harmonic distortion monitoring of power distribution systems," *IEEE Transactions on Instrumentation and Measurement*, vol. 58, no. 5, pp. 1771–1777, May 2009.

[10] ON Semiconductor, *Power Factor Correction Handbook*, 2014.

[11] J. Das, "Passive filters - potentialities and limitations," *IEEE Transactions on Industry Applications*, vol. 40, no. 1, pp. 232–241, 2004.

[12] L. Gyugyi, C. D. Schauder, C. W. Edwards, and M. Sarkozi, "Apparatus and method for dynamic voltage restoration of utility distribution networks," 1994, US Patent 5,329,222.

[13] T. Green and J. Marks, "Ratings of active power filters," *IEE Proceedings - Electric Power Applications*, vol. 150, no. 5, pp. 607–614, 2003.

[14] H. Akagi, E. H. Watanabe, and M. Aredes, *Instantaneous Power Theory and Applications to Power Conditioning.* Wiley, 2007.

[15] P. Roncero-Sánchez, E. Acha, J. Ortega-Calderón, V. Feliu, and A. García-Cerrada, "A versatile control scheme for a dynamic voltage restorer for power-quality improvement," *IEEE Transactions on Power Delivery*, vol. 24, pp. 277–284, 2009.

[16] H. Awad, H. Nelsen, F. Blaabjerg, and M. Newman, "Operation of static series compensator under distorted utility conditions," *IEEE Transactions on Power Systems*, vol. 20, no. 1, pp. 448–457, Feb 2005.

[17] B. Delfino, F. Fornari, and R. Procopio, "An effective SSC control scheme for voltage sag compensation," *IEEE Transactions on Power Delivery*, vol. 20, no. 3, pp. 2100–2107, July 2005.

[18] Y. W. Li, "Control and resonance damping of voltage-source and current-source converters with filters," *IEEE Transactions on Industrial Electronics*, vol. 56, no. 5, pp. 1511–1521, 2009.

[19] P. T. Cheng, J. M. Chen, and C. L. Ni, "Design of a state-feedback controller for series voltage-sag compensators," *IEEE Transactions on Industry Applications*, vol. 45, no. 1, pp. 260–267, 2009.

[20] P. C. Loh and D. G. Holmes, "Analysis of multiloop control strategies for LC/CL/LCL-filtered voltage-source and current-source inverters," *IEEE Transactions on Industry Applications*, vol. 41, no. 2, pp. 644–654, 2005.

[21] J. Hung, "Feedback control with posicast," *IEEE Transactions on Industrial Electronics*, vol. 50, no. 1, pp. 94–99, 2003.

[22] J. Roldán-Pérez, A. García-Cerrada, J. L. Zamora-Macho, P. Roncero-Sánchez, and E. Acha, "Adaptive repetitive controller for a three-phase dynamic voltage restorer," in *Proceedings of the 3rd IEEE International Conference on Power Engineering, Energy and Electrical Drives*, May 2011.

[23] M. Liserre, R. Teodorescu, and F. Blaabjerg, “Multiple harmonics control for three-phase grid converter systems with the use of PI-RES current controller in a rotating frame,” *IEEE Transactions on Power Electronics*, vol. 21, no. 3, pp. 836–841, 2006.

[24] A. Yepes, F. Freijedo, J. Doval-Gandoy, O. López, J. Malvar, and P. Fernandez-Comesaña, “Effects of discretization methods on the performance of resonant controllers,” *IEEE Transactions on Power Electronics*, vol. 25, no. 7, pp. 1692–1712, 2010.

[25] K. Zhou and D. Wang, “Digital repetitive learning controller for three-phase CVCF PWM inverter,” *IEEE Transactions on Industrial Electronics*, vol. 48, pp. 820–830, 2001.

[26] A. García-Cerrada, O. Pinzón-Ardila, V. Feliu-Batlle, P. Roncero-Sánchez, and P. García-González, “Application of a repetitive controller for a three-phase active power filter,” *IEEE Transactions on Power Electronics*, vol. 22, no. 1, pp. 237–246, 2007.

[27] M. Steinbuch, S. Weiland, and T. Singh, “Design of noise and period-time robust high-order repetitive control, with application to optical storage,” *Automatica*, vol. 43, pp. 2086–2095, 2007.

[28] I. Chung, D. Win, S. Park, S. Moon, and J. Park, “The DC-link energy control method in dynamic voltage restorer system,” *International Journal of Electrical Power & Energy Systems*, vol. 27, no. 7, pp. 525–531, 2003.

[29] H. Al-Hadidi, A. Gole, and D. Jacobson, “Minimum power operation of cascade inverter-based dynamic voltage restorer,” *IEEE Transactions on Power Delivery*, vol. 23, no. 2, pp. 889–898, 2008.

[30] M. Haque, “Voltage sag correction by dynamic voltage restorer with minimum power injection,” *IEEE Power Engineering Review*, vol. 21, no. 5, pp. 56–58, 2001.

[31] J. G. Nielsen, “Design and control of a dynamic voltage restorer,” Ph.D. dissertation, Aalborg University, 2002.

[32] D. Ramirez, S. Martinez, C. Platero, F. Blazquez, and R. de Castro, “Low-voltage ride-through capability for wind generators based on dynamic voltage restorers,” *IEEE Transactions on Energy Conversion*, vol. 26, no. 1, pp. 195–203, 2011.

[33] Y. Kim, J. Kim, and S. Ko, “Three-phase three-wire series active power filter, which compensates for harmonics and reactive power,” *IEE Proceedings - Electric Power Applications*, vol. 151, no. 3, pp. 276–282, 2004.

[34] J. Roldán-Pérez, A. García-Cerrada, J. L. Zamora-Macho, P. Roncero-Sánchez, and E. Acha, “Troubleshooting a digital repetitive controller for a versatile dynamic voltage restorer,” *International Journal of Electrical Power & Energy Systems*, vol. 57, no. 0, pp. 105–115, 2014.

[35] L. Zhan and M. Bollen, “Characteristic of voltage dips (sags) in power systems,” *IEEE Transactions on Power Delivery*, vol. 15, no. 2, pp. 827–832, 2000.

[36] P. Heine and M. Lehtonen, “Voltage sag distributions caused by power system faults,” *IEEE Transactions on Power Systems*, vol. 18, no. 4, pp. 1367–1373, 2003.

[37] P. Roncero-Sánchez and E. Acha, “Dynamic voltage restorer based on flying capacitor multilevel converters operated by repetitive control,” *IEEE Transactions on Power Delivery*, vol. 24, no. 1, pp. 277–284, 2009.

[38] M. Bollen, “Characterisation of voltage sags experienced by three-phase adjustable-speed drives,” *IEEE Transactions on Power Delivery*, vol. 12, no. 4, pp. 1666–1671, 1997.

[39] R. C. Leborgne, “Voltage sags: single event characterisation, system performance and source locations,” Ph.D. dissertation, Chalmers University of Technology, 2007.

[40] M. Bollen, *Understanding Power Quality Problems:Voltage Sags and Interruptions.* Wiley-IEEE Press, 2000.

[41] M. Bollen and L. Zhang, “Different methods for classification of three-phase unbalanced voltage dips due to faults,” *Electric Power Systems Research*, vol. 66, no. 1, pp. 59–69, 2003.

[42] V. Ignatova, P. Granjon, and S. Bacha, “Space vector method for voltage dips and swells analysis,” *IEEE Transactions on Power Delivery*, vol. 24, no. 4, pp. 2054–2061, 2009.

[43] M. Bollen, “Voltage recovery after unbalanced and balanced voltage dips in three-phase systems,” *IEEE Transactions on Power Delivery*, vol. 18, no. 4, pp. 1376–1381, 2003.

[44] J. Acharya and W. Xu, “Characteristics of voltage swell in multigrounded systems,” *IEEE Transactions on Power Delivery*, vol. 22, no. 2, pp. 1259–1260, 2007.

[45] E. Owen, “Power disturbance and quality: light flicker voltage requirements,” *IEEE Industry Applications Magazine*, vol. 2, no. 1, pp. 20–27, 1996.

[46] S. Halpin, R. Bergeron, T. Blooming, R. Burch, L. Conrad, and T. Key, "Voltage and lamp flicker issues: should the ieee adopt the iec approach?" *IEEE Transactions on Power Delivery*, vol. 18, no. 3, pp. 1088–1097, 2003.

[47] "IEEE recommended practice–adoption of IEC 61000-4-15:2010, electromagnetic compatibility (EMC)–testing and measurement techniques–flickermeter–functional and design specifications," *IEEE Std 1453-2011*, pp. 1–89, 2011.

[48] "IEEE guide–adoption of IEC/TR 61000-3-7:2008, electromagnetic compatibility (EMC)–limits–assessment of emission limits for the connection of fluctuating installations to MV, HV and EHV power systems," *IEEE Std 1453.1-2012 (Adoption of IEC/TR 61000-3-7:2008)*, pp. 1–78, 2012.

[49] Y. J. Hsu, K. H. Chen, P. Y. Huang, and C. N. Lu, "Electric arc furnace voltage flicker analysis and prediction," *IEEE Transactions on Instrumentation and Measurement*, vol. 60, no. 10, pp. 3360–3368, 2011.

[50] C. Vilar Moreno, H. Amarís Duarte, and J. Usaola Garcia, "Propagation of flicker in electric power networks due to wind energy conversions systems," *IEEE Transactions on Energy Conversion*, vol. 17, no. 2, pp. 267–272, 2002.

[51] F. Z. Peng, "Application issues of active power filters," *IEEE Industry Applications Magazine*, vol. 4, no. 5, pp. 21–30, 1998.

[52] C. Wessels, F. Gebhardt, and F. Fuchs, "Fault ride-through of a dfig wind turbine using a dynamic voltage restorer during symmetrical and asymmetrical grid faults," *IEEE Transactions on Power Electronics*, vol. 26, no. 3, pp. 807–815, 2011.

[53] N. Amatha and B. K. Kumar, "Improving fault ride-through capability of wind generation system using DVR," *International Jounal of Electrical Power and Energy Systems*, vol. 46, pp. 326–33, 2013.

[54] J. Nielsen and F. Blaabjerg, "A detailed comparison of system topologies for dynamic voltage restorers," *IEEE Transactions on Industry Applications*, vol. 41, no. 5, pp. 1272–1280, 2005.

[55] Z. Wang, Q. Wang, W. Yao, and J. Liu, "A series active power filter adopting hybrid control approach," *IEEE Transactions on Power Electronics*, vol. 16, no. 3, pp. 301–310, 2001.

[56] F. Peng, "Harmonic sources and filtering approaches," *IEEE Industry Applications Magazine*, vol. 7, no. 4, pp. 18–25, 2001.

[57] L. Moran, I. Pastorini, J. Dixon, and R. Wallace, "Series active power filter compensates current harmonics and voltage unbalance simultaneously," *IEE Proceedings - Generation, Transmission and Distribution*, vol. 147, no. 1, pp. 31–36, 2000.

[58] P. G. Barbosa, J. Santisteban, and E. Watanabe, "Shunt-series active power filter for rectifiers AC and DC sides," *IEE Proceedings - Electric Power Applications*, vol. 145, no. 6, pp. 577–584, 1998.

[59] M. Hamad, M. Masoud, and B. Williams, "Medium-voltage 12-pulse converter: Output voltage harmonic compensation using a series APF," *IEEE Transactions on Industrial Electronics*, vol. 61, no. 1, pp. 43–52, 2014.

[60] S. Litrán and P. Salmerón, "Analysis and design of different control strategies of hybrid active power filter based on the state model," *IET Power Electronics*, vol. 5, no. 8, pp. 1341–1350, 2012.

[61] H. Fujita and H. Akagi, "A practical approach to harmonic compensation in power systems-series connection of passive and active filters," *IEEE Transactions on Industry Applications*, vol. 27, no. 6, pp. 1020–1025, 1991.

[62] F. Z. Peng, H. Akagi, and A. Nabae, "A new approach to harmonic compensation in power systems-a combined system of shunt passive and series active filters," *IEEE Transactions on Industry Applications*, vol. 26, no. 6, pp. 983–990, 1990.

[63] J. Tian, Q. Chen, and B. Xie, "Series hybrid active power filter based on controllable harmonic impedance," *IET Power Electronics*, vol. 5, no. 1, pp. 142–148, 2012.

[64] A. Varschavsky, J. Dixon, M. Rotella, and L. Moran, "Cascaded nine-level inverter for hybrid-series active power filter, using industrial controller," *IEEE Transactions on Industrial Electronics*, vol. 57, no. 8, pp. 2761–2767, 2010.

[65] H. L. Jou, J. C. Wu, Y. J. Chang, and Y. T. Feng, "A novel active power filter for harmonic suppression," *IEEE Transactions on Power Delivery*, vol. 20, no. 2, pp. 1507–1513, 2005.

[66] L. Jianben, D. Shaojun, C. Qiaofu, and T. Kun, "Modelling and industrial application of series hybrid active power filter," *IET Power Electronics*, vol. 6, no. 8, pp. 1707–1714, 2013.

[67] R. M. Renfrew, "Successful uninterruptible power systems for computers," *IEEE Transactions on Industry and General Applications*, vol. IGA-5, no. 6, pp. 693–698, 1969.

[68] C. Wessels, N. Hoffmann, M. Molinas, and F. Fuchs, "StatCom control at wind farms with fixed-speed induction generators under asymmetrical grid faults," *IEEE Transactions on Industrial Electronics*, vol. 60, no. 7, pp. 2864–2873, 2013.

[69] K. Li, J. Liu, Z. Wang, and B. Wei, "Strategies and operating point optimization of STATCOM control for voltage unbalance mitigation in three-phase three-wire systems," *IEEE Transactions on Power Delivery*, vol. 22, no. 1, pp. 413–422, 2007.

[70] R. Gupta, A. Ghosh, and A. Joshi, "Performance comparison of VSC-based shunt and series compensators used for load voltage control in distribution systems," *IEEE Transactions on Power Delivery*, vol. 26, no. 1, pp. 268–278, 2011.

[71] A. Arulampalam, J. Ekanayake, and N. Jenkins, "Application study of a STATCOM with energy storage," *IEE Proceedings - Generation, Transmission and Distribution*, vol. 150, no. 3, pp. 373–384, 2003.

[72] A. Rodríguez-Monter, "Contributions to cascade linear control strategies applied to grid-connected voltage-source converters," Ph.D. dissertation, Universidad de Alcalá, 2013.

[73] P. Sensarma, K. R. Padiyar, and V. Ramanarayanan, "Analysis and performance evaluation of a distribution STATCOM for compensating voltage fluctuations," *IEEE Transactions on Power Delivery*, vol. 16, no. 2, pp. 259–264, 2001.

[74] Q. N. Trinh and H. H. Lee, "An advanced current control strategy for three-phase shunt active power filters," *IEEE Transactions on Industrial Electronics*, vol. 60, no. 12, pp. 5400–5410, 2013.

[75] V. Khadkikar and A. Chandra, "UPQC-S: A novel concept of simultaneous voltage sag/swell and load reactive power compensations utilizing series inverter of UPQC," *IEEE Transactions on Power Electronics*, vol. 26, no. 9, pp. 2414–2425, 2011.

[76] V. Khadkikar, "Enhancing electric power quality using UPQC: A comprehensive overview," *IEEE Transactions on Power Electronics*, vol. 27, no. 5, pp. 2284–2297, 2012.

[77] W. Guo, L. Xiao, S. Dai, and L. Lin, "Control strategy of a 0.5 MVA/1 MJ SMES based dynamic voltage restorer," *IEEE Transactions on Applied Superconductivity*, vol. 20, no. 3, pp. 1329–1333, 2010.

[78] R. Weissbach, G. Karady, and R. G. Farmer, "A combined uninterruptible power supply and dynamic voltage compensator using a flywheel energy storage system," *IEEE Transactions on Power Delivery*, vol. 16, no. 2, pp. 265–270, 2001.

[79] V. Ramachandaramurthy, C. Fitzer, A. Arulampalam, C. Zhan, M. Barnes, and N. Jenkins, "Control of a battery supported dynamic voltage restorer," *IEE Proceedings - Generation, Transmission and Distribution*, vol. 149, no. 5, pp. 533–542, 2002.

[80] C. J. Huang, S. J. Huang, and F. S. Pai, "Design of dynamic voltage restorer with disturbance-filtering enhancement," *IEEE Transactions on Power Electronics*, vol. 18, no. 5, pp. 1202–1210, 2003.

[81] J. Shi, Y. Tang, K. Yang, L. Chen, L. Ren, J. Li, and S. Cheng, "SMES based dynamic voltage restorer for voltage fluctuations compensation," *IEEE Transactions on Applied Superconductivity*, vol. 20, no. 3, pp. 1360–1364, 2010.

[82] C. Zhan, A. Arulampalam, and N. Jenkins, "Four-wire dynamic voltage restorer based on a three-dimensional voltage space vector PWM algorithm," *IEEE Transactions on Power Electronics*, vol. 18, no. 4, pp. 1093–1102, 2003.

[83] S. Naidu and D. Fernandes, "Dynamic voltage restorer based on a four-leg voltage source converter," *IET Generation, Transmission & Distribution*, vol. 3, no. 5, pp. 437–447, 2009.

[84] A. Ghosh, A. Jindal, and A. Joshi, "Design of a capacitor-supported dynamic voltage restorer (DVR) for unbalanced and distorted loads," *IEEE Transactions on Power Delivery*, vol. 19, no. 1, pp. 405–413, 2004.

[85] T. Jimichi, H. Fujita, and H. Akagi, "Design and experimentation of a dynamic voltage restorer capable of significantly reducing an energy-storage element," *IEEE Transactions on Industry Applications*, vol. 44, no. 3, pp. 817–825, 2008.

[86] P. Kanjiya, B. Singh, A. Chandra, and K. Al-Haddad, "SRF theory revisited to control self-supported dynamic voltage restorer (DVR) for unbalanced and nonlinear loads," *IEEE Transactions on Industry Applications*, vol. 49, no. 5, pp. 2330–2340, 2013.

[87] J. Nielsen, M. Newman, H. Nielsen, and F. Blaabjerg, "Control and testing of a dynamic voltage restorer (DVR) at medium voltage level," *IEEE Transactions on Power Electronics*, vol. 19, no. 3, pp. 806–813, 2004.

[88] M. Newman, D. Holmes, J. Nielsen, and F. Blaabjerg, "A dynamic voltage restorer (DVR) with selective harmonic compensation at medium voltage level," *IEEE Transactions on Industry Applications*, vol. 41, no. 6, pp. 1744–1753, 2005.

[89] E. Sng, S. Choi, and D. Vilathgamuwa, "Analysis of series compensation and DC-link voltage controls of a transformerless self-charging dynamic voltage restorer," *IEEE Transactions on Power Delivery*, vol. 19, no. 3, pp. 1511–1518, 2004.

[90] B. Li, S. Choi, and D. Vilathgamuwa, "Transformerless dynamic voltage restorer," *IEE Proceedings - Generation, Transmission and Distribution*, vol. 149, no. 3, pp. 263–273, 2002.

[91] B. Wang and G. Venkataramanan, "Dynamic voltage restorer utilizing a matrix converter and flywheel energy storage," *IEEE Transactions on Industry Applications*, vol. 45, no. 1, pp. 222–231, 2009.

[92] E. Babaei and M. Kangarlu, "Voltage quality improvement by a dynamic voltage restorer based on a direct three-phase converter with fictitious dc link," *IET Generation, Transmission & Distribution*, vol. 5, no. 8, pp. 814–823, 2011.

[93] E. Babaei, M. Kangarlu, and M. Sabahi, "Mitigation of voltage disturbances using dynamic voltage restorer based on direct converters," *IEEE Transactions on Power Delivery*, vol. 25, no. 4, pp. 2676–2683, 2010.

[94] S. Subramanian and M. K. Mishra, "Interphase AC-AC topology for voltage sag supporter," *IEEE Transactions on Power Electronics*, vol. 25, no. 2, pp. 514–518, 2010.

[95] J. Rosas-Caro, F. Mancilla-David, J. Ramirez-Arredondo, and A. Bakir, "Two-switch three-phase AC-link dynamic voltage restorer," *IET Power Electronics*, vol. 5, no. 9, pp. 1754–1763, 2012.

[96] P. C. Loh, D. Vilathgamuwa, S. K. Tang, and H. Long, "Multilevel dynamic voltage restorer," *IEEE Power Electronics Letters*, vol. 2, no. 4, pp. 125–130, 2004.

[97] A. Massoud, S. Ahmed, P. Enjeti, and B. Williams, "Evaluation of a multilevel cascaded-type dynamic voltage restorer employing discontinuous space vector modulation," *IEEE Transactions on Industrial Electronics*, vol. 57, no. 7, pp. 2398–2410, 2010.

[98] B. Wang, G. Venkataramanan, and M. Illindala, "Operation and control of a dynamic voltage restorer using transformer coupled H-bridge converters," *IEEE Transactions on Power Electronics*, vol. 21, no. 4, pp. 1053–1061, 2006.

[99] J. Barros and J. Silva, "Multilevel optimal predictive dynamic voltage restorer," *IEEE Transactions on Industrial Electronics*, vol. 57, no. 8, pp. 2747–2760, Aug. 2010.

[100] D. Vilathgamuwa, H. M. Wijekoon, and S. Choi, "A novel technique to compensate voltage sags in multiline distribution system amp: The interline dynamic voltage restorer," *IEEE Transactions on Industrial Electronics*, vol. 53, no. 5, pp. 1603–1611, 2006.

[101] M. Vilathgamuwa, A. Perera, and S. Choi, "Performance improvement of the dynamic voltage restorer with closed-loop load voltage and current-mode control," *IEEE Transactions on Power Electronics*, vol. 17, no. 5, pp. 824–834, 2002.

[102] C. Zhan, V. Ramachandaramurthy, A. Arulampalam, C. Fitzer, S. Kromlidis, M. Bames, and N. Jenkins, "Dynamic voltage restorer based on voltage-space-vector PWM control," *IEEE Transactions on Industry Applications*, vol. 37, no. 6, pp. 1855–1863, 2001.

[103] P. C. Krause, O. Wasynczuk, and S. D. Sudhoff, *Analysis of Electric Machinery and Drive Systems*, 2nd ed. Wiley-IEEE Press, Feb. 2002.

[104] T. Jimichi, H. Fujita, and H. Akagi, "An approach to eliminating DC magnetic flux from the series transformer of a dynamic voltage restorer," *IEEE Transactions on Industry Applications*, vol. 44, no. 3, pp. 809–816, 2008.

[105] P. T. Cheng, W. T. Chen, Y. H. Chen, C. L. Ni, and J. Lin, "A transformer inrush mitigation method for series voltage sag compensators," *IEEE Transactions on Power Electronics*, vol. 22, no. 5, pp. 1890–1899, 2007.

[106] C. Fitzer, A. Arulampalam, M. Barnes, and R. Zurowski, "Mitigation of saturation in dynamic voltage restorer connection transformers," *IEEE Transactions on Power Electronics*, vol. 17, no. 6, pp. 1058–1066, 2002.

[107] H. Al-Hadidi, A. Gole, and D. Jacobson, "A novel configuration for a cascade inverter-based dynamic voltage restorer with reduced energy storage requirements," *IEEE Transactions on Power Delivery*, vol. 23, no. 2, pp. 881–888, 2008.

[108] C. Lam, M. Wong, and Y. Han, "Voltage swell and overvoltage compensation with unidirectional power flow controlled dynamic voltage restorer," *IEEE Transactions on Power Delivery*, vol. 23, no. 4, pp. 2513–2521, 2008.

[109] T. Jimichi, H. Fujita, and H. Akagi, "A dynamic voltage restorer equipped with a high-frequency isolated DC-DC converter," *IEEE Transactions on Industry Applications*, vol. 47, no. 1, pp. 169–175, 2011.

[110] F. Badrkhani Ajaei, S. Afsharnia, A. Kahrobaeian, and S. Farhangi, "A fast and effective control scheme for the dynamic voltage restorer," *IEEE Transactions on Power Delivery*, vol. 26, no. 4, pp. 2398–2406, 2011.

[111] B. H. Li, S. Choi, and D. Vilathgamuwa, "Design considerations on the line-side filter used in the dynamic voltage restorer," *IEE Proceedings - Generation, Transmission and Distribution*, vol. 148, no. 1, pp. 1–7, 2001.

[112] F. Mahdianpoor, R. Hooshmand, and M. Ataei, "A new approach to multifunctional dynamic voltage restorer implementation for emergency control in distribution systems," *IEEE Transactions on Power Delivery*, vol. 26, no. 2, pp. 882–890, 2011.

[113] S. Choi, B. Li, and D. Vilathgamuwa, "Design and analysis of the inverter-side filter used in the dynamic voltage restorer," *IEEE Transactions on Power Delivery*, vol. 17, no. 3, pp. 857–864, 2002.

[114] C. Zhan, X. G. Wu, S. Kromlidis, V. K. Ramachandaramurthy, M. Barnes, N. Jenkins, and A. J. Ruddell, "Two electrical models of the lead-acid battery used in a dynamic voltage restorer," *IEE Proceedings - Generation, Transmission and Distribution*, vol. 150, no. 2, pp. 175–182, 2003.

[115] R. Omar and N. Rahim, "Voltage unbalanced compensation using dynamic voltage restorer based on supercapacitor," *International Journal of Electrical Power & Energy Systems*, vol. 43, no. 1, pp. 573–581, 2012.

[116] "Red Eléctrica de España (REE). Procedimiento de Operación 12.3 (P.O. 12.3). Requisitos de respuesta frente a huecos de tensión de las instalaciones de producción de régimen especial. BOE 254, 18485, 24-12-2006, pp. 37017-37019."

[117] D. Vilathgamuwa, A. Perera, and S. Choi, "Voltage sag compensation with energy optimized dynamic voltage restorer," *IEEE Transactions on Power Delivery*, vol. 18, no. 3, pp. 928–936, 2003.

[118] S. Choi, B. Li, and D. Vilathgamuwa, "Dynamic voltage restoration with minimum energy injection," *IEEE Transactions on Power Systems*, vol. 15, no. 1, pp. 51–57, 2000.

[119] M. Bollen, "Algorithms for characterizing measured three-phase unbalanced voltage dips," *IEEE Transactions on Power Delivery*, vol. 18, no. 3, pp. 937–944, 2003.

[120] M. Bollen, T. Tayjasanant, and G. Yalcinkaya, "Assessment of the number of voltage sags experienced by a large industrial customer," *IEEE Transactions on Industry Applications*, vol. 33, no. 6, pp. 1465–1471, 1997.

[121] M. I. Marei, A. B. Eltantawy, and A. A. El-Sattar, "An energy optimized control scheme for a transformerless DVR," *Electric Power Systems Research*, vol. 83, no. 1, pp. 110–118, 2012.

[122] M. Banaei, S. Hosseini, S. Khanmohamadi, and G. Gharehpetian, "Verification of a new energy control strategy for dynamic voltage restorer by simulation," *Simulation Modelling Practice and Theory*, vol. 14, no. 2, pp. 112–125, 2006.

[123] A. Ghosh and G. Ledwich, “Compensation of distribution system voltage using DVR,” *IEEE Transactions on Power Delivery*, vol. 17, no. 4, pp. 1030–1036, 2002.

[124] M. Banaei, S. Hosseini, and G. Gharehpetian, “Inter-line dynamic voltage restorer control using a novel optimum energy consumption strategy,” *Simulation Modelling Practice and Theory*, vol. 14, no. 7, pp. 989 – 999, 2006.

[125] E. Babaei and M. F. Kangarlu, “Sensitive load voltage compensation against voltage sags/swells and harmonics in the grid voltage and limit downstream fault currents using DVR,” *International Journal of Electric Power Systems Research*, vol. 83, pp. 80–90, 2012.

[126] F. Badrkhani Ajaei, S. Farhangi, and R. Iravani, “Fault current interruption by the dynamic voltage restorer,” *IEEE Transactions on Power Delivery*, vol. 28, no. 2, pp. 903–910, 2013.

[127] Y. W. Li, M. D. Vilathgamuwa, P. C. Loh, and F. Blaabjerg, “A dual-functional medium voltage level DVR to limit downstream fault currents,” *IEEE Transactions on Power Electronics*, vol. 22, no. 4, pp. 1330–1340, 2007.

[128] A. Y. Goharrizi, S. H. Hossein, M. Sabahi, and G. B. Charehpetian, “Three-phase HFL-DVR with independently controlled phases,” *IEEE Transactions on Power Electronics*, vol. 27, no. 4, pp. 1706–1718, 2012.

[129] H. Kim and S. K. Sul, “Compensation voltage control in dynamic voltage restorers by use of feed forward and state feedback scheme,” *IEEE Transactions on Power Electronics*, vol. 20, no. 5, pp. 1169–1177, 2005.

[130] C. Ho, H. Chung, and K. Au, “Design and implementation of a fast dynamic control scheme for capacitor-supported dynamic voltage restorers,” *IEEE Transactions on Power Electronics*, vol. 23, no. 1, pp. 237–251, 2008.

[131] Y. W. Li, F. Blaabjerg, D. Vilathgamuwa, and P. C. Loh, “Design and comparison of high performance stationary-frame controllers for DVR implementation,” *IEEE Transactions on Power Electronics*, vol. 22, no. 2, pp. 602–612, 2007.

[132] A. García-Cerrada, P. Roncero-Sánchez, P. García-González, and V. Feliu-Batlle, “Detailed analysis of closed-loop control of output-voltage harmonics in voltage-source inverters,” *IEE Proceedings on Electric Power Applications*, vol. 151, no. 6, pp. 734–743, 2004.

[133] A. Le Roux, H. Mouton, and H. Akagi, “DFT-based repetitive control of a series active filter integrated with a 12-pulse diode rectifier,” *IEEE Transactions on Power Electronics*, vol. 24, no. 6, pp. 1515–1521, 2009.

[134] P. Roncero-Sánchez, E. Acha, J. Ortega-Calderón, V. Feliu-Batlle, and A. García-Cerrada, "Repetitive control for a dynamic voltage restorer for power-quality improvement," in *13th European Conference on Power Electronics and Applications (EPE '09)*, 2009, pp. 1–10.

[135] S. Sasitharan and M. Mishra, "Constant switching frequency band controller for dynamic voltage restorer," *IET Power Electronics*, vol. 3, no. 5, pp. 657–667, 2010.

[136] F. Jowder, "Design and analysis of dynamic voltage restorer for deep voltage sag and harmonic compensation," *IET Generation, Transmission & Distribution*, vol. 3, no. 6, pp. 547–560, 2009.

[137] A. Teke, K. Bayindir, and M. Tumay, "Fast sag/swell detection method for fuzzy logic controlled dynamic voltage restorer," *IET Generation, Transmission & Distribution*, vol. 4, no. 1, pp. 1–12, 2010.

[138] F. Jurado, "Neural network control for dynamic voltage restorer," *IEEE Transactions on Industrial Electronics*, vol. 51, no. 3, pp. 727–729, 2004.

[139] A. Elnady and M. Salama, "Mitigation of voltage disturbances using adaptive perceptron-based control algorithm," *IEEE Transactions on Power Delivery*, vol. 20, no. 1, pp. 309–318, 2005.

[140] V. Blasko and V. Kaura, "A novel control to actively damp resonance in input LC filter of a three-phase voltage source converter," *IEEE Transactions on Industry Applications*, vol. 33, no. 2, pp. 542–550, 1997.

[141] A. Hasanzadeh, C. Edrington, B. Maghsoudlou, F. Fleming, and H. Mokhtari, "Multi-loop linear resonant voltage source inverter controller design for distorted loads using the linear quadratic regulator method," *IET Power Electronics*, vol. 5, no. 6, pp. 841–851, 2012.

[142] S. Saleh, C. Moloney, and M. Azizur Rahman, "Implementation of a dynamic voltage restorer system based on discrete wavelet transforms," *IEEE Transactions on Power Delivery*, vol. 23, no. 4, pp. 2366–2375, 2008.

[143] C. Rech, H. Pinheiro, H. Grundling, H. Hey, and J. Pinheiro, "Comparison of digital control techniques with repetitive integral action for low cost PWM inverters," *IEEE Transactions on Power Electronics*, vol. 18, no. 1, pp. 401–410, 2003.

[144] ——, "A modified discrete control law for UPS applications," *IEEE Transactions on Power Electronics*, vol. 18, no. 5, pp. 1138–1145, 2003.

[145] K. Zhang, Y. Kang, J. Xiong, and J. Chen, "Direct repetitive control of spwm inverter for ups purpose," *IEEE Transactions on Power Electronics*, vol. 18, no. 3, pp. 784–792, 2003.

[146] G. Ramos, R. Costa-Castelló, and J. M. Olm, "Analysis and design of a robust odd-harmonic repetitive controller for an active filter under variable network frequency," *Control Engineering Practice*, vol. 20, no. 9, pp. 895–903, 2012.

[147] R. Griñó, R. Cardoner, R. Costa-Castelló, and E. Fossas, "Digital repetitive control of a three-phase four-wire shunt active filter," *IEEE Transactions on Industrial Electronics*, vol. 54, no. 3, pp. 1495–1503, 2007.

[148] G. Ramos and R. Costa-Castelló, "Power factor correction and harmonic compensation using second-order odd-harmonic repetitive control," *IET Control Theory Applications*, vol. 6, no. 11, pp. 1633–1644, 2012.

[149] G. Escobar, M. Hernández-Gómez, P. Martínez, and M. Martínez-Montejano, "A repetitive-based controller for a power factor precompensator," *IEEE Transactions on Circuits and Systems I*, vol. 54, no. 9, pp. 1968–1976, 2007.

[150] Z. Cao and G. Ledwich, "Adaptive repetitive control to track variable periodic signals with fixed sampling rate," *IEEE/ASME Transactions on Mechatronics*, vol. 7, no. 3, pp. 378–384, 2002.

[151] J. C. Doyle, B. A. Francis, and A. R. Tannenbaum, *Feedback Control Theory.* Macmillan Publishing Company, 1992.

[152] K. J. Åström and R. M. Murray, *Feedback Systems. An Introduction for Scientists and Engineers.* Princeton University Press, 2008.

[153] R. Braatz, "On internal stability and unstable pole-zero cancellations," *IEEE Control Systems Magazine*, vol. 32, no. 5, pp. 15–16, 2012.

[154] R. Costa-Castelló, R. Griñó, and E. Fossas, "Odd-harmonic digital repetitive control of a single-phase current active filter," *IEEE Transactions on Power Electronics*, vol. 19, no. 4, pp. 1060–1068, 2004.

[155] K. Zhou, K.-S. Low, Y. Wang, F.-L. Luo, B. Zhang, and Y. Wang, "Zero-phase odd-harmonic repetitive controller for a single-phase pwm inverter," *IEEE Transactions on Power Electronics*, vol. 21, no. 1, pp. 193–201, 2006.

[156] W. Lu, K. Zhou, D. Wang, and M. Cheng, "A generic digital $nk \pm m$-order harmonic repetitive control scheme for PWM converters," *IEEE Transactions on Industrial Electronics*, vol. 61, no. 3, pp. 1516–1527, 2014.

[157] D. Chen, J. Zhang, and Z. Qian, "Research on fast transient and $6n\pm1$ harmonics suppressing repetitive control scheme for three-phase grid-connected inverters," *IET Power Electronics*, vol. 6, no. 3, pp. 601–610, 2013.

[158] W. Lua, K. Zhoub, and D. Wangc, "General parallel structure digital repetitive control," *International Journal of Control*, vol. 86, no. 1, pp. 70–83, 2012.

[159] R. Bojoi, G. Griva, V. Bostan, M. Guerriero, F. Farina, and F. Profumo, "Current control strategy for power conditioners using sinusoidal signal integrators in synchronous reference frame," *IEEE Transactions on Power Electronics*, vol. 20, no. 6, pp. 1402–1412, 2005.

[160] F. Freijedo, A. Yepes, J. Malvar, O. López, P. Fernandez-Comesaña, A. Vidal, and J. Doval-Gandoy, "Frequency tracking of digital resonant filters for control of power converters connected to public distribution systems," *IET Power Electronics*, vol. 4, no. 4, pp. 454–462, 2011.

[161] A. Yepes, F. Freijedo, O. López, and J. Doval-Gandoy, "Analysis and design of resonant current controllers for voltage-source converters by means of nyquist diagrams and sensitivity function," *IEEE Transactions on Industrial Electronics*, vol. 58, no. 11, pp. 5231–5250, 2011.

[162] X. Yuan, W. Merk, H. Stemmler, and J. Allmeling, "Stationary-frame generalized integrators for current control of active power filters with zero steady-state error for current harmonics of concern under unbalanced and distorted operating conditions," *IEEE Transactions on Industry Applications*, vol. 38, no. 2, pp. 523–532, 2002.

[163] O. Pinzón-Ardila, "Compensación selectiva de armónicos mediante filtros activos de potencia," Ph.D. dissertation, Comillas Pontifical University, Madrid, 2007.

[164] I. Egido, F. Fernández-Bernal, P. Centeno, and L. Rouco, "Maximum frequency deviation calculation in small isolated power systems," *IEEE Transactions on Power Systems*, vol. 24, no. 4, pp. 1731–1738, 2009.

[165] B. Singh and J. Solanki, "An implementation of an adaptive control algorithm for a three-phase shunt active filter," *IEEE Transactions on Industrial Electronics*, vol. 56, no. 8, pp. 2811–2820, 2009.

[166] S. Arya and B. Singh, "Performance of DSTATCOM using leaky LMS control algorithm," *IEEE Journal of Emerging and Selected Topics in Power Electronics*, vol. 1, no. 2, pp. 104–113, 2013.

[167] A. Luo, X. Xu, H. Fang, H. Fang, J. Wu, and C. Wu, “Feedback-feedforward PI-type iterative learning control strategy for hybrid active power filter with injection circuit,” *IEEE Transactions on Industrial Electronics*, vol. 57, no. 11, pp. 3767–3779, 2010.

[168] P. Zanchetta, M. Degano, J. Liu, and P. Mattavelli, “Iterative learning control with variable sampling frequency for current control of grid-connected converters in aircraft power systems,” *IEEE Transactions on Industry Applications*, vol. 49, no. 4, pp. 1548–1555, 2013.

[169] P. Mattavelli, “A closed-loop selective harmonic compensation for active filters,” *IEEE Transactions on Industry Applications*, vol. 37, no. 1, pp. 81–89, 2001.

[170] ——, “Synchronous-frame harmonic control for high-performance AC power supplies,” *IEEE Transactions on Industry Applications*, vol. 37, no. 3, pp. 864–872, 2001.

[171] M. Ochoa-Giménez, J. Roldán-Pérez, A. García-Cerrada, and J. Zamora-Macho, “Space-vector-based controller for current-harmonic suppression with a shunt active power filter,” *European Power Electronics (EPE) Journal*, vol. 24, 2014.

[172] P. García-González, “Modelado, control y aplicación de dispositivos “FACTS” basados en inversores fuente de tensión,” Ph.D. dissertation, Universidad Pontificia Comillas, 2009.

[173] K. J. Åström and B. Wittenmark, *Computer Controlled Systems.* Prentice-Hall, 1984.

[174] P. García-González and A. García-Cerrada, “Control system for a PWM-based STATCOM,” *IEEE Transactions on Power Delivery*, vol. 15, no. 4, pp. 1252–1257, Oct 2000.

[175] K. J. Astrom and T. Hagglund, *PID Controllers: Theory, Design, and Tuning*, 2nd ed. International Society for Measurement and Con, Jan. 1995.

[176] B. Kuo, *Digital Control Systems.* Oxford University Press, 1992.

[177] ——, *Automatic control system.* Prentice-Hall International London, 1962.

[178] B. Friedland, *Control system design: an introduction to state-space methods*, ser. McGraw-Hill series in electrical engineering: Control theory. McGraw-Hill, 1986.

[179] J. Brunke and K. Frohlich, “Elimination of transformer inrush currents by controlled switching. I. theoretical considerations,” *IEEE Transactions on Power Delivery*, vol. 16, no. 2, pp. 276–280, 2001.

[180] ——, "Elimination of transformer inrush currents by controlled switching. II. application and performance considerations," *IEEE Transactions on Power Delivery*, vol. 16, no. 2, pp. 281–285, 2001.

[181] G. Pipeleers, B. Demeulenaere, J. D. Schutter, and J. Swevers, "Robust high-order repetitive control: Optimal performance trade-offs," *Automatica*, vol. 44, no. 10, pp. 2628–2634, 2008.

[182] B. Francis and W. Wonham, "The internal model principle of control theory," *Automatica*, vol. 12, pp. 456–465, 1976.

[183] S. Chen, Y. Lai, S. Tan, and C. Tse, "Analysis and design of repetitive controller for harmonic elimination in pwm voltage source inverter systems," *IET Power Electronics*, vol. 1, no. 4, pp. 497–506, 2008.

[184] Y. Y. Tzou, R. S. Ou, S. L. Jung, and M. Y. Chang, "High-performance programmable AC power source with low harmonic distortion using DSP-based repetitive control technique," *IEEE Transactions on Power Electronics*, vol. 12, no. 4, pp. 715–725, 1997.

[185] M. Steinbuch, "Repetitive control for systems with uncertain period-time," *Automatica*, vol. 38, no. 12, pp. 2103 – 2109, 2002.

[186] M. Tomizuka, "Zero phase error tracking algorithm for digital control," *Journal of Dynamic Systems, Measurement, and Control*, vol. 109, no. 1, pp. 65–68, 1987.

[187] R. W. Longman, "Iterative learning control and repetitive control for engineering practice," *International Journal of Control*, vol. 73, no. 10, pp. 930–954, 2000.

[188] Y. Y. Tzou, S. L. Jung, and H. C. Yeh, "Adaptive repetitive control of PWM inverters for very low THD AC-voltage regulation with unknown loads," *IEEE Transactions on Power Electronics*, vol. 14, no. 5, pp. 973–981, 1999.

[189] T. Doh, J. Ryoo, and M. Chung, "Design of a repetitive controller: an application to the track-following servo system of optical disk drives," *IEE Proceedings on Control Theory and Applications*, vol. 153, no. 3, pp. 323–330, 2006.

[190] X. Chen and M. Tomizuka, "New repetitive control with improved steady-state performance and accelerated transient," *IEEE Transactions on Control Systems Technology*, vol. PP, no. 99, pp. 1–1, 2013.

[191] R. G. Lyons, *Understanding digital signal processing.* Addison Wesley Pub. Co Reading, Mass, 1997.

[192] A.V. Oppenheim, R.W. Schafer, *Digital signal processing.* Prentice-Hall, 1975.

[193] Y. Ye, B. Zhang, K. Zhou, D. Wang, and Y. Wang, "High-performance cascade-type repetitive controller for CVCF PWM inverter: analysis and design," *IET Electric Power Applications*, vol. 1, no. 1, pp. 112–118, 2007.

[194] G. Escobar, P. Mattavelli, M. Hernandez-Gomez, and P. Martinez-Rodriguez, "Filters with linear-phase properties for repetitive feedback," *IEEE Transactions on Industrial Electronics*, vol. 61, no. 1, pp. 405–413, 2014.

[195] T. C. Tsao, Y. X. Quian, and M. Nemani, "Repetitive control for asymptotic tracking of periodic signals with an unknown period," *Journal of Dynamic Systems, Measurement, and Control*, vol. 122, no. 2, pp. 364–369, 2000.

[196] J. Olm, G. Ramos, and R. Costa-Castelloó, "Stability analysis of digital repetitive control systems under time-varying sampling period," *IET Control Theory Applications*, vol. 5, no. 1, pp. 29–37, 2011.

[197] T. Laakso, V. Valimaki, M. Karjalainen, and U. Laine, "Splitting the unit delay [FIR/all pass filters design]," *IEEE Signal Processing Magazine*, vol. 13, no. 1, pp. 30–60, 1996.

[198] K. Tammy, "Active control of radial rotor vibrations," Ph.D. dissertation, Helsinki University of Technology (Espoo, Finland), 2007.

[199] J. Thiran, "Recursive digital filters with maximally flat group delay," *IEEE Transactions on Circuit Theory*, vol. 18, no. 6, pp. 659–664, 1971.

[200] *IEC 61000-3-6. Technical Report. Limits assessment of emission limits of the connection of distorting installations to MV, HV and EHV*, International Electrotecnical Comission (IEC) Std., 2008.

[201] G. Escobar, P. Hernandez-Briones, P. Martínez, M. Hernandez-Gomez, and R. Torres-Olguin, "A repetitive-based controller for the compensation of $6l \pm 1$ harmonic components," *IEEE Transactions on Industrial Electronics*, vol. 55, no. 8, pp. 3150–3158, 2008.

[202] G. Escobar, J. Leyva-Ramos, P. Martinez, and A. Valdez, "A repetitive-based controller for the boost converter to compensate the harmonic distortion of the output voltage," *IEEE Transactions on Control Systems Technology*, vol. 13, no. 3, pp. 500–508, 2005.

[203] P. Loh, Y. Tang, F. Blaabjerg, and P. Wang, "Mixed-frame and stationary-frame repetitive control schemes for compensating typical load and grid harmonics," *IET Power Electronics*, vol. 4, no. 2, pp. 218–226, 2011.

[204] R. Costa-Castelló, D. Wang, and R. Griñó, "A passive repetitive controller for discrete-time finite-frequency positive-real systems," *IEEE Transactions on Automatic Control*, vol. 54, no. 4, pp. 800–804, 2009.

[205] J. Na, R. Griñó, R. Costa-Castelló, X. Ren, and Q. Chen, "Repetitive controller for time-delay systems based on disturbance observer," *IET Control Theory Applications*, vol. 4, no. 11, pp. 2391–2404, 2010.

[206] W. Lu, K. Zhou, D. Wang, and M. Cheng, "A general parallel structure repetitive control scheme for multiphase DC-AC PWM converters," *IEEE Transactions on Power Electronics*, vol. 28, no. 8, pp. 3980–3987, 2013.

[207] T. Inoue, "Practical repetitive control system design," in *Proceedings of the 29th IEEE Conference on Decision and Control*, vol. 3, 1990, pp. 1673–1678.

[208] W. S. Chang, I. H. Suh, and T. W. Kim, "Analysis and design of two types of digital repetitive control systems," *Automatica*, vol. 31, no. 5, pp. 741–746, 1995.

[209] G. Pipeleers, B. Demeulenaere, F. Al-Bender, J. De Schutter, and J. Swevers, "Optimal performance tradeoffs in repetitive control: Experimental validation on an active air bearing setup," *IEEE Transactions on Control Systems Technology*, vol. 17, no. 4, pp. 970–979, 2009.

[210] G. Pipeleers, B. Demeulenaere, J. De Schutter, and J. Swevers, "Generalised repetitive control: relaxing the period-delay-based structure," *IET Control Theory Applications*, vol. 3, no. 11, pp. 1528–1536, 2009.

[211] A. Yepes, F. Freijedo, O. López, and J. Doval-Gandoy, "High-performance digital resonant controllers implemented with two integrators," *IEEE Transactions on Power Electronics*, vol. 26, no. 2, pp. 563–576, 2011.

[212] M. Abramowitz and I. A. Stegun, *Handbook of Mathematical Functions with Formulas, Graphs, and Mathematical Tables*, 9th ed. New York: Dover, 1964.

[213] I. Gradshteyn and I. Ryzhik, *Table of integrals, series, and products*, 7th ed. Elsevier/Academic Press, Amsterdam, 2007.

[214] J. Roldán-Pérez, M. Ochoa-Giménez, A. García-Cerrada, and J. Zamora, "Efficient real-time computation of harmonics in power systems using multiple reference frames," in *Seminario Anual de Automática, Electrónica industrial e Instrumentación (SAAEI2013)*, 2013.

[215] M. Ochoa-Giménez, J. Roldán-Pérez, A. García-Cerrada, and J. L. Zamora, "Space-vector-based controller for current-harmonic suppression with a shunt active power filter," in *15th European Conference on Power Electronics and Applications (EPE)*, 2013, pp. 1–10.

[216] A. Rodríguez-Monter, E. Bueno, A. García-Cerrada, F. Rodríguez, and F. Sánchez, "Detailed analysis of the implementation of frequency-adaptive resonant and repetitive current controllers for grid-connected converters," *Electric Power Systems Research*, vol. 116, pp. 231–242, 2014.

[217] *dSpace DS1103 User Manual.*

[218] O. Montero-Hernandez and P. Enjeti, "A fast detection algorithm suitable for mitigation of numerous power quality disturbances," *IEEE Transactions on Industry Applications*, vol. 41, no. 6, pp. 1684–1690, Nov 2005.

[219] R. Naidoo and P. Pillay, "A new method of voltage sag and swell detection," *IEEE Transactions on Power Delivery*, vol. 22, no. 2, pp. 1056–1063, April 2007.

[220] D. Granados-Lieberman, R. Romero-Troncoso, R. Osornio-Rios, A. Garcia-Perez, and E. Cabal-Yepez, "Techniques and methodologies for power quality analysis and disturbances classification in power systems: a review," *IET Generation, Transmission & Distribution*, vol. 5, no. 4, pp. 519–529, April 2011.

[221] B. Bae, J. Jeong, J. Lee, and B. Han, "Novel sag detection method for line-interactive dynamic voltage restorer," *IEEE Transactions on Power Delivery*, vol. 25, no. 2, pp. 1210–1211, April 2010.

[222] B. Bae, J. Lee, J. Jeong, and B. Han, "Line-interactive single-phase dynamic voltage restorer with novel sag detection algorithm," *IEEE Transactions on Power Delivery*, vol. 25, no. 4, pp. 2702–2709, Oct 2010.

[223] B. Polajzer, G. Stumberger, S. Seme, and D. Dolinar, "Detection of voltage sag sources based on instantaneous voltage and current vectors and orthogonal clarke's transformation," *IET Generation, Transmission & Distribution*, vol. 2, no. 2, pp. 219–226, March 2008.

[224] C. Fitzer, M. Barnes, and P. Green, "Voltage sag detection technique for a dynamic voltage restorer," *IEEE Transactions on Industry Applications*, vol. 40, no. 1, pp. 203–212, Jan 2004.

[225] Y. Liang, "A new time domain positive and negative sequence component decomposition algorithm," in *IEEE Power Engineering Society General Meeting, 2003*, vol. 3, July 2003.

[226] G. H. Hardy, J. E. Littlewood, and G. Plya, *Inequalities*, ser. Cambridge mathematical library. Cambridge: Cambridge University Press, 1994.

Appendix A

Prototype Description

This appendix describes the hardware of the SAC prototype, the data acquisition system, and a method to measure the execution time of the control algorithms.

A.1 Hardware Description

The laboratory test-rig used throughout this work is depicted in Fig. A.1. The nominal line-to-line voltage at the PCC has been set to 230 V (phase-to-phase) and 50 Hz. The grid is emulated with an AMX-Pacific 3120 12 kVA three-phase voltage source. This voltage source can be used to generate voltage sags with a programmable amplitude and phase for each of the three-phases. Furthermore, the output voltage waveform can be modified with harmonics up to the 65th component. The fundamental frequency can be varied between 20 Hz and 100 Hz. The maximum line-to-ground voltage is 150 V (260 V line-to-line) and the maximum current is 32 A, although during transients the current can be much larger. The line impedance is emulated with an inductor of $L_g = 700\ \mu$H and $R_g = 40$ mΩ rated at 30 A.

The SAC consists of a 2-level 3-leg IGBT-based VSC based on the commercial package SKS22F B6U. This package provides a VSC, a diode rectifier, a DC capacitor (1.3 mF, 750 V), a DC-DC converter ("braking chopper"), and a soft-charge circuit. The VSC is rated at 380 V phase-to-phase (maximum of 750 V DC) and 22 A. The efficiency is 97 % at rated conditions and the absolute maximum switching frequency is 15 kHz. A resistor of 17 Ω (maximum of 10 kW in 10 s, or 1 kW continuously) is used together with the DC-DC converter to protect the SAC in case of DC over voltage. A 1.8 mH inductor has been added to the AC side of the diode rectifier to limit the harmonic content of its current. This rectifier can be connected to (a) an auxiliary electrical network, (b) to the grid-side of the SAC, or (c) to the load-side of the SAC. Therefore, many experiments can be carried out changing only the rectifier connection.

Loads are connected downstream the SAC using a manual breaker rated at 400 V

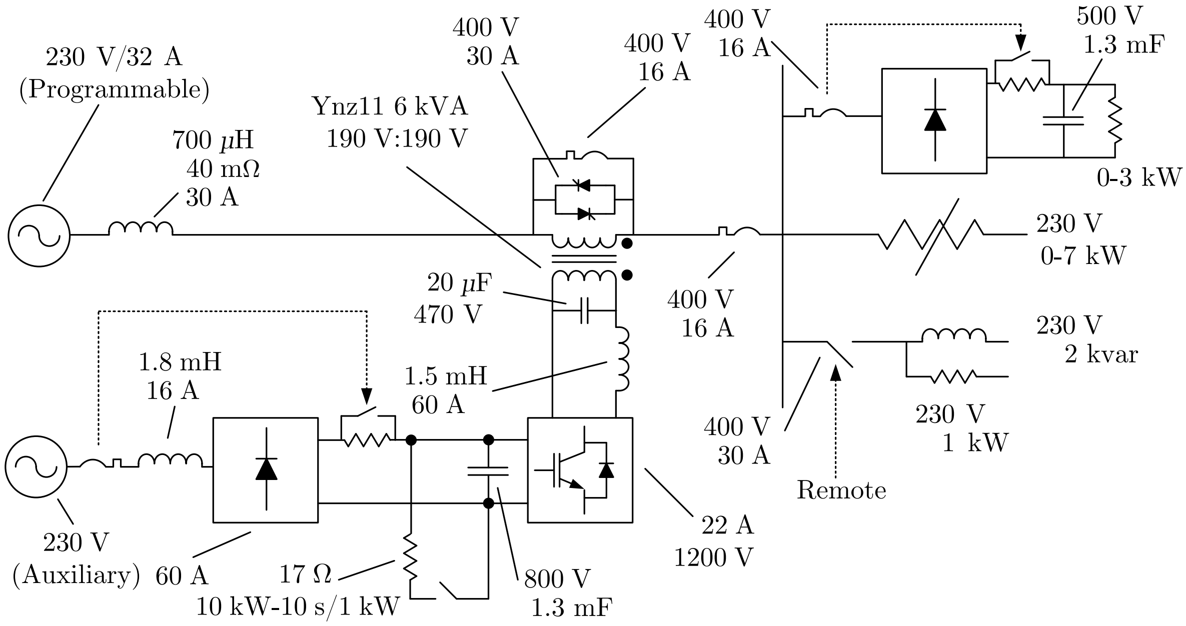

Figure A.1: Schematics of the prototype. The power can be taken from (a) an auxiliary electrical network, (b) the grid-side of the SAC, or (c) the load-side of the SAC.

and 16 A. The load used consists of a linear load and a non-linear load. The linear load is divided in two parts. The first one is remotely controlled an consist of a parallel RL circuit that consumes 1 kW and 2 kvar at rated conditions. The second part is resistive and consumes between 0 kW and 7 kW at rated conditions with steps of 1 kW. This configuration allows a wide variety of power factors. The standard load used for the tests consumes 3 kW and 2 kvar at rated voltage (0.88 power factor). Also, a 1 kW single-phase resistive load can be added between two phases to emulate unbalanced loads. The non-linear load consist of a diode rectifier with a soft-charge circuit. The DC-side of the load can be used with an inductive or a capacitive filter. The DC capacitor value is 1.3 mF, the DC inductor value is 39 mH, and the DC load can consume between 0 and 3 kW at 320 V DC.

The series-coupling transformer is a 6 kVA three-phase transformer with unity turn ratio (190 V:190 V) and Ynz11 connection. This connection, although is not very common, redistribute the current through the windings when the loads are unbalanced. This transformer was chosen because it was deemed the most adequate among the ones available in the laboratory. The Y side of the transformer is connected to the VSC. This transformer has a series resistance and a leakage inductance of $R_t = 0.15\ \Omega$ and $L_t = 3$ mH, respectively. The filter capacitor value for the AC filter is $C_f = 20\ \mu$F and the filter inductor is $L_f = 1.5$ mH, giving a 918 Hz cut-off frequency for the $L_f + C_f$ filter. When the SAC is not connected to the grid, it is bypassed using three independent solid-state relays (SSR) rated at 400 V and 30 A. Also, a manual breaker is added in parallel to the SSRs to bypass the SAC when it is not going to be used. During the experiments reported in this thesis the SAC was always connected to the grid because voltage distortion at the load voltage was one of the problems to be addressed. However, in DVR applications the device is connected only when a voltage sag is detected.

A.2 Data Acquisition and Control System

A.2.1 Measurement Chains

Currents are measured using current sensors *LEM LA25-NP* (1 mA/1 A) with one turn, while voltages are measured using voltage sensors *LEM LV25-P* (500 V). All the measurements are filtered using low-pass filters before the data acquisition system. The filters were selected as fifth-order Bessel's filters with 2600 Hz cut-off frequency and they were implemented using the integrated circuit *LT1065*. The operational amplifiers *AD8031AN* and *AD8032AN* were used to improve the signal-to-noise ratio before measuring with the analog-to-digital converters (ADCs). The Bessel's filters mentioned above can be approximated by one-sampling-period delay in each measured signal, so they can be easily taken into account in the controller designs [26].

A.2.2 Controller Implementation and Data Logging

The platform *dSpace DS1103* was used to run the control algorithms and to generate the PWM signals for the VSC and the DC-DC converter. The control systems were developed in a PC using *MATLAB R2010b* and *Simulink*. The control algorithms were tested first in simulation and then compiled and downloaded to the DSP using a compiler provided by *dSpace*. The DSP is connected to the PC using a high-speed fiber-optic link, thanks to which a large number of variables can be stored simultaneously in real time. The visualization and the capture of the results were done using *ControlDesk v5.5*, which was included with the *dSpace* platform.

A.2.3 Pulse-Width Modulation

The PWM calculations are carried out in an slave DSP *TM320F240*, which is included in the *dSpace* platform. The inverter switching frequency and the sampling frequency have been made constant and equal to 5.4 kHz. The main DSP updates the PWM values and triggers the slave DSP each sampling period, so both processes run synchronized. The PWM strategy is a symmetric sinusoidal PWM with constant switching frequency [217].

A.3 Execution Time Measurement

The *dSpace* platform gives access to a variable, called *turnaroundTime*, that contains the execution time of the whole control system for each sampling period. To measure the execution time of a group of calculations, all of them must be included in a *Simulink* subsystem with an *Enable* block. The method to measure the execution time can be easily understood with the following example.

Fig. A.2 shows the total execution time required to compute the control system of the SAC. Eventually, a subsystem is enabled and the computational burden increases. In order to obtain an averaged value of the execution time, a moving-average filter of 108 samples (1 grid cycle) is applied to the measured value. Finally, the initial execution time is subtracted from the final execution time to obtain the execution time of the subsystem (3.8 μs in the example).

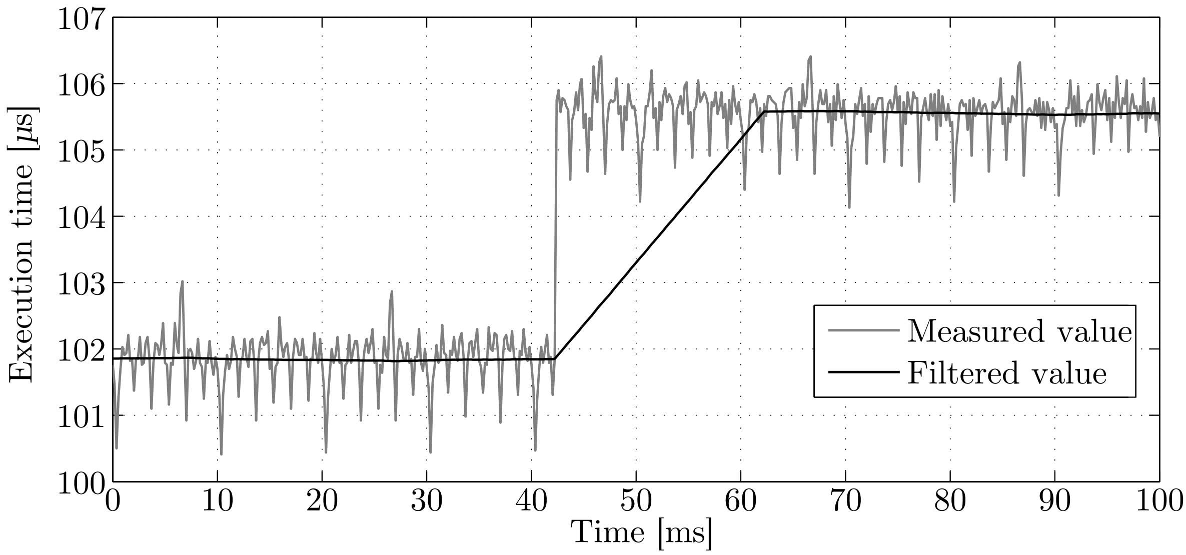

Figure A.2: Total execution time in the dSpace platform when a subsystem is enabled.

Appendix B

Sag Detection Algorithm

This appendix describes a sag detection algorithm that has been developed in close relation to the work done in this thesis. The algorithm is analysed and later tested in the SAC prototype to show its viability.

B.1 Sag Detection Techniques Overview

Voltage sags can be identified using the RMS value of the grid voltage, the peak value, or any other simple measurement [218, 219]. These methods are robust, but also slow and they can lead to erroneous results when the grid voltage is distorted. Other methods are based on complex operations, like Kalman filters [220], DFTs [221, 222], or wavelets [220]. These alternative methods can provide good results, but their computational burden is high and they are, sometimes, difficult to implement.

A sag detection algorithm can be implemented in a SRF, a stationary RF, or using natural magnitudes [220, 223]. However, space-vector techniques (using both a stationary or a SRF) require to split the negative- and the positive-sequence components [224]. In the method proposed here the magnitude of each phase voltage is estimated separately and it is not necessary to identify the negative-sequence component of the grid voltage. This algorithm is inspired by the one proposed by Liang [225], although the analysis method is completely different.

B.2 Algorithm Description

B.2.1 A First Approach to Voltage Sag Detection

The voltage of one phase in a three-phase system can be modelled, ideally, as:

$$u(t) = U_g \cos(\omega_g t),\ t \geq 0, \tag{B.1}$$

where $\omega_g = 2\pi t_g$ is the grid frequency and U_g is the peak value. If $u'(t)$ is a signal in quadrature with $u(t)$, the amplitude of $u(t)$ can be computed as $U_g = \sqrt{u^2(t) + u'^2(t)}$ to assess whether a voltage sag took place. Under ideal conditions the value of $u'(t)$ can be estimated, for instance, delaying $u(t)$ a quarter period,

$$u'(t) = u(t - t_g/4). \tag{B.2}$$

This method is straightforward to implement, but it is slow because it requires $t_g/4$ s to compute the quadrature signal (5 ms for a 50 Hz signal).

B.2.2 Improving the Quadrature Signal Estimation

Voltage sags can be detected faster if the quadrature signal is calculated faster than in (B.2), and this the objective of this section.

A possible description of a time-varying phasor using $u(t)$ and $u'(t)$ is:

$$\overline{u}(t) = u(t) + ju'(t), \tag{B.3}$$

which can be rotated using an arbitrary angle φ_r, yielding:

$$\overline{u}_r(t) = e^{-j\varphi_r}\overline{u}(t) = (\cos\varphi_r + j\sin\varphi_r)\overline{u}(t), \tag{B.4}$$

or in matrix form,

$$\begin{bmatrix} u_r(t) \\ u_r'(t) \end{bmatrix} = \begin{bmatrix} \cos\varphi_r & \sin\varphi_r \\ -\sin\varphi_r & \cos\varphi_r \end{bmatrix} \begin{bmatrix} u(t) \\ u'(t) \end{bmatrix}. \tag{B.5}$$

From the first row of (B.5):

$$u'(t) = \frac{1}{\sin\varphi_r}\left(u(t)\cos\varphi_r - u_r(t)\right). \tag{B.6}$$

The value of $u_r(t)$ in (B.6) can be obtained delaying $u(t)$ a time φ_r/ω_g, yielding:

$$u_r(t) = u(t - \varphi_r/\omega_g). \tag{B.7}$$

Replacing (B.7) in (B.6) and transforming the result to the discrete-time domain:

$$u'[k] = \frac{1}{\sin\varphi_r}\left(u\left[k - \frac{\varphi_r}{\omega_g t_s}\right] - u[k]\cos\varphi_r\right). \tag{B.8}$$

Equation (B.8) shows how to calculate $u'[k]$ using an arbitrary sample of $u[k]$. For a simple realisation, $N_r = \varphi_r/(\omega_g t_s) \in \mathbb{N}$ so that $u[k - N_r]$ can be computed using an integer delay. However, if ω_g changes during operation, the value of φ_r should be modified to maintain the ratio $\varphi_r/(\omega_g t_s)$ constant:

$$\varphi_r = \omega_g\left(\varphi_r^*/\omega_g^*\right), \tag{B.9}$$

where φ_r^* and ω_g^* are the design values of φ_r and ω_g, respectively. For the practical implementation, ω_g is taken from the PLL and it is filtered with a LPF.

B.2.3 Parameter Design

From Section B.2.2, it is obvious that the value N_r modifies the time required to estimate $u'[k]$: a small value of N_r will speed up the detection, while a large value will slow it down. Moreover, (B.8) shows that, actually, $u'[k]$ is computed with a FIR filter in which the coefficients are calculated according to φ_r, ω_g, and t_s. Therefore, the dynamics of this filter can be assessed using z-domain techniques.

Fig. B.1 shows the frequency response of $U'(z)/U(z)$ (z-domain transfer function that relates $u'[k]$ and $u[k]$) for different values of N_r. For low values of N_r the magnitude at high frequencies is large and, therefore, noise is greatly amplified. For higher values of N_r the magnitude at high frequencies is smaller and there are frequencies in which the frequency response of $U'(z)/U(z)$ has minimum values. For example, when $N_r = 18$ samples ($\varphi_r = 60$ deg), the frequency response has minima (magnitude) at frequencies $6h\omega_g$ and its magnitude at the $6h \pm 1$ harmonics is equal to one. Therefore, this alternative seems to be a good a choice when the grid voltage is polluted with harmonics.

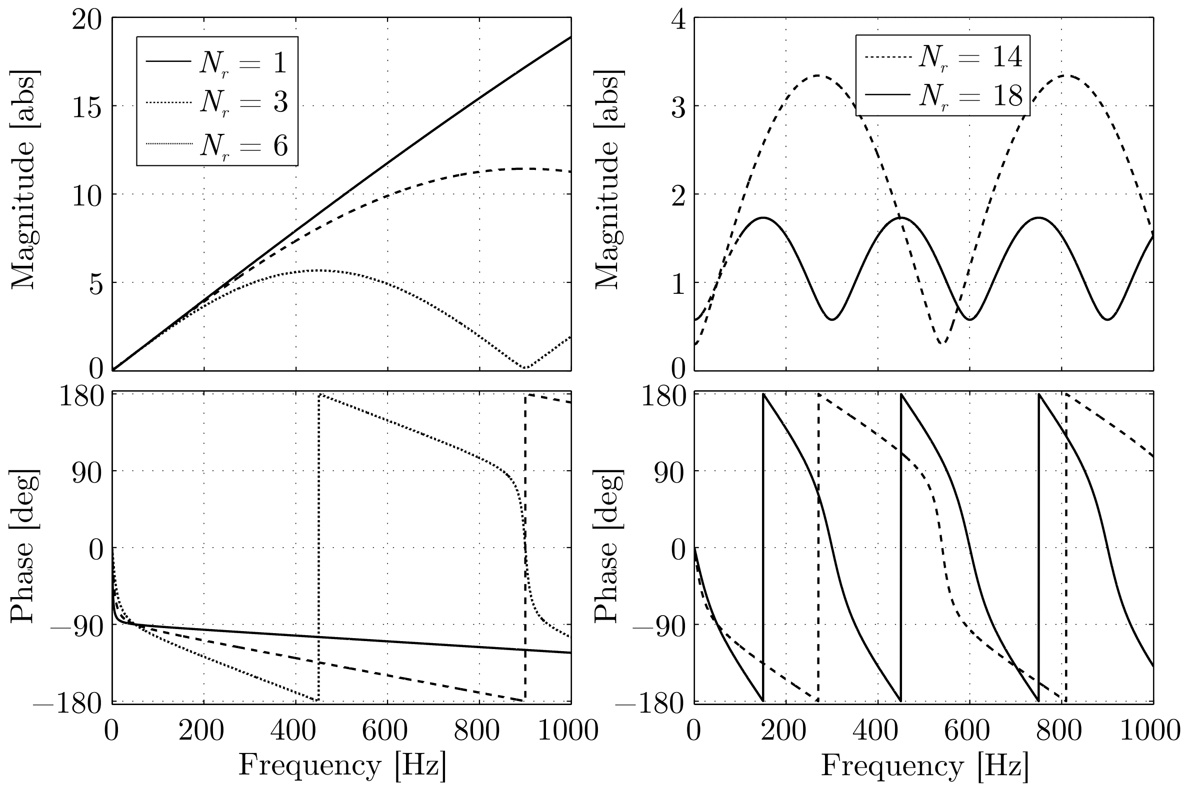

Figure B.1: Bode diagram of $U'(z)/U(z)$ for different values of N_r.

B.3 Experimental Results

The sag-detection algorithm was tested in the SAC protytpe (see Appendix A), where $t_s = 1/5400$ s and $\omega_g^* = 2\pi 50$ rad/s. During the tests, the SAC was working to maintain a constant and clean load voltage using a SF controller and a RC (see Chapter 4).

Fig. B.2 (a to d) shows the grid voltage during a voltage sag and the voltage-phasor modulus estimated by the detection algorithm for different values of N_r. The lower the value of N_r is, the faster the sag is detected, but the higher the noise amplification is. Notice that the error during the transient is higher when N_r is low. Fig. B.2 (e) shows the grid voltage during a voltage sag, but in this case it is polluted with harmonics. In Fig. B.2 (f) ($N_r = 12$) and Fig. B.2 (h) ($N_r = 24$), the harmonics are clearly amplified but, when $N_r = 18$, the harmonics are not amplified a great deal and detection is easier.

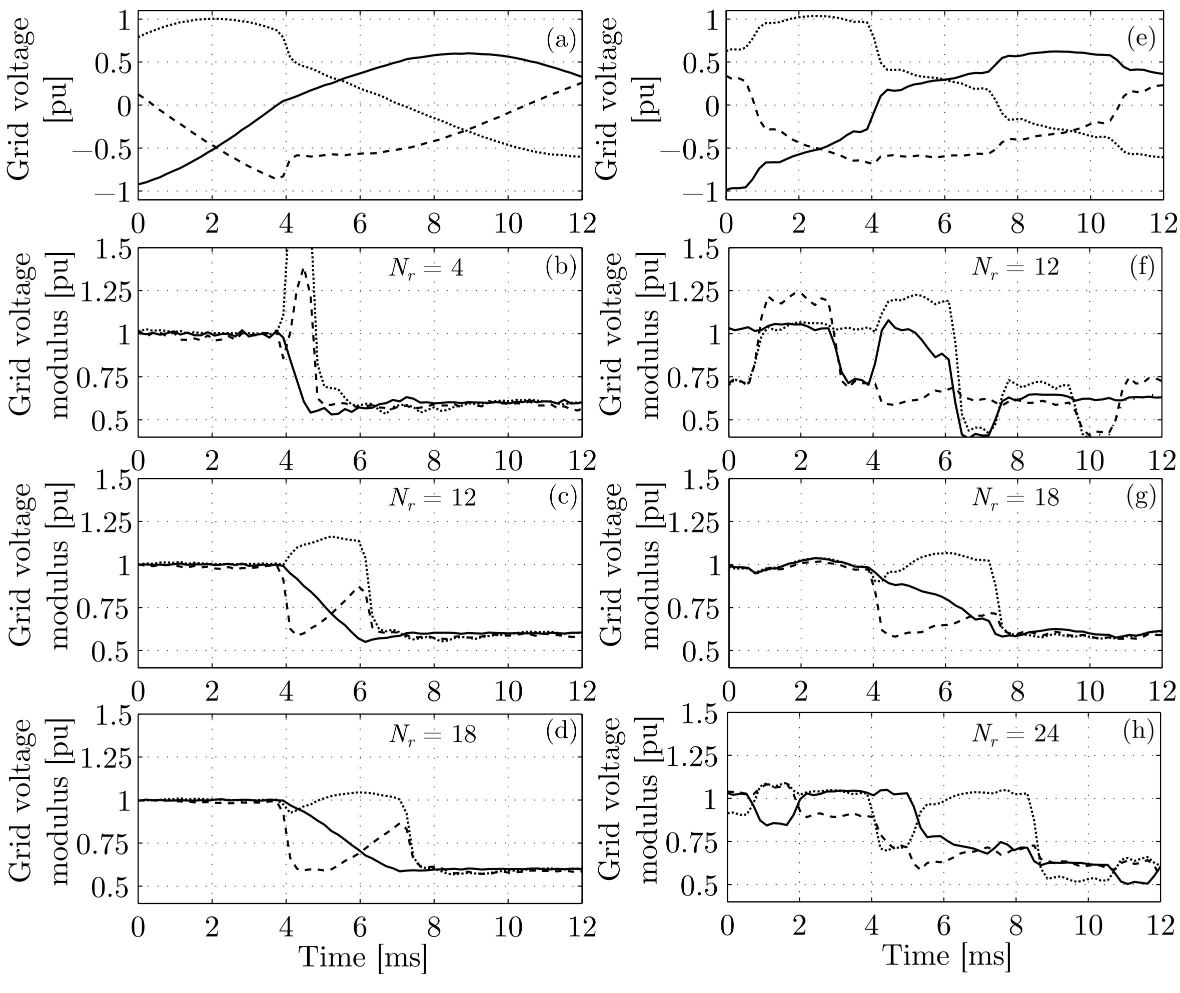

Figure B.2: Performance of the sag detection algorithm for a three-phase voltage sag (60% retained voltage), (a to d) without and (e to h) with harmonics, (solid) phase-a, (dashed) phase-b, and (dotted) phase-c.

Appendix C

Repetitive Controller Proofs

C.1 High-Order Repetitive Controllers

C.1.1 Stability-Based Constraints for HORCs

This analysis is carried out assuming that $Q(z) = 1$ in the RC formulation in Chapter 4. The filter $L(z)$ is included to evaluate its impact on stability. First of all, $|H(e^{j\omega t_s})|$ is computed as follows (see (4.12) for the definition of $H(z)$):

$$\left|H(e^{j\omega t_s})\right| = \left|\sum_{i=1}^{n} W_i L^i(e^{j\omega t_s}) e^{-jNi\omega t_s}\right|. \tag{C.1}$$

Recalling the stability condition in (4.11), it is clear that the stability margins will not be deteriorated if $|H(e^{j\omega t_s})| \leq 1 \; \forall\omega$. Applying the triangular inequality to (C.1) [226]

$$\left|\sum_{i=1}^{n} W_i L^i(e^{j\omega t_s}) e^{-jNi\omega t_s}\right| \leq \sum_{i=1}^{n} \left|W_i L^i(e^{j\omega t_s}) e^{-jNi\omega t_s}\right|, \tag{C.2}$$

and (C.2) becomes

$$|H(e^{jN\omega t_s})| \leq \sum_{i=1}^{n} |W_i| \left|L^i(e^{j\omega t_s}) e^{-jNi\omega t_s}\right|, \tag{C.3}$$

which gives an upper bound for (C.1). Clearly, in (C.3), $|e^{-jNi\omega t_s}| = 1$ and $|L^i(e^{j\omega})| = 1$ $\forall\omega$ when $L(z)$ is implemented using a normalised all-pass filter like in Section 4.5.1. Therefore,

$$\left|L^i(e^{j\omega t_s}) e^{-jNi\omega t_s}\right| = 1. \tag{C.4}$$

Recalling that the right hand side of (C.3) is an upper bound for $|H(e^{j\omega t_s})|$ and taking into account (C.4), it follows that

$$\sum_{i=1}^{n} |W_i| \leq 1, \text{ which implies that } \left|H(e^{j\omega t_s})\right| = \left|\sum_{i=1}^{n} W_i L^i(e^{j\omega t_s}) z^{-jNi\omega t_s}\right| \leq 1. \quad \text{(C.5)}$$

If (C.5) is satisfied, the stability margins related to the HORC will be higher than or equal to those of a RC.

C.1.2 Period-Robust RC Coefficients Derivation

In the period-robust repetitive controller [185]

$$\frac{\partial H(e^{j\omega_g h t_s})}{\partial \omega_g} = 0, \text{ with } h = 1, 2, 3, ..., N/2. \quad \text{(C.6)}$$

Evaluating (C.6):

$$\frac{\partial \left(\sum_{i=1}^{n} W_i e^{-jNi\omega_g h t_s} \right)}{\partial \omega_g} = -\sum_{i=1}^{n} W_i jNih t_s = 0, \quad \text{(C.7)}$$

which can be reduced to

$$\sum_{i=1}^{n} W_i i = 0. \quad \text{(C.8)}$$

For an mth-order HORC, there are m weighting coefficients to select and, therefore, m constraints can be added. Recalling that all the weighting factors must sum one to provide perfect-tracking of harmonics, the first constraint becomes

$$\sum_{i=1}^{n} W_i = 1. \quad \text{(C.9)}$$

Once (C.9) has been added, there are $m-1$ degrees of freedom to select the weighting factors. These degrees of freedom can be used to make $m-1$ derivatives equal zero [185]:

$$\sum_{i=1}^{k} W_i i^{(k-1)} = 0, \text{ with } k = 2, 3, ..., m. \quad \text{(C.10)}$$

Appendix D

Additional Paper: Helping All Generations of Photo-Voltaic Inverters Ride Through Voltage Sags

Abstract

The late Spanish grid code established that, to avoid island operation, renewable power sources had to be disconnected from the grid in the case of a voltage sag. This would threaten the system stability in case of massive penetration of renewable sources and motivated a recent revision of the code. The new code establishes strict ratios between active and reactive currents during the sag and requests that the plant must quickly resume its normal operation, when the voltage sag ends. Existing installations are also affected if they want to enjoy the premiums associated with renewable generation. When full upgrading of existing installations is not practical, this paper proposes a plug-in shunt-connected power electronics device to help solar plants comply with the new grid code, without modifying the solar inverters. The device and its control algorithm are explained in this paper and experimental results using photo-voltaic inverters without low-voltage ride-through capability are presented. Solar inverters remain unaware of the voltage sag and they can be led quickly and smoothly back into the grid when the sag is over.

Keywords – Photovoltaic power systems, Power control, Power convertors, Voltage control

D.1 Introduction

Since 2010, renewable electricity plants in Spain regularly produce more than 20% of the total national demand [1]. This volume has long raised concerns in the power system operator. The previous Spanish grid code established that the renewable generators had to be disconnected from the grid in case of a voltage sag to avoid island operation [2, 3]. This could threaten the system stability with the present and expected levels of penetration of renewable power sources [4]. Massive disconnection of renewable sources can have a disastrous chain effect if they can not be reconnected promptly after the voltage sag is over [5]. Consequently, the new Spanish grid code establishes that, if the voltage sag can be included within the limits of the shadowed part of Fig. D.1 (b), renewable (wind/solar) power plants must [6]:

1. have a reactive current-over-total current ratio during the voltage sag within the shadowed area in Fig. D.1(a) and

2. the power plant must quickly resume the pre-sag generation level, after the sag.

The high ratio Reactive current/Total current during deep sags in Fig. D.1 (a) suggests that the active current injected during the sag must be reduced while adjusting the reactive power injection to comply with the requirements.

Solar plants willing to start operation after 31-12-2011 in Spain have to comply with the new code. Meanwhile, although solar plants scheduled for operation (or already in operation) before that date were built to comply with the previous code, they would need upgrading before 1-1-2013, if they want to enjoy the economic incentives of complying with the new one. The cheapest upgrading alternative would require the manufacturer of the solar inverters to provide ad-hoc modifications of the existing equipment to implement the new features, costing between 4-to-15 € per kW. However,

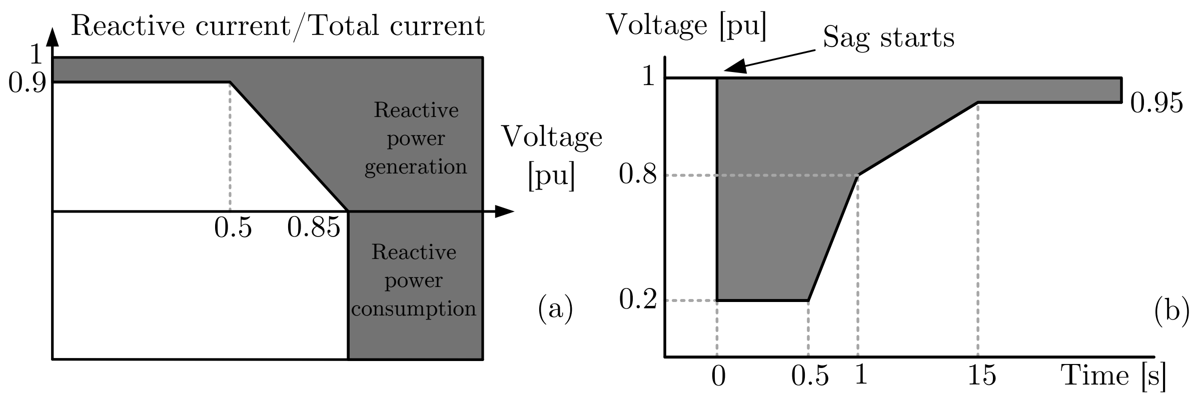

Figure D.1: (a) Reactive current in the new Spanish grid code and (b) sag duration in the new Spanish grid code.

in many occasions, replacement of the obsolete inverters (the ones already in operation that do not comply with the new grid code) may be the only alternative left for the plant owners and plant upgrading may not be cost effective (estimated 110-160 € per kW). This paper proposes a solution to provide the required low-voltage ride-through capability to a group of pre-installed solar inverters (often called photo-voltaic or PV inverters) without depending on the manufacturer's cooperation. The solution is based on a power electronics device and would be more economical than replacing all PV inverters (estimated 55-100 € per kW for a 100 kW inverter), although it will add extra looses to the system.

A voltage compensator in series with the installation to be protected would seem the most natural solution to compensate a voltage sag (Dynamic Voltage Restorer or DVR) as suggested by some industry applications [7, 8, 9, 10]. However, the use of a DVR in a solar application is complicated because the current injected by the PV inverter during the voltage sag (if any) must be mostly reactive (see Fig. D.1 (a)) and, therefore, the DVR should quickly impose a phase rotation to the voltage seen by the PV inverter [10], so the DVR absorbs the excess of active power. Obsolete PV inverters may then interpret this phase rotation as a frequency change which would trigger a shutting-down sequence. Alternatively, this paper proposes a shunt-connected device which resembles an off-line Uninterruptible Power Supply [11]. The proposed device will rapidly substitute the grid and restore the voltage seen by the PV inverters in the case of a voltage sag, so they remain unaware of the abnormal situation. Furthermore, the PV inverters will be quickly and smoothly reconnected to the grid when the sag is over. However, unlike the proposed solution, a DVR could provide short-circuit-current limitation [12]. The proposed device and its control algorithms are explained in detail in the paper and the performance is demonstrated on a 5 kVA prototype with obsolete PV inverters.

D.2 Proposed Solution

D.2.1 Device Topology and Principles

The proposed solution is based on a Voltage Source Converter (VSC) connected between the grid and the PV inverters (Fig. D.2). Upstream the point of connection, there is a static switch (INT) which is normally closed. When a voltage sag occurs, the static switch is opened and the voltage u_g is controlled by the VSC. In this situation, the power injected by the PV inverters will flow into the DC-link capacitor (C_{dc}) and will have to be dissipated in a resistance (R_{dc}) using an auxiliary DC-DC converter. Notice that no active power is injected into the grid, so the application of Fig. D.1 (a) is unnecessary. When the voltage sag ends, u_g will be synchronised with the grid voltage u_s, and the static switch will be closed, providing a soft reconnection. Reactive power

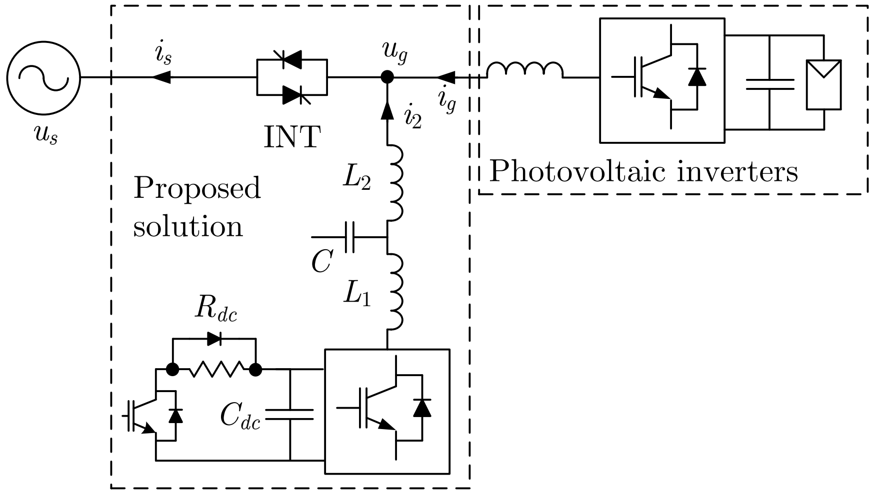

Figure D.2: Schematics of the proposed solution.

can be supplied to the grid during the sag placing a small capacitor upstream the static switch. The different control modes are as follows.

D.2.2 Grid-Connected Controller

Fig. D.3 shows the controller structure without voltage sag. The inverter voltage (u_g) is imposed by the grid ($u_g = u_s$), and the proposed device controls its current (i_2) to provide the required reactive power compensation and to maintain its DC-link charged at the rated value (u_{dc}^*). This situation will be called "current-controlled mode" or CCM in subsequent sections. The AC-current controller is accomplished using a synchronous dq reference frame synchronised with u_g. The active and reactive power injected by the device are [13]:

$$p(t) = i_{2-d}u_{g-d} + i_{2-q}u_{g-q}, \tag{D.1}$$

$$q(t) = i_{2-d}u_{g-q} - i_{2-q}u_{g-d}. \tag{D.2}$$

Typically, $u_{s-q} = 0$ so the active power is controlled with i_{2-d}, and the reactive power with i_{2-q}. Voltage synchronisation requires a Phase Locked Loop (PLL). The d-axis reference current (i_{2-d}^*) is calculated using a DC-link voltage controller, to maintain a constant DC capacitor voltage. The q-axis reference current is calculated from the reactive-power compensation required.

D.2.3 Grid-Isolated Controller

Fig. D.4 depicts the control strategy when the proposed device is isolated from the grid. Voltage (u_g) must remain constant regardless the current injected by the PV

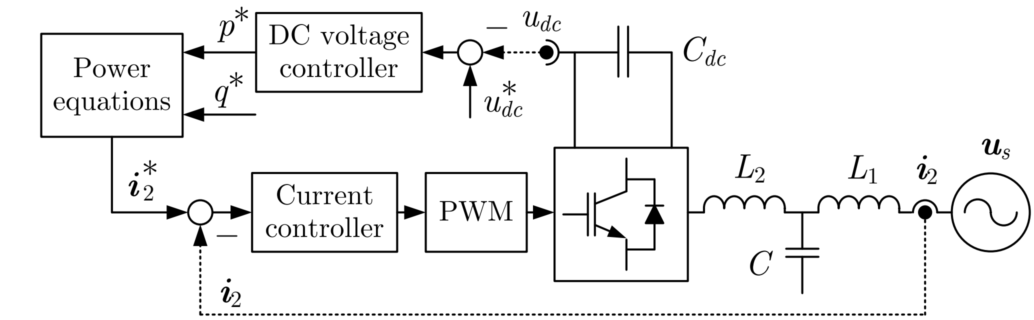

Figure D.3: Block diagram when the proposed device is connected to the grid.

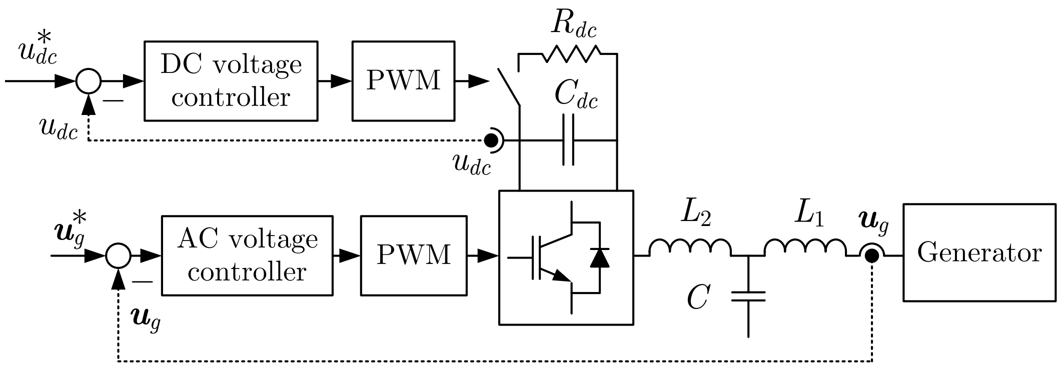

Figure D.4: Block diagram when the proposed device is isolated from the grid.

generator. The DC-link voltage (u_{dc}) is maintained below its maximum specified value (u^*_{dc-brk}) using a DC-DC converter and a resistor, similarly to a braking resistor in motor applications. This situation will be called "voltage-controlled mode" or VCM in subsequent sections. The AC-voltage controller is accomplished using an artificial synchronous reference frame whose initial angle (θ_o) and frequency (ω^*) can be set equal to the pre-sag values to minimise unwanted transients. In this reference frame, the d-axis reference voltage (u^*_{g-d}) is made equal to the grid nominal voltage, and the q-axis reference voltage is $u^*_{g-q} = 0$.

D.3 Controller Elements

D.3.1 Synchronous Reference Frame

Any three-phase magnitude (with subscripts a, b and c), can be represented in vector form using [14]

$$\boldsymbol{y}_{\boldsymbol{\alpha\beta}}(t) = \frac{2}{3}\left(y_a(t) + y_b(t)e^{j\frac{2\pi}{3}} + y_c(t)e^{-j\frac{2\pi}{3}}\right). \tag{D.3}$$

Vector $\boldsymbol{y_{\alpha\beta}}(t)$ (complex number, $y_\alpha + jy_\beta$) is rotating in an α-β plane and can be transformed into a synchronous reference frame using

$$\boldsymbol{y}(t) = e^{-j\omega_s t}\boldsymbol{y_{\alpha\beta}}(t), \tag{D.4}$$

where $\boldsymbol{y}(t)$ contains the vector coordinates in the synchronous reference frame, and ω_s is the synchronous frequency.

D.3.2 State-Variable Modelling

The VSC output voltage often requires LCL or LC filters to provide sufficient attenuation of the switching frequency. These filters have resonances which are not easily tackled using simple PI controllers while state-feedback controllers are a robust and flexible alternative to actively damp these resonances [15], and have been used in the proposed device.

A discrete-time state-space model for a linear system can be written as $\boldsymbol{x}[k+1] = \boldsymbol{\Phi x}[k] + \boldsymbol{\Gamma u}[k]$, where $\boldsymbol{x}[k]$ is the state-variable vector, $\boldsymbol{u}[k]$ is the input vector and $\boldsymbol{\Phi}$ and $\boldsymbol{\Gamma}$ are matrices with constant-value elements which can be obtained from the continuous-time model of the system [16]. This model can be easily expanded to include the integrals of the errors in the variables to be controlled, so a servo-control problem can be tackled. Superscript e will be used to mark the state-space representation of the expanded model in the rest of the paper.

D.3.3 Decoupling Equations

In a synchronous reference frame, d-axis and q-axis dynamics are coupled. The system state-space representation will look like [17]

$$\begin{bmatrix} \boldsymbol{x_d} \\ \boldsymbol{x_q} \end{bmatrix}_{k+1} = \overbrace{\begin{bmatrix} \boldsymbol{\Phi_d} & \boldsymbol{\Phi_c} \\ -\boldsymbol{\Phi_c} & \boldsymbol{\Phi_q} \end{bmatrix}}^{\boldsymbol{\Phi}} \begin{bmatrix} \boldsymbol{x_d} \\ \boldsymbol{x_q} \end{bmatrix}_{k} + \overbrace{\begin{bmatrix} \boldsymbol{\Gamma_d} & \boldsymbol{\Gamma_c} \\ -\boldsymbol{\Gamma_c} & \boldsymbol{\Gamma_q} \end{bmatrix}}^{\boldsymbol{\Gamma}} \begin{bmatrix} u_d \\ u_q \end{bmatrix}_{k}, \tag{D.5}$$

but two virtual inputs $w_d[k]$ and $w_q[k]$ can be used to decouple d- and q-dynamics in (D.5):

$$\begin{bmatrix} \boldsymbol{x_d} \\ \boldsymbol{x_q} \end{bmatrix}_{k+1} = \begin{bmatrix} \boldsymbol{\Phi_d} & \boldsymbol{0} \\ \boldsymbol{0} & \boldsymbol{\Phi_q} \end{bmatrix} \begin{bmatrix} \boldsymbol{x_d} \\ \boldsymbol{x_q} \end{bmatrix}_{k} + \begin{bmatrix} \boldsymbol{\Gamma_d} & \boldsymbol{0} \\ \boldsymbol{0} & \boldsymbol{\Gamma_q} \end{bmatrix} \begin{bmatrix} w_d \\ w_q \end{bmatrix}_{k}. \tag{D.6}$$

Virtual inputs $w_d[k]$ and $w_q[k]$ are calculated by the controllers while the actual system inputs $u_d[k]$ and $u_q[k]$ are computed as

$$\begin{bmatrix} u_d \\ u_q \end{bmatrix}_{k} = \boldsymbol{\Gamma}^{+} \begin{bmatrix} \boldsymbol{\Gamma_d} & \boldsymbol{0} \\ \boldsymbol{0} & \boldsymbol{\Gamma_q} \end{bmatrix} \begin{bmatrix} w_d \\ w_q \end{bmatrix}_{k} - \boldsymbol{\Gamma}^{+} \begin{bmatrix} \boldsymbol{0} & \boldsymbol{\Phi_c} \\ -\boldsymbol{\Phi_c} & \boldsymbol{0} \end{bmatrix} \begin{bmatrix} \boldsymbol{x_d} \\ \boldsymbol{x_q} \end{bmatrix}_{k}, \tag{D.7}$$

where $\mathbf{\Gamma}^+ = (\mathbf{\Gamma}^t\mathbf{\Gamma})^{-1}\mathbf{\Gamma}^t$ denotes the left pseudo-inverse of the non-square matrix $\mathbf{\Gamma}$ (t means transposed).

D.3.4 Incremental Controller

The controller function and parameters must change from CCM to VCM and back to CCM, which can cause large variations in the command signal, and oscillations in the controlled variables. This type of transitions can be eased using incremental controllers [18]. The sate-variable vector must be differentiated as

$$\begin{bmatrix}\Delta \boldsymbol{x_d^e} \\ \Delta \boldsymbol{x_q^e}\end{bmatrix}_k = \begin{bmatrix}\boldsymbol{x_d^e} \\ \boldsymbol{x_q^e}\end{bmatrix}_k - \begin{bmatrix}\boldsymbol{x_d^e} \\ \boldsymbol{x_q^e}\end{bmatrix}_{k-1}, \tag{D.8}$$

and the command must be computed using

$$\begin{bmatrix}w_d \\ w_q\end{bmatrix}_{k+1} = \begin{bmatrix}\boldsymbol{K_d} & \boldsymbol{K_q}\end{bmatrix}\begin{bmatrix}\Delta \boldsymbol{x}_d^e \\ \Delta \boldsymbol{x}_q^e\end{bmatrix}_k + \begin{bmatrix}w_d \\ w_q\end{bmatrix}_k. \tag{D.9}$$

Now, it is enough to change from the voltage-mode gain set ($\boldsymbol{K_d^u}$ and $\boldsymbol{K_q^u}$) to the current-mode set ($\boldsymbol{K_d^i}$ and $\boldsymbol{K_q^i}$) to switch from the CCM to VCM. Only the incremental part of the command signals will changed and a smooth transition can be expected.

D.4 CCM Modelling and Control

The equivalent circuit for the CCM is depicted in Fig. D.5 (INT closed) where the grid is modelled using an ideal voltage source plus an impedance $Z_s \approx R_s + j\omega_s L_s$. Knowledge of Z_s is important in the case of weak grids. A current source (i_g in Fig. D.5) models the PV inverters because they typically use current controllers with integral

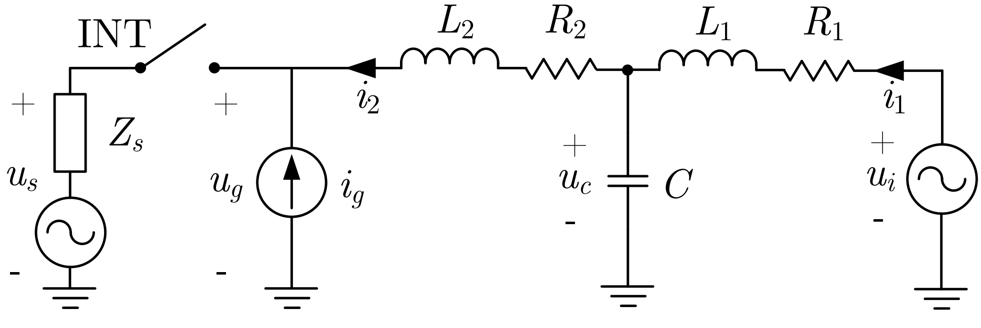

Figure D.5: Schematics for the proposed device in CCM (INT closed) and VCM (INT open).

action [19, 20, 21]. If the PV inverter output impedance is significantly higher than the grid impedance in CCM, one can write

$$\frac{d\boldsymbol{i_1}}{dt} = -\frac{R_1}{L_1}\boldsymbol{i_1} - \frac{\boldsymbol{u_c}}{L_1} + \frac{\boldsymbol{u_i}}{L_1} - j\omega_s\boldsymbol{i_1}, \tag{D.10}$$

$$\frac{d\boldsymbol{u_c}}{dt} = \frac{\boldsymbol{i_1}}{C} - \frac{\boldsymbol{i_2}}{C} - j\omega_s\boldsymbol{u_c}, \tag{D.11}$$

$$\frac{d\boldsymbol{i_2}}{dt} = \frac{\boldsymbol{u_c}}{L_2'} - \frac{R_2'}{L_2'}\boldsymbol{i_2} - \frac{\boldsymbol{u_s}}{L_2'} - j\omega_s\boldsymbol{i_2}, \tag{D.12}$$

where $L_2' = L_2 + L_s$ and $R_2' = R_2 + R_s$, and all variables have been presented using complex numbers. State-variables are $\boldsymbol{i_1}$, $\boldsymbol{u_c}$ and $\boldsymbol{i_2}$, the input is $\boldsymbol{u_i}$ and $\boldsymbol{u_s}$ is a disturbance which will include the effect of $\boldsymbol{i_g}$. Park's transformation produces the coupling terms in (D.10), (D.11), and (D.12) [14], but the state-space model can be discretised and decoupled (see Section D.3). Besides, the delays introduced by the microprocessor (computation) and the anti-aliasing filters can be modelled as a one-sampling-period delay each, on the command (two new state variables: u_i' and u_i'', respectively) [22]

$$\boldsymbol{u_i'}[k+1] = \boldsymbol{u_i}[k]\,, \quad \boldsymbol{u_i''}[k+1] = \boldsymbol{u_i'}[k]\,. \tag{D.13}$$

An integral action is added as a state-variable to achieve zero error in steady-state for the positive sequence components i_2 (one for the d-axis and another one for the q-axis)

$$\boldsymbol{x_i}[k+1] = \boldsymbol{x_i}[k] + t_s\underbrace{(\boldsymbol{i_2^*}[k] - \boldsymbol{i_2}[k])}_{\boldsymbol{e_i}[k]}. \tag{D.14}$$

Although the reference current can be tuned to contain only positive-sequence components, a voltage sag can easily produce a negative-sequence voltage component at the point of coupling [23], and this will generate currents of the same sequence flowing through the shunt converter. These currents have to be tackled adding a resonant controller to the state-variable representation (one for each axis) [24]

$$\begin{bmatrix}\boldsymbol{x_{is}}\\ \boldsymbol{x_{ic}}\end{bmatrix}_{k+1} = \begin{bmatrix}2\cos(\omega_r t_s) & 1\\ -1 & 0\end{bmatrix}\begin{bmatrix}\boldsymbol{x_{is}}\\ \boldsymbol{x_{ic}}\end{bmatrix}_k + \begin{bmatrix}0\\1\end{bmatrix}\boldsymbol{e_i}[k]\,, \tag{D.15}$$

where ω_r is the resonant frequency of the resonant controller ($\omega_r = 2\omega_s$ rad/s). The extended state-variable vector for the d axis is shown below (a similar one can be written for the q axis)

$$\boldsymbol{x_d^e} = \left[i_{1-d}\; u_{c-d}\; i_{2-d}\; u_{i-d}'\; u_{i-d}''\; x_{i-d}\; x_{is-d}\; x_{ic-d}\right]^t. \tag{D.16}$$

The controller gains ($\boldsymbol{K_d^i}$ and $\boldsymbol{K_q^i}$) can be calculated using a pole-placement algorithm in the current-mode extended state-space representation.

D.5 VCM Modelling and Control

The equivalent electrical circuit for the VCM is depicted in Figure D.5 (open INT), and can be described using (D.10), (D.11), and

$$\boldsymbol{u_g} = \boldsymbol{u_c} - R_2 \boldsymbol{i_2} - L_2 \frac{d\boldsymbol{i_2}}{dt} + jL_2 \omega_s \boldsymbol{i_2}. \tag{D.17}$$

State variables are $\boldsymbol{i_1}$ and $\boldsymbol{u_c}$, and the input is $\boldsymbol{u_i}$. Again, all variables are written as complex numbers. The current through the inductor L_2 ($\boldsymbol{i_2}$) is not considered a state variable because this inductance is in series with a current source. Since the PV inverter current is used as a feed-forward signal by the auxiliary converter, the interaction between both converters should be ameliorated but it has to be assessed for each installation to be protected. The voltage drop across the output inductor (L_2) has some negative impact on $\boldsymbol{u_g}$, which can be reduced, if necessary, modelling $\boldsymbol{i_2}$ and $d\boldsymbol{i_2}/dt$ as input variables. Finally, the computation delay and the delay introduced by the anti-aliasing filters can be modelled as in the CCM case (D.13).

To achieve zero steady-state error for the positive-sequence voltage references, an integral controller can be added to the VCM state-space representation:

$$\boldsymbol{x_u}[k+1] = \boldsymbol{x_u}[k] + t_s \underbrace{\left(\boldsymbol{u_g^*}[k] - \boldsymbol{u_g}[k]\right)}_{\boldsymbol{e_u}[k]}. \tag{D.18}$$

The reference voltage ($\boldsymbol{u_g^*}$) will not contain negative sequence components but the current injected by the PV inverters can cause a negative-sequence voltage drop on the LCL filter. This disturbance can be rejected using a resonant controller (one for each axis):

$$\begin{bmatrix} \boldsymbol{x_{us}} \\ \boldsymbol{x_{uc}} \end{bmatrix}_{k+1} = \begin{bmatrix} 2\cos(\omega_r t_s) & 1 \\ -1 & 0 \end{bmatrix} \begin{bmatrix} \boldsymbol{x_{us}} \\ \boldsymbol{x_{uc}} \end{bmatrix}_{k} + \begin{bmatrix} 0 \\ 1 \end{bmatrix} \boldsymbol{e_u}[k], \tag{D.19}$$

giving a state-variable vector for the VCM (d-axis shown),

$$\boldsymbol{x_d^e} = \left[i_{1-d}\ u_{c-d}\ u'_{i-d}\ u''_{i-d}\ x_{u-d}\ x_{us-d}\ x_{uc-d}\right]^t. \tag{D.20}$$

The AC-voltage controllers can be designed as two independent state-feedback controllers (one for the d-axis, and another one for the q-axis), obtaining the values of $\boldsymbol{K_d^v}$ and $\boldsymbol{K_q^v}$. Nevertheless, it is worth mentioning that, if the PV inverter generates harmonic currents, additional resonant controllers should be added to the control system in order to avoid harmonic voltage drops.

D.6 DC-Voltage Modelling and Control

D.6.1 DC-Voltage Controller in CCM

The energy absorbed from/released into the grid in CCM can be controlled modifying the d-axis reference current (i^*_{2-d}). Any energy absorption will increase the DC capacitor voltage, so the total energy stored is $E_{dc} = (1/2)C_{dc}u^2_{dc}$, and

$$\frac{dE_{dc}}{dt} = \frac{1}{2}C_{dc}\frac{du^2_{dc}}{dt} = -p_{loss} - p_{ext}, \tag{D.21}$$

where p_{ext} is the power exchanged with the grid and p_{loss} are the device losses. If u^2_{dc} is chosen as the controlled variable, (D.21) is linear. Finally, the d-axis reference current can be calculated as ($i^*_{2-d} = p_{ext}/u_{s-d}$).

D.6.2 DC-Voltage Controller in VCM

In VCM the energy coming from the PV inverter needs to be handled by a resistor (R_{dc}) with an on-time controlled by a power switch. An average-variable model is

$$C_{dc}\frac{d\overline{u}_{dc}}{dt} = -\frac{D\overline{u}_{dc}}{R_{dc}} - \overline{i}_i, \tag{D.22}$$

where D is the duty ratio of the DC-DC converter, and $\overline{u}_{dc}$ and $\overline{i}_i$ are the average DC voltage and current, respectively. Equation (D.22) can be linearised and the DC-link voltage can be controlled using a PI controller.

D.7 Synchronous Reference Frame Generation

In CCM pre-sag situation, the proposed device has to be synchronised with the grid voltage because everything has to be described in a synchronously-rotating reference frame and, when the sag is over, synchronisation with the grid voltage is necessary because transferring the PV inverter to the grid has to be done quickly but smoothly. Only during the sag, synchronisation is not relevant because the shunt converter imposes the voltage. A Phase Locked Loop (PLL) is used to estimate the grid angle (θ_{pll}) to synchronise with the grid and to perform Park's transformations. A Dual Second Order Generalised Integrator PLL (DSOGI-PLL) has been used here [25]. In CCM, the angle estimated by the PLL (θ_{pll}) is directly used for the system reference frame, then $\theta = \theta_{pll}$.

When a voltage sag takes place, the grid angle can have a phase jump. To mitigate its effect on the PV inverters, the restored voltage reference frame should start in-phase with the pre-sag reference-frame. Once the system is in VCM, the PLL angle is frozen and the actual angle (θ) would be the integral of the grid nominal frequency

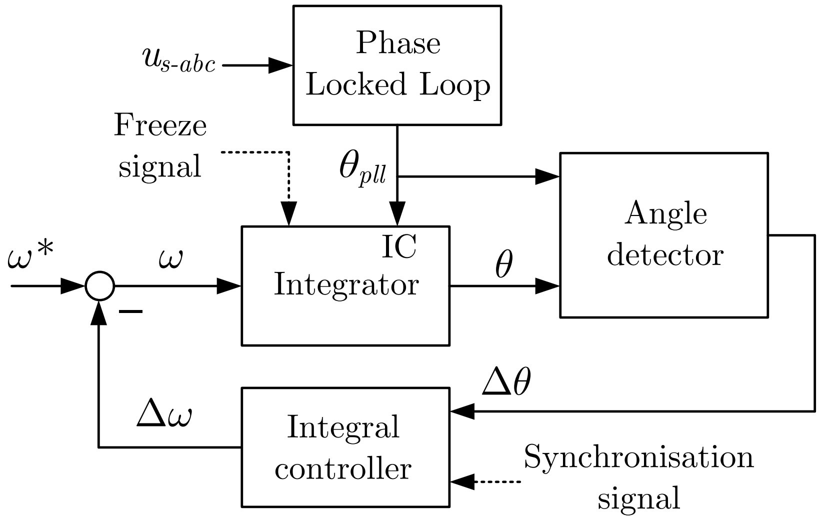

Figure D.6: Block diagram of the reference-frame generation to control the proposed device.

$(\omega = \omega^*)$. The initial condition for this integration is the last sample of the grid angle (θ_{pll}). The process is in the block called "Integrator", in Fig. D.6. Once the grid voltage has recovered, the synchronisation signal is activated (see Figure D.6), and the actual angle (θ) can be computed as the integral of (ω). This angle can be accelerated (or decelerated) adding $\Delta\omega$, together with an integral controller as in

$$\theta = \int \overbrace{(\omega^* + \Delta\omega)}^{\omega} dt, \text{ with } \Delta\omega = K_\theta \int \overbrace{(\theta_{pll} - \theta)}^{\Delta\theta} dt, \tag{D.23}$$

where K_θ controls how fast the difference between θ and θ_{pll} is reduced. K_θ has to be small enough not to disturb the PV inverter operation during the synchronisation. $\Delta\theta$ can be more easily computed using

$$\Delta\theta \approx \sin\Delta\theta = \sin(\theta_{pll})\cos(\theta) - \cos(\theta_{pll})\sin(\theta). \tag{D.24}$$

Fig. D.7 shows the simulation results for the synchroniser when an unbalance voltage sag occurs. The device takes a few milliseconds to swap the controller after the sag is detected. Once the controller has changed, θ grows linearly. When the sag ends, the synchronisation signal is activated and θ is synchronised with the grid angle θ_{pll}. Reconnection takes place when $\theta = \theta_{pll}$, and the reference frame angle (θ) remains equal to the PLL angle (θ_{pll}).

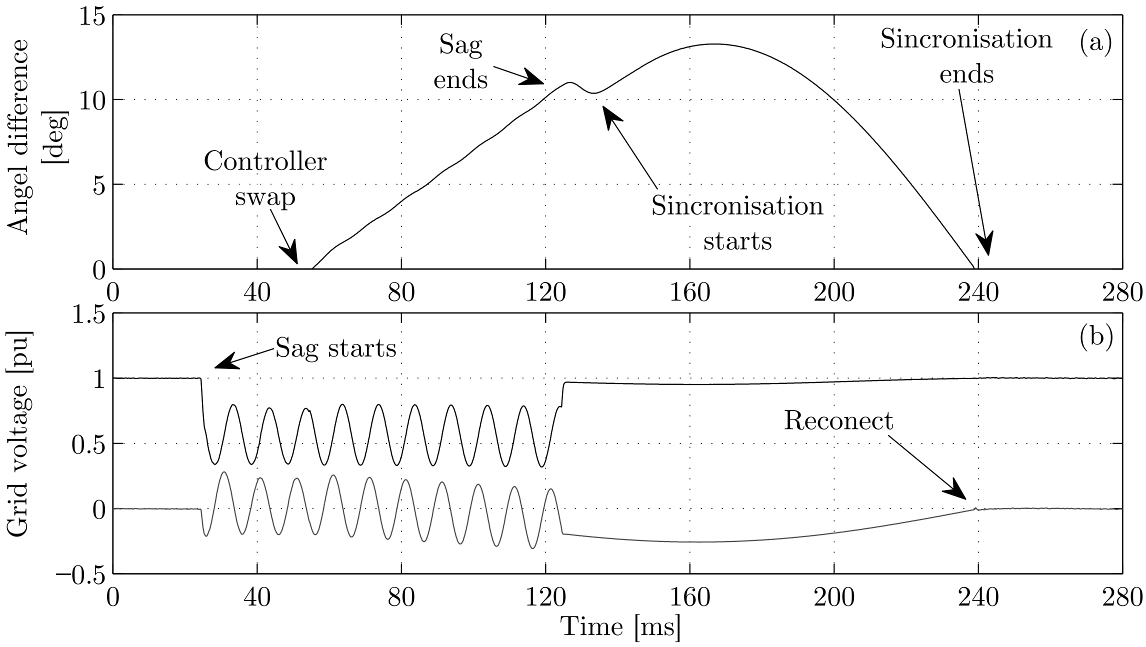

Figure D.7: (a) Difference between θ_{pll} and θ during an unbalanced voltage sag and (b) grid voltage d-axis (black) and q-axis (grey).

D.8 Prototype Description

A prototype with base magnitudes of 5 kVA and 230 V (Fig. D.2) has been built. The grid is produced with an AMX-Pacific 3120 three-phase voltage source to which an auxiliary three-phase shunt resistance has been added to avoid power flow into the power source. Weak-grid conditions have been emulated with an inductor in series with the power source. The static switch (INT) consists of three single-phase SCR-based Solid State Relays (SSR) rated at 30 Amps. The PV plant has been emulated with three single-phase PV inverters Fronious IG-30 with Maximum Power Point (MPP) search. The PV inverters were connected to the grid using a transformer. The energy has been supplied to the PV inverters using three single-phase diode rectifiers with a high inductor in the AC-side to limit the power injected by the PV inverters.

The parameters of the prototype are: $L_1 = 4$ mH, $L_2 = 1.5$ mH, $C = 30$ μF, $C_{dc} = 1.3$ mF, $R_{dc} = 17$ Ω, $L_s = 0.7$ mH.

D.9 Results

A symmetric three-phase voltage sag (20 % retained voltage) is shown in Fig. D.8 and Fig. D.9. Before the sag, the current of the PV inverters is equal to the grid current (no reactive power injected). When the voltage sag starts, the PV-inverter current and the

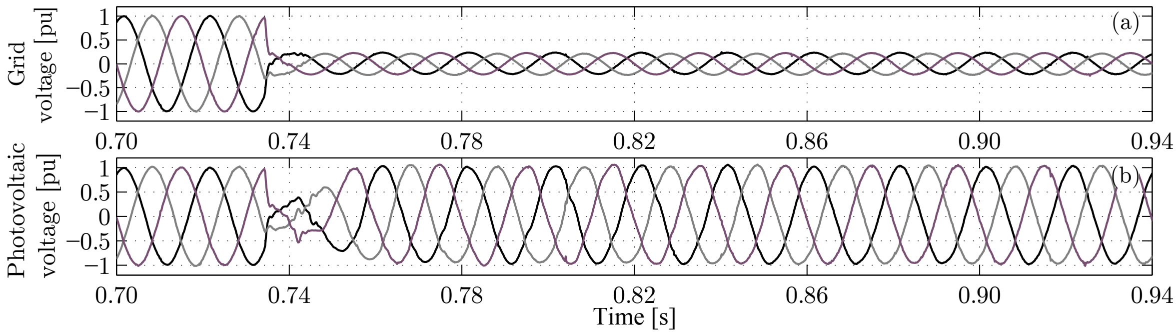

Figure D.8: Three-phase voltage sag: (a) grid voltage and (b) PV inverter voltage.

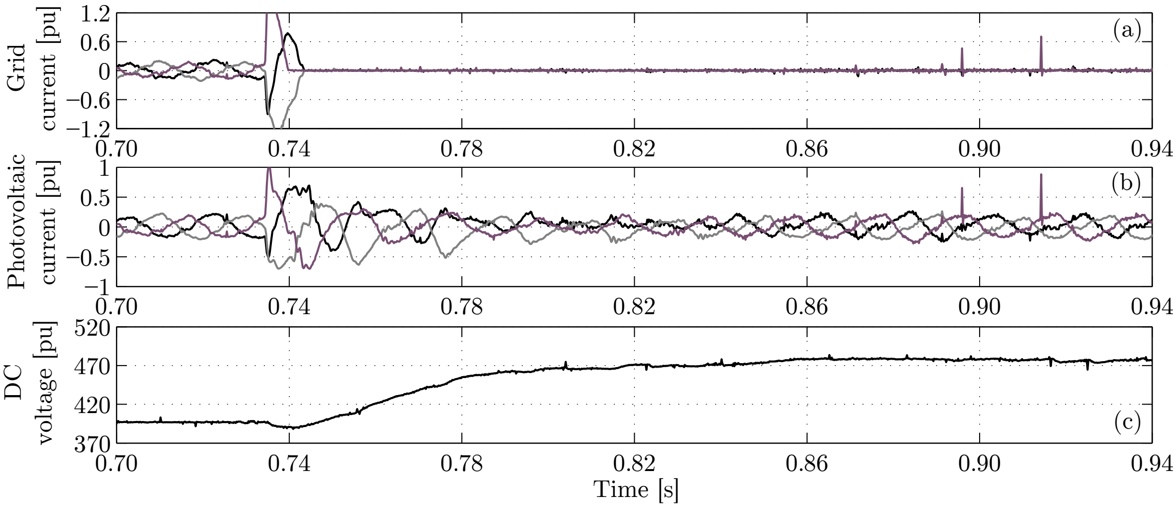

Figure D.9: Three-phase voltage sag: (a) grid current, (b) PV-inverter current, and (c) DC voltage.

proposed device current increase rapidly. After a few milliseconds, when the voltage sag is detected, the SSRs are ordered to open and they are eventually opened at the next zero crossing. Thereafter, the current injected by the PV inverters flows into the proposed device increasing the DC voltage till the DC-DC converter starts. Meanwhile, the AC voltage controller of the shunt converter takes the PV-plant voltage (u_g) to its nominal value in spite of the transient behaviour of the current of the PV inverters. After 100 ms, the current provided by the PV inverters returns to its pre-sag value.

Reconnection is shown in Fig. D.10. Once the grid voltage has recovered, the voltage u_g is accelerated until $u_g = u_s$ when the INT is closed and the group of PV inverters are reconnected to the grid. From this point, the DC-voltage level returns, gradually, to its nominal value. The exact moment of reconnection is clearly marked when the angle difference in Fig. D.10 (d) reaches 0.

Fig. D.11 investigates the previous three-phase voltage sag using a synchronous

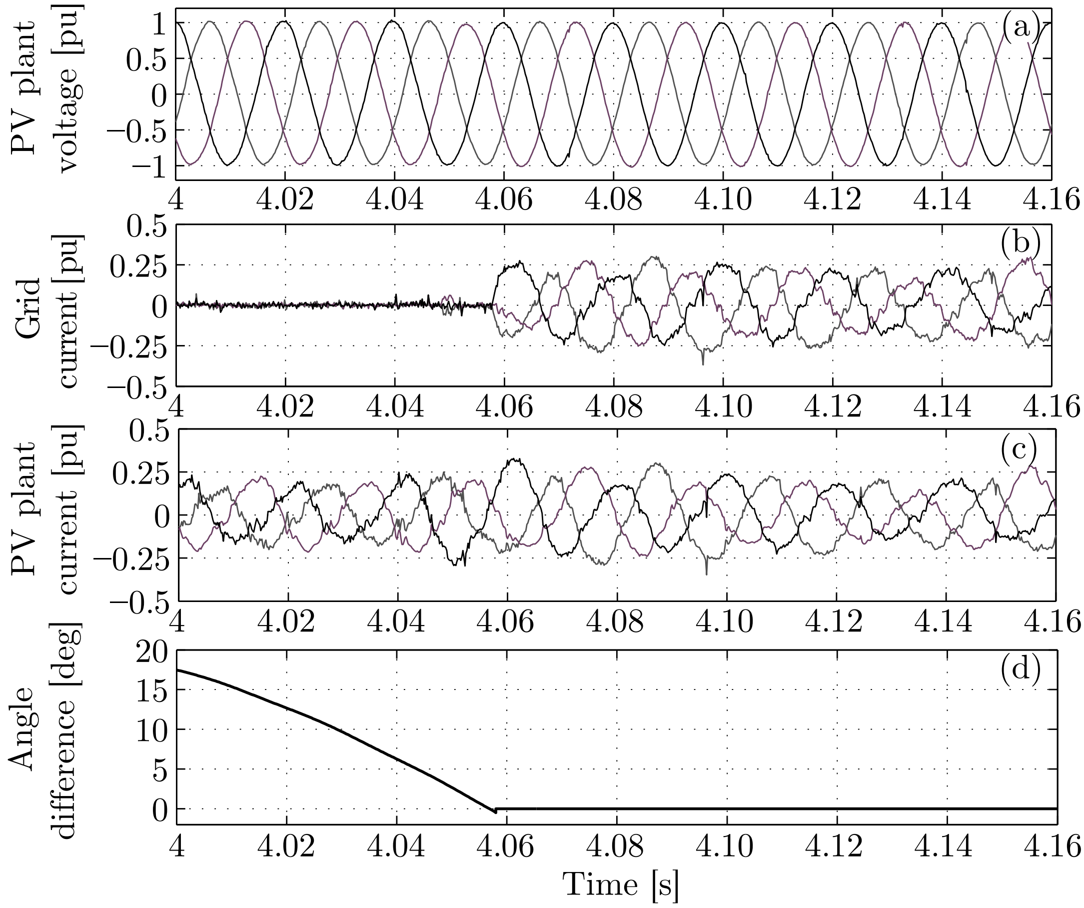

Figure D.10: Reconnection: (a) PV-inverter voltage, (b) grid current, (c) PV current, and (d) angle difference between the grid and the PV inverters.

reference frame. When the voltage sag starts, the PV-inverter voltage is rapidly restored to its nominal value (1 pu). During the sag, the power (d-axis current) flows from the PV inverters to the auxiliary device. The power delivered to the grid after the voltage sag is the same as it was before the sag. The time instants when the controllers are changed can be clearly identified when the angle difference in Fig. D.11 (d) takes off (CCM to VCM) and when it lands (VCM to CCM).

Fig. D.12 shows an unbalance voltage sag. The 100-Hz components in dq are due to the grid voltage negative components but the transient is similar to the case of a balanced voltage sag.

The PV-inverter protection systems were all in place during this experiments proving that the inverters remain unaware of the disturbances.

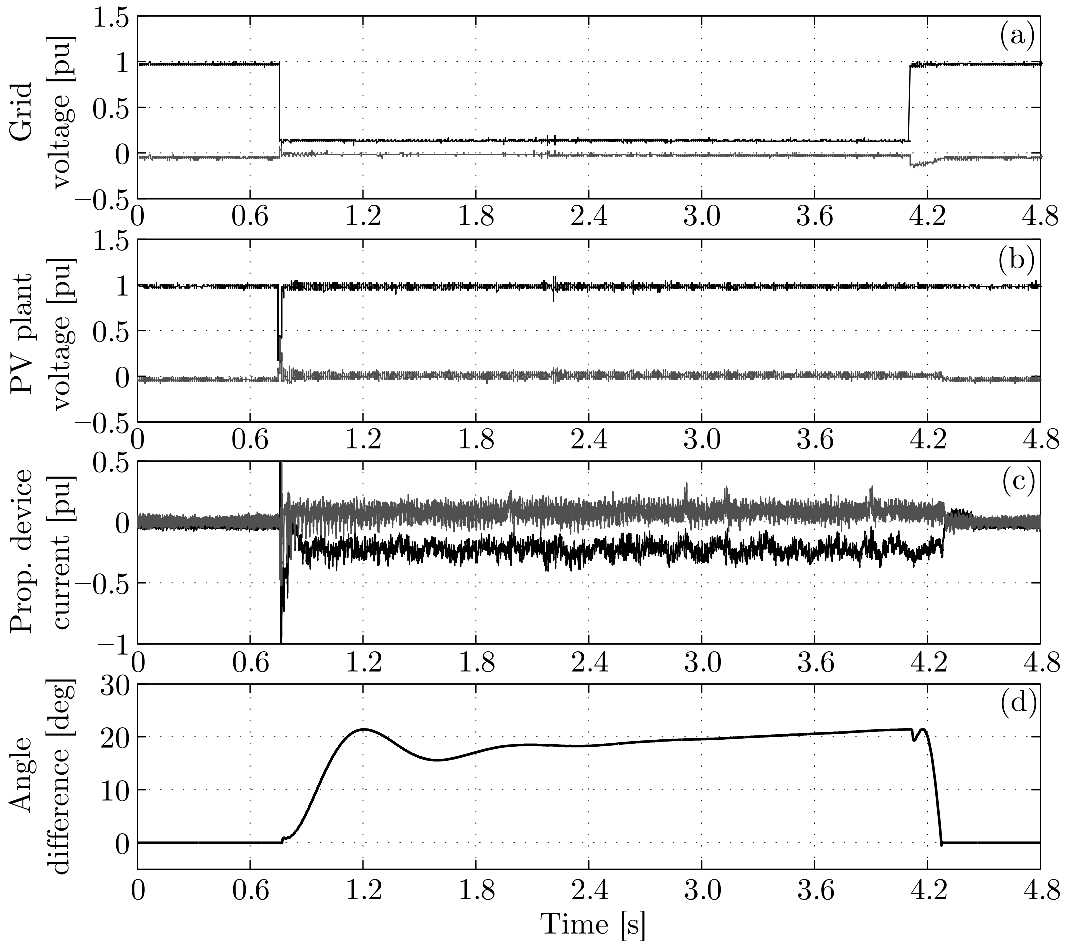

Figure D.11: Three-phase voltage sag. (a) (black) d-axis and (grey) q-axis of the grid voltage, (b) PV-inverter voltage, (c) proposed device current, and (d) angle difference between the grid and the PV inverters.

D.10 Conclusion

This paper has presented a shunt-connected power electronics device which can help existing PV inverters to comply with the new Spanish grid code. When the voltage sag is detected, this device isolates the solar plant and restores the voltage at the PV inverter output before the protection system can detect any disturbance. During the sag, the solar inverters pour their power into the DC-link of the proposed device, and the power not used is dissipated in a resistance with an auxiliary DC-DC converter. When the voltage sag is over, the solar plant is smoothly-but-quickly reconnected to the grid. The experimental results show that the new grid objectives are complied in a 5 kVA prototype for different types of voltage sags.

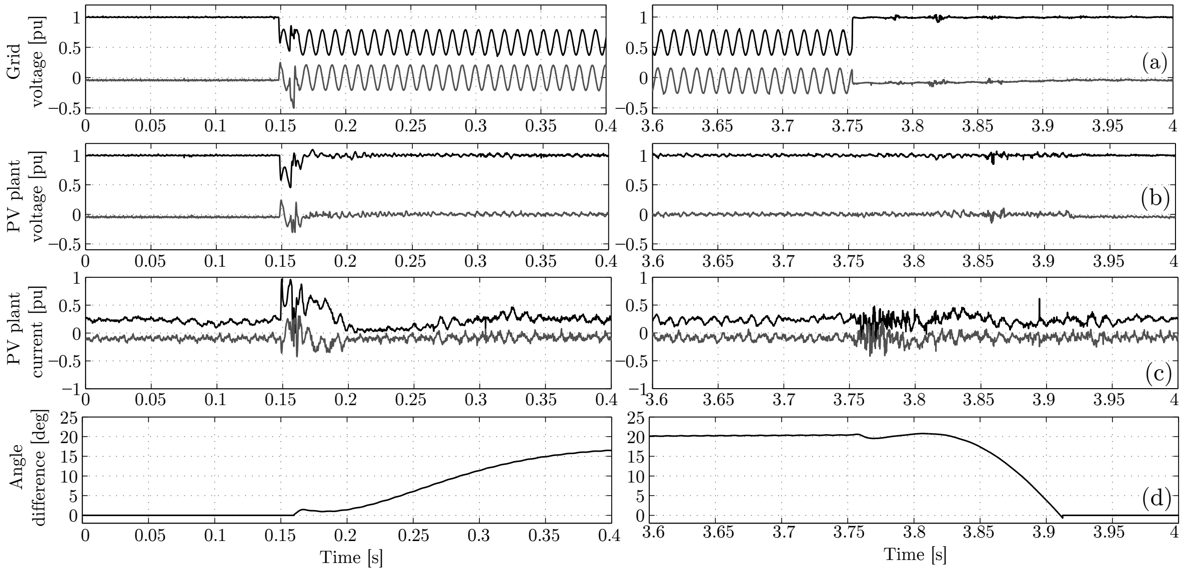

Figure D.12: Unbalanced voltage sag beginning and end: (a) d-axis (black) and q-axis (grey) of the grid voltage, (b) PV-inverter voltage, (c) PV-inverter current, and (d) phase difference between the grid and PV inverters.

Acknowledgments

Thanks are due to INDRA for the financial support in this project and to the Spanish Government's R & D programme that supports the Power Electronics Laboratory (ENE2011-28527-C04-01).

Bibliography

[1] Barroso, L., Rudnick, H., Sensfuss, F., Linares P.: 'The Green Effect', IEEE Power and Energy Magazine, 2010, 8, (5), pp. 22–35.

[2] Carrasco, J., Franquelo, L., Bialasiewicz, J., Galván, E, Portillo Guisado, R., Martín Prats, M. A., León, J. I., Moreno-Alfonso, N: 'Power-Electronic Systems for the Grid Integration of Renewable Energy Sources: A Survey', IEEE Transactions on Industrial Electronics. 2006, 53, (4), pp. 1002–1016.

[3] Estebanez, E. J., Moreno, V. M., Pigazo, A., Liserre, M., Dell'Aquila, A.: 'Performance Evaluation of Active Islanding-Detection Algorithms in Distributed-Generation Photovoltaic Systems: Two Inverters Case', IEEE Transactions on Industrial Electronics, 2011, 58, (4), pp.1185–1193.

[4] Morales, A., Robe, X., Sala, M., Prats, P., Aguerri, C., Torres, E.: 'Advanced grid requirements for the integration of wind farms into the Spanish transmission system', IET Renewable Power Generation, 2008, 2, (1), pp. 47–59.

[5] Eriksen, P. B., Ackermann, T., Abildgaard, H., Smith, P., Winter, W., Rodriguez Garcia, J. M.: 'System operation with high wind penetration', IEEE Power and Energy Magazine, 2005, 3, (6), pp. 65–74.

[6] Red Eléctrica de España (REE). Procedimiento de Operación 12.3 (P.O. 12.3). 'Requisitos de respuesta frente a huecos de tensión de las instalaciones de producción de régimen especial,', BOE 254, 18485, 24-12-2006, pp. 37017–37019.

[7] Nielsen, J. G., Blaabjerg, F.: 'A detailed comparison of system topologies for dynamic voltage restorers', IEEE Transactions on Industry Applications, 2005, 41, (5), pp. 1272–1280.

[8] Roncero-Sánchez, P., Acha, E.: 'Dynamic Voltage Restorer Based on Flying Capacitor Multilevel Converters Operated by Repetitive Control', IEEE Transactions on Power Delivery, 2009, 24, (1), pp. 277–284.

[9] Roldán-Pérez, J., García-Cerrada, A., Zamora-Macho, J. L., Roncero-Sánchez, P., Acha, E.: 'Troubleshooting a digital repetitive controller for a versatile dynamic voltage restorer', International Journal of Electrical Power & Energy Systems. 2014, 57, (0), pp. 105–115.

[10] Ramirez, D., Martinez, S., Platero, C. A., Blazquez, F., de Castro, R. M.: 'Low-Voltage Ride-Through Capability for Wind Generators Based on Dynamic Voltage Restorers', IEEE Transactions on Energy Conversion, 2011, 26, (1), pp. 195–203.

[11] Kwon, B. H., Choi, J. H., Kim, T. W.: 'Improved single-phase line-interactive UPS', IEEE Transactions on Industrial Electronics, 2001, 48, (4), pp. 804–811.

[12] Li, Y. W., Vilathgamuwa, D. M., Loh, P. C., Blaabjerg, F.: 'A Dual-Functional Medium Voltage Level DVR to Limit Downstream Fault Currents', IEEE Transactions on Power Electronics, 2007, 22, (4), pp. 1330–1340.

[13] Akagi, H., Kanazawa, Y., Nabae, A.: 'Instantaneous Reactive Power Compensators Comprising Switching Devices without Energy Storage Components', IEEE Transactions on Industry Applications, 1984, IA-20, (3), pp. 625–630.

[14] Krause, P. C., Wasynczuk, O., Sudhoff, S. D.: 'Analysis of Electric Machinery and Drive Systems', (Wiley-IEEE Press, 2002, 2nd. ed., New York).

[15] Dannehl, J., Fuchs, F. W., Thogersen, P. B.: 'PI State Space Current Control of Grid-Connected PWM Converters With LCL Filters', IEEE Transactions on Power Electronics, 2010, 25, (9), pp. 2320–2330.

[16] Åström, KJ, Wittenmark, B.: 'Computer Controlled Systems', (Prentice-Hall; 2011, Upper Saddle River, NJ).

[17] García-González, P., García-Cerrada, A.: 'Control system for a PWM-based STATCOM', IEEE Transactions on Power Delivery, 2000, 15, (4), pp. 1252–1257.

[18] Åström, K. J., Hagglund, T.: 'PID Controllers: Theory, Design, and Tuning', (International Society for Measurement and Control, 1995, 2nd ed., Research Triangle Park, NC).

[19] Timbus, A., Liserre, M., Teodorescu, R., Rodríguez, P., Blaabjerg, F.: 'Evaluation of Current Controllers for Distributed Power Generation Systems', IEEE Transactions on Power Electronics, 2009, 24, (3), pp. 654–664.

[20] Vasquez, J., Mastromauro, R., Guerrero, J., Liserre, M.: 'Voltage Support Provided by a Droop-Controlled Multifunctional Inverter', IEEE Transactions on Industrial Electronics, 2009, 56, (11), pp. 4510–4519.

[21] Castilla, M., Mire, J., Sosa, J. L., Matas J., de Vicuña, L. G.: 'Grid-Fault Control Scheme for Three-Phase Photovoltaic Inverters With Adjustable Power Quality Characteristics', IEEE Transactions on Power Electronics, 2010, 25, (12), pp. 2930–2940.

[22] Garcia-Cerrada, A., Pinzon-Ardila, O., Feliu-Batlle, V., Roncero-Sanchez, P., Garcia-Gonzalez, P.: 'Application of a Repetitive Controller for a Three-Phase Active Power Filter', IEEE Transactions on Power Electronics, 2007, 22, (1), pp. 237–246.

[23] Sannino, A., Bollen, M., Svensson, J.: 'Voltage Tolerance Testing of Three-Phase Voltage Source Converters', IEEE Transactions on Power Delivery, 2005, 20, (2), pp. 1633–1639.

[24] Lascu, C., Asiminoaei, L., Boldea, I., Blaabjerg, F.: 'High Performance Current Controller for Selective Harmonic Compensation in Active Power Filters', IEEE Transactions on Power Electronics, 2007, 22, (5), pp. 1826–1835.

[25] Teodorescu, R., Liserre, M., Rodríguez, P.: 'Grid Converters for Photovoltaic and Wind Power Systems', (Wiley, 2011, Chichester).